SiC Growth by Laser CVD and Process Analysis

A Thesis
Presented to
The Academic Faculty

by

Jian Mi

In Partial Fulfillment
of the Requirements for the Degree
Doctor of Philosophy

The George W. Woodruff School of Mechanical Engineering
Georgia Institute of Technology
May 2006

SiC Growth by Laser CVD and Process Analysis

Approved by:

Dr. W. Jack Lackey
Advisor
School of Mechanical Engineering
Georgia Institute of Technology

Dr. Joe K. Cochran
School of Material Science and Engineering
Georgia Institute of Technology

Dr. Steven Danyluk
School of Mechanical Engineering
Georgia Institute of Technology

Dr. Andrei G. Fedorov
School of Mechanical Engineering
Georgia Institute of Technology

Dr. David W. Rosen
School of Mechanical Engineering
Georgia Institute of Technology

Dr. ZhongLin Wang
School of Material Science and Engineering
Georgia Institute of Technology

Date Approved 04/05/2006

This thesis is dedicated to my husband Fang Li, who gives me unbelievable assistance without any hesitation. He is always there for me no matter what happens. I will cherish his love and support forever.

ACKNOWLEDGEMENTS

The research of this thesis would not even be possible without the help of many people. The first and the most important person that make this happened is Dr. Lackey, my Ph.D. advisor. Without him, I even could not continue my Ph.D study. He is the most helpful advisor ever from my point of view. His solid experience of CVD-SiC made my research as smooth as possible. He is my model not just for how to do research, but also for how to be a human being. The five years of study in his group is the most important and unforgettable time in my life.

In addition to Dr. Lackey, I want to thank my Ph.D reading committee members for their suggestions and their time. They are Professor Joe K. Cochran, Professor Steven Danyluk, Professor Andrei G. Fedorov, Professor David W. Rosen, and Professor ZhongLin Wang.

I must thank Dr. Ryan Johnson, a prior student of our lab. He is the one who offered me all of the knowledge for operating the LCVD equipment and helped me fix the equipment. I would also like to thank all of my other lab mates for their support and advice. They are Dr. Chad Duty, Dr. Dan Jean, Dr. Mingxuan Jiang, Dr. Scott Bondi, Mr. Joshus Gillespie, Mr. David Beaulieu, and Mr. Tarek Elkhatib.

There are so many people who helped me to characterize the SiC deposits. Dr. Lisa Detter-Holkin from GTRI kindly gave the training and access for using their SEM. She helped me solve many material characterization problems. Dr. Iuliana Cernatescu from MSE helped me do the XRD examination of the SiC fibers. Dr. Ding Yong from MSE helped me perform the TEM studies of LCVD samples. Their assistance is greatly appreciated.

Finally I must thank my parents Mr. Zhonghua Mi and Mrs. Yanglin Li for their unconditional support and love. Without them, everything that I have would not be possible. It is them who gave me the confidence and courage to pursue whatever I want. Finally, I also want to thank my dear little brother Shuo Mi for his support.

TABLE OF CONTENTS

LIST OF TABLES

LIST OF FIGURES

SUMMARY

Laser Chemical Vapor Deposition (LCVD) is capable of fabricating small complex shaped parts with various materials. LCVD is derived from the conventional Chemical Vapor Deposition (CVD) process. Instead of uniformly heating the substrate as with the CVD process, LCVD utilizes a laser to locally heat the substrate and cause a small amount of material to be deposited on the substrate. The LCVD technique is one of several candidates for rapid prototyping ceramic or metal parts.

The goal of this research was to investigate how to deposit SiC material from a methyltrichlorosilane (MTS) and H_2 mixture using the LCVD technique. Two deposit geometries were targeted. One is a SiC fiber, and the other is a SiC line. Through preliminary experiments, it was found that the volcano effect is a major problem for LCVD-SiC deposition. In order to solve this problem, a thermodynamics model was developed to determine the feasibility of eliminating the volcano effect. In addition, it also provided the deposiiton temperature ranges that will not cause the volcano effect, theoretically. With the aid of the thermodynamic calculations and further experimental explorations, the processing conditions for SiC fibers and lines without the volcano effect were found. It was shown that fibers no possessing the volcano effect could be deposited for H_2 to MTS ratios of 10 and 20 by keeping the maximum deposition temperature below 1400 K. For lines, the above conditions produced volcano-free deposits when the laser scan speed was in the range 0.04 to 0.08 in/min. The experimental relationships between the volcano effect and the deposition temperatures were achieved. As for the SiC lines, the deposition conditions for eliminating the volcano effect were determined with the help of surface response experiments and the experience of SiC fiber depositions.

The LCVD process of SiC deposition was characterized by performing a kinetic study of SiC deposition. Multiple regression permitted determination of the influence of temperature and the MTS concentration on deposition rate. The resulting equation was shown in

Equation (1).

$$J = 216e^{(-163/RT)}C_{MTS}^{0.36} \tag{1}$$

The deposits were characterized by polishing, chemical etching, and examination via SEM. A coupled thermal and structural model was created to calculate the thermal residual stress present in the deposits. Except for the bottom surface of the fiber, the maximum thermal residual stress within the main body of the SiC fiber was predicted to be about 500 MPa. This value is smaller than the reported tensile strength of CVD-SiC. This means that there should be no cracks generated within the main body of the LCVD-SiC fibers, which was verified repeatedly by the experiments.

The successfully deposited SiC fibers and lines are the prerequisite for complex SiC structures prepared with the LCVD technique.

CHAPTER I

INTRODUCTION

Silicon carbide (SiC) is an outstanding material with extensive potential applications. It is extremely hard, with good thermal conductivity, and excellent resistance to corrosion and thermal shock. Therefore, it is presently being used or considered primarily for use in critical parts for uncooled gas turbine and adiabatic diesel engines and high temperature bearings. It also has high electrical breakdown field and a wide band gap energy, which make it a good candidate for semiconductor devices, especially for high temperature, high frequency, and high power electronic applications.

For structural applications, SiC can be processed by different sintering techniques. For example pressure-less sintering, reaction sintering, etc., or by hot pressing. Because of its strong covalency, SiC is difficult to sinter to high density unless sintering aids are added. SiC can also be processed by the CVD (Chemical Vapor Deposition) technique using different kinds of precursors. CVD-SiC has much better material properties than material made by sintering or hot-pressing. Single crystal SiC wafers have been commercialized since 1991 by Cree Research, Inc and ATMI using the seeded sublimation method. [1], [2], [3] Because single crystal SiC boule grown from either a melt or solution would require excessive temperatures (>3200°C) and very high pressures(>100,000 atm), physical vapor deposition via seeded sublimation is the most commonly used approach.

Laser Chemical Vapor Deposition (LCVD) is a process that uses a laser to initialize a chemical reaction of the gaseous reactants, which results in solid deposits on selected heated areas of the substrate. The deposited materials are dense, pure, and have desirable properties. It can be expected that by using LCVD we can make very desirable SiC because of the advantages of CVD over the traditional means of making SiC. Also, the LCVD process has excellent potential for the manufacture of micro-scale 3-D parts with complex shapes.

LCVD is a relatively new manufacturing technique and very little research on the synthesis of SiC by LCVD has been conducted. Thermodynamics and kinetic studies of the LCVD of SiC will help to better understand the growth process and to determine the processing conditions that will produce crack free fibers without the volcano-like morphology often observed in LCVD deposits. [4] The volcano effect is a depression at the top of the deposit. Uniformly shaped deposits are a prerequisite for rapid prototyping small 3-D SiC parts. Heat transfer and mass transport models determine the temperature distribution and concentrations of precursors during the SiC growth process via LCVD, which assists the understanding of the new process, as well as guide the selection of growth conditions for achieving the desired morphology or material properties. A coupled thermal and structural FEM model was built to investigate the residual stresses present in the SiC deposits. Material characterization of LCVD-SiC was employed to analyze its properties and to understand growth mechanisms.

CHAPTER II

LCVD INTRODUCTION

2.1 CVD

CVD (Chemical Vapor Deposition) is a process where solid material deposited on a heated substrate surface due to chemical reactions in the gas phase or on the solid surface. [5] Three types of chemical reactions including reduction, thermal decomposition, and displacement can be used for depositing solid materials, among which reduction is most commonly used. Generally, a CVD system consists of three main parts: reagent supply system, reaction chamber, and effluent gas handling equipment. The reagents keep flowing into the reaction chamber, and chemical reaction occurs only on the heated surface of the substrate resulting in solid deposit being formed on the surface of the substrate, at the same time the byproduct gases transport away from the substrate and flow out of the chamber. If the gases are toxic or harmful, they have to be cleaned by passing through a solid or liquid scrubber or cold trap. The substrate can be heated by radiation or resistively or inductively. If both the reactor wall and the substrate are heated during the process, this kind of CVD system is called hot-wall CVD. In hot-wall CVD process, solid materials are deposited on both the inside walls of the reactor and the substrate surface. On the contrary, in a cold-wall CVD system, only the substrate is heated during the process and there is no deposition on the inside wall of the reactor. Each type of CVD has its special applications.

Normally, the reagents are gaseous at the time entering the reaction chamber. But in fact, the source reagents can be gases, liquids, or solids. For liquid reagents, like methyltrichlorosilane (MTS) which is used to deposit SiC, a vaporizer or bubbler is used to vaporize the liquid, and then the vaporized gaseous reagents flow into the reaction chamber. As for the solid reagents, like $ZrCl_4$ that is used to deposit Zr, a sublimator is required to sublimate the materials before they enter the reaction chamber.

2.2 Laser CVD

Laser Chemical Vapor Deposition (LCVD) is derived from Chemical Vapor Deposition (CVD). There are thermal (pyrolytic) and photochemical (photolytic) LCVD techniques depending on the mechanism by which the laser energy is absorbed. For thermally driven LCVD, the wavelength of the laser is chosen so that the reagents are transparent and the substrate is absorbent, resulting in a hot spot on the substrate where pyrolytic deposition occurs. On the contrary, in the case of photochemical LCVD, the wavelength of the laser is selected to make the reactant gases absorbent, which creates a high concentration of reacting species near the substrate resulting in a localized deposition on the substrate. Large areas can be coated using photochemical LCVD by directing the laser parallel to the substrate. [6]

In pyrolytic LCVD, a laser is used to initiate the chemical reaction, which results in deposition only in the region where the laser interacts with the substrate. Because of the laser, LCVD has two advantages over the traditional CVD process, directionality and monochromaticity. Directionality means that the laser energy can be precisely focused on an area having a size on the order of the wavelength of the laser. Monochromaticity refers to the laser energy being directly deposited into the reacting molecules (i.e., photolytic LCVD) by exciting either electronic or vibrational energy levels in the reacting species.

Because of the highly localized heating of a spot on the substrate, a much higher reaction temperature is often used in LCVD than for CVD. For the same reason, the volume preheating of the reagents from the heated surface is minimized and therefore higher reagent concentrations can be used without significant gas phase reactions. Also, the diffusion of the reagents to the heated surface is increased. Because of the combined effects mentioned above, for some special reactant systems, very rapid deposition rates (greater than 100 $\mu m/s$) and high scan speeds for line deposition (greater than 10 cm/s) can be achieved by the LCVD process. [7]

Normally, the laser intensity is assumed to have a Gaussian distribution. Therefore, the initial deposition thickness is a Gaussian shape. It is found that the diameter of the deposition can be much less than the corresponding laser diameter, because the deposition rate is not linear but an exponential function of the substrate temperature. This phenomenon

is called the "resolution enhancement" effect.

2.3 Fundamentals of LCVD

There are a lot of variables that will influence the LCVD process. These include laser power, pressure, deposition temperature, reactant concentrations, flow rates, deposition geometry, substrate material, and so on. Morphology and properties of deposit can be controlled by carefully adjusting the process variables.

Generally, the LCVD process consists of following series of steps: introduce the gas reagents into the reaction chamber; turn on the laser, reagents diffusion through a gas boundary layer to the substrate surface; surface chemical reaction resulting in solid materials deposited on the surface; desorption of the byproduct vapor species away from the reaction site; diffusion of the byproduct vapor species to the bulk gas region. Among those processes, gas diffusion to and from the substrate surface through the boundary layer and chemical reaction on the substrate surface are two key steps that often control the deposition rate. The slower one of those two steps controls the rate of the overall CVD process.

2.3.1 Diffusion

From Fick's first law, the diffusion rate can be expressed as Eqn (1). Figure 1 shows a simple schematic explanation of the diffusion process. Here J_{dif} is the moles of gas diffusing through the boundary layer per unit area per second (mole/cm^2/s), D is diffusion coefficient (cm^2/s), $\triangle C/\triangle X$ is concentration gradient, and $\triangle C = C^s$ - C^o where C^s is the reagent concentration at the substrate and C^o is the concentration in the flowing gas stream (moles/cm^3), $\triangle X$ = d, is the thickness of the boundary layer.

$$J_{dif} = -D\triangle C/\triangle X \tag{2}$$

Because of the difference of the gas concentrations on the substrate and in the flowing gas stream, gas diffusion towards the substrate can occur. Rewriting the equation by using the ideal gas law:$Pv = nRT$ and $C = n/v = P/RT$, we get

$$J_{dif} = \frac{D(P^o - P^s)}{dRT} \tag{3}$$

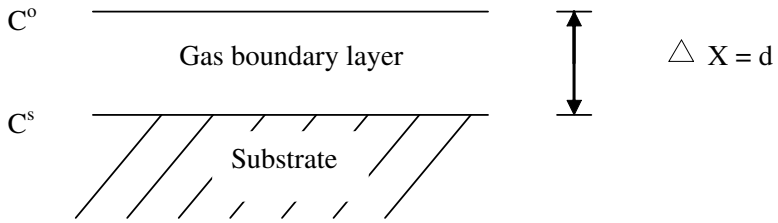

Figure 1: Gas diffusion to the substrate

Or if we write the equation for each gas species of interest, we have

$$J_{dif_i} = \frac{D_i(P_i^o - P_i^s)}{d_i RT} \tag{4}$$

Here P_i^o is the partial pressure of gas specie i in the flowing gas stream and P_i^s is the partial pressure of specie i at the substrate. This equation shows how the diffusion rate is controlled.

2.3.2 Kinetics

Assuming that the deposition rate is proportional to some power of gas concentration. It follows that

$$J_{depo} = kC_i^n \tag{5}$$

J_{depo} = deposition rate (mole/cm^2/s), n = the order of the reaction, k = rate constant (cm/s), C_i = concentration (mole/cm^3). For simplicity, assuming n=1, then

$$J_{depo} = kC_i \tag{6}$$

Combining with ideal gas law, $C_i = P_i^s/RT$, we obtain

$$J_{depo} = kC_i = kP_i^s/RT \tag{7}$$

For steady state, there are no accumulative effects, so J_{depo} is equal to J_{diff}. Solving for J by combining equation (3) and (6) and using the above condition $J_{depo} = J_{diff}$, finally we obtain

$$J = \frac{P_i^o/RT}{D_i/d_i + 1/k} \tag{8}$$

J is the deposition rate of the CVD process at steady state. D_i/d_i can be interpreted as the diffusion resistance and $1/k$ is called the kinetic resistance. In fact, k is a function of temperature,

$$k = k_0 e(-Q/RT) \tag{9}$$

Here k_0 is a constant, Q is the activation energy, R is the gas constant, and T is the temperature in K.

At low temperature, $1/k$ is much larger than D_i/d_i. From Eqn. (7), the diffusion effect is negligible compared to the kinetic effects. So at low temperature, the CVD deposition rate is mainly controlled by the kinetics of the chemical reaction. This kind of CVD process is said to be in the kinetic-limited regime. In fact, at low temperature, the chemical reaction rate is slow while the diffusion rate is relatively independent of temperature. So the reaction rate is lower than the diffusion rate. That is why the CVD process is kinetic-limited at low temperature.

As temperature increases, $1/k$ decreases rapidly and becomes smaller than D_i/d_i so that the diffusion effect D_i/d_i becomes more significant. At high temperature, the CVD process is in the diffusion-limited regime, which means the diffusion rate is slower than the reaction rate so that the deposition rate is controlled mainly by the diffusion process. The relationship between the deposition rate and the temperature is shown in Figure 2.

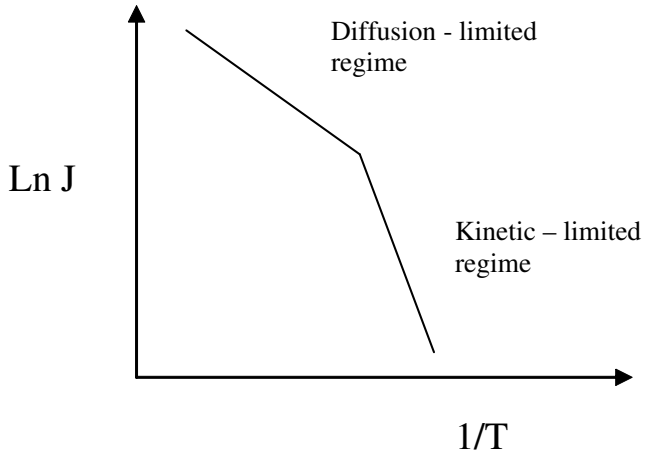

Figure 2: Deposition rate vs temperature.

In the kinetically limited regime, the deposition profiles are relatively uniform so that many CVD reactors used to produce electronic and other devices are operated under these conditions. But when high growth rates are more important than thickness uniformity, the deposition process may be operated in the diffusion-limited regime where the rate is now determined by the diffusion or transport of the reactant gases to the substrate surface. Because the transport phenomenon is relatively independent of temperature, the deposition rate does not change much as the substrate temperature is varied.

2.4 Applications of LCVD

LCVD is one of the best techniques for the production of high precision, complex, small parts with its strong advantages including micron level accuracy, and the ability to fabricate 3-D structures and parts containing multiple materials. Since the first structure was produced using LCVD in 1972, different shaped structures with different materials had been developing, i.e., fibers, lines, micro-springs, scaffolds, micro-solenoids,and antennae. [4], [8], [9], [10], [11], [12], [13] Using basic structures as building blocks, complex shaped parts can be fabricated using LCVD. LCVD has also been used as a ceramic welding process for joining of ceramic tubes. With large laser spots, LCVD can be used to coat a thin uniform layer onto thermally conductive materials. Titanium carbide was coated onto tool steel by Zergioti *et al.*, a relatively uniform layer of coat was achieved. [14] Chen *et al.* coated steel onto carbon fibers with a 3 mm diameter laser as the heating source. [15] Hiura *et al.* successfully produced high insulating quality SiO_2 film in the order of 10μm thick using photochemical LCVD with SiH_6/N_2O. [16]

LCVD can be used to deposit dielectric films for microelectronics and optoelectronics because of its low deposition temperature and one-step processing such as direct writing or projection printing. LCVD can be used to repair the defects in photomasks and repair or reroute the conductor lines in integrated circuits or microelectronic packages. Metals such as gold, copper, aluminium, tungsten, and silicon have been deposited onto silicon successfully. [17], [18], [19], [20] By nucleating the substrate first, the low energy visible laser can be used to deposit metallic features on the transparent substrate successfully. Moreover,

the nucleation layer also increases the sticking probability of the metallic deposition. The metallic deposition can also be removed from the substrate or selectively deposit metal on the substrate by varying laser parameters, which is very useful in the microelectronics industry. [21]

LCVD can make high purity metal with high speed, which makes it a very promising technique for microelectronic applications. LCVD can be applied to fabricate on-chip-reroute of 3D memory cubes that are used in high speed and/or high memory density applications. [22] Lines of silicon can be deposited for use as a resistor. Moilanen *et al.* deposited strain sensitive silicon resistors onto diaphragms to fabricate pressure sensors. [23], [24]

Photonic band-gap structures have been fabricated by growing fibers in a certain pattern, by which a certain frequency can be blocked based on a specific spacing of the fibers. Wanke *et al.* fabricated a structure with a stacked grid of aluminum oxide rods. The rods were 40 μm in diameter with 133 μm spacing between the rods. This structure can block frequencies of 2THz. [25]

CHAPTER III

LITERATURE REVIEW OF SPECIAL TOPICS

3.1 Silicon Carbide

3.1.1 Material Properties of Silicon Carbide

SiC is well known as a material having numerous polytypes, about 200 of which have been discovered. [26] All SiC polytypes are characterized by the fact that any given atom is tetrahedrally bonded with heterogeneous atoms as shown in Figure 1, where the distances a and C-Si in Figure 1 are 3.08Åand 1.89 Årespectively, and are heterogeneous structures formed by one-dimensional stacking differences. The stacking sequence of the closely-packed plane, which is the (111) plane in cubic crystals and (0001) in hexagonal crystals, can be shown by the well-known ABC notation. β-SiC, which is the only cubic SiC, has the stacking order ABCABC... of closely-packed plane. The Ramsdell notation uses a number indicating the number of layers needed for periodicity and uses the following letter refering to the crystal system to which the polytype belongs, where C represents cubic system, H a hexagonal structure, R a rhombohedral one, and T a trigonal one. β-SiC can be expressed as 3C-SiC by using the Ramsdell notation. If the stacking order of closely-packed plane is ABAB..., then the SiC crystal is hexagonal and can be referred as 2H-SiC. All of the other polytypes except 3C-SiC and 2H-SiC are a mixture of cubic and hexagonal bonding. There is an equal number of cubic and hexagonal bonds in 4H-SiC, and two thirds of cubic bonds and one-third hexagonal bonds in 6H-SiC. In spite of the presence of cubic bonds in those two polytypes, the overall crystal structure is still hexagonal. All of the hexagonal SiC polytypes are grouped as α-SiC. Table 1 shows the basic SiC polytypes described by the Ramsdell notation and ABC notation and their lattice structure properties.

The electrical properties of basic SiC polytypes are shown in Table 2. The data included in Table 2 are dependent on the temperature, test method used, quality of the material, and dopant concentration and species and most of the electronic properties vary widely between

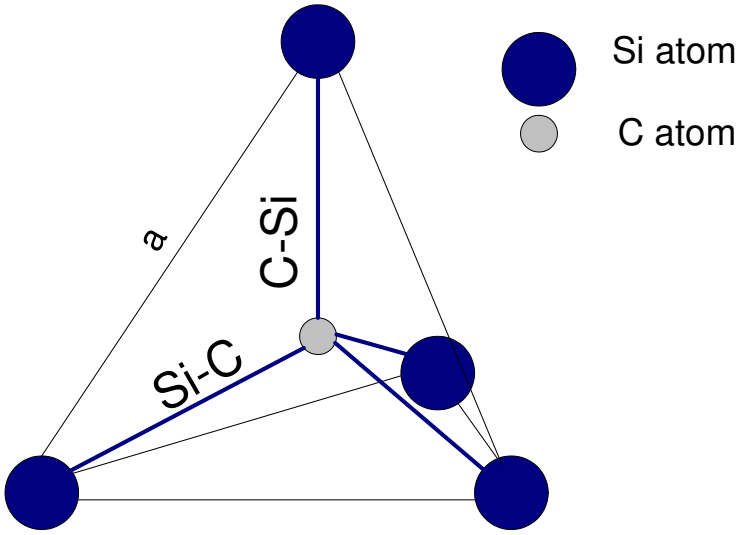

Figure 3: The tetragonal bonding of a carbon atom with four Si atoms

Table 1: Basic SiC Polytypes

Ramsdell notation	*ABC notation*	*Lattice Structure*	*Lattice constant a(Å)*
2H	AB	hexagonal	3.0817
3C	ABC	face-centered cubic	4.359
4H	ABCB	hexagonal	3.079
15R	ABCBACABACBCACB	rhombohedral	3.079
6H	ABCACB	hexagonal	3.0817

Table 2: Electrical Properties of SiC Polytypes and Si

Quantity	3C-SiC	4H-SiC	6H-SiC	Si [27]
E_g(eV) at T <5 K	2.40 [28]	3.26 [29]	3.02 [29]	1.12
$E_{crit}(MV/cm)$	2.12 [30]	2.2 [30]	2.5 [30]	0.25
$E_{crit}(N_D)(kV/cm)$	\	\	$10.64 \cdot N_D^{0.142}$	\
$K(W/cm \cdot K)$at $300K$[1]	3.2 [31]	3.7 [31]	4.9 [32]	1.5
$n_i(cm^{-3})$ at 300 K[2]	1.5×10^{-1}	5×10^{9}	1.6×10^{-6}	1.0×10^{10}
$\nu_{sat}(cm/s)$[3]	\	2.0×10^{7} [1]	2.0×10^{7} [33]	1.0×10^{7}
$\mu_e(cm^2/Vs)$	800 [34]	1000 [35]	400 [35]	1400
$\mu_\perp/\mu_\parallel$ at 300 K	\	0.7-0.83 [32]	6 [35]	\
$\mu_h(cm^2/Vs)$	40 [36]	115 [37]	10 [37]	471
χ(eV) at 300 K	\	2.70 [38]	2.95 [38]	3.15
refractive index (n)	2.7	2.712	2.7	3.5
ε_s	9.72 [39]	\	9.66 [39]	11.7

[1] doped at around $10^{17}cm^{-3}$
[2] $N_c, N_v \simeq 10^{19}cm^{-3}$
[3] parallel to $c-$ axis

different polytypes. For comparison, the electrical properties of Si [27]are also included in Table 2. The three important electrical properties of SiC, which make it a better candidate than Si and G_aA_s for high-temperature, high-power, and high-frequency operation, are thermal conductivity (K), electric field breakdown strength(E_{crit}), and bandgap (E_g). SiC also has a much higher thermal conductivity (K), about 8 to 10 times, than G_aA_s at 300 K, a bandgap (E_g) of about twice that of G_aA_s's, while possessing a peak saturation velocity (ν_{sat}) of $2.0\times10^7(cm/s)$, just as same as G_aA_s. Due to the saturation velocity overshoot phenomenon in G_aA_s, ν_{sat} of SiC at high electric fields is superior to that of G_aA_s.

Electron mobility(μ_e) and hole mobility (μ_h) are carrier velocity per unit drift field, and are critically important device parameters affecting the microwave performance, transconductance, output gain of FET's (Field Effect Transistor), on-resistance of power FET's, and other parameters. The low, anisotropic electron mobility in 6H-SiC is one of the primary reasons for the popularity of 4H-SiC for electronic applications, which has a higher and much less anisotropic electron mobility. In 4H-SiC, $(\mu_\perp)/(\mu_\parallel)$ is about 0.7-0.83 at 300 K, [35], [32] while the same ratio is about 6 in 6H-SiC. [35]

The intrinsic carrier concentration (n_i) is directly proportional to N_c and N_v, which are the conduction band and valence band density of states respectively, as shown in Eqn.

Table 3: Physical and Mechanical properties of SiC

Properties	*Values*
Density	3.14 g/cm^2
Hardness	2400 kg/mm^2
Elastic Young's modulus	46 GPa
Poisson ratio	0.16
Flexural strength	60 MPa
Compressive strength	340 MPa
Fracture toughness	4.6 $MN/m^{3/2}$

(9). Intrinsic carrier concentration(n_i) is important in high-temperature device applications, where pn junction leakage currents in devices are normally proportional to n_i, when diffusion currents dominate the total leakage current. N_c and N_v have an empirical temperature dependence ($T^{3/2}$). However, due to the fundamental change in energy between the electron states, n_i has an exponential dependence upon temperature, as well as E_g. [40]

$$n_i = \sqrt{N_c \cdot N_v} \;\; e^{(-E_g/2kT)} \tag{10}$$

Beside the attractive electronic properties, SiC has a strong covalency, low thermal expansion coefficient, high thermal conductivity, high strength, and high hardness. Table 3 shows the physical and mechanical properties of SiC. Moh's hardness of SiC is 13, just slightly softer than diamond (15) and boron carbide(14). SiC has relatively high thermal stability, with decomposition beginning at temperatures of 2000°C or more in air with dissociation temperature of approximate 2400 °C. The elastic modulus of SiC is high, around 460 GPa, but its constituent atoms are relatively light, and its atomic weight difference is small. In return, the lattice vibrations easily become harmonic, giving the material a high thermal conductivity for a ceramic, which is above 3 ($W/cm \cdot K$) compared to 0.3 for alumina, 0.4 for SiN and 0.8 to 1.5 ($W/cm \cdot K$) for AlN.

In solids, the distance between atoms is maintained in a state of equilibrium by balancing the potential energy between the interatomic tensile and repulsive forces. Due to its strong interatomic bond, SiC has a small thermal expansion coefficient, which is 4.3×10^{-6}/°C. Also SiC is extremely stable, showing no corrosion even when boiled in HCl, H_2SO_4, HF, or HF + HNO_3. In air, oxidation starts at temperatures of approximately 850°C, forming a

rather protective SiO_2 film. The oxidation resistance is mainly determined by the properties of SiO_2 film.

3.1.2 Applications of Silicon Carbide

SiC is one of the most mature wide-bandgap semiconductors (2.0 eV $< E_g <$ 7.0 eV). SiC has high thermal conductivity, about 3.3 times that of Si at 300 K for 6H-SiC, high electric field breakdown strength, about 10 times that of Si for 6H-SiC, and wide bandgap, about 3 times that of Si for 4H-SiC and 6H-SiC). The wide bandgap makes it ideally suited for high-temperature, high power, high-frequency, and high-radiation environments. Most traditional silicon based integrated circuit devices are not able to operate at temperatures above 250°C, especially when high operating temperatures are combined with high-power, high-frequency, and high radiation environments. High-temperature circuit operations from 350 to 500°C is desired for applications in the aerospace industry including turbine engines and the more electric aircraft initiative, nuclear power instrumentation, satellites, space exploration, and geothermal wells. Furthermore, SiC is expected to revolutionize optoelectronics with a new generation of optical data storage and communication devices.

For example, replacing bulky hydraulic-driven flight control actuators and engine-gearbox driven fuel pumps with power electronics capable of high temperature and high efficient operations, can yield tremendous weight saving. The hydraulic-based system also provides cooling to aircraft electronics, thus the removal of the hydraulic systems will allow reduced or elimination of cooling systems, which in return could reduce the aircraft weight, maintenance efforts, down time, and ground supplies, and at the same time improving the aircraft's performance, flying range, efficiency, and reliability.

SiC is a promising material for high-temperature structural and wear-resistant applications, especially in harsh environments (heavy loads, high corrosion, etc.). Materials normally used as mechanical seals are WC and Al_2O_3. Since mechanical seals often rotate at high speed while maintaining a seal against different types of liquids, good resistance to abrasion, corrosion and thermal shock, a high elastic Young's modulus, a low friction coefficient, and a low specific gravity are required. SiC is good in each of these areas, and

therefore is starting to replace WC and Al_2O_3 in environments that do not allow the use of the conventional materials. In addition, due to the high strength of SiC, more and more pump shafts, bearings, sleeves, and abrasion resistant liners are made of SiC.

In order to improve thermal efficiency, SiC materials are enthusiastically considered for applications in several parts of gas turbine and gas turbine engines including combustors, turbocharger rotors, vanes, and blades. In the high-temperature industries, it is important to maintain high thermal efficiency as well as circulation and pressurized transport of gas without reducing gas temperatures, which makes SiC a good candidate for heat exchangers and fans at high temperatures.

3.2 Processed SiC Materials

3.2.1 SiC processed with CVD

Low-pressure chemical vapor deposition (LPCVD) can be used to manufacture asymmetric SiC membranes, with the $SiH_4/C_2H_2/Ar$ reagent system at 800°C. [41] Such membranes are used in liquid-phase separations as Microfiltration (MF) and Ultrafiltration (UF). The pore size of the membrane was able to be reduced to increase the selectivity at the cost of the performance. Nanoscale CVD is very suitable for this type of applications.

SiC fibers are very useful in ceramic−and metal− matrix composite materials due its attractive properties. SiC fibers manufactured using the CVD process processes low porosity and high chemical purity. Lackey *et al.* have produced small-diameter, high-strength, thermally stable SiC fibers by a continuous CVD technique. [42] SiC whiskers are also very useful in various composite materials as the fibrous reinforcements. Leu *et al.* have grown SiC whiskers by decomposing methylthrichlorosilane (MTS) at 1300°C on Ni-coated graphite substrates using the CVD method. [43]

SiC nanosized powder is the major type of reinforcements in nanocomposite materials because the nanocrystalline SiC materials contain a lot of grain and interphase boundaries, which is about 50% of the volume, making the materials have attractive physical, electrical, and mechanical properties. High purity, low oxygen content nanosized SiC powders have been successfully produced by Huang *et al.* using CVD of dimethyldichlorosilane (DMS)

at temperatures from 1100 to 1400°C. [44] The powders grown at 1400°C are small β-SiC crystallites, while powders grown below 1300°C, the powders consist of amorphous phases and small β-SiC crystallites. Fine, submicrometer and quasispherical SiC powders have also been synthesized using CVD with the $SiH_4 - C_2H_2/Ar$ reagent system. [45]

The attractive properties of SiC, such as high stiffness to weight ratio, high strength, high thermal conductivity, high hardness, and low thermal expansion coefficient, make it an excellent material for optical applications. But the SiC materials made by traditional process are usually porous and multiphased that cannot give a good optical face after polishing. Large pieces of monolithic polycrystalline β-SiC without voids have been fabricated using CVD, which has high polishability. and therefore can be used in vacuum ultraviolet (VUV) and X-ray applications. [46]

3.2.2 SiC Processed with Laser

Noda *et al.* [47] deposited SiC from $SiH_6/C_2H_2/H_2$ using photolytic-LCVD with an ArF excimer laser on a carbon substrate at 518 K. It was reported that the deposition rate was determined by the photolysis of SiH_6 alone. The structure of the SiC films was changed from amorphous to crystalline β-SiC while the amount of SiH_6 was increasing, and was independent of the concentration of C_2H_2 . [48] Suzuki *et al.* directed the laser beam in the directions of perpendicular or parallel to the graphite substrate to grow SiC films with photolytic-LCVD technique. [49] In the perpendicular case, microcrystalline β-SiC was the major constituent of the deposit. In the parallel case, only amorphous SiC with some carbon was obtained.

Crocker *et al.* applied SALDVI (Selective Area Laser Deposition Vapor Infiltration) to deposit SiC materials into the spaces between different powders to consolidate them. [50] A CO_2 laser was used to selectively heat the powders to the target temperature of 1000°C. The gas precursor they used to deposit SiC was $Si(CH_3)_4$, and the pressure was maintained at 10 Torr. It was indicated that the properties of the powder affected the surface roughness and internal structure of the grown SiC matrix multiple layer parts. The laser scan speed influenced both the uniformity of the microstructure of each layer and

the infiltration density in the interior of the powder layer significantly. Ghayad *et al.* [51] used the SALD (Selective Area Laser Deposition) method to join ceramic parts with SiC materials, trying to manufacture complex ceramic parts. It was shown that a good shaped SiC spot joints can be produced on thin and dense silicon nitride substrates. The laser power, the thermal conductivity of the substrate, and the substrate size influenced the spot joining process significantly.

3.3 Thermodynamics of SiC Growth

Thermodynamic analysis is very important in understanding and optimizing the CVD process. First, whether a given chemical reaction is feasible or not, is perhaps the most important issue. Information on partial pressure of the gaseous species and on the nature of the condensed phases is another important factor for CVD process. Due to the lack of kinetic information for many chemical reaction systems, thermodynamics calculations provide good guidance for the formation of the possible gaseous species and condensed phases for reagent types and concentrations and under different temperatures and pressures.

Generally, the procedure of the thermodynamics calculation is to determine the resultant composition by minimizing the free energy of the system, under given conditions, such as temperature, total pressure, gas concentrations, etc.. Writing all the possible reactions, given the Gibbs free energy change for all the reactions, permits calculation of the reaction path yielding the lowest free energy state. The free energy change must be negative for the reaction to occur. The more negative the free energy change, the easier the reaction occurs. This is a very good way to theoretically predict the resultant composition of the CVD process.

Thermodynamic analyses on SiC fabrication from tetramethylsilane (TMS), methyltrichlorosilane (MTS), and the mixture Si_2H_6/C_2H_2 were explored by Sun *et al.* [52] using the CET89 code. Using MTS or TMS as the precursor, condensed graphite and SiC were present at almost the same temperature range, and thus imposing difficulties in obtaining high purity SiC from MTS. On the contrary, with the mixture of Si_2H_6/C_2H_2 as the reagent gases, the solid silicon phase only appeared at temperatures below 500 K, graphite formed

only above 2750 K, and pure β-SiC was predicted to form between 500 and 2500 K, which shows the possibility to fabricate pure SiC using the mixture of Si_2H_6/C_2H_2. Comprehensive CVD SiC phase diagrams from different mixtures of precursors were investigated by Angus *et al.* [53]

For a hot-wall CVD process, traditional CVD phase diagrams may not accurately predict the phases in the deposits on the substrate because there are chemical reactions along the reactor present consuming precursors and generating intermediate gaseous species. Due to this depletion effect, the local gaseous species concentrations at the substrate may be significantly different from the input gaseous concentration. While doing the equilibrium calculations of hot-wall CVD of SiC from MTS and H_2, Chiu *et al.* [54]coupled the thermodynamics calculations with a kinetic model representing the depletion effect and the obtained new CVD phase diagrams which had better agreement with experiments than the traditional ones.

Ignoring the hetergeneous surface chemical reactions, the homogenous chemistry of the thermal decomposition of MTS was thoroughly studied by Papasouliotis *et al.*. [55] The compounds that existed in a significant amount in the gas phase, and thus may influence the chemistry of the process dramatically, as well as the major deposition paths were determined. Initial compositions of the precursors and process conditions which may lead to stoichiometric SiC deposits were suggested.

3.4 Kinetics of SiC Growth

The MTS and H_2 mixture is very often chosen as the precursors for CVD of SiC because of both economical and theoretical reasons. The growth mechanism of SiC by CVD from MTS and H_2 is complicated. The study of CVD growth kinetics should be very useful to obtaining high quality SiC.

The kinetics of hot-wall CVD of SiC from MTS were modeled by incorporating both the homogeneous gas phase and heterogeneous surface reactions. [56] The model included three major processes: decomposition of MTS molecules into two major intermediates, silicon contained and carbon contained species, adsorption of the two intermediates onto

the substrate surface, and chemical reactions forming SiC. The kinetics constants for all of the three processes were obtained and the apparent activation energy for the SiC formation process was $265.1 KJ/mol$.

At low pressure, 3.3 KPa, the influence of deposition temperature, flow rate and concentration of precursors (MTS and H_2) on the CVD SiC deposition rate were investigated. [57] Under the specified process conditions, the SiC deposition rate was independent of the reactant partial pressure implying that neither bulk gas flow, diffusion of precursors onto the surface sites, nor adsorption of a reactant species was rate limiting. It was thus likely that under these conditions the deposition process was either controlled by diffusion of an adatom across the surface to an energetically favored position for inclusion into the coating, or a decomposition surface reaction which allows silicon or carbon contained molecules to lose bonded hydrogen or chlorine.

The SiC deposition rate onto the carbon-coated Nicalon fibers from MTS and H_2 was investigated as a function of temperature, pressure, total flow rate, and simulated reactant depletion. [58] Based on the way MTS decomposed, two deposition mechanisms were suggested, one was MTS directly decomposing and forming SiC, and the other was MTS first decomposing into $SiHCl_3$ and CH_4 and then they reacting with each other to form SiC. Further, it was found that the byproduct of HCl had a strong negative effect on the SiC CVD deposition rate and a simple etch model was constructed to obtain a kinetic expression for the effect of HCl on the SiC deposition rate.

Sone *et al.* conducted another kinetic study of CVD SiC from MTS and H_2. [59] In their model, in situ growth rate measurements were accomplished by converting from the weight of the SiC deposits using thermogravimetry. It was found that the growth rate was limited by surface reaction at temperatures lower than 1300^OC and by mass transport at temperatures above 1300^OC. A two-site competitive adsorption model based on $SiCl_3$ and CH_3 was built and it was suggested that the rate limited process was the adsorption of the carbon-containing molecules on the Si sites, which means the growth rate of SiC was controlled by the amount of CH_3 adsorbed onto the Si sites. In Loumagne's kinetic model of SiC deposition from MTS and H_2, the transition from chemical reaction control to mass

transport was found and the transition can be induced by decreasing the total flow rate, or by increasing the growth temperature and/or total pressure. [60]

3.5 Heat Transfer and Mass Transport Model of LCVD

LCVD (Laser Chemical Vapor Deposition) is a thermally activated process, and thus temperature is the driving force which determines the location, quantity, morphology, and material properties of the deposits. Therefore, it is extremely important to know how heat is generated and distributed within the deposits and substrate, and in return what are the temperature distributions of the deposits and substrate. A good mathematical thermal model of the temperature distribution on the substrate will allow us to optimize the control of the process. The thermal models can also be used to determine the important chemical reaction zone in the LCVD process, which is defined as the regions on the substrate where their temperature is equal to or higher than the chemical reaction temperature.

Precursor concentration right above the reaction zone is another important factor for the LCVD process. It determines whether the deposition rate is limited by the chemical reaction process or by the species diffusion process, and thus has a big effect on the morphology of the deposits. In order to incorporate the reagent gases consumption by the chemical reaction, the kinetic data has to be obtained first from kinetic models of the deposition process.

Yu *et al.* first developed a mathematical model incorporating both the heat transfer and fluid transport phenomena associated with growing fibers with LCVD process. [61] In their model, an incompressible, laminar flow and steady state was assumed and a mixture of silane (SiH_4) and hydrogen (H_2) was used as the fluid medium. The model showed that there was a distinct temperature variation along the depth of the fiber and the incident laser energy was absorbed most at a small depth near the surface. Also the temperature rises on the fiber tip surface increased linearly with the incident laser power.

There are a lot of thermal models dealing with infinite and semi-infinite substrates, which work very well on big substrates compared with the laser spot. But it is not appropriate to apply those kind of models to deposition process with small substrates, such as fibers. Considering this, a thermal model based on a finite substrate was developed by A. Kar and

J. Mazumder to determine the three-dimensional temperature field on the substrate for a moving laser. [62] Both the convective and radiative heat losses from the boundary layers of the substrate are involved in the energy equation, the laser profile is assumed to be Gaussian, and the thermophysical properties of the substrate are temperature dependent. Using Kirchoff's transformations and Taylor series to linearize the equations first and applying Fourier transforms in the x, y, z directions to solve the equations, an analytical expression for the three-dimensional and transient temperature distribution on the substrate was obtained.

Garrido *et al.* developed a numerical model to calculate temperature distribution within the LCVD spots and lines with temperature dependent thermal conductivities of the deposits and substrate. [63] A similar simulation of the pyrolytic laser 3-D direct writing was developed by Arnold *et al.*. [64] The temperature distribution induced by the laser heating, with temperature dependent properties of the substrate and deposits, was calculated. A self-consistent model of the deposition process was built to explain the oscillations in the height and width of the lines. Tungsten (W) deposition from WCl and H_2, Si deposition from SiH_4, and C deposition from CH_4, C_2H_2 or C_2H_4 were analyzed.

The LCVD process involves transport of the reagents to and transport of the byproducts away from the interface of the gas region and substrate surface. Diffusion and convection are two major transport mechanisms. Copley made two different steady-state mass transport models for LCVD, which both had a hemispherical source/sink geometry. [65] In his first model, only diffusion was involved, while the second one included both diffusion and convection. Convection resulted from the mole number change of vapor species in the reaction and was modeled as the radial flow of an incompressible flux from a point source. A comparison between the results of the two models and the LCVD of Ni from $Ni(CO_4)$ was made and the second model provided a better agreement with the experiments than the first one.

A 2-D heat transfer model concerning the Georgia Tech LCVD system was developed to compare the thermal behavior of different substrate materials heated by CO_2 laser. [66], [67] The geometry of the model is shown in Figure 4, where the 2-D model was axisymmetric about the centerline of the shaft and substrate. The modeling results showed that the

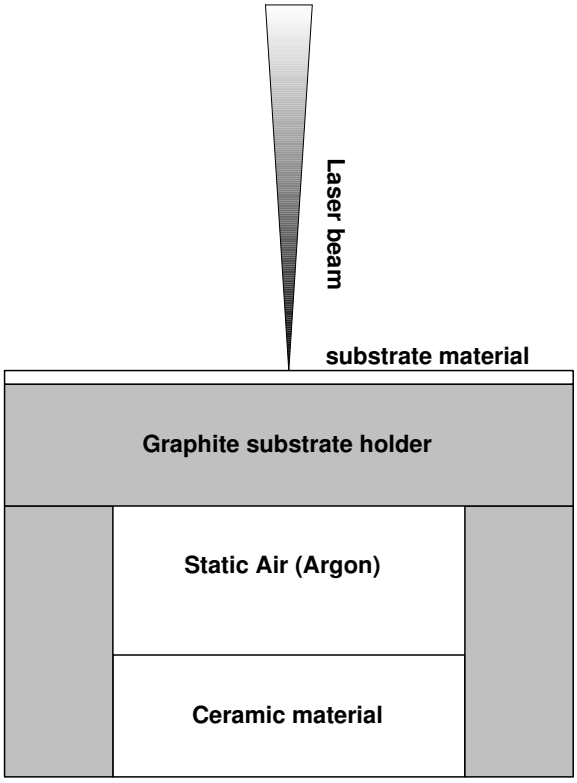

Figure 4: Geometry of 2-D heat transfer model

maximum temperature of the substrate is around the center of the laser beam due to the heating and the Gaussian profile laser beam. The temperature distribution of the substrate was highly localized. For most of the cases, the temperatures were changed from over 2000°C to around 150° within 200 μm laser spot size, resulting in 10 °C/μm temperature gradient. The substrate material had a big effect on the maximum temperature and the temperature gradient of the substrate. It was shown that Si substrate has higher maximum temperature and temperature gradient than those of graphite substrate based on the modeling results, which is probably due to the low thermal conductivity of Si material. Actually, the reflectivity of the surface of the substrate can affect the amount of energy absorbed by the substrate dramatically, as a return, the maximum temperature of the heated substrate will be changed too.

In order to evaluate the cooling effects and the efficiency of gas delivery function of an angled gas-jet of Georgia Tech LCVD system, a 3-D model combining fluid flow and heat transfer was built. [66] [67] Due to the angled gas-jet, there is only one symmetric plane that

can be used to simplify the modeling geometry, which is the plane that is orthogonal to the substrate surface and coincident with the axis of the gas-jet. The 3-D model geometry was shown in Figure 3. This model not only included the substrate and a portion of the shaft, but also extended into the reagent gases region right above the substrate. Three primary components was included in this model. A graphite cylinder with 25 mm thick and 75 mm in diameter was represented the substrate holder. The second component of the model was an angled gas-jet with 1 mm in diameter. The gas-jet was inclined at 45° angle with respect to the substrate and had a 10 mm standoff from the substrate surface. The last component was fluid field, which encompassed most of the angled gas-jet to characterize the effects of gas-jet at the fluid behavior.

The velocity profiles for both horizontal and vertical component are similar, zero at the substrate surface, increasing to the maximum velocity at about 1 mm above from the substrate surface, then reaching zero at regions far from the gas jet exit. With respect to the horizontal velocity, the effective momentum boundary layer thickness is the distance from the substrate surface to where the maximum velocity is achieved. The boundary layer thickness will decrease with increasing inflow velocity, but will fall in the range of 200 to 400 μm. It was estimated that if the horizontal velocity is above 4 m/s, there will be enough fresh gases within the boundary layer. A mass transport model is required to check whether the gas-jet can enhance the gas delivery to the reaction zone (region centered at the laser spot) or not.

For both of graphite and Si substrates, the peak temperatures within the laser spot on the substrate surfaces decreased with increasing flow rate of gas through the gas-jet, showing an obvious cooling effect of the gas-jet. The cooling effect of the gas-jet was more significant when the flow rate of gas in the gas-jet was below 1000 $sccm$. And there were more temperature drop occurred on Si substrate than on graphite substrate according to the modeling results. The isothermal curves within the laser spot on the substrate surface were concentric regardless of the flow rate inside the gas-jet, which predicts that the morphologies of the LCVD deposits should not affected by the inflow rate of the gas-jet gas. The temperature distribution of the gases right above the substrate was shown to be

affected by the gas flow rate in the gas-jet too. The thermal boundary layer of the reagent gases kept decreasing with higher flow rate of gas from the gas-jet. The heated zone of the reagent gases exhibited uneven pattern, a steeper temperature gradient and a thinner boundary layer at the side close to the gas-jet exit than the other side.

The novel angled gas-jet was designed to increase the deposition rate of LCVD process. A 2-D mass transport model was generated to test that given the cooling effect of the gas-jet at the substrates and the reagent gases, whether the gas-jet can improve the actual deposition rate of LCVD or not. [66], [67]The finite difference technique was applied to the modeling process and the Matlab was the software that was used to program the calculations. It was shown that for kinetically limited deposition process, gas-jet had a negative effect at the deposition rate, but would increase the deposition rate if the deposition reaction was in diffusion controlled regime. Unfortunately, most of the LCVD-carbon growth were estimated in the kinetically limited region. [4], [68]

A comprehensive 3-D model of the Georgia Tech LCVD system, integrating the mass transport, heat transfer, and chemical reaction, was created to further understanding of the LCVD deposition process. [69] The model showed that for the LCVD-carbon process, higher laser power increases the deposition rate with the same shape of rate profile across the reaction zone, which is a combined effect of the increased resulting reaction zone temperature and the decreased reagent gas concentration inside the reaction zone given that the LCVD-carbon growth is in kinetically limited reaction zone. On the contrary, increased gas flow rate exiting the angled gas-jet produced the exact opposite results, which were lower deposition rate resulted from the decreased temperature and increased reagent gas concentration inside the reaction zone while increasing the gas flow rate through the gas-jet.

CHAPTER IV

THERMODYNAMICS

Thermodynamic calculations are extremely useful for analyzing the combination of condensed phases that will most stably deposit during LCVD process. The thermodynamics of CVD-SiC from MTS and H_2 have been studied extensively. The results of thermodynamic calculations with proper interpretation, are applicable for the LCVD process. However, most of the previous studies emphasized the condensed phase diagram and the concentrations of the gaseous species. [53], [70] Here, a set of thermodynamic calculations was carried out to predict the actual amount of SiC that would be deposited at equilibrium, which offers guidance for deposition of SiC fibers by the LCVD technique.

Thermodynamic calculations applied to the C-H-Si-Cl system, which involves solid β-SiC, solid α-SiC, solid C and Si, liquid Si and lots of gaseous chemical components, are an essential first step in predicting the processing conditions for a desired LCVD-SiC morphology. Because of the large temperature gradient across the laser spot, deposition rates vary radially within the region heated by the laser and knowledge of this variation, obtained from the thermodynamic predictions, permits identifying processing conditions which minimize the variation in deposition rate and thus permit growth of flat-topped deposits, as opposed to those having a volcano-like shape.

Thermodynamic calculations were performed using the SOLGASMIX-PV computer program. [71], [72] This software calculates the quantity of solid phases formed and the partial pressure of all gas species considered by minimization of the Gibbs free energy, i.e., equilibrium is assumed. The system was defined by specifying pressure, temperature, and the amount of each element involved. By holding the pressure and temperature constant, the volume of the system can expand and contract during reaction depending on the given pressure and temperature. Because the calculations are based upon equilibrium thermodynamics, the final results are independent of the initial form of the elements. Therefore,

Table 4: Species used in the C-H-Si-Cl (MTS) System

Equilibrium gas species				
C(g)	Si_2(g)	C_2Cl_2(g)	C_4(g)	$SiCl_3$(g)
CCl(g)	CH_2Cl_2(g)	C_2Cl_4(g)	C_5(g)	$SiHCl_3$(g
CCl_2(g)	CH_3(g)	C_2Cl_6(g)	Cl(g)	$SiCl_4$(g)
CCl_3(g)	CH_3Cl(g)	C_2H(g)	HCl(g)	H(g)
CCl_4(g)	CH_3SiCl_3(g)	C_2HCl(g)	SiH_3Cl(g)	SiH(g)
CH(g)	CH_4(g)	C_2H_2(g)	SiCl(g)	H_2(g)
CHCl(g)	SiC(g)	C_2H_4(g)	$SiCl_2$(g)	SiH_4(g)
$CHCl_3$(g)	Si_2C(g)	SiC_2(g)	Cl_2(g)	Si(g)
CH_2(g)	C_2(g)	C_3(g)	SiH_2Cl_2(g)	
Equilibrium condensed phases				
C[s]	Si[l]	Si[s]	$\alpha-$SiC[s]	$\beta-$SiC[s]

we input the number of moles of each element. For the calculations to be applicable, it is assumed that the reaction in the gas phase come to equilibrium very quick.

Two sets of thermodynamic calculations were performed: one using methyltrichlorosilane (MTS, CH_3SiCl_3), and hydrogen (H_2), which were the actual precursors for the LCVD-SiC experiments, and the other one using CCl_4, $SiCl_4$, and hydrogen (H_2), which was performed to check our calculations with those of Kingon. [53] For the MTS calculations, we included 44 gas species and 5 condensed phases (graphite, liquid silicon, solid silicon, α-SiC, and β-SiC). Those species are listed in Table 4. For the calculations for CCl_4 and $SiCl_4$, we used exactly the same species Kingon used, which are shown in Table 5. [53] The enthalpies of formation and entropies of formation were taken from the JANAF Thermodynamical Tables. [73] For each set of calculations, the input enthalpy and entropy values for the growth temperature of interest were used, instead of using one fixed set of enthalpy and entropy values as is sometimes done. Only the enthalpy and entropy for the chemical species at 1500 K are presented in Table 6.

Table 5: Species Used in the C-H-Si-Cl (CCl_4, $SiCl_4$) System

Equilibrium gas species				
CCl(g)	C_2H(g)	SiH_3Cl(g	$SiCl_3$(g)	H_2(g)
CCl_4(g)	C_2H_2(g)	SiCl(g)	$SiHCl_3$(g)	SiH_4(g)
CH_3(g)	C_2H_4(g)	$SiCl_2$(g)	$SiCl_4$(g)	Si(g)
CH_3Cl(g)	Cl(g)	Cl_2(g)	H(g)	
CH_4(g)	HCl(g)	SiH_2Cl_2(g)	SiH(g)	
Equilibrium condensed phases				
C[s]	Si[l]	Si[s]	$\alpha-$SiC[s]	$\beta-$SiC[s]

Table 6: Thermodynamic Data Used in SOLGASMIX-PV Calculations

Species	1500 K	
	$\Delta_f \mathbf{H}^\circ$ ***(KJ/mol)***	$\mathbf{S}_f{}^\circ$ ***(J/molK)***
C(g)	718.415	191.71
CCl(g)	500.033	281.784
CCl_2(g)	239.895	354.638
CCl_3(g)	83.105	419.02
CCl_4(g)	-85.806	469.835
CH(g)	591.314	233.318
CHCl(g)	333.341	312.78
$CHCl_3$(g)	-102.212	434.832
CH_2(g)	379.299	260.74
Si_2(g)	578.658	294.779
CH_2Cl_2(g)	-102.442	391.163
CH_3(g)	134.662	277.327
CH_3Cl(g)	-96.935	339.823
CH_3SiCl_3(g)	-587.547	568.12
CH_4(g)	-92.553	279.763
SiC(g)	715.648	281.167

Table 6: (continued)

Species	1500 K	
	$\Delta_f \mathbf{H}^\circ$ ***(KJ/mol)***	$\mathbf{S}_f{}^\circ$ ***(J/molK)***
Si_2C(g)	519.228	331.239
C_2(g)	835.528	259.869
C_2Cl_2(g)	213.026	395.09
C_2Cl_4(g)	-2.244	532.228
C_2Cl_6(g)	-107.011	667.971
C_2H(g)	470.837	282.188
C_2HCl(g)	212.487	351.905
C_2H_2(g)	185.216	298.567
C_2H_4(g)	35.456	341.877
SiC_2(g)	604.907	323.732
C_3(g)	802.255	304.372
C_4(g)	964.753	338.748
C_5(g)	973.524	381.756
Cl(g)	125.863	201.323
HCl(g)	-95.16	236.219
SiH_3Cl(g	-149.606	374.51
SiCl(g)	190.341	297.755
$SiCl_2$(g)	-175.663	371.59
Cl_2(g)	0	282.052
SiH_2Cl_2(g)	-324.49	423.037
$SiCl_3$(g)	-391.218	445.696
$SiHCl_3$(g)	-495.845	463.724
$SiCl_4$(g)	-657.454	495.623
H(g)	224.836	148.299

Table 6: (continued)

Species	1500 K	
	$\Delta_f \mathbf{H}^\circ$ ***(KJ/mol)***	$\mathbf{S}_f{}^\circ$ ***(J/molK)***
SiH(g)	367.684	250.076
H_2(g)	0	178.846
SiH_4(g)	23.548	317.348
Si(g)	444.803	202.36
C[s]	0	33.718
Si[l]	50.512	88.399
Si[s]	0	58.411
αSiC[s]	-71.241	84.41
βSiC[s]	-72.851	84.619

4.1 MTS/H_2 System

Twenty series of thermodynamic calculations were performed over the temperature range 300-2900 K based on five pressure values, 5, 100, 300, 500 and 760 torr and four H_2 to MTS ratios, 10, 20, 60, and 100. The initial input compositions were based on the four ratios of H_2 to MTS. The number of moles of each element were the actual quantity in the reaction chamber, based on the ratio of H_2 to MTS, multiplied by 1000. Multiplication by 1000 was done because, for some cases, the mole values were too small to get reasonable results. The mole values for each element that were used to perform the calculations are listed in Table 7.

Table 7: Input Quantity of Each Element

MTS: H_2	*C (mole)*	*H (mole)*	*Si (mole)*	*Cl (mole)*
1:10	4.672	107.456	4.672	14.016
1:20	4.672	200.896	4.672	14.016
1:60	4.672	574.565	4.672	14.016
1:100	4.672	948.416	4.672	14.016

4.1.1 Gaseous Species

The gaseous species, which were predicted to have significant quantities for a H_2 to MTS ratio of 10 for five different pressures, are plotted in Figures 5-9. The x axis is the temperature in K, and the y axis is the quantity of the species in mole presenting in logarithm fashion.

As shown in Figures 5-9, at low temperatures the dominant carbon-containing species is CH_4, which manitains a relatively constant quantity of 3.6 mole and then decreasing sharply to 0 moles. The temperature corresponding to the sharp decrease is 700 K for 5 torr, 800 K for 100 torr , 900 K for 300 torr, and about 1000 K for 500 and 760 torr pressures. At low temperatures, the dominant silicon-containing species is $SiCl_4$. It undergoes a similar behavior as CH_4, maintaining a relatively constant quantity, 3 moles, and then decreases significantly with temperature. The sharp decrease in the quantity of $SiCl_4$ occurs within the temperature range 800 to 1000 K and the temperature of the decrease is not as obvious as it was for CH_4. The secondary dominant silicon containing species at relatively low temperatures is $SiHCl_3$, the amount of which is under 1 mole and decreases with temperature.

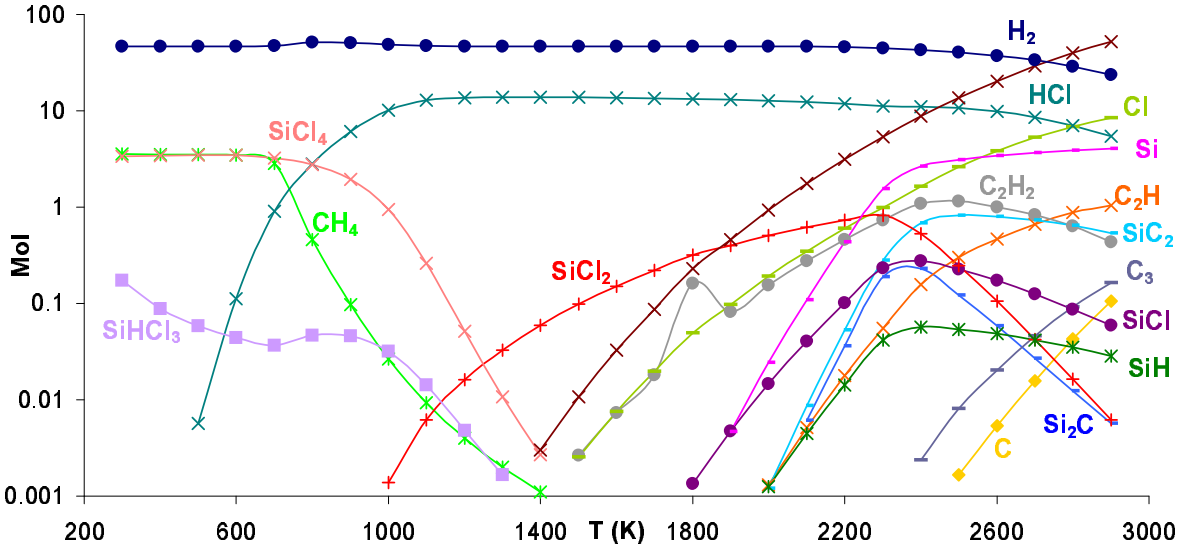

Figure 5: Gaseous species of the system MTS/H_2 with H_2/MTS ratio =10, and P=5 torr.

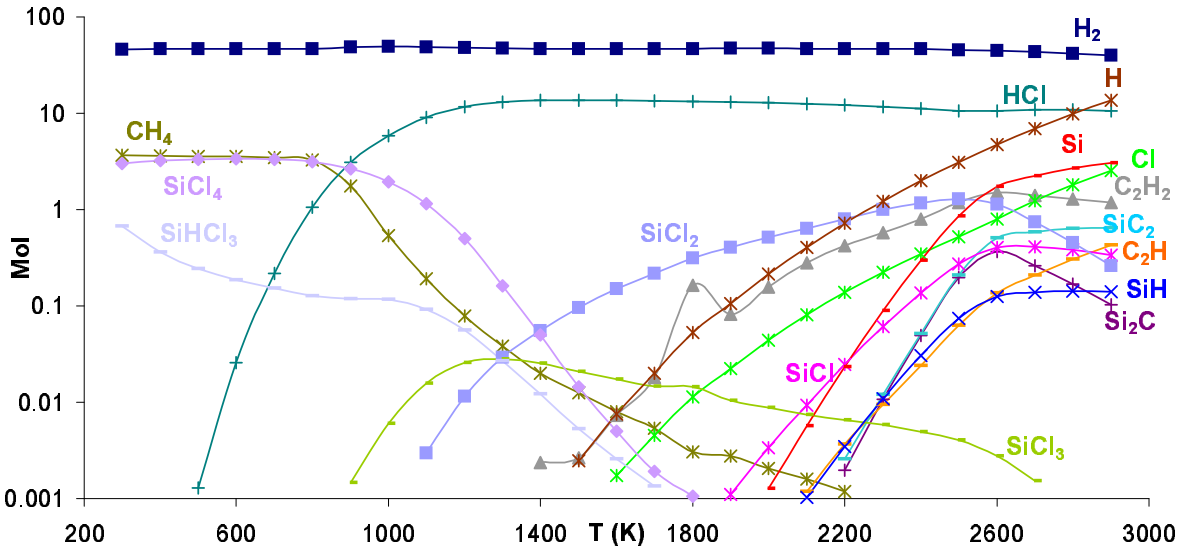

Figure 6: Gaseous species of the system MTS/H_2 with H_2/MTS ratio =10, and P=100 torr.

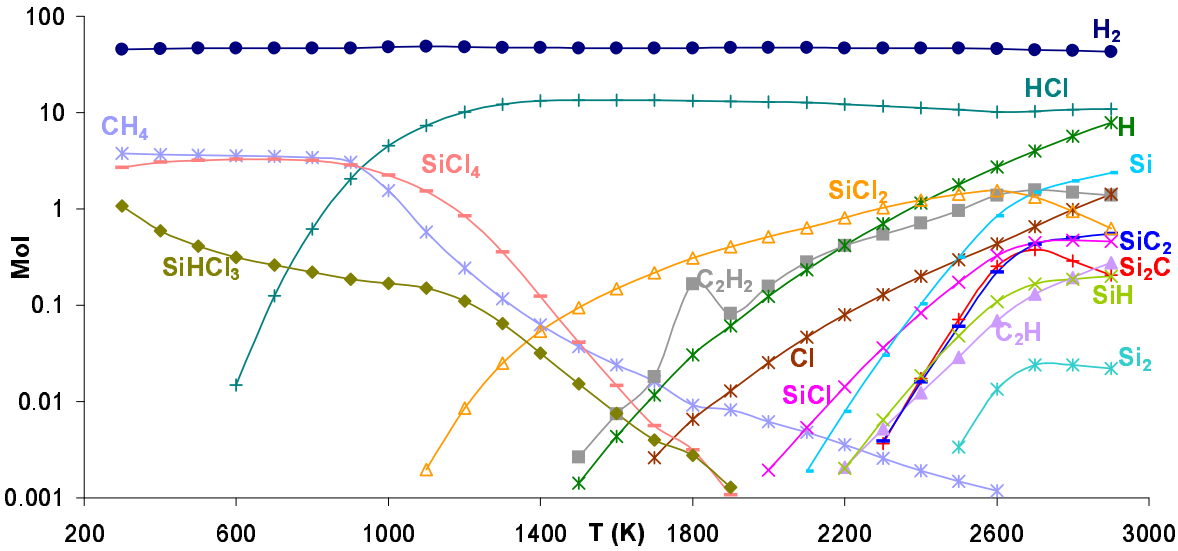

Figure 7: Gaseous species of the system MTS/H_2 with H_2/MTS ratio =10, and P=300 torr.

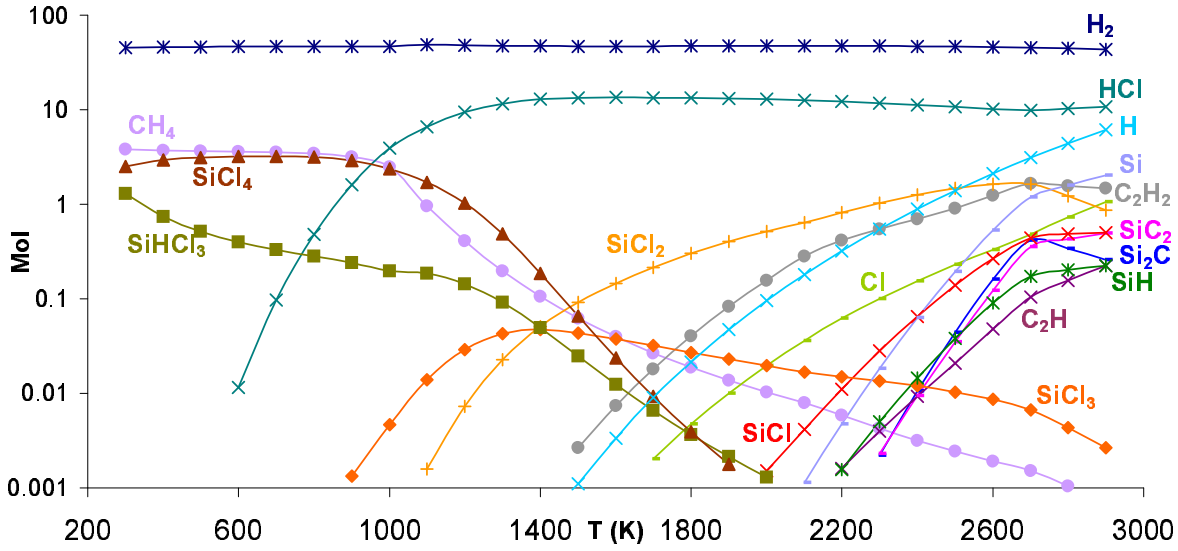

Figure 8: Gaseous species of the system MTS/H_2 with H_2/MTS ratio =10, and P=500 torr.

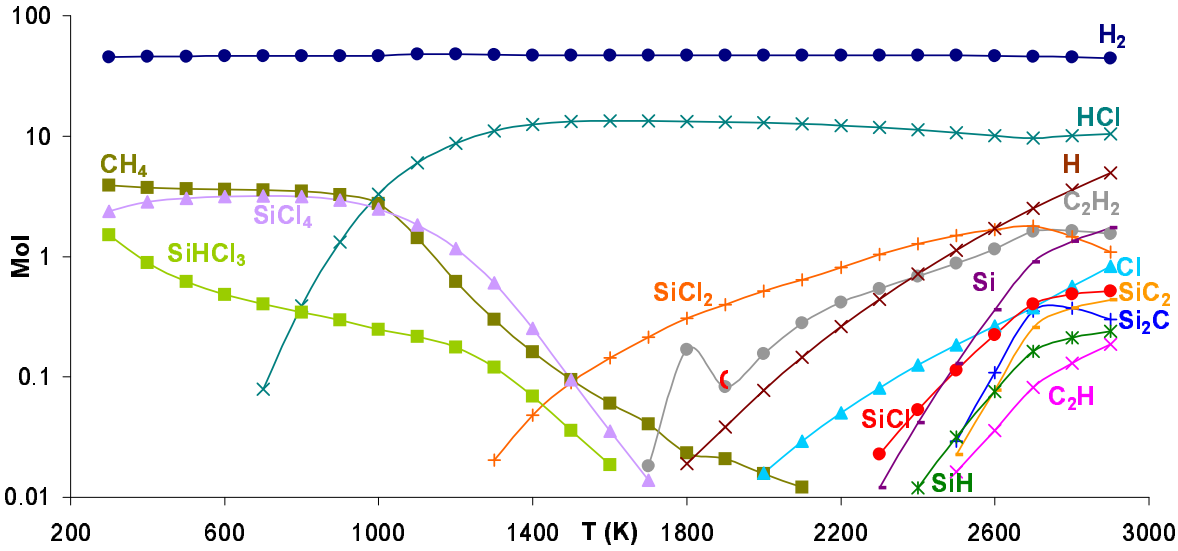

Figure 9: Gaseous species of the system MTS/H_2 with H_2/MTS ratio =10, and P=760 torr.

At high temperatures, the carbon-containing species include C_2H_2, C_2H, SiC_2, and Si_2C, among which C_2H_2 is slightly more significant in comparison with the others. But most of the time the amount of C_2H_2 is just up to 1 mole as a maximum. SiC_2 is the secondary significant carbon-containing molecule at high temperatures, whose quantity increases with temperature except for the 5 torr pressure case. At high temperatures, the silicon-containing species are Si, SiC_2, $SiCl_2$, SiCl, Si_2C, and SiH, among which the relatively significant species are Si, SiC_2, and $SiCl_2$. The amount of gaseous Si always increases with temperature and reaches its maximum at 2900 K. On the contrary, the amount of the remainder of the species initially increases with temperature and then drops slowly with further increases of temperatures.

At low temperatures, there is almost no Cl predicted. After passing a critical temperature, which increased with the pressure, the amount of Cl increased sharply with temperature and reached the maximum value at 2900 K. The maximum value keeps decreasing with increasing pressure. Maximum values were 8.5, 2.5, 1.4, 1, and 0.83 moles for 5, 100, 300, 500, and 760 torr, respectively. According to Besmann [58], for temperatures below 1500 K, the byproduct HCl might retard the formation of SiC. For all of the five pressure cases, the amount of HCl initially increased with temperature, reached a maximum and then remained relatively constant. The temperatures corresponding to the leveling off of the quantity of HCl was 1400 K for all of the different pressures except 5 torr. For 5 torr the temperature was 1200 K. Also, for the 5 torr case, for temperatures above 2100 K, the amount of HCl decreased slowly with temperature.

The quantity of H_2 at different temperatures and pressures is rather constant at about 40 moles. There was a slight decrease with increasing temperature and a larger decrease to 24 moles at 2900 K when the pressure were 5 torr. The atomic H increased with temperature for all pressures.

The gaseous species with significant quantities for H_2 to MTS = 20 under five different pressures, are shown in Figures 10-14. The y axis gives the quantity of the species in mole and the x is the temperature in K.

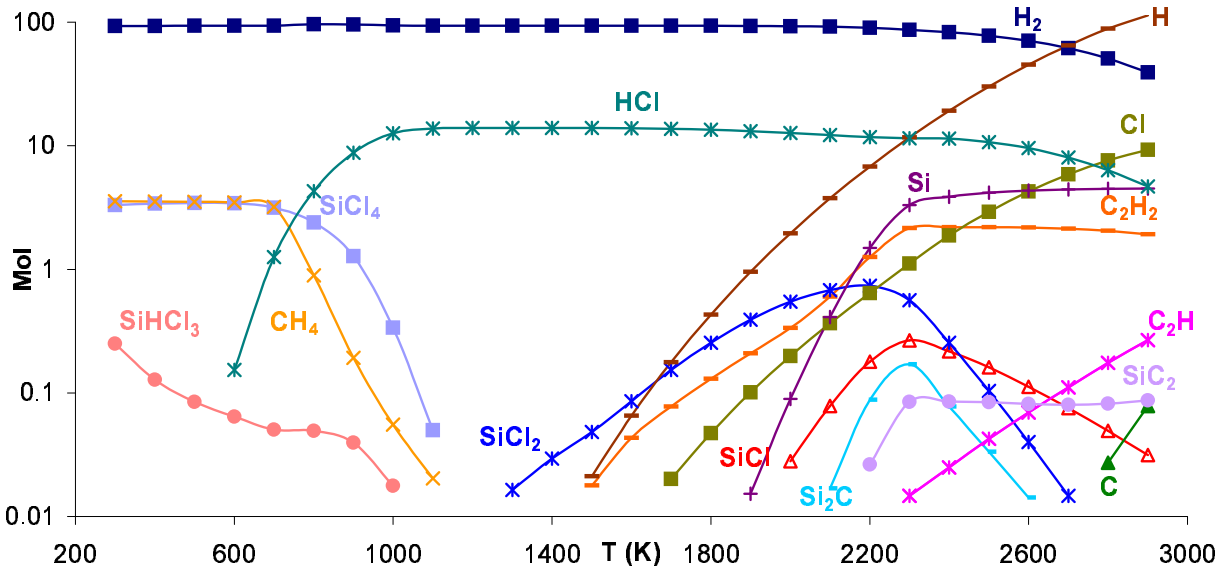

Figure 10: Gaseous species of the system MTS/H_2 with H_2/MTS ratio =20, and P=5 torr.

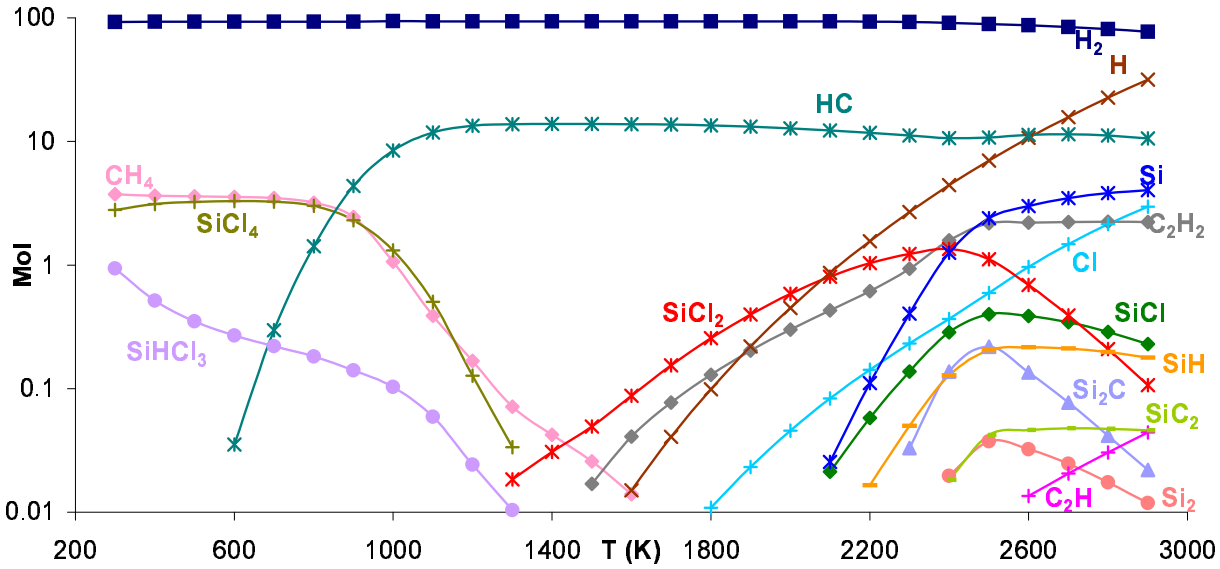

Figure 11: Gaseous species of the system MTS/H_2 with H_2/MTS ratio =20, and P=100 torr.

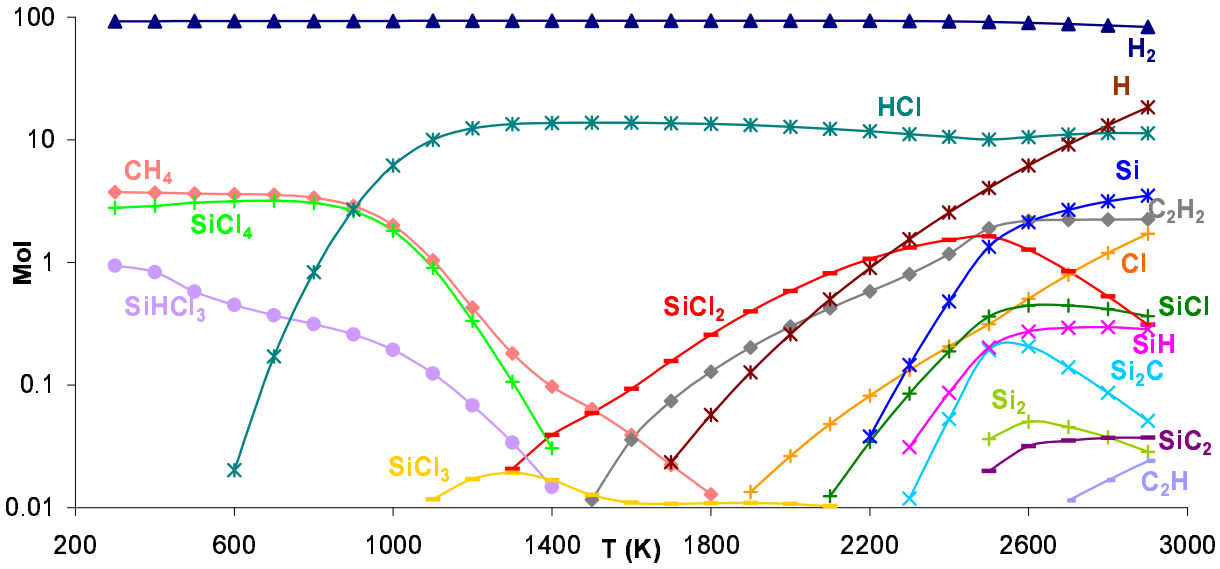

Figure 12: Gaseous species of the system MTS/H_2 with H_2/MTS ratio =20, and P=300 torr.

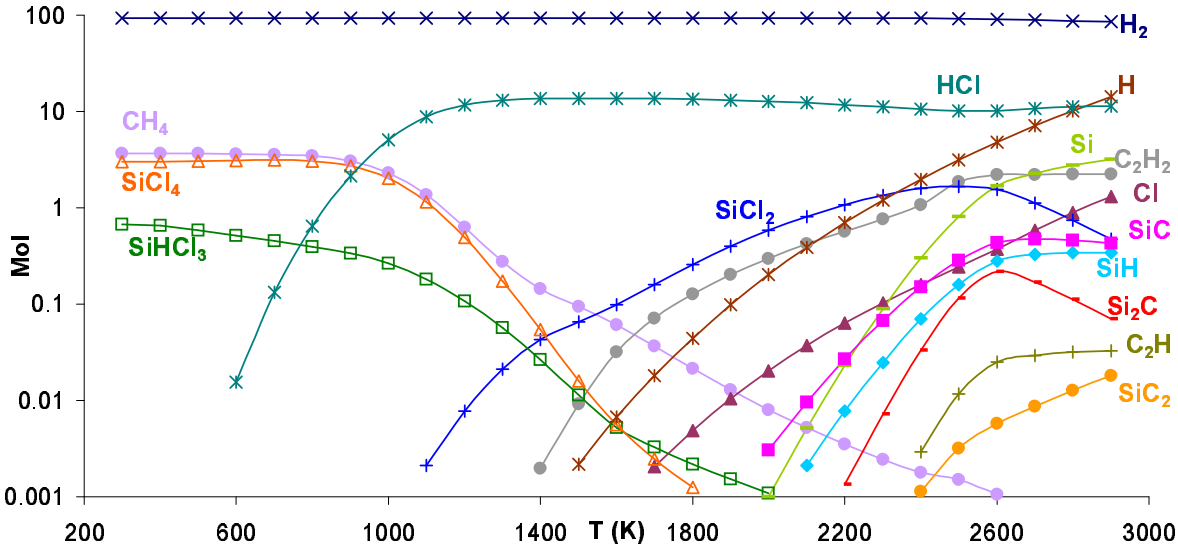

Figure 13: Gaseous species of the system MTS/H_2 with H_2/MTS ratio =20, and P=500 torr.

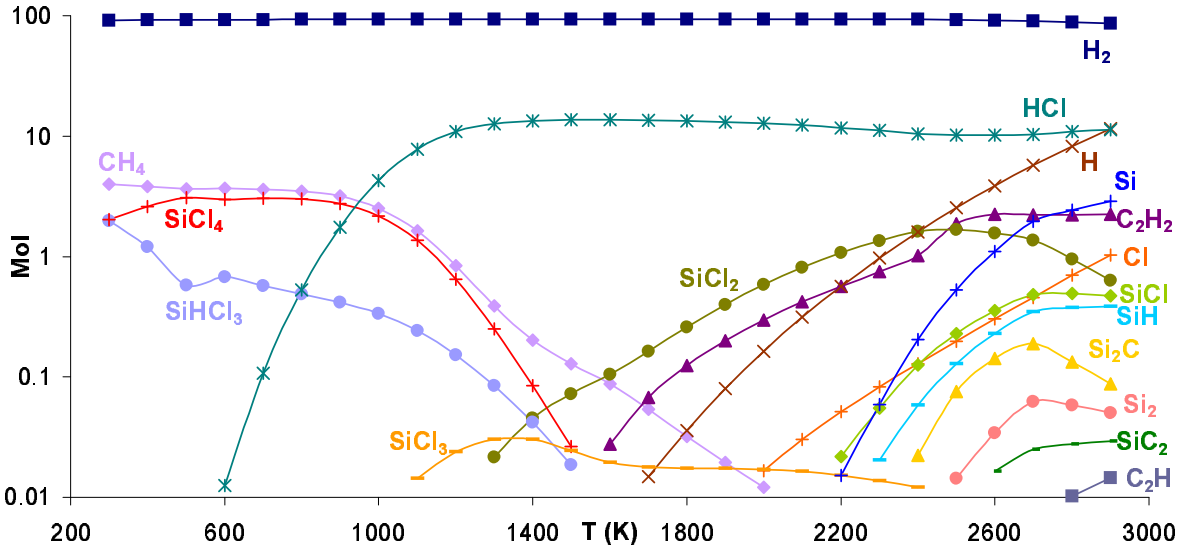

Figure 14: Gaseous species of the system MTS/H_2 with H_2/MTS ratio =20, and P=760 torr.

For the carbon-containing species, at low temperatures, the dominant species is still CH_4, keeping a relatively constant amount between 3 and 4 mole in the beginning, then starts to decrease sharply at a critical temperature, and finally reaches virtually 0 moles. The critical temperature is 700 K for 5 the torr case, 800 K for 100 and 300 torr, and 900K for 500 and 760 torr. The low temperature silicon-containing species are $SiCl_4$ and $SiHCl_3$, while $SiCl_4$ is much more significant than the other. $SiCl_4$ undergoes a similar pattern with the CH_4, keeping a relatively constant amount in the range of 2.7 to 3.3 and then decreasing with temperature dramatically. The critical temperatures are almost the same as those of CH_4's. The second dominant silicon containing species, $SiHCl_3$, keeps decreasing with temperature, and most of the time the values are below 1 mole. The amount of $SiHCl_3$ increases as pressure increases.

The high temperature carbon-containing species includes C_2H_2, C_2H, SiC_2, and Si_2C. C_2H_2 is the dominant species. The amount of C_2H_2 increases with temperature and maintains the maximum at temperatures beyond 2500 K. Most of the time, the amounts of the remainder of the carbon-containing species are lower than 0.5 mole, which are much less significant than C_2H_2.

There are no big changes concerning the behaviors of Cl, HCl, H, and H_2 between H_2/MTS=10 and 20. At low temperatures, almost no Cl is present, as shown in Figures 10-14. Beyond a critical temperature, which increased with the pressure, Cl increased sharply with temperature and reached the maximum values at 2900 K. The maximum value keeps decreasing with increasing pressure. For all of the five pressure cases, the amount of HCl initially increased sharply with temperature, reached a maximum, and then remained the relatively constant except for the 5 torr case, where beyond 2500 K, the amount of HCl decreased slowly with temperature. The temperatures where the maximum values were achieved were 1000 K for the 5 torr case, 1100 K for 100 torr, 1200 K for both 300 and 500 torr, and 1300 K for 760 torr. The amount of atomic H increased with temperature for all of the five pressure cases, and were larger at higher pressures. The amounts of H_2 were relatively stable for all of the temperatures and pressures, typically around 90 moles. But at very high temperatures, there were slight decreases, especially for the 5 torr case, where

the amount of H_2 was about 40 moles at 2900K.

The significant gaseous species for H_2 to MTS ratios of 60 and 100 for five different pressures, are shown in Figures 15-24. As for the two cases with high H_2 to MTS ratios (60, 100), the carbon containing and silicon containing species at low and high temperatures have similar behavior as the two low H_2 to MTS ratios (10, 20). But when the H_2 to MTS equals 60 or 100, SiH is another significant high temperature species besides gaseous Si and Si_2C.

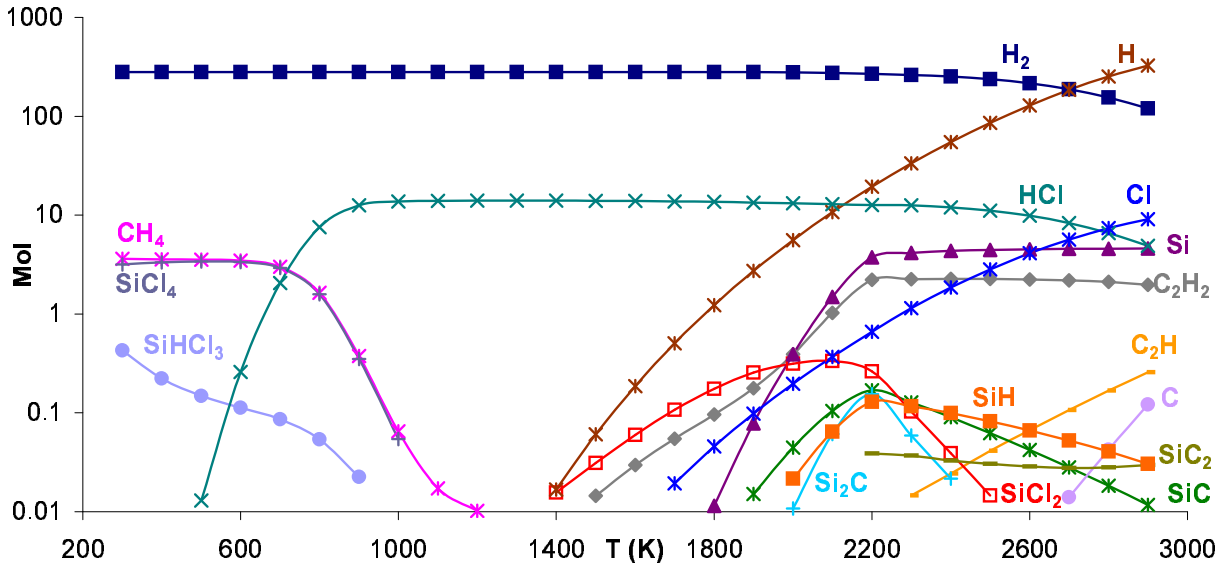

Figure 15: Gaseous species of the system MTS/H_2 with H_2/MTS ratio =60, and P=5 torr.

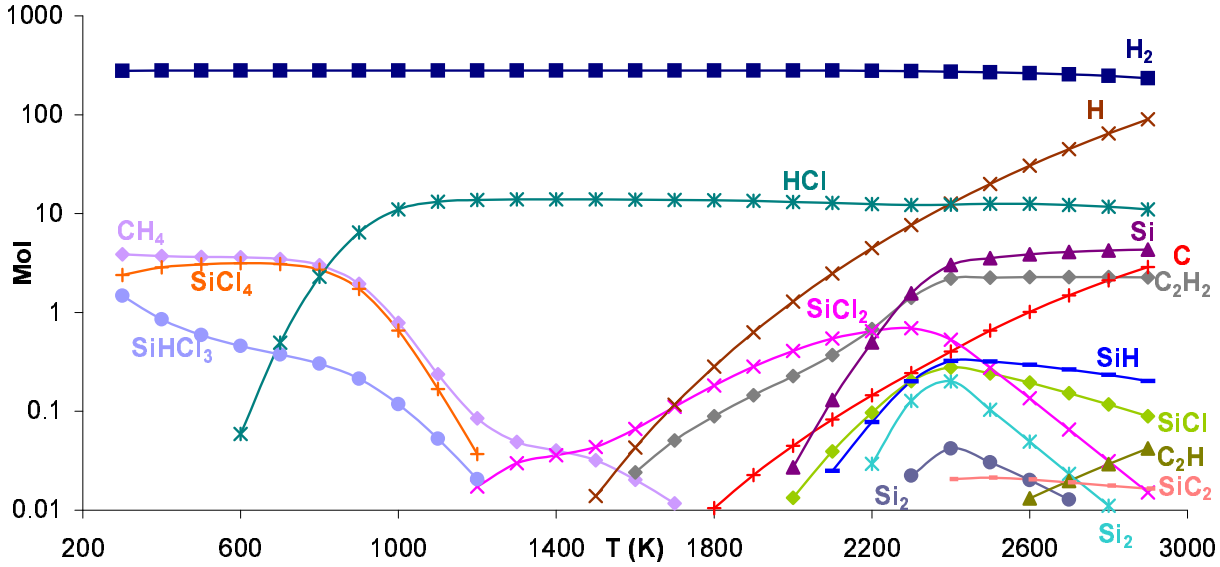

Figure 16: Gaseous species of the system MTS/H_2 with H_2/MTS ratio =60, and P=100 torr.

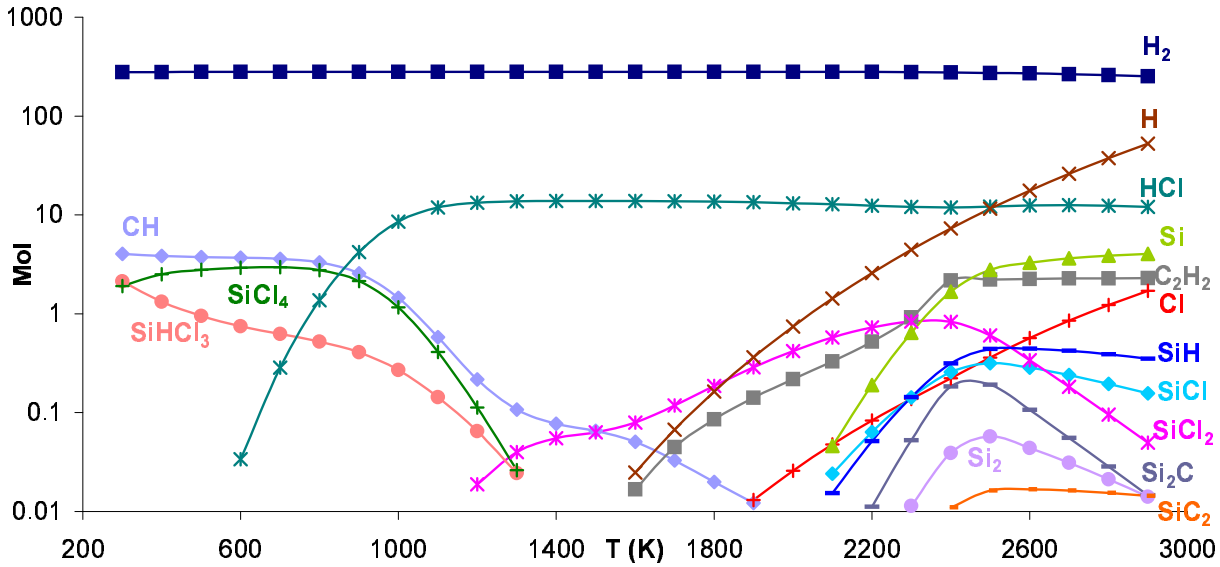

Figure 17: Gaseous species of the system MTS/H_2 with H_2/MTS ratio =60, and P=300 torr.

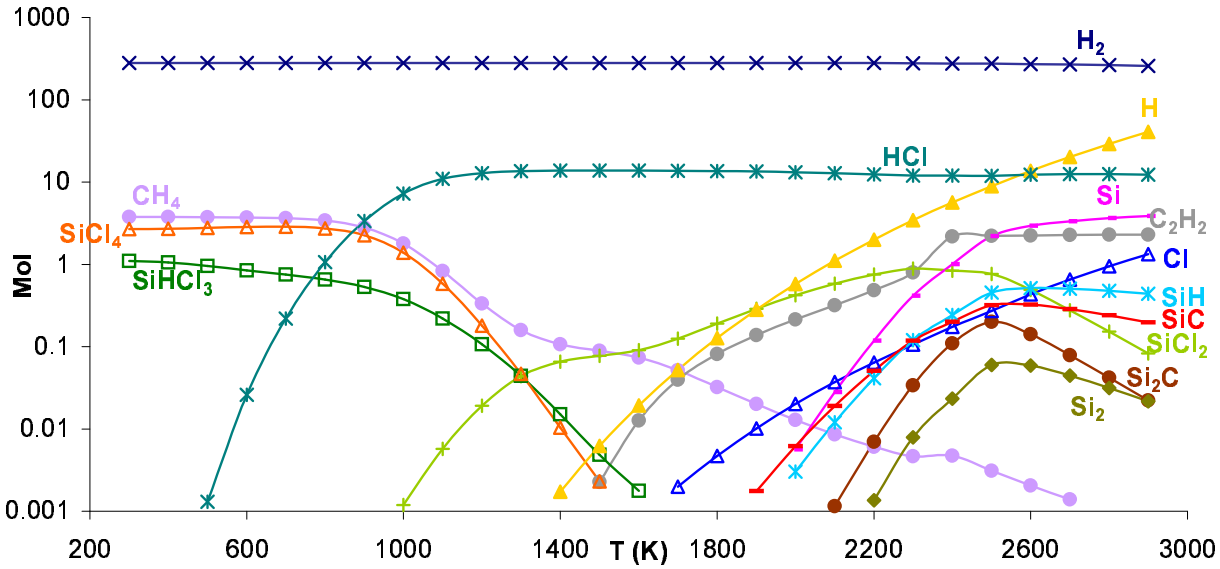

Figure 18: Gaseous species of the system MTS/H_2 with H_2/MTS ratio =60, and P=500 torr.

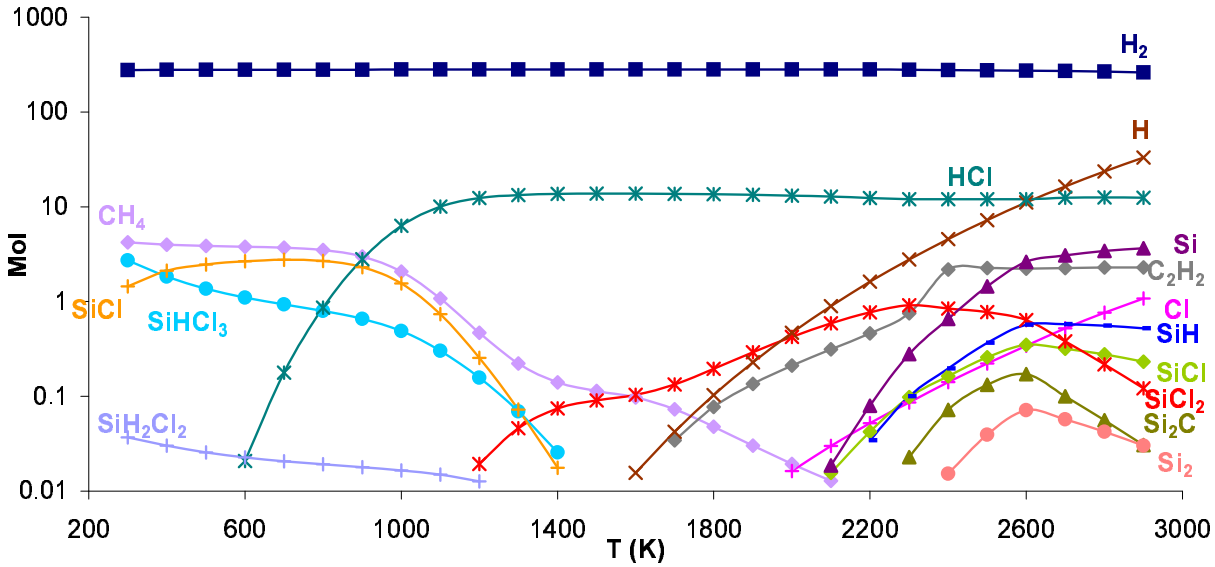

Figure 19: Gaseous species of the system MTS/H_2 with H_2/MTS ratio =60, and P=760 torr.

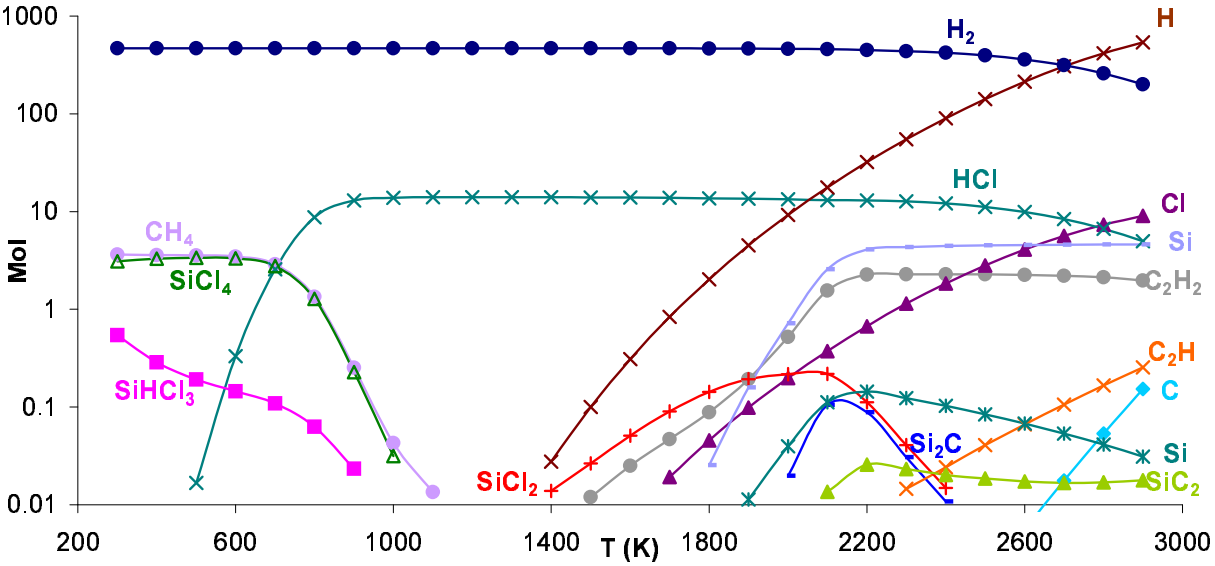

Figure 20: Gaseous species of the system MTS/H_2 with H_2/MTS ratio =100, and P=5 torr.

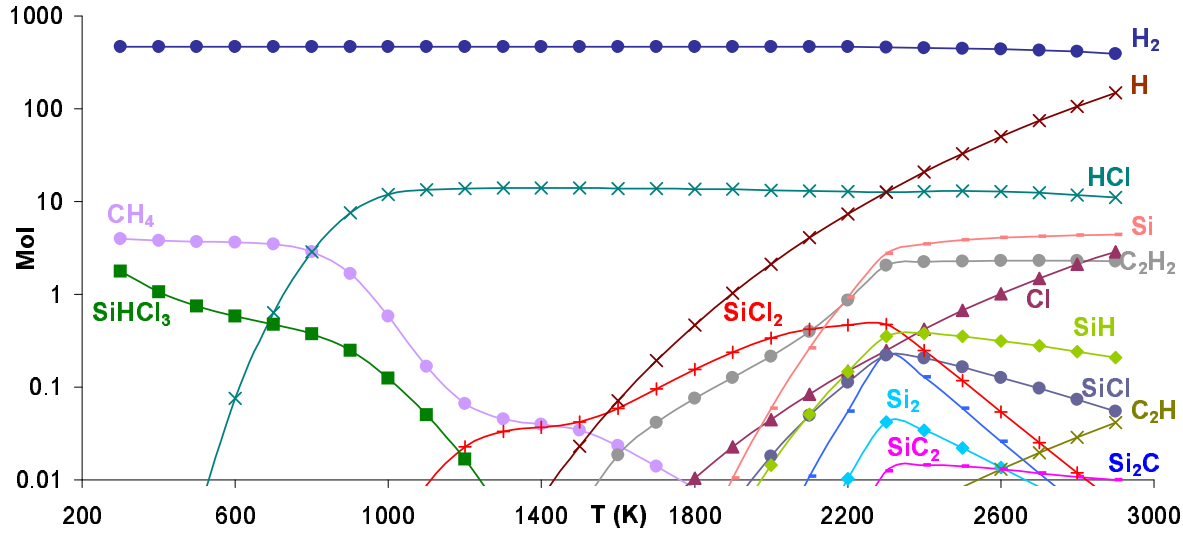

Figure 21: Gaseous species of the system MTS/H_2 with H_2/MTS ratio =100, and P=100 torr.

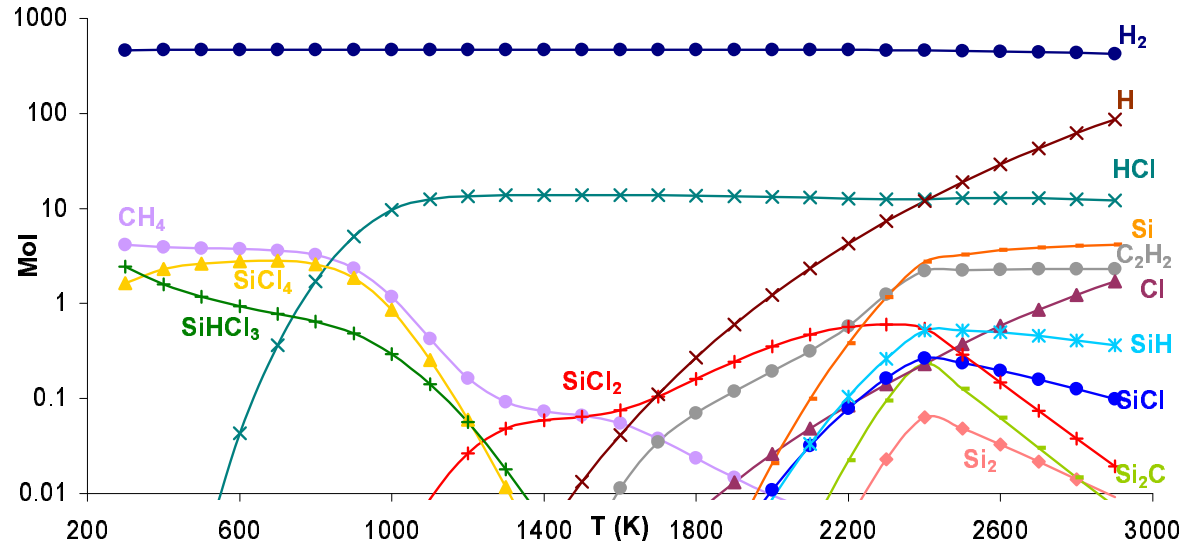

Figure 22: Gaseous species of the system MTS/H_2 with H_2/MTS ratio =100, and P=300 torr.

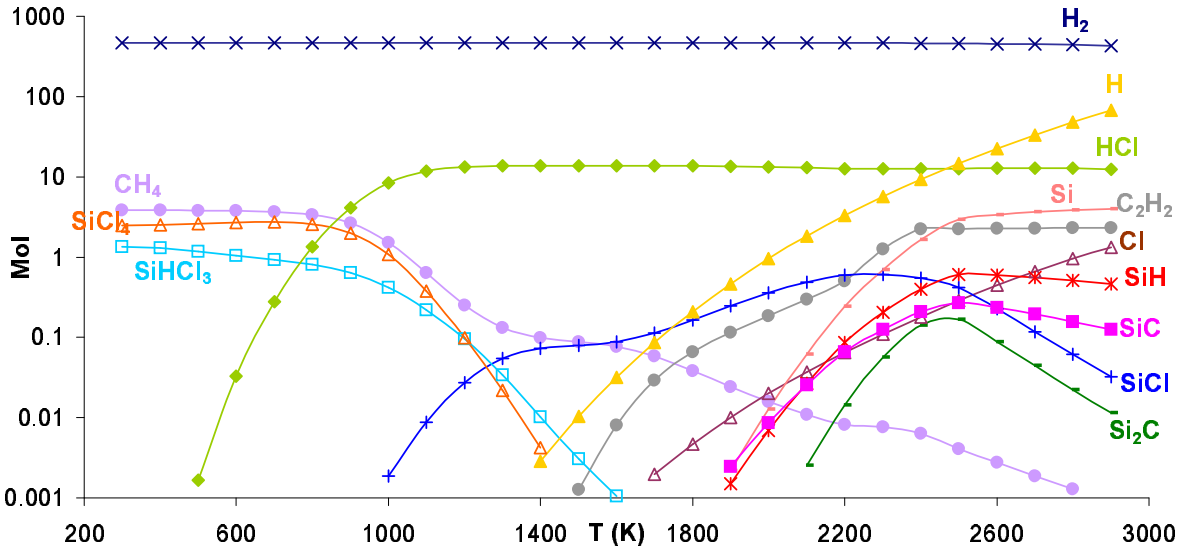

Figure 23: Gaseous species of the system MTS/H_2 with H_2/MTS ratio =100, and P=500 torr.

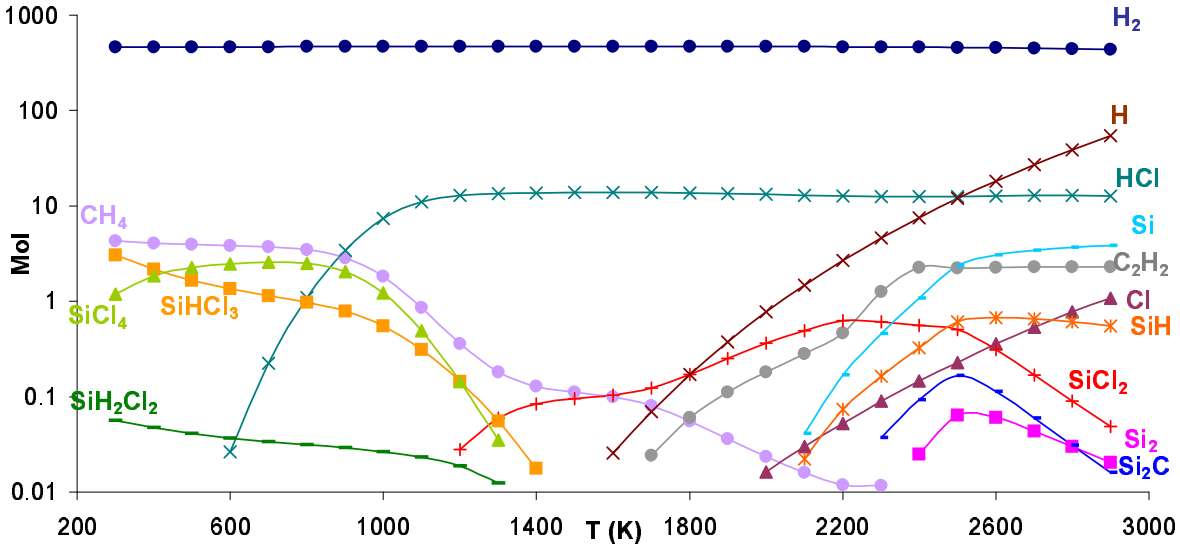

Figure 24: Gaseous species of the system MTS/H_2 with H_2/MTS ratio =100, and P=760 torr.

From all of the gaseous species figures (Figures 5-24), it is likely that at low temperatures, MTS decomposes into CH_4, $SiCl_4$, and $SiHCl_3$ and so on. Due to the low temperatures, the chemical reactions resulting in the formation of solid SiC can not be initialized and conducted. Once the temperatures become higher and higher, those decomposed species will react with each other and generate the solid SiC deposits. The reactions will become easier and faster with increasing temperature, which results in the sharp decrease of the carbon-containing and silicon containing species at intermediate temperatures. A the intermediate temperatures, the forward chemical reactions for the formation of solid SiC are dominate. But when the temperatures are extremely high, the formation of a number of gaseous carbon-containing and silicon containing species occurs. at such high temperatures, the backward chemical reactions, i.e., decomposition of solid SiC, are dominant. The higher the temperatures, the easier the decomposition of solid SiC, which explains why the amount of those gaseous species increase at the highest temperatures.

The pressure difference effects on the significant gaseous species are shown in Figures 25-28. Consider the quantity of CH_4, the major low temperatures carbon-containing species, as pressure increases, the quantity of CH_4 increases. Also, for increasing pressure, the temperature at which the quantity of CH_4 starts to decrease is seen to increase. It is seen in Figures 25-28 that the MTS/H_2 ratio does not have a big effect on the CH_4.

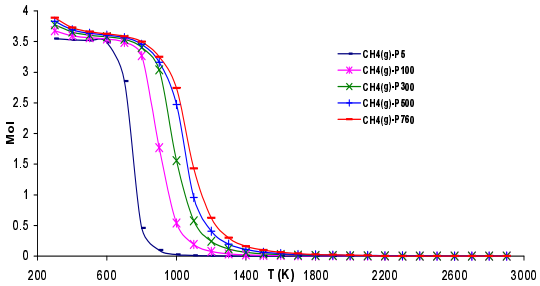

(a) Low Temperature Carbon Containing Species, CH_4

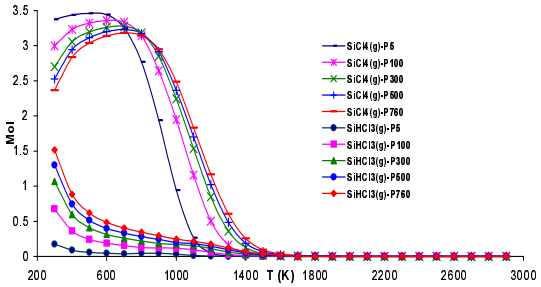

(b) Low Temperature Silicon Containing Species, $SiCl_4$, $SiHCl_3$

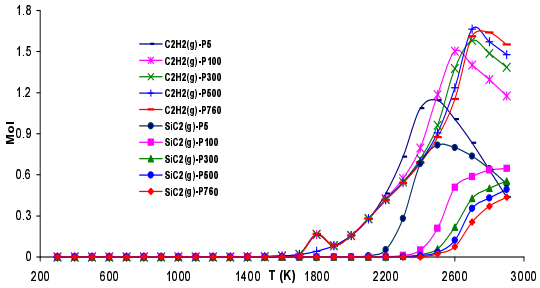

(c) High Temperature Carbon Containing Species, C_2H_2, SiC_2

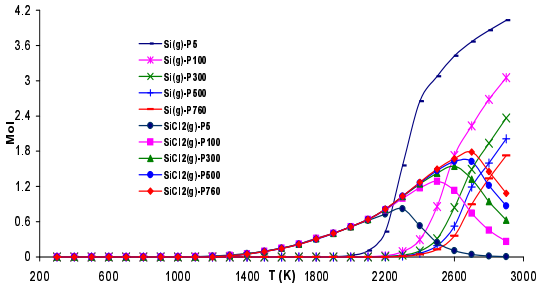

(d) High Temperature Silicon Containing Species, Si, $SiCl_2$

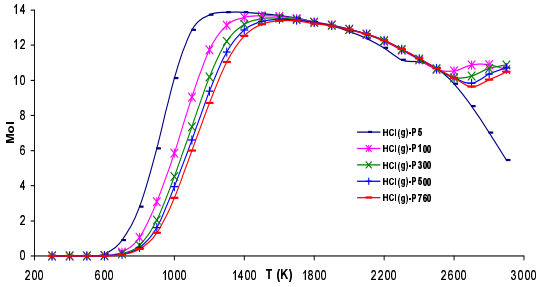

(e) HCl

Figure 25: Pressure Effects on the Significant Gaseous Species of system H_2/MTS =10.

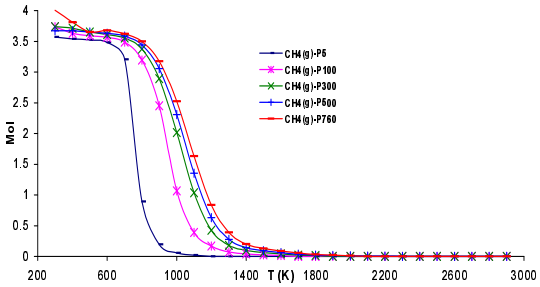

(a) Low Temperature Carbon Containing Species, CH_4

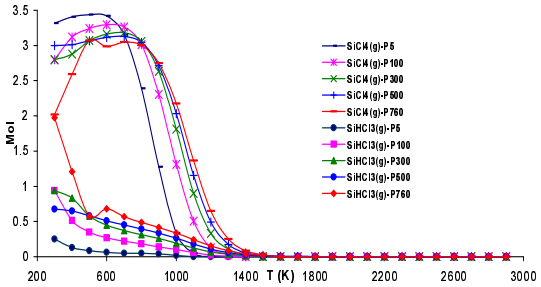

(b) Low Temperature Silicon Containing Species, $SiCl_4$, $SiHCl_3$

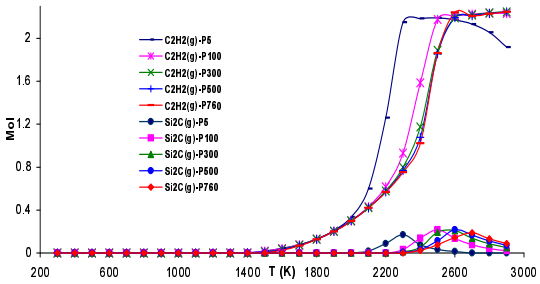

(c) High Temperature Carbon Containing Species, C_2H_2, Si_2C

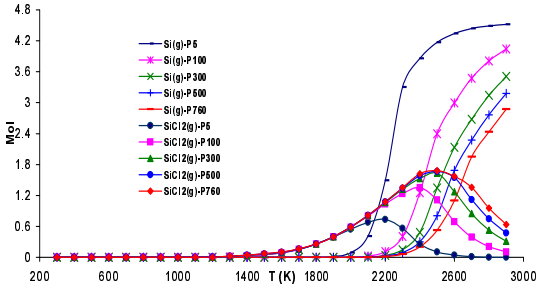

(d) High Temperature Silicon Containing Species, Si, $SiCl_2$

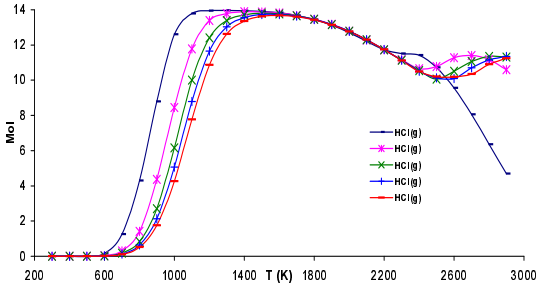

(e) HCl

Figure 26: Pressure Effects on the Significant Gaseous Species of system H_2/MTS =20.

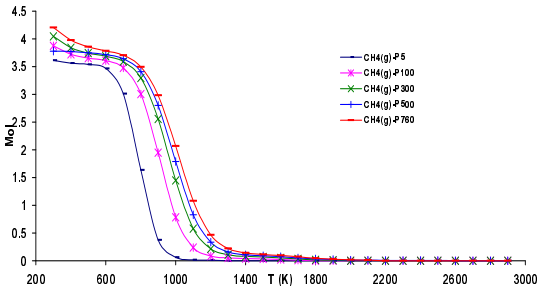

(a) Low Temperature Carbon Containing Species, CH_4

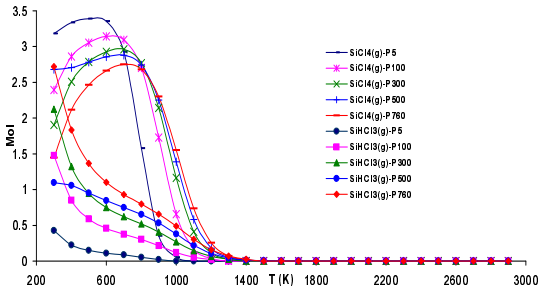

(b) Low Temperature Silicon Containing Species, $SiCl_4$, $SiHCl_3$

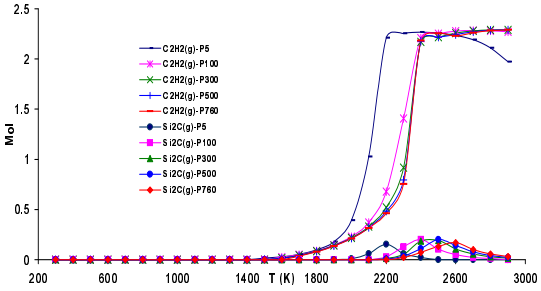

(c) High Temperature Carbon Containing Species, C_2H_2, Si_2C

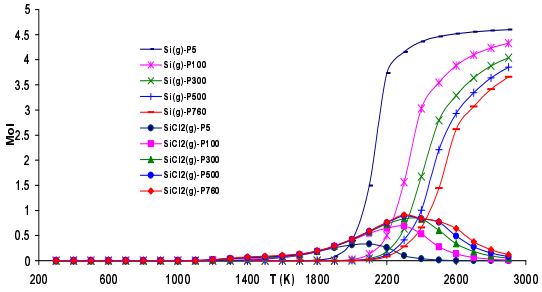

(d) High Temperature Silicon Containing Species, Si, $SiCl_2$

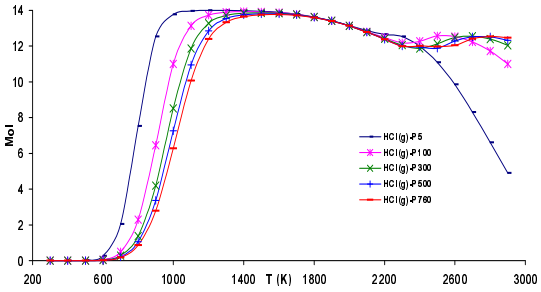

(e) HCl

Figure 27: Pressure Effects on the Significant Gaseous Species of system H_2/MTS =60.

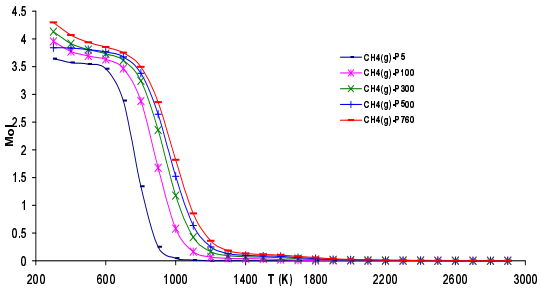

(a) Low Temperature Carbon Containing Species, CH_4

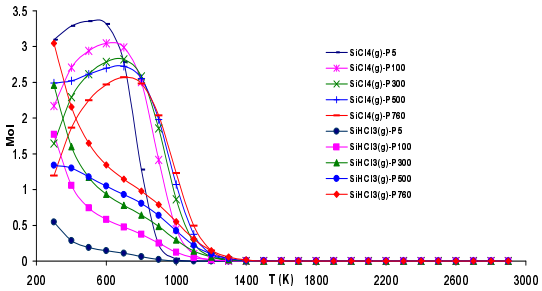

(b) Low Temperature Silicon Containing Species, $SiCl_4$, $SiHCl_3$

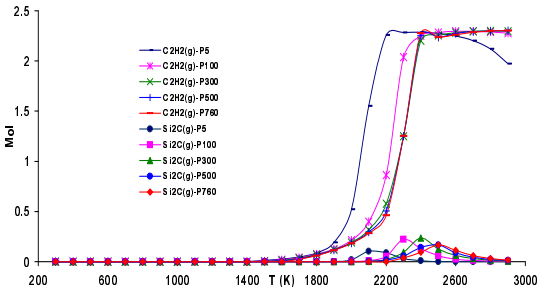

(c) High Temperature Carbon Containing Species, C_2H_2, Si_2C

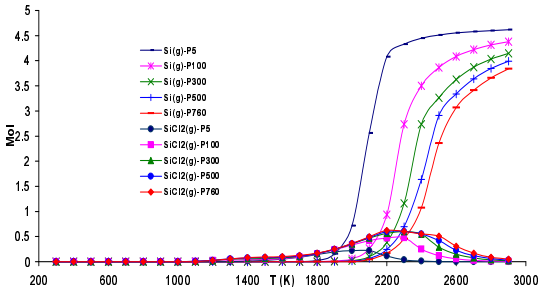

(d) High Temperature Silicon Containing Species, Si, $SiCl_2$

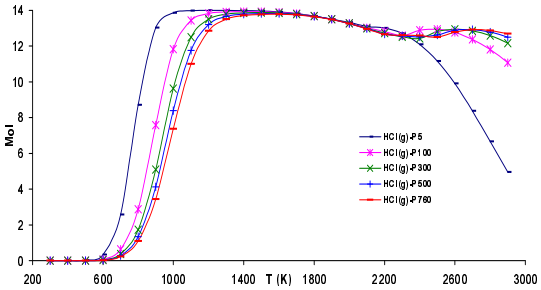

(e) HCl

Figure 28: Pressure Effects on the Significant Gaseous Species of system H_2/MTS =100.

As for the major silicon containing species at low temperatures, $SiCl_4$ is more significant than $SiHCl_3$. At low temperatures, the quantity of $SiCl_4$ decreases with pressure, but beyond a specific temperature, the effect of pressure on the $SiCl_4$ is exactly the opposite, i.e., larger quantity of $SiCl_4$ at higher pressure. The quantity of $SiHCl_3$ consistently increases with pressures as shown in Figures 25-28 for all of the four different MTS concentrations. As the MTS concentration decreases, i.e., increase in H_2/MTS ratio, the quantity of $SiHCl_3$ has a tendency to increase, and the pressure effects on both $SiCl_4$ and $SiHCl_3$ become more significant.

At high temperatures, when the H_2/MTS ratio is 10, the major carbon containing species are C_2H_2 and SiC_2, but as the H_2/MTS ratio is higher than 10, C_2H_2 and Si_2C instead of SiC_2 are the major species. Also, the quantity of Si_2C is much less significant than SiC_2 in comparison with C_2H_2. The quantity of C_2H_2 increases with temperatures in the beginning, after reaching its maximum, it decreases with temperature. The decrease is very significant for the case of H_2/MTS =10, but for the rest of the H_2/MTS ratios, this is only true when the pressure is 5 torr. When the H_2/MTS ratio is other than 10, except the 5 torr case, the quantity of C_2H_2 dose not decrease with temperature after reaching the maximum. The amount of C_2H_2 generally increases with H_2/MTS ratio, which means C_2H_2 is favorable at lower MTS concentrations.

The quantity of gaseous Si, which is the major silicon containing species at high temperatures, keeps increasing with temperature. But the quantity of $SiCl_2$, the secondary major silicon containing species at high temperatures, increases with temperature in the beginning and then decreases with temperatures after reaching its maximum. The gaseous Si is favorable at low pressure, while the $SiCl_2$ is more abundant high pressure. For decreasing MTS concentration, the amount of gaseous Si and $SiCl_2$ also decrease.

HCl has the relatively same behavior for different pressures other than the 5 torr case, where it increases with temperature then decreases with temperature, and finally increases slightly at the highest temperatures. But for the 5 torr case, after it reaches its maximum, HCl keeps decreasing sharply.

From the above discussion, it is evident that pressure, precursor concentration, and

temperature have a big effect on the SiC deposition process. The very low pressure case is much different than those above 100 torr.

4.1.2 Condensed Species

The calculated results for the condensed phases for different MTS concentrations, pressures, and temperatures are shown in Figures 29 to 33. Based on the calculations, only solid β-SiC, solid C, and liquid Si can exist under the conditions of interest, which can be seen in Figures 29-33. In fact, according to the data in the JANAF Tables, [73] β-SiC is more stable than α-SiC. Therefore, no α-SiC was expected to be formed based on this calculation. For the temperature range of 300 to 2900 K, β-SiC is always the dominant condensed phase present.

Sometimes, liquid silicon (Si) or solid carbon (C) predicted to co-deposit with β-SiC. The curves for β-SiC have similar shape for all five pressures and four MTS concentrations. This means that the quantity of β-SiC is expected to increase with temperature over the low temperature range, then reach a maximum at a specific temperature, and finally, in the high temperature range, decrease to zero moles. It seems that solid C is favorable at low temperatures with low pressure and high MTS concentrations. On the contrary, liquid silicon is easier to form at high temperature with high pressure and low MTS concentration. As shown in Figures 29(c),(d) and 30(c),(d), single phase β-SiC is predicted to deposit at pressures lower than 100 torr and high MTS concentration, i.e., H_2/MTS no greater than 20.

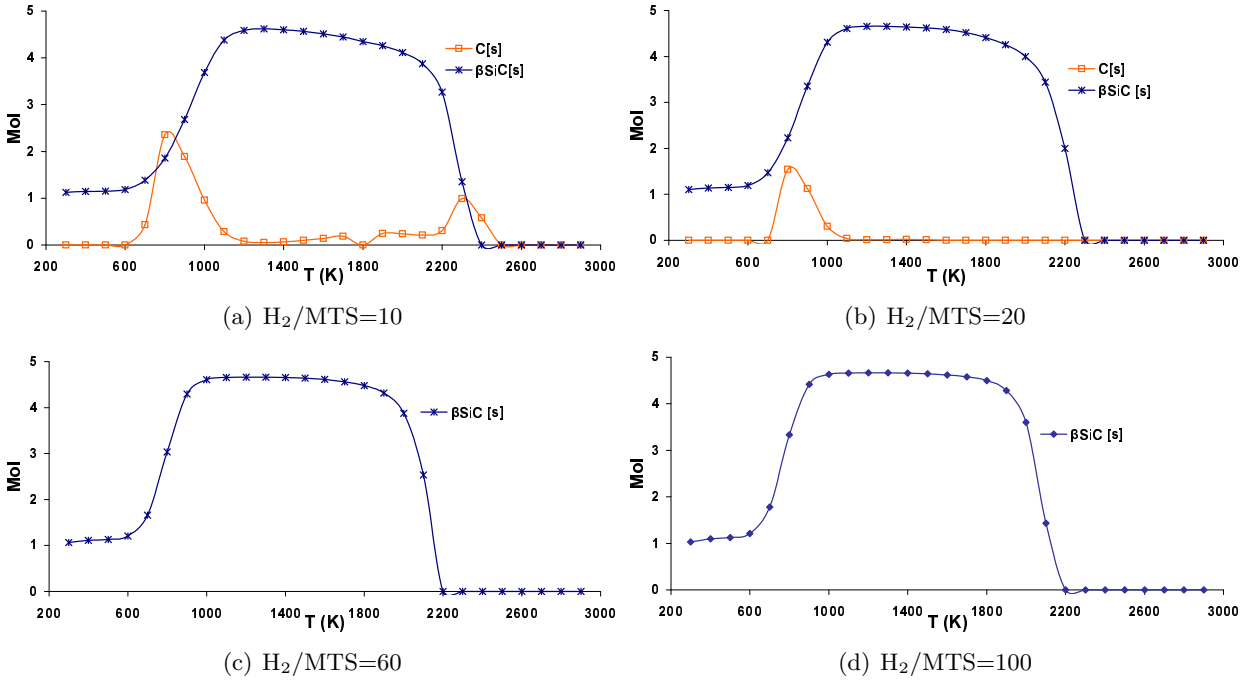

(a) H_2/MTS=10 (b) H_2/MTS=20

(c) H_2/MTS=60 (d) H_2/MTS=100

Figure 29: The condensed phases of system H_2/MTS at pressure 5 Torr with four H_2/MTS ratios.

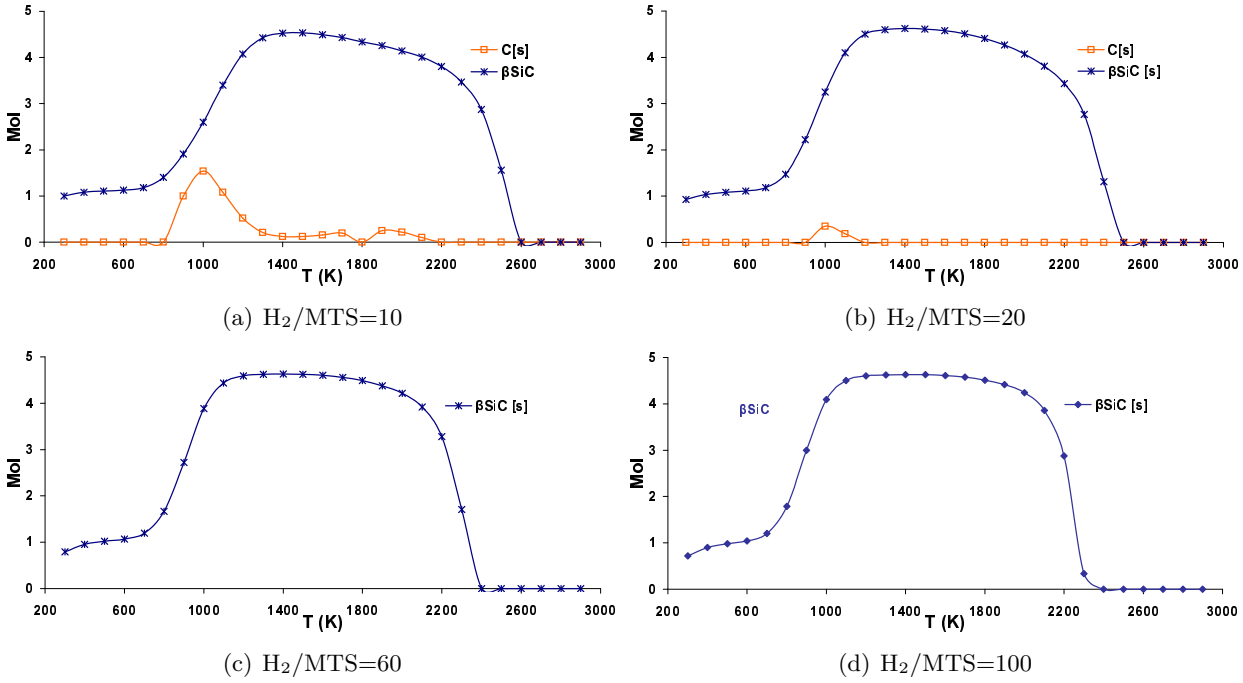

(a) H_2/MTS=10 (b) H_2/MTS=20

(c) H_2/MTS=60 (d) H_2/MTS=100

Figure 30: The condensed phases of system H_2/MTS at pressure 100 Torr with four H_2/MTS ratios.

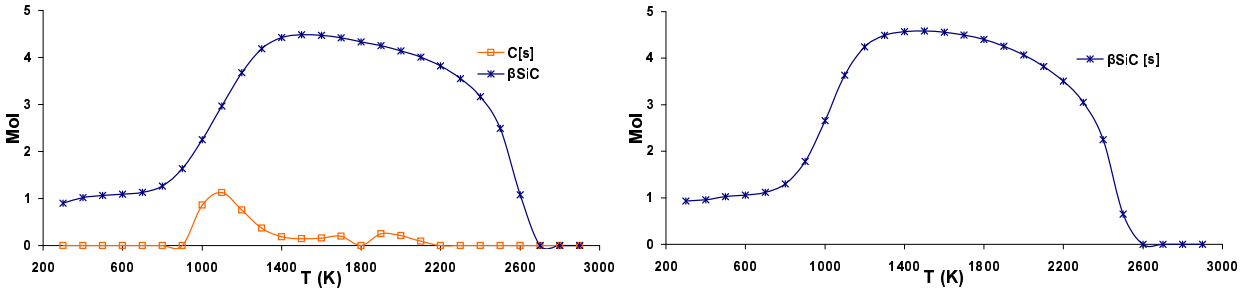

(a) H_2/MTS=10

(b) H_2/MTS=20

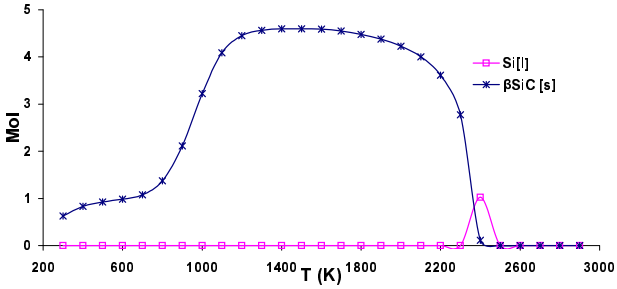

(c) H_2/MTS=60

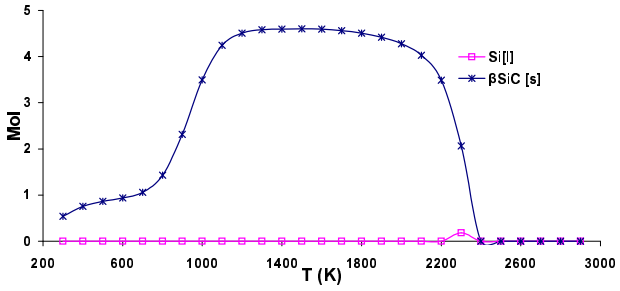

(d) H_2/MTS=100

Figure 31: The condensed phases of system H_2/MTS at pressure 300 Torr with four H_2/MTS ratios.

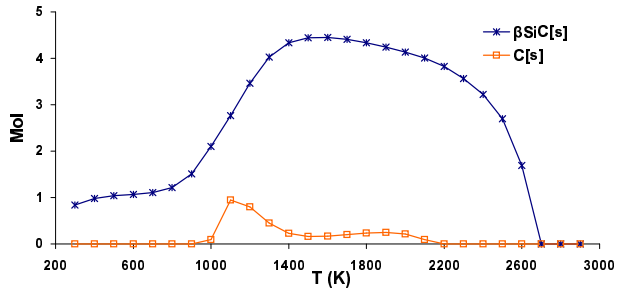

(a) H_2/MTS=10

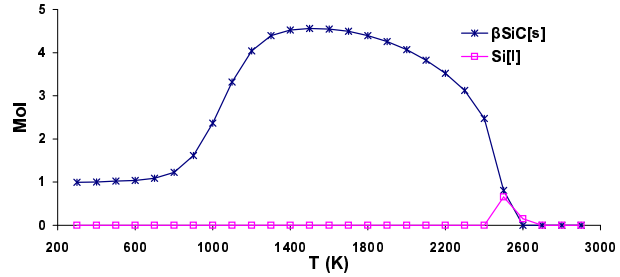

(b) H_2/MTS=20

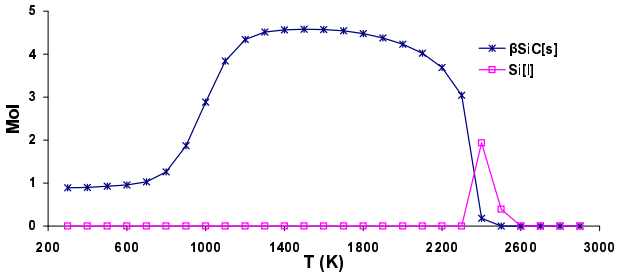

(c) H_2/MTS=60

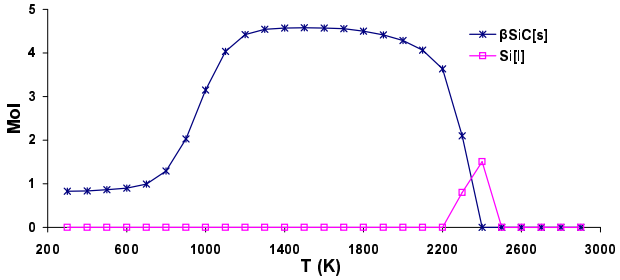

(d) H_2/MTS=100

Figure 32: The condensed phases of system H_2/MTS at pressure 500 Torr with four H_2/MTS ratios.

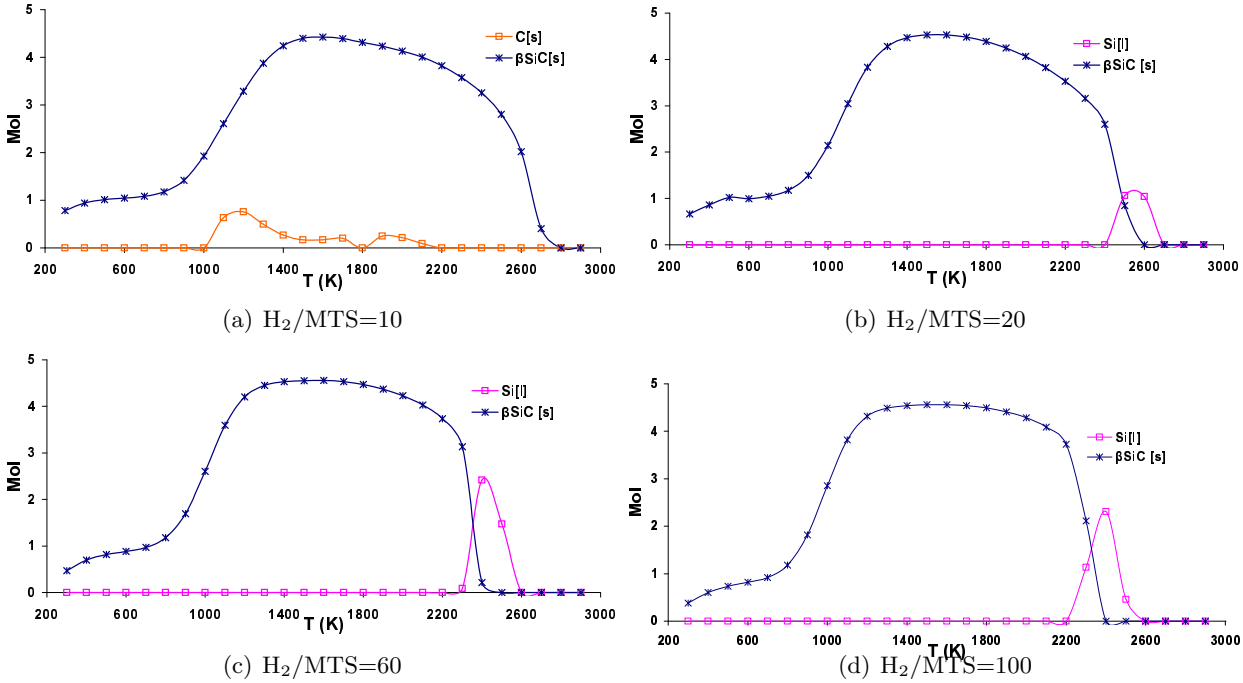

(a) H_2/MTS=10 (b) H_2/MTS=20

(c) H_2/MTS=60 (d) H_2/MTS=100

Figure 33: The condensed phases of system H_2/MTS at pressure 760 Torr with four H_2/MTS ratios.

Figures 34 to 37 and 38 to 43 show the β-SiC curves at different pressures for the four MTS to H_2 ratios (α). It is clear that the growth temperature markedly affects the amount of β-SiC predicted to form over a wide range of pressure and H_2/MTS ratios, shown in these figures. The quantity of SiC first increases with increasing temperature, reaches a broad maximum, and then decreases with further increase of temperature, eventually reaches zero. It is indicated that the critical temperatures, at which the amount of SiC stops increasing and starts to decrease, decrease with pressure. At low temperatures (less than about 2000 K), low MTS concentrations (high H_2/MTS) favor the formation of more SiC. For high temperatures (greater than 2200 K, or 1900 K for the 5 torr case) the behavior reversed, i.e., high MTS concentrations favor SiC formation. Similar trends were observed for the effect of pressure. That is, at low temperatures, low pressures favor the formation of more SiC, but at high temperatures, high pressure favors SiC formation. These calculation results are very important for eliminating the volcano effects of SiC fibers. Chapter V will further discuss this.

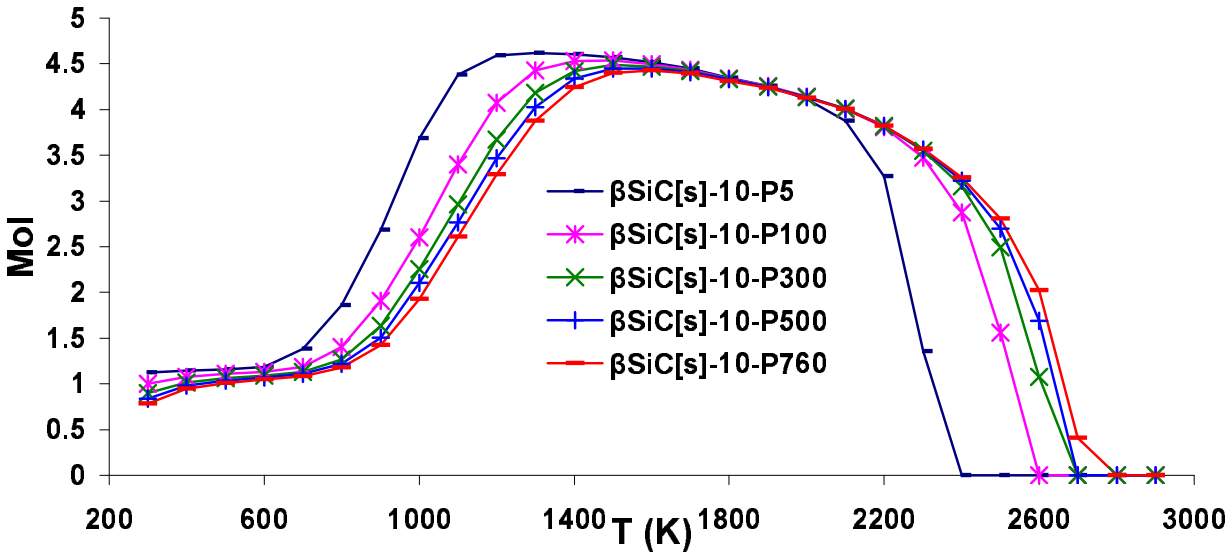

Figure 34: Quantity of β-SiC at different pressures with H_2/MTS =10.

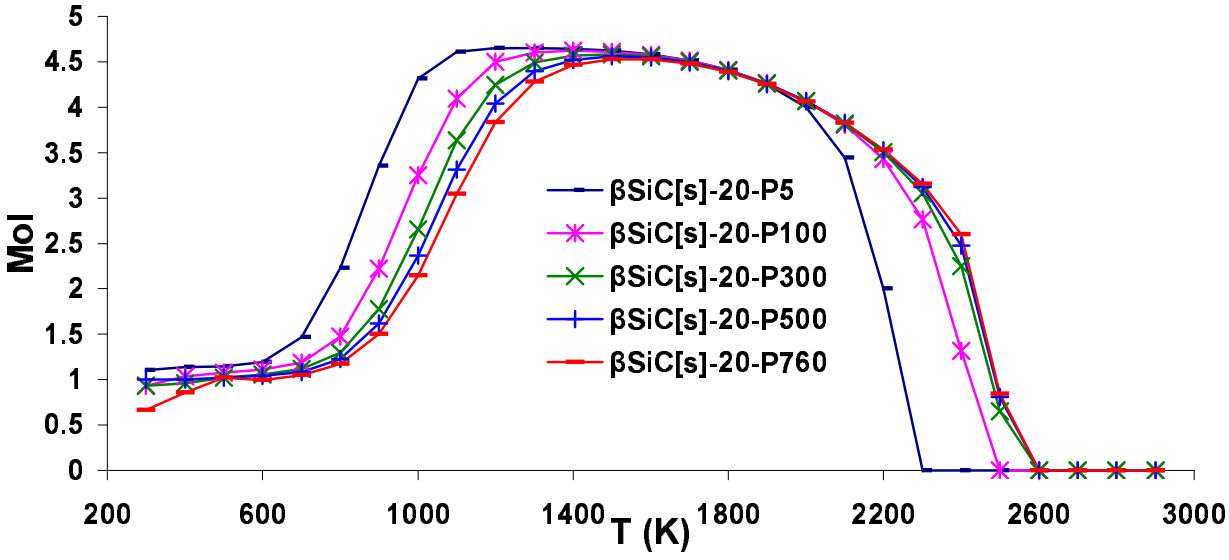

Figure 35: Quantity of β-SiC at different pressures with H_2/MTS =20.

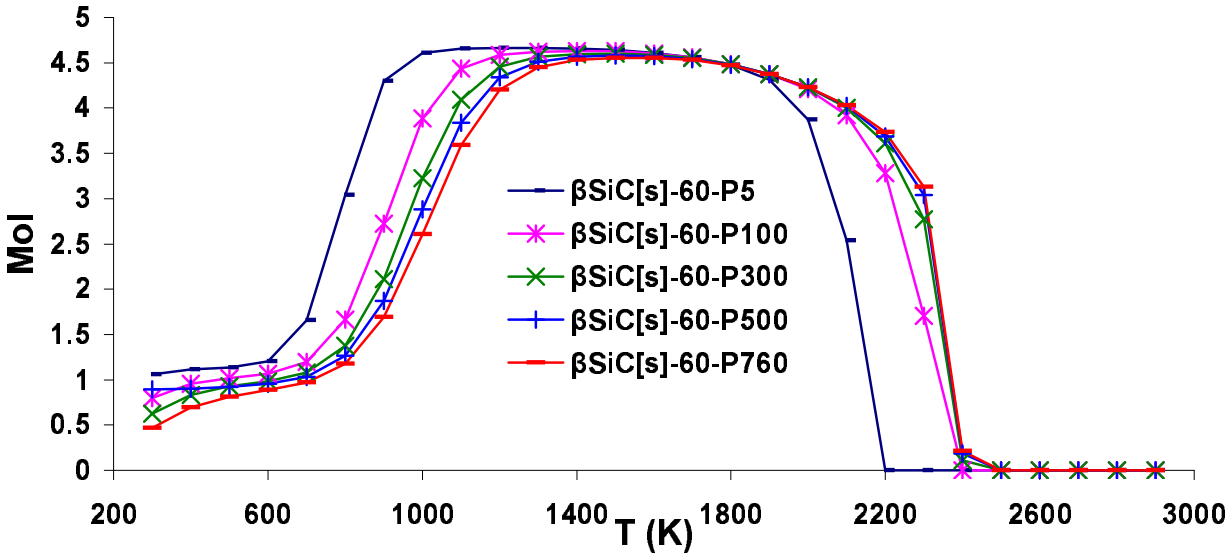

Figure 36: Quantity of β-SiC at different pressures with H_2/MTS =60.

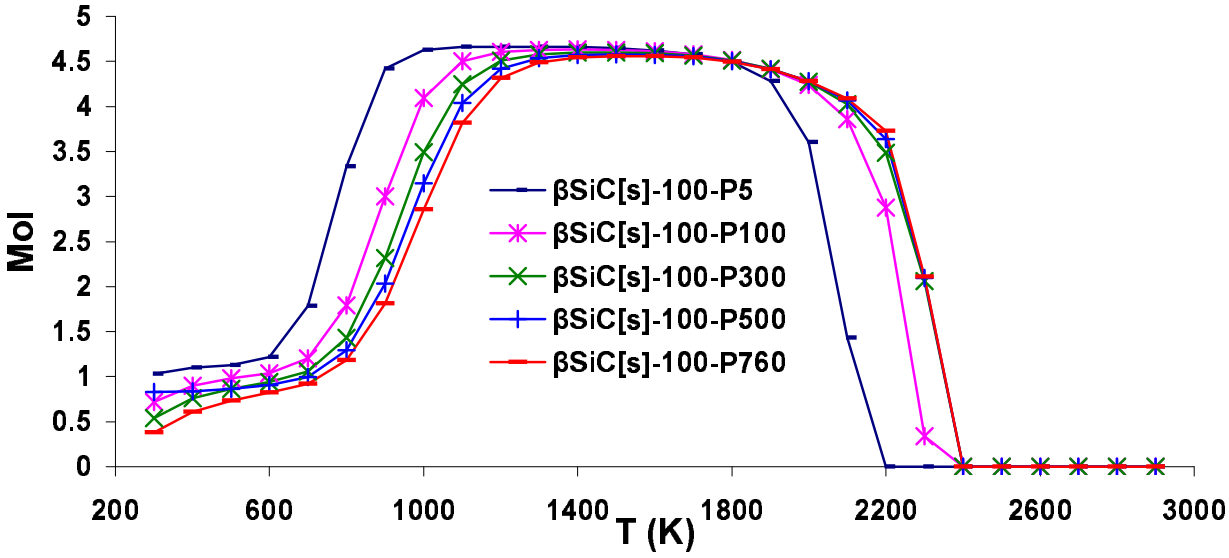

Figure 37: Quantity of β-SiC at different pressures with H_2/MTS =100.

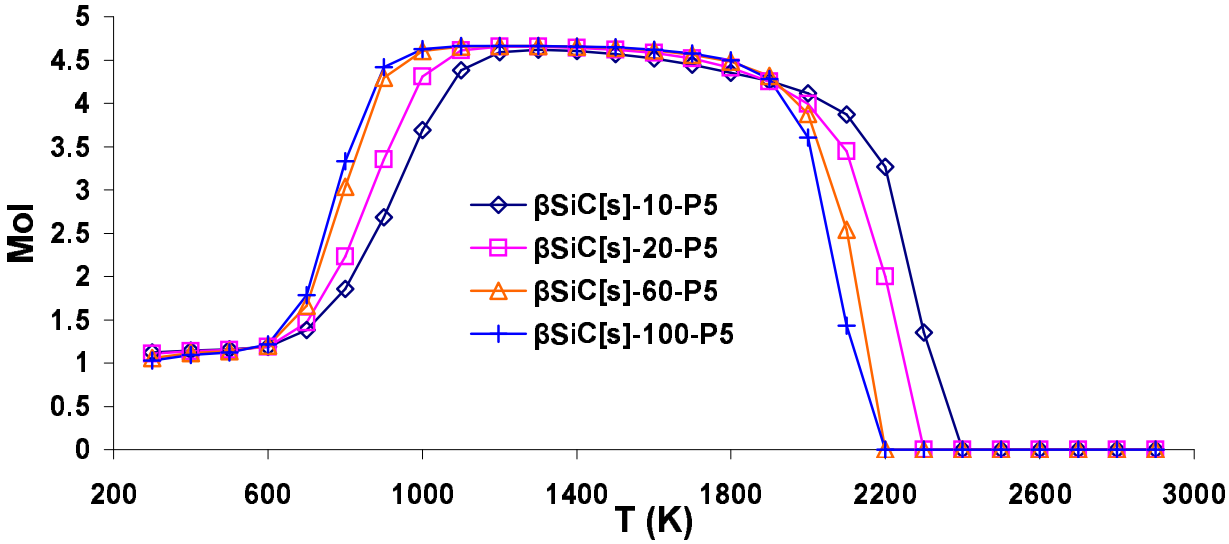

Figure 38: Quantity of β-SiC at different H_2/MTS ratios for pressure of 5 Torr.

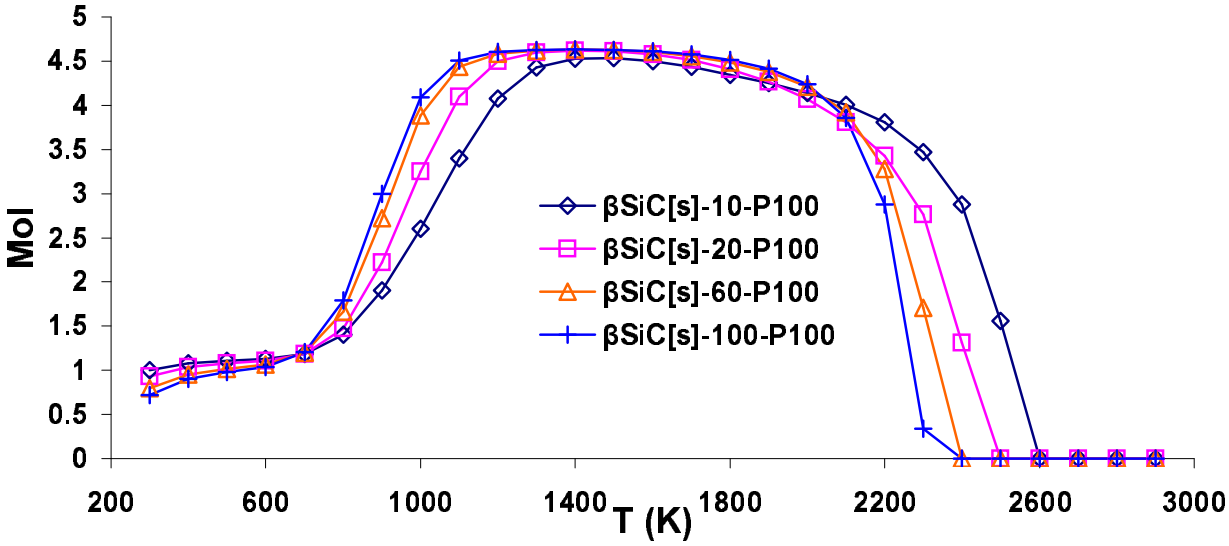

Figure 39: Quantity of β-SiC at different H_2/MTS ratios for pressure of 100 Torr.

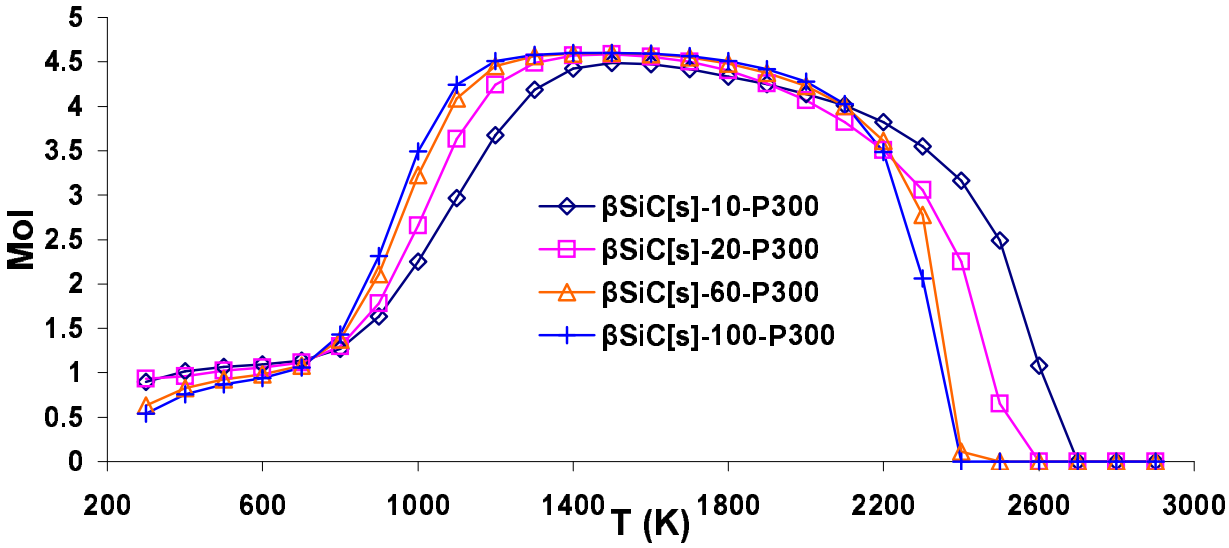

Figure 40: Quantity of β-SiC at different H_2/MTS ratios for pressure of 300 Torr.

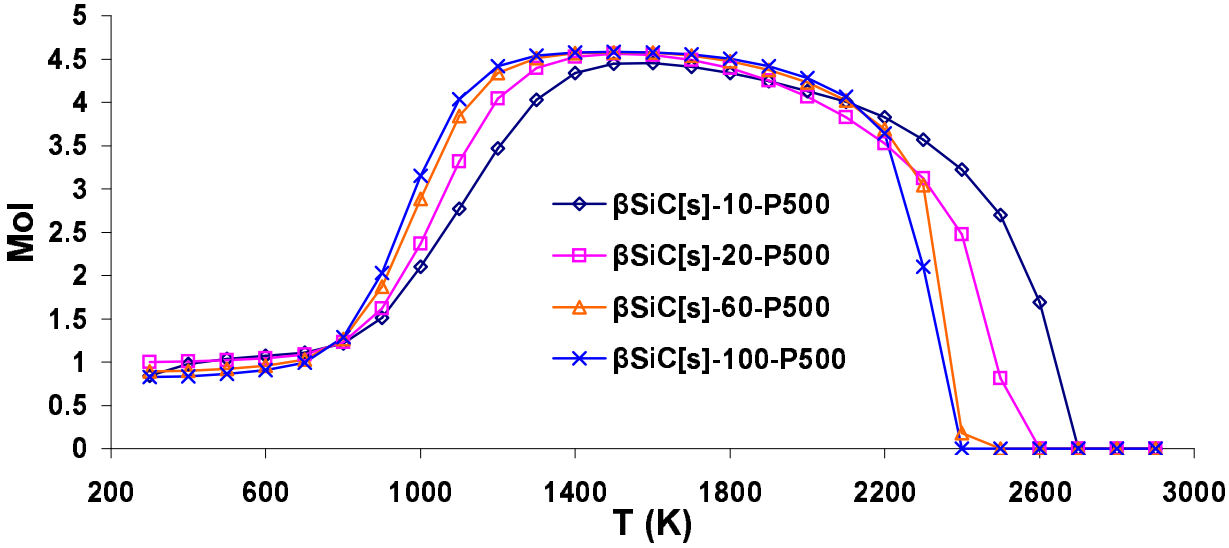

Figure 41: Quantity of β-SiC at different H_2/MTS ratios for pressure of 500 Torr.

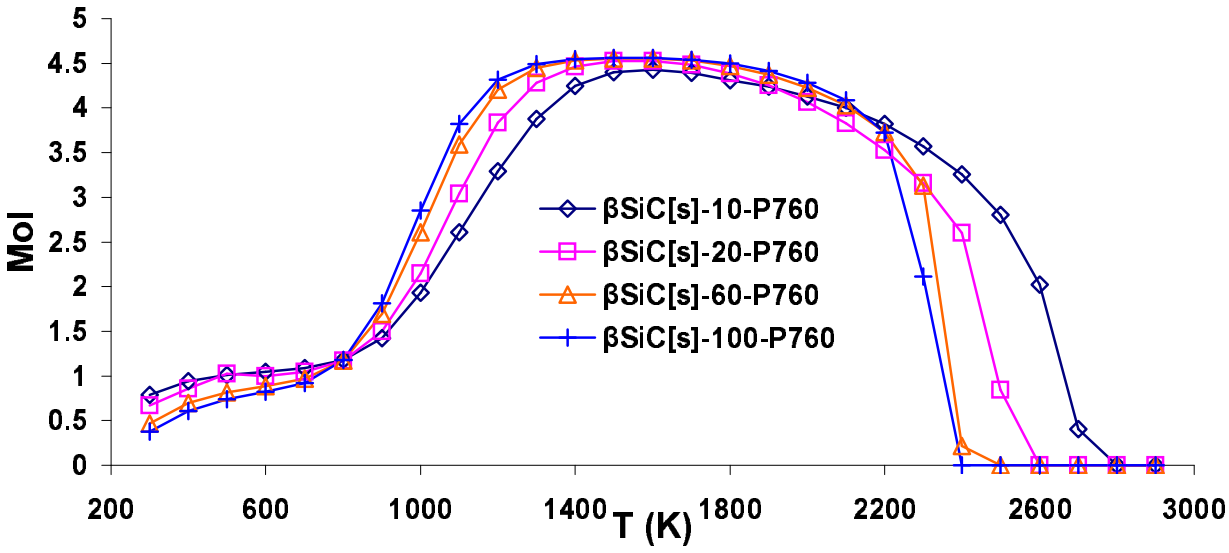

Figure 42: Quantity of β-SiC at different H_2/MTS ratios for pressure of 760 Torr.

4.1.3 Calculation Error Study

In fact, it is very difficult to find the thermodynamic data over a wide temperature range for all the chemical species that might need to be included in the thermodynamic calculations. Sometimes, researchers just use a fixed set of thermodynamic data for the middle temperature of the temperature range of interest. For example, for the temperature range of 1000 K to 2000 K, the data for 1500 K might be applied for all the calculations from 1000 K to 2000 K. Of course, this will cause some error. But,this approach is kind of reasonable. For the calculation that I performed, it seems that the free Gibbs energy of the chemical species have almost a constant relative ratio with each other at different temperatures. I also used this method to recalculate the first case of the MTS and H_2 system, where H_2 to MTS ratio equaled 20; the temperature was from 1000 K to 2000 K; the entropies and enthalpies of all chemicals were the values of 1500 K only. Figure 45 shows the results of the two methods. The biggest error was 3.6% at temperature of 2000 K, which is acceptable.

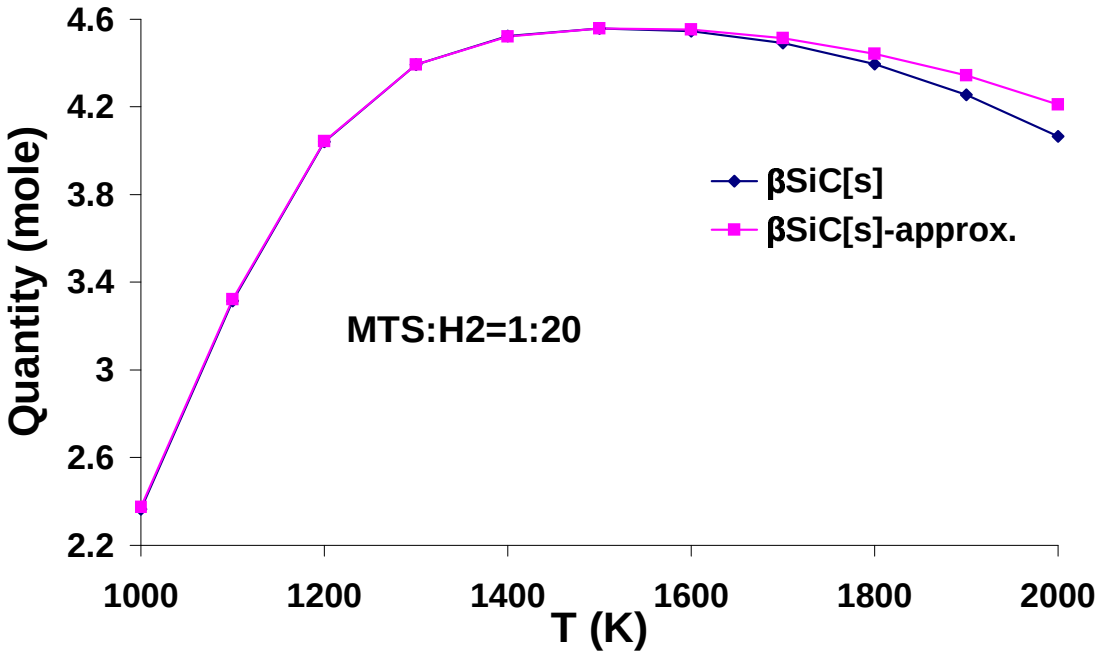

Figure 43: β-SiC mole values from two calculation methods.

In order to check the role of less stable chemicals in the thermodynamic calculations, I recalculated the case with a ratio of H_2/MTS equal to 20 by including more chemicals. The new system contained 76 gaseous phases and 5 condensed phases, which are shown in Table 8. The bold chemicals were the new-added less stable chemicals. The calculated results and errors compared with the old system are shown in Table 9. The errors, except for $C_2H_2Cl_2$, were less than 0.0055% at 1000 K, less than 0.067% at 1500 K. Although the error for $C_2H_2Cl_2$ was much bigger, close to 100%, the predicted amount of this species was really small, less than 10^{-4} mole. Therefore, it seems that excluding the less stable chemicals in the calculations dose not cause large errors. Based on those calculations, for the calculations in this thesis, the old chemical list was used. This list contains the 44 gaseous species and 5 condensed phases shown in Table 5.

Table 8: Species Considered in the New C-H-Si-Cl (MTS) System.

Equilibrium gas phases				
C(g)	CH_4(g)	**$C_2H_2Cl_2$(g)**	**C_4H_6(g)**	SiCl(g)
CCl(g)	SiC(g)	**C_2HCl_3(g)**	**C_4H_8(g)**	$SiCl_2$(g)
CCl_2(g)	Si_2C(g)	C_2H_4(g)	**C_4H_9(g)**	Cl_2(g)
CCl_3(g)	C_2(g)	**C_2H_4Cl(g)**	**C_4H_9Cl(g)**	SiH_2Cl_2
CCl_4(g)	C_2Cl_2	**$C_2H_3Cl_2$(g)**	**C_4H_{10}(g)**	$SiCl_3$(g)
CH(g)	C_2Cl_4(g)	**C_2H_5(g)**	**$Si(CH_3)_4$(g)**	$SiHCl_3$(g)
CHCl(g)	C_2Cl_6(g)	**C_2H_6(g)**	C_5(g)	$SiCl_4$(g)
$CHCl_3$(g)	C_2H(g)	**C_3H_8(g)**	**C_5H_{10}(g)**	H(g)
CH_2(g)	C_2HCl(g)	SiC_2(g)	**C_5H_{12}(g)**	SiH(g)
CH_2Cl(g)	C_2H_2(g)	C_3(g)	**C_6Cl_6(g)**	H_2(g)
$CHCl_2$(g)	$C_2H_2Cl_3$(g)	**C_3H_2(g)**	**C_6H_6(g)**	SiH_4(g)
Si2(g)	**C_2HCl_4(g)**	**C_4H_2(g)**	**C_6H_{14}(g)**	Si(g)
CH_2Cl_2(g)	**C_2Cl_5(g)**	**C_3H_6(g)**	**C_6H_5(g)**	
CH_3(g)	**C_2H_3(g)**	**C_3H_7(g)**	Cl(g)	
CH_3Cl(g)	**C_3H_5(g)**	**C_3H_7Cl(g)**	HCl(g)	
CH_3SiCl_3(g)	**C_2H_3Cl(g)**	C_4(g)	SiH_3Cl(g)	
Equilibrium condensed phases				
C[s]	Si[l]	Si[s]	$\alpha-$SiC[s]	$\beta-$SiC[s]

Table 9: The differences of two systems with H_2/MTS ratio equaling 20

New system	*New 1000K*	*Old 1000K*	*error%*	*Old system*	*New 1500K*	*Old 1500K*	*error%*
C(g)	0.0E+00	0.0E+00	0.0E+00	C(g)	2.0E-15	2.0E-15	0.0249
CCl(g)	0.0E+00	0.0E+00	0.0E+00	CCl(g)	4.8E-15	4.8E-15	0.0232
CCl_2(g)	0.0E+00	0.0E+00	0.0E+00	CCl_2(g)	4.0E-14	4.0E-14	0.0223
CCl_3(g)	0.0E+00	0.0E+00	0.0E+00	CCl_3(g)	3.1E-17	3.1E-17	0.0257
CCl_4(g)	0.0E+00	0.0E+00	0.0E+00	CCl_4(g)	1.2E-20	1.2E-20	0.0241
CH(g)	0.0E+00	0.0E+00	0.0E+00	CH(g)	1.3E-13	1.3E-13	0.0233
CHCl(g)	1.6E-20	1.6E-20	0.0E+00	CHCl(g)	2.0E-12	2.0E-12	0.0246
$CHCl_3$(g)	2.1E-19	2.2E-19	0.0E+00	$CHCl_3$(g)	9.6E-15	9.6E-15	0.0241
CH_2(g)	1.9E-16	1.9E-16	0.0E+00	CH_2(g)	1.4E-09	1.4E-09	0.0221

Table 9: (continued)

New system	*New 1000K*	*Old 1000K*	*error%*	*Old system*	*New 1500K*	*Old 1500K*	*error%*
$CH_2Cl(g)$	1.5E-12		1.5E-12		2.7E-08		0.0000
$CHCl_2(g)$	8.3E-18		8.3E-18		8.5E-12		0.0000
$S_{i2}(g)$	0.0E+00	0.0E+00	0.0E+00	$Si_2(g)$	2.3E-13	2.3E-13	-0.0438
$CH_2Cl_2(g)$	5.3E-08	1.9E-12	-1.0E+02	$CH_2Cl_2(g$	4.4E-05	7.1E-10	-99.9984
$CH_3(g)$	1.4E-07	1.4E-07	0.0E+00	$CH_3(g)$	5.3E-05	5.3E-05	0.0225
$CH_3Cl(g)$	3.3E-06	3.3E-06	0.0E+00	$CH_3Cl(g)$	1.3E-05	1.3E-05	0.0227
$CH_3SiCl_3(g)$	5.7E-04	5.7E-04	0.0E+00	CH_3SiCl_3	1.6E-05	1.6E-05	0.0000
$CH_4(g)$	2.3E+00	2.3E+00	0.0E+00	$CH_4(g)$	9.4E-02	9.4E-02	0.0212
SiC(g)	0.0E+00	0.0E+00	0.0E+00	SiC(g)	1.1E-15	1.1E-15	0.0000
$Si_2C(g)$	0.0E+00	0.0E+00	0.0E+00	$Si_2C(g)$	2.7E-11	2.7E-11	-0.0225
$C_2(g)$	0.0E+00	0.0E+00	0.0E+00	$C_2(g)$	7.5E-18	7.6E-18	0.0437
$C_2Cl_2(g)$	0.0E+00	0.0E+00	0.0E+00	$C_2Cl_2(g)$	5.6E-13	5.6E-13	0.0465
$C_2Cl_4(g)$	0.0E+00	0.0E+00	0.0E+00	$C_2Cl4(g)$	0.0E+00	0.0E+00	0.0000
$C_2Cl_6(g)$	0.0E+00	0.0E+00	0.0E+00	$C_2Cl_6(g)$	0.0E+00	0.0E+00	0.0000
$C_2H(g)$	1.9E-17	1.9E-17	5.4E-03	$C_2H(g)$	8.9E-09	8.9E-09	0.0448
$C_2HCl(g)$	2.6E-14	2.6E-14	0.0E+00	$C_2HCl(g)$	4.5E-08	4.5E-08	0.0444
$C_2H_2(g)$	2.9E-07	2.9E-07	0.0E+00	$C_2H_2(g)$	9.1E-03	9.1E-03	0.0438
$C_2H_2Cl_3(g)$	0.0E+00		0.0E+00		3.3E-20		0.0000
$C_2HCl_4(g)$	0.0E+00		0.0E+00		0.0E+00		0.0000
$C_2Cl_5(g)$	0.0E+00		0.0E+00		0.0E+00		0.0000
$C_2H_3(g)$	4.7E-14		4.7E-14		1.1E-08		0.0000
$C_3H_5(g)$	5.7E-14		5.7E-14		1.1E-10		0.0000
$C_2H_3Cl(g)$	4.5E-11		4.5E-11		3.0E-08		0.0000
$C_2H_2Cl_2(g)$	3.8E-17		3.8E-17		1.4E-12		0.0000

Table 9: (continued)

New system	*New 1000K*	*Old 1000K*	*error%*	*Old system*	*New 1500K*	*Old 1500K*	*error%*
C_2HCl_3(g)	0.0E+00		0.0E+00		9.3E-17		0.0000
C_2H_4(g)	6.2E-06	6.2E-06	1.6E-03	C_2H_4(g)	7.1E-05	7.1E-05	0.0434
C_2H_4Cl(g)	4.2E-16		4.2E-16		1.7E-12		0.0000
$C_2H_3Cl_2$(g)	0.0E+00		0.0E+00		3.7E-16		0.0000
C_2H_5(g)	4.4E-11		4.4E-11		4.3E-09		0.0000
C_2H_6(g)	1.0E-05		1.0E-05		3.6E-07		0.0000
C_3H_8(g)	1.8E-10		1.8E-10		3.6E-12		0.0000
SiC_2(g)	0.0E+00	0.0E+00	0.0E+00	SiC_2(g)	1.6E-11	1.6E-11	0.0256
C_3(g)	0.0E+00	0.0E+00	0.0E+00	C_3(g)	2.8E-16	2.8E-16	0.0667
C_3H_2(g)	0.0E+00		0.0E+00		3.8E-13		0.0000
C_4H_2(g)	0.0E+00		0.0E+00		2.1E-17		0.0000
C_3H_6(g)	9.1E-10		9.1E-10		3.6E-09		0.0000
C_3H_7(g)	1.0E-15		1.0E-15		5.5E-14		0.0000
C_3H_7Cl(g)	3.5E-15		3.5E-15		2.3E-15		0.0000
C_4(g)	0.0E+00	0.0E+00	0.0E+00	C_4(g)	0.0E+00	0.0E+00	0.0000
C_4H_6(g)	1.3E-16		1.3E-16		3.2E-13		0.0000
C_4H_8(g)	1.3E-14		1.3E-14		1.9E-14		0.0000
C_4H_9(g)	1.5E-20		1.5E-20		5.0E-19		0.0000
C_4H_9Cl(g)	2.3E-20		2.3E-20		0.0E+00		0.0000
C_4H_{10}(g)	3.3E-15		3.3E-15		4.0E-17		0.0000
$Si(CH_3)_4$(g)	1.9E-15		1.9E-15		3.4E-19		0.0000
C_5(g)	0.0E+00	0.0E+00	0.0E+00	C_5(g)	0.0E+00	0.0E+00	0.0000
C_5H_{10}(g)	0.0E+00		0.0E+00		0.0E+00		0.0000
C_5H_{12}(g)	4.5E-20		4.5E-20		0.0E+00		0.0000

Table 9: (continued)

New system	*New 1000K*	*Old 1000K*	*error%*	*Old system*	*New 1500K*	*Old 1500K*	*error%*
C_6Cl_6(g)	0.0E+00		0.0E+00		0.0E+00		0.0000
C_6H_6(g)	5.8E-15		5.8E-15		1.3E-12		0.0000
C_6H_{14}(g)	0.0E+00		0.0E+00		0.0E+00		0.0000
C_6H_5(g)	0.0E+00		0.0E+00		1.1E-16		0.0000
Cl(g)	1.4E-08	1.4E-08	0.0E+00	Cl(g)	2.6E-04	2.6E-04	0.0039
HCl(g)	5.1E+00	5.1E+00	0.0E+00	HCl(g)	1.4E+01	1.4E+01	0.0000
SiH_3Cl(g)	1.3E-05	1.3E-05	0.0E+00	SiH_3Cl(g)	4.2E-05	4.2E-05	-0.0215
SiCl(g)	4.5E-13	4.5E-13	0.0E+00	SiCl(g)	1.4E-06	1.4E-06	-0.0212
$SiCl_2$(g)	4.2E-04	4.2E-04	2.4E-03	$SiCl_2$(g)	6.6E-02	6.6E-02	-0.0197
C_{l2}(g)	8.1E-12	8.1E-12	-1.2E-03	Cl_2(g)	1.2E-07	1.2E-07	0.0000
SiH_2Cl_2(g)	3.7E-03	3.7E-03	2.7E-03	SiH_2Cl_2(g)	1.3E-03	1.3E-03	-0.0157
$SiCl_3$(g)	5.9E-03	5.9E-03	0.0E+00	$SiCl_3$(g)	1.8E-02	1.8E-02	-0.0165
$SiHCl_3$(g)	2.6E-01	2.6E-01	0.0E+00	$SiHCl_3$(g)	1.1E-02	1.1E-02	-0.0177
$SiCl_4$(g)	2.0E+00	2.0E+00	0.0E+00	$SiCl_4$(g)	1.6E-02	1.6E-02	-0.0125
H(g)	2.7E-07	2.7E-07	0.0E+00	H(g)	2.2E-03	2.2E-03	0.0000
SiH(g)	1.3E-15	1.3E-15	0.0E+00	SiH(g)	4.3E-08	4.3E-08	-0.0235
H_2(g)	9.3E+01	9.3E+01	0.0E+00	H_2(g)	9.3E+01	9.3E+01	0.0000
SiH_4(g)	2.1E-08	2.1E-08	0.0E+00	SiH_4(g)	5.6E-07	5.6E-07	-0.0213
Si(g)	2.5E-17	2.5E-17	0.0E+00	Si(g)	1.7E-08	1.7E-08	-0.0229
C[s]	0.0E+00	0.0E+00	0.0E+00	C[s]	0.0E+00	0.0E+00	0.0000
Si[l]	0.0E+00	0.0E+00	0.0E+00	Si[l]	0.0E+00	0.0E+00	0.0000
Si[s]	0.0E+00	0.0E+00	0.0E+00	Si[s]	0.0E+00	0.0E+00	0.0000
α-SiC[s]	0.0E+00	0.0E+00	0.0E+00	α-SiC[s]	0.0E+00	0.0E+00	0.0000
β-SiC[s]	2.4E+00	2.4E+00	0.0E+00	β-SiC[s]	4.6E+00	4.6E+00	0.0000

4.2 $SiCl_4$, CCl_4 and H_2 System

Calculations for the $CCl_4/SiCl_4/H_2$ system were performed as a check. As will be shown, since the calculations for the $CCl_4/SiCl_4/H_2$ system were in close agreement with the previously published results, this gave confidence in our calculations, even for the H_2/MTS system. For the $CCl_4/SiCl_4/H_2$ system, the total amount of Si and C was fixed at 10 moles, the ratio of H_2 to (Si+C) was 10, and the amount of Cl was 40 moles. The detail information that was used to specify the calculations is shown in Table 10. Each set of calculations had a specific pressure and a Si/(Si+C) ratio, and the temperature was ranged from 1000 K to 2000 K. The calculated results are shown in Figures 46 to 50. Our calculations were in good agreement with Kingon's results in this specific set of system specifications, which gives us a big confidence for the MTS/H_2 calculations. [53]

Table 10: Conditions used to specify the system of $CCl_4/SiCl_4/H_2$

Pressure (Pa)	*Si/(Si+C)*				
10^2	0.1	0.3	0.5	0.7	0.9
10^4	0.1	0.3	0.5	0.7	0.9
10^5	0.1	0.3	0.5	0.7	0.9
10^6	0.1	0.3	0.5	0.7	0.9

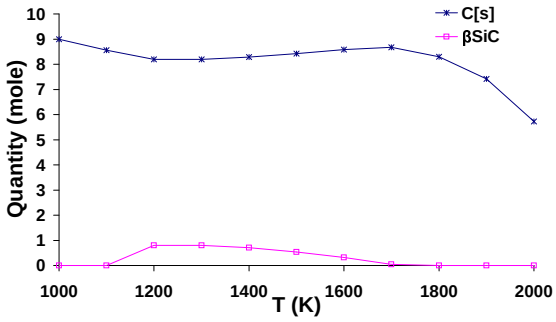

(a) $SiCl_4/CCl_4$=0.1, P=10^2Pa

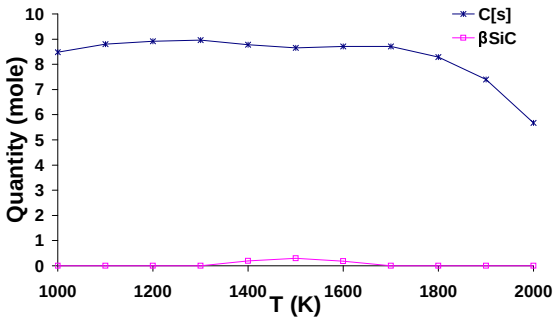

(b) $SiCl_4/CCl_4$=0.1, P=10^4Pa

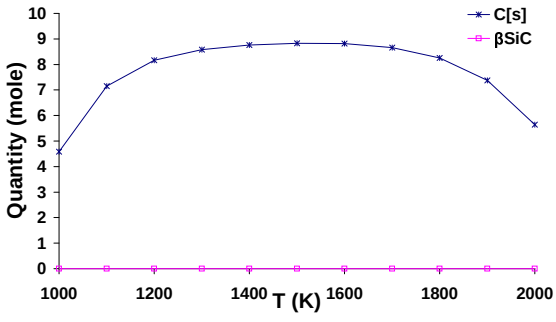

(c) $SiCl_4/CCl_4$=0.1, P=10^5Pa

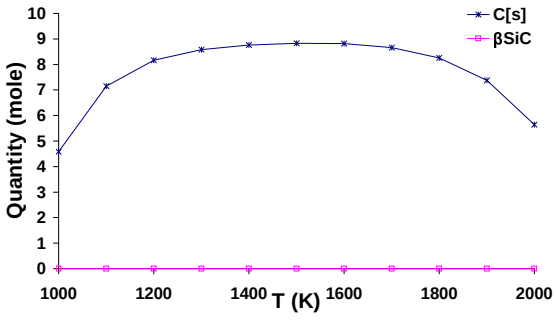

(d) $SiCl_4/CCl_4$=0.1, P=10^6Pa

Figure 44: $CCl_4/SiCl_4/H_2$ system with Si/(Si+C)=0.1.

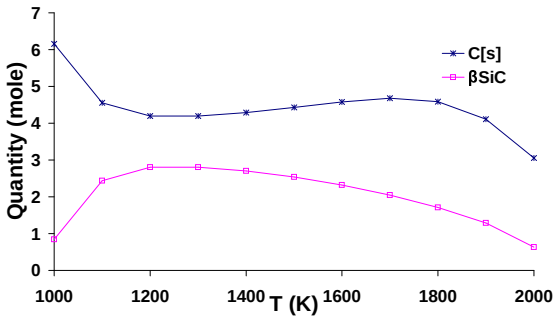

(a) $SiCl_4/CCl_4$=0.3, P=10^2Pa

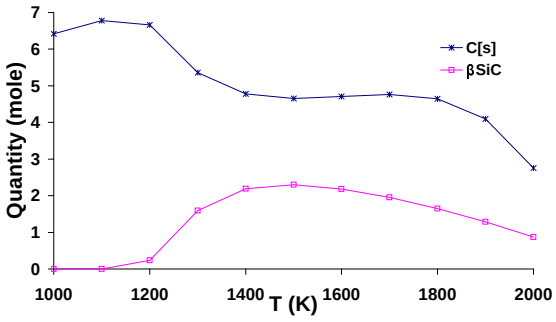

(b) $SiCl_4/CCl_4$=0.3, P=10^4Pa

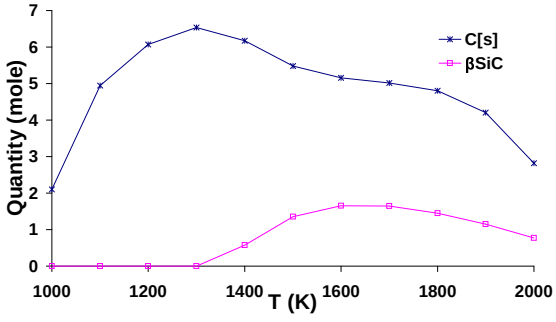

(c) $SiCl_4/CCl_4$=0.3, P=10^5Pa

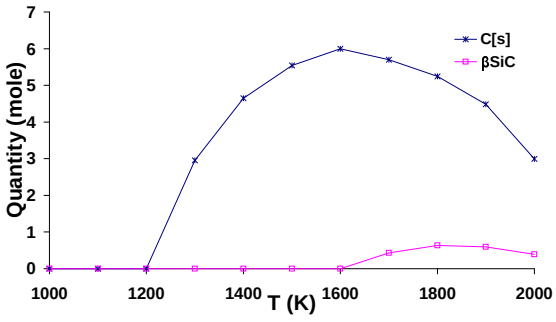

(d) $SiCl_4/CCl_4$=0.3, P=10^6Pa

Figure 45: $CCl_4/SiCl_4/H_2$ system with Si/(Si+C)=0.3.

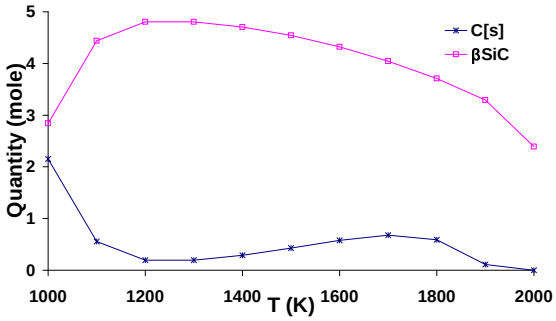

(a) $SiCl_4/CCl_4$=0.5, P=10^2Pa

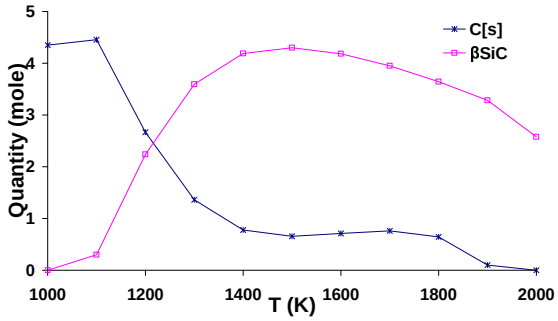

(b) $SiCl_4/CCl_4$=0.5, P=10^4Pa

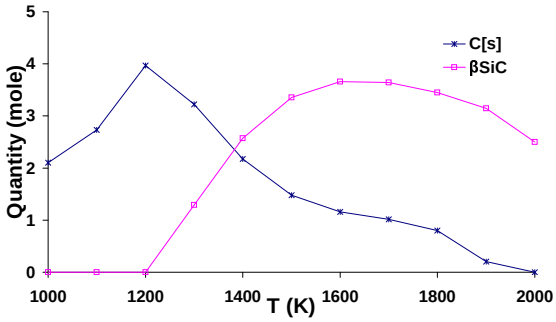

(c) $SiCl_4/CCl_4$=0.5, P=10^5Pa

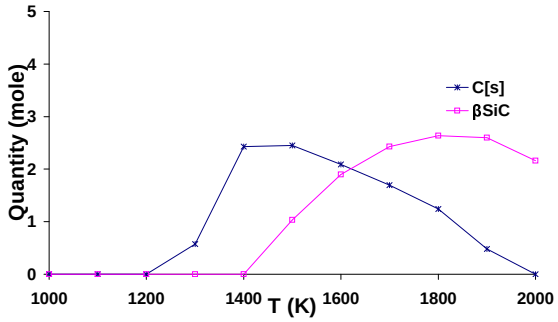

(d) $SiCl_4/CCl_4$=0.5, P=10^6Pa

Figure 46: $CCl_4/SiCl_4/H_2$ system with Si/(Si+C)=0.5.

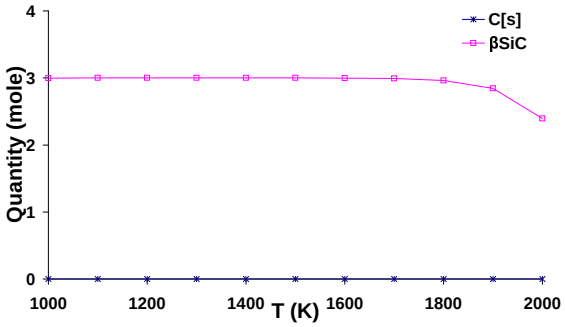

(a) $SiCl_4/CCl_4$=0.7, P=10^2Pa

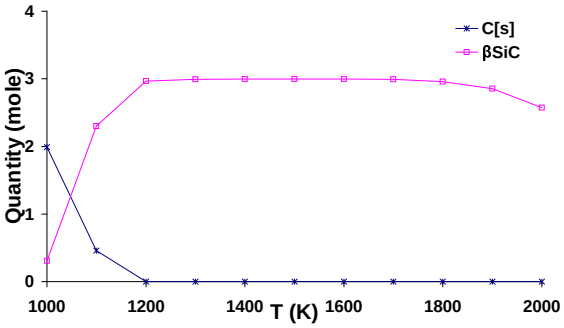

(b) $SiCl_4/CCl_4$=0.7, P=10^4Pa

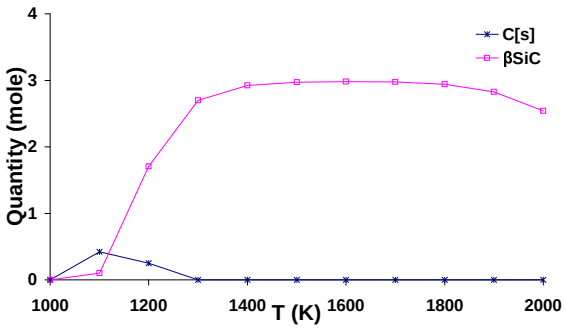

(c) $SiCl_4/CCl_4$=0.7, P=10^5Pa

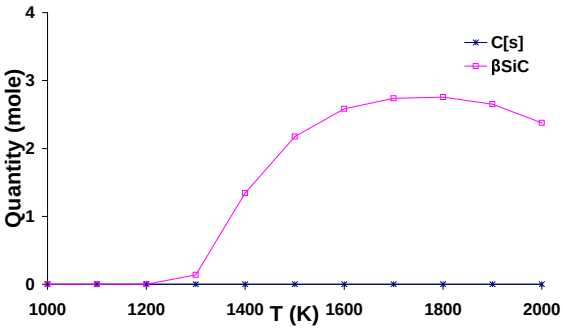

(d) $SiCl_4/CCl_4$=0.7, P=10^6Pa

Figure 47: $CCl_4/SiCl_4/H_2$ system with Si/(Si+C)=0.7.

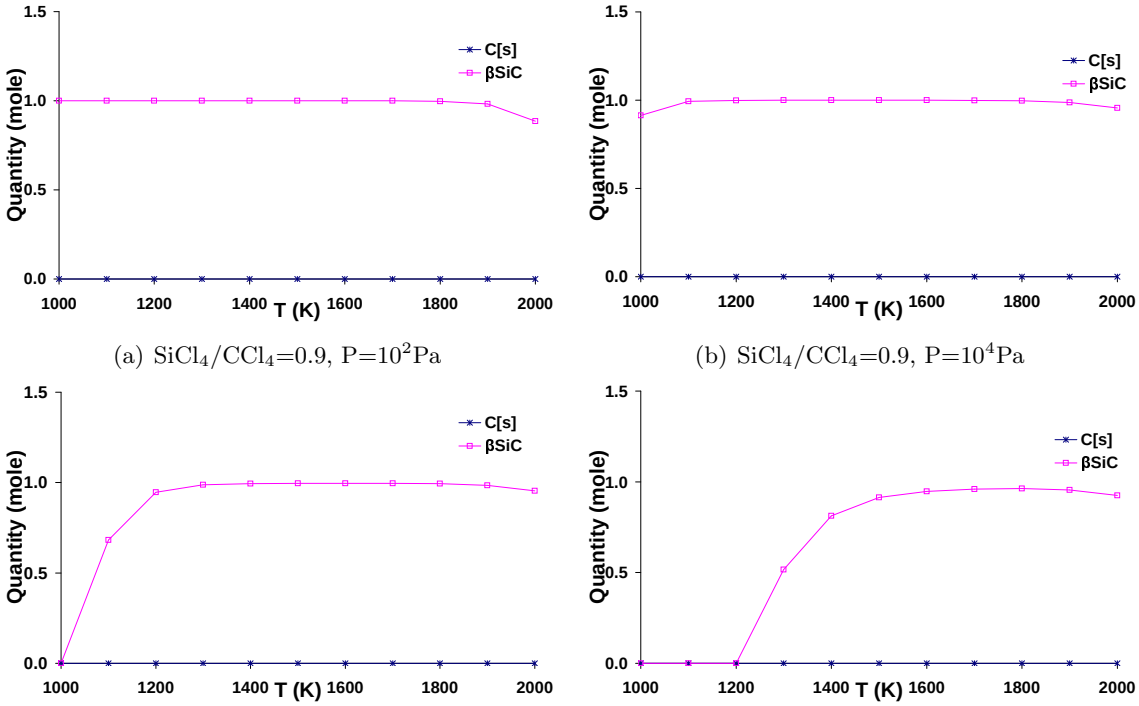

(a) $SiCl_4/CCl_4$=0.9, P=10^2Pa

(b) $SiCl_4/CCl_4$=0.9, P=10^4Pa

(c) $SiCl_4/CCl_4$=0.9, P=10^5Pa

(d) $SiCl_4/CCl_4$=0.9, P=10^6Pa

Figure 48: $CCl_4/SiCl_4/H_2$ system with Si/(Si+C)=0.9.

CHAPTER V

SIC FIBER DEPOSITION

Silicon carbide fiber was grown using methyltrichlorosilane (MTS) and H_2 mixture. This chapter explores the deposition rate of SiC fibers grown under different conditions. The volcano effect of SiC fibers were studied. Deposition conditions that will not generate the volcano effect were identified. A kinetic study was performed to correlate the deposition rate of fibers with the concentration of MTS and growth temperature. The relationship was expressed in term of the Arrhenius relationship. Finally, the microstructures of deposits were revealed by means of polishing, chemical etching, and SEM examination.

5.1 Experimental Procedure

All SiC fibers were prepared using an automated LCVD system which has previously been described in detail. [67], [74] Briefly, a 200 μm diameter Gaussian CO_2 laser beam was used to heat a spot on a graphite (SK-85) substrate. Temperatures within the heated spot were measured with a Mikron M9100 thermal imager. Figure 49 shows the color image of a laser spot during the deposition of a SiC fiber. [4], [68] The average temperature is defined as the average for all pixels within a circle of fixed size surrounding the tip of the fiber.

MTS is liquid at room temperature and under one atmosphere. In order to transfer MTS into the LCVD system, a vaporizer was needed, as shown in Figure 50. First, hydrogen is introduced into the vaporizer; then the vapor mixture of MTS and hydrogen flows out of the vaporizer through the outlet pipe. As a steady state is reached, the fixed flow rates of MTS vapor and hydrogen can be determined. Down stream of the vaporizer, more hydrogen can be introduced to achieve the desired flow rates of MTS and hydrogen.

In the beginning of the deposition process, the deposition chamber was filled with the mixture of MTS and H_2. A total 67 KPa (500 torr) pressure of the deposition chamber was maintained during the entire deposition process. Two H_2/MTS ratios were used. They

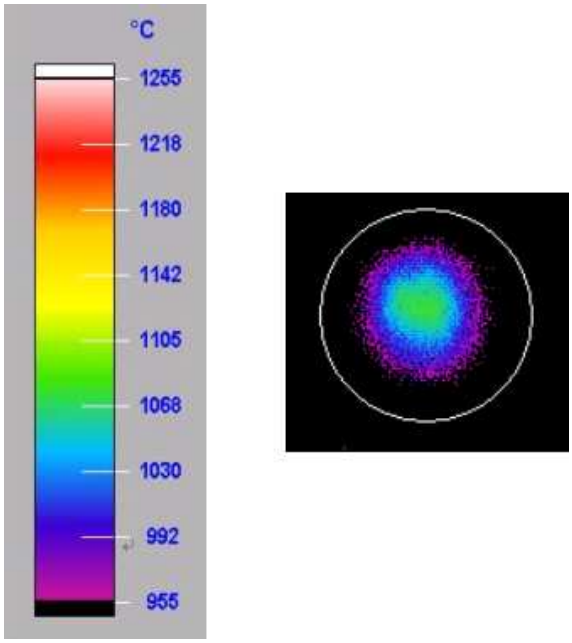

Figure 49: Thermal image of the tip of a fiber during SiC deposition process.

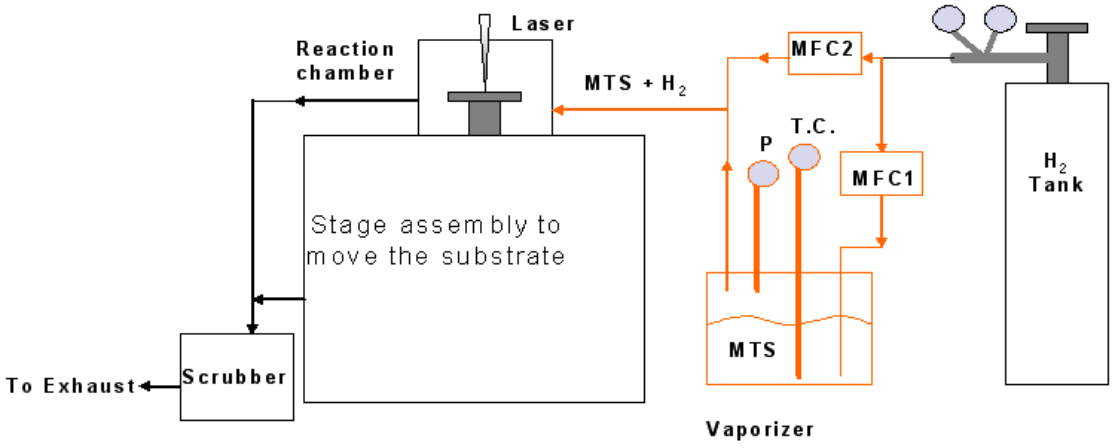

Figure 50: The configuration of vaporizing and transferring the liquid MTS for LCVD-SiC process.

were 10 and 20. The processing conditions were selected based on results from prior CVD experimentation [75] and our LCVD preliminary trials.

During the fiber deposition process, the laser beam was not moved relative to the substrate, and thus fibers of 80 to 280 μm long were grown during the 5 to 15 minutes processing time. During growth of an individual fiber, a high laser power was first used to initiate the chemical reaction, and the laser power was then decreased manually until the average temperature was close to the desired value. At this point in time, automatic laser power control was initiated. [4] This control system uses the average temperature read by the thermal imager to adjust the applied laser power. The average temperature within the circle and the maximum temperature were automatically recorded as a function of time. Plots of the input laser power and average temperature for two fibers throughout their growth are shown in Figure 51.

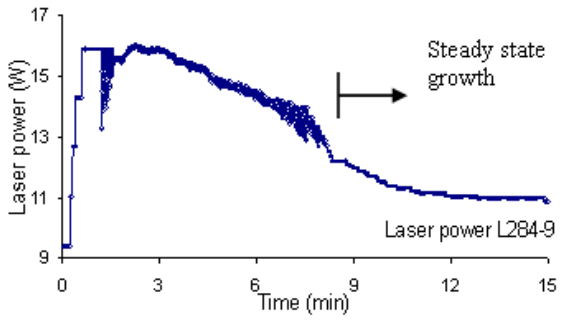

(a) Laser power of fiber L284-9

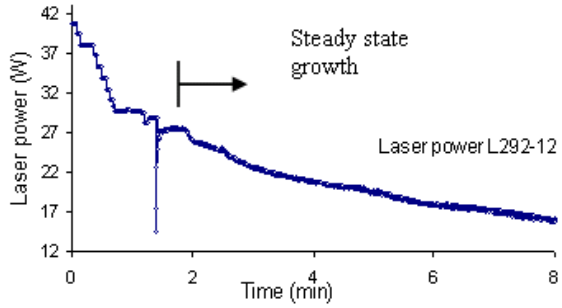

(b) Laser power of fiber L292-12

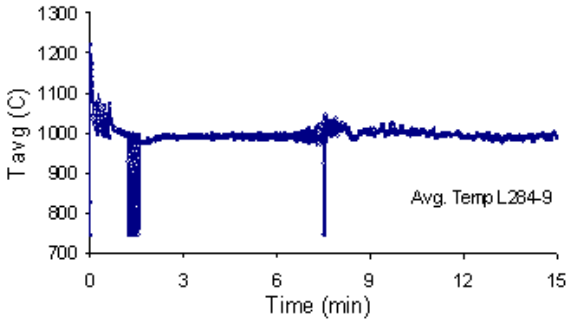

(c) Average Temperature of fiber L284-9

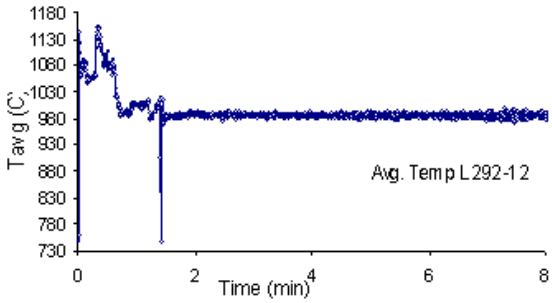

(d) Average Temperature of fiber L292-12

Figure 51: Laser power and average temperature for two typical SiC fibers.

5.2 Volcano Effect

The volcano effect is a depression at the top of the deposit. Uniformly shaped deposits are a prerequisite for rapid prototyping small 3-D SiC parts. Because of the Gaussian energy distribution in the laser beam and conduction within the substrate, there is a large temperature gradient across the spot heated by the laser. [67] As shown in Figures 34 to 43 of Chapter IV, if the temperature is too high in the center of the spot heated by the laser, less deposition will occur there. This, or reduced mass transport, or depletion of reagent, could account for the formation of volcano-like deposits. [4]

To find out whether thermodynamics was responsible for the volcano effect, fibers were grown under the same conditions as those used for the calculations shown in Figures 32(a) and (b) of chapter IV. Examinations performed via SEM (Scanning Electron Microscopy) permitted assigning integer values between 0 and 4 which reflect the severity of the volcano-like depression observed at the tip of growing fibers. A value of zero indicated no depression while a fiber having a severe volcano-like morphology was assigned a value of 4.

Typical SEM micrographs of SiC fibers with no volcano effect, slight volcano effect, and significant volcano effect are shown in Figure 52 (a), (b), and (c), respectively. The experimentally observed relationships between volcano effect and the growth temperature are shown in Figure 53. The vertical axis represents the volcano effect level observed. The horizontal axis represents the maximum growth temperature recorded within the laser spot.

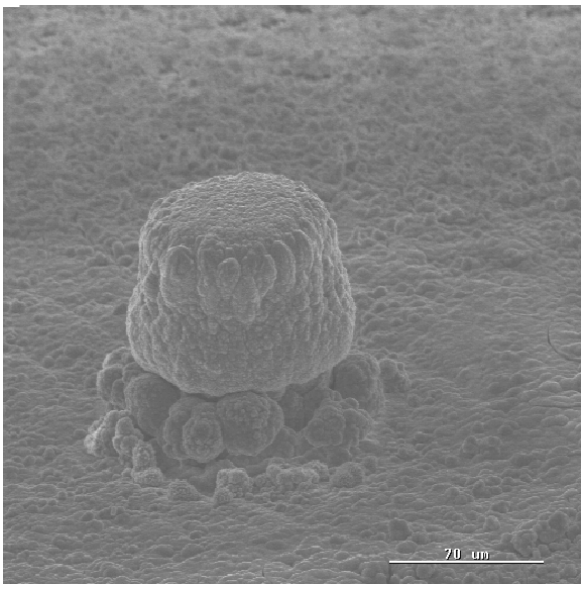

(a) L284-7, T_{max} =1090 ˚ C

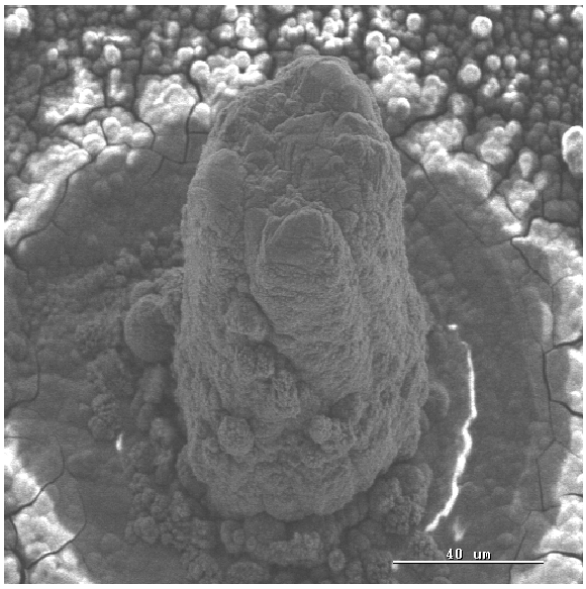

(b) L285-8, T_{max} = 1161 ˚ C

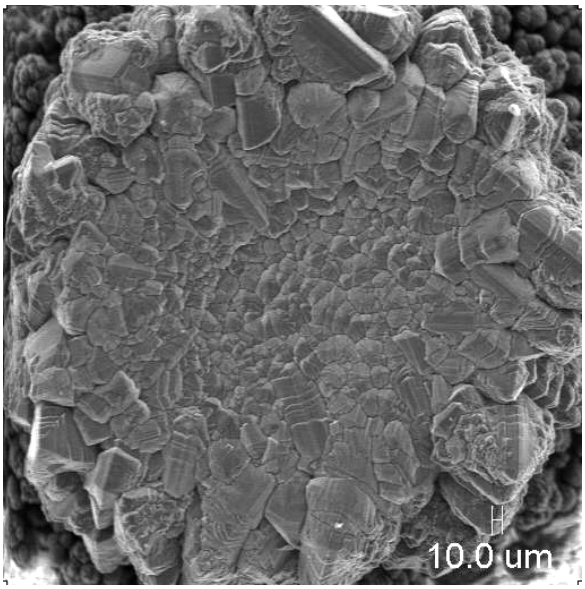

(c) L251-2, T_{max}>1450 ˚ C

Figure 52: LCVD of SiC fibers with H_2/MTS =20.

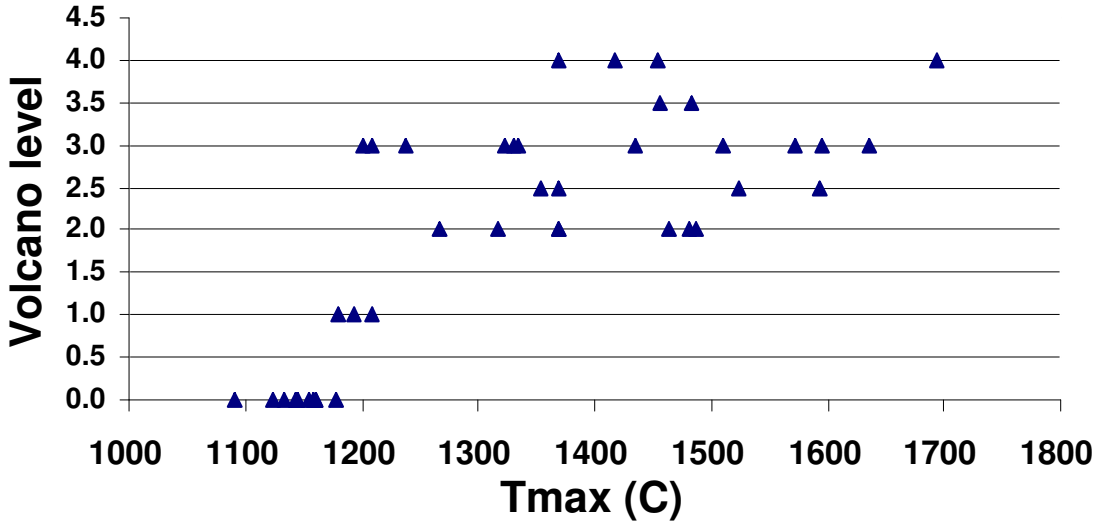

(a) H_2/MTS=10

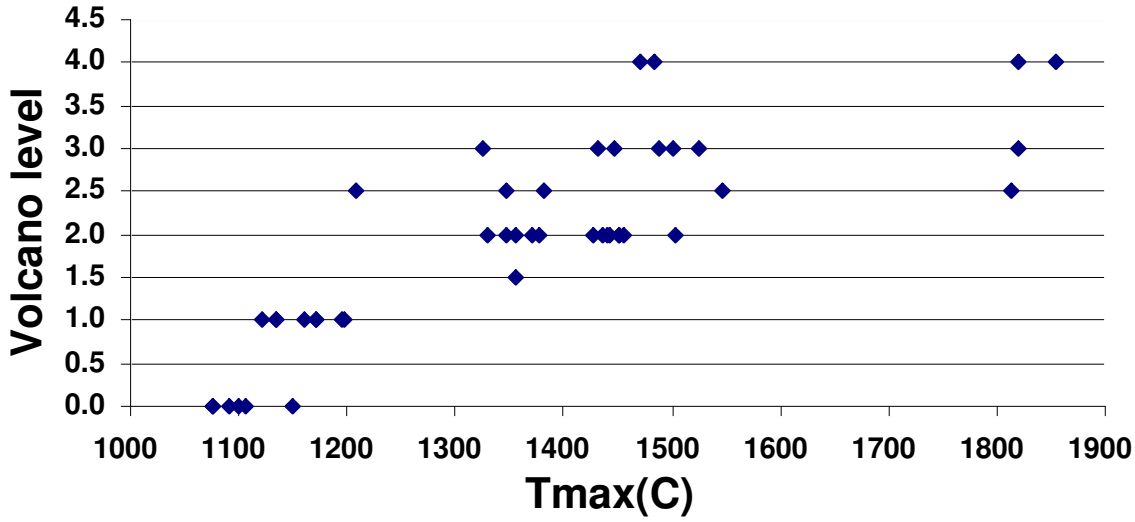

(b) H_2/MTS=20

Figure 53: The relationships between volcano-effect and growth temperature.

Consider the growth of SiC using a H_2/MTS ratio equal to 10. When the maximum temperature over the laser spot was lower than about 1180 $^\circ$C, or 1453 K, no volcano effect was found in the SiC fibers; when the maximum temperature over the laser spot was slightly higher than about 1180 $^\circ$C, very shallow depressions were found in the SiC fibers; and when the maximum temperature over the laser spot was much higher than 1180 $^\circ$C, a significant volcano effect commonly occurred in the SiC fibers. Similar behavior was observed for a H_2/MTS ratio of 20. These results show that volcano-like deposits are not formed when the deposition temperature is low, but invariably form when high deposition temperatures are used. This is consistent with the predicted quantity of SiC shown in Figures 32(a) and (b) of Chapter IV.

As shown in Figures 32(a) and (b) of Chapter IV, at low temperatures, the quantity of SiC deposited increases with increasing deposition temperature, more deposition occurs in the center hotter portion of the laser spot, and a dome-shaped deposit is formed. For higher processing temperatures, the center of the laser spot is so hot that less deposition occurs there and thus a volcano-like deposit is formed. Comparisons of the maximum temperatures given in Figures 32(a) and (b) with the curves in Figure 52 verify this explanation. The agreement of the thermodynamic calculations with the experimentally observed temperature where the volcano effect appears supports the hypothesis that thermodynamics rather than mass transport or reagent depletion is responsible for the growth of volcano-like deposits. A similar approach has been used to show that the thermodynamic effect is also responsible for the occurrence of volcano-like LCVD carbon deposits when too high growth temperatures are used. [4], [68]

5.3 Kinetics

There are two barriers to study the kinetics of the LCVD of SiC. First is the large variation in temperature over the deposition area and the difficulty in accurately measuring temperatures within the small spot heated by the laser. Second, the deposits are often nonuniform, e.g. volcano-like, which complicates identification of a growth rate. In this study, careful, high spatial resolution temperature measurements permitted an experimental kinetic model

to be developed which furthers the understanding of the LCVD SiC deposition process from MTS and H_2.

Table 11 lists the process conditions and the results for measurements of fiber size and growth rate for SiC deposited from MTS and H_2. Before performing any kinetic analysis, it was important to determine whether the deposition reaction was in the kinetically limited regime. Since for LCVD, diffusion occurs from many directions around the small laser spot, as opposed to the linear diffusion for the conventional CVD process, and since the growth temperatures were below 1250 $^\circ$C, it was assumed that the growth process should be kinetically limited. In other words, the reaction rate on the surface of the substrate was slower than the possible diffusion rate of reagent to the substrate.

Table 11: SiC Fibers Grown from MTS and H_2

Sample #	*H_2/MTS ration*	*Peak Temp $^\circ C$*	*Height (μm)*	*Growth time (min)*	*Steady state height (μm)*	*Steady state growth time (min)*	*Linear growth rate (μm/min)*
L251-2*	20	$>$ 1450	–	–	–	–	–
L284-4	20	1076	98.0	15	48.79	7.35	6.64
L284-7	20	1090	115.4	15	37.99	4.15	9.16
L284-8	20	1101	140.8	15.28	64.39	7.71	8.35
L284-9	20	1107	156.4	15	63.99	6.66	9.61
L285-4	20	1149	171.0	15	147.98	10.19	14.52
L285-5	20	1161	222.3	15	191.97	13.64	14.07
L285-6	20	1171	249.3	16	206.67	13.07	15.81
L285-7	20	1172	228.3	15	187.07	10.55	17.73
L285-8	20	1196	243.3	15	145.28	8.65	16.80
L285-9	20	1197	278.4	15	207.17	10.59	19.56
L292-2	10	1229	232.6	10	161.38	7.78	20.74

Table 11: (continued)

Sample #	*H_2/MTS ratio*	*Peak Temp°C*	*Height (μm)*	*Growth time (min)*	*Steady state height (μm)*	*Steady state growth time (min)*	*Linear growth rate (μm/min)*
L292-3	10	1219	229.0	10	194.71	7.14	27.27
L292-6	10	1178	150.5	8	112.85	6.61	17.07
L292-7	10	1133	94.5	9.05	81.99	8.21	9.99
L292-9	10	1124	97.5	7	79.79	8.71	9.16
L292-10	10	1091	79.1	8	19.55	2.3	8.50
L292-11	10	1143	181.9	9	122.93	7.15	17.19
L292-12	10	1155	159.1	8.05	104.34	6.08	17.16
L292-13	10	1161	146.4	5	82.79	4.25	19.48
L292-14	10	1146	136.3	6	83.94	4.16	20.18
L292-15	10	1158	200.9	6	117.93	4.21	28.01
L293-1	10	1161	183.6	6	45.32	2.93	15.47
L293-2	10	1180	200.5	5	152.48	3.44	44.32
L293-3	10	1208	221.0	5	173.97	3.44	50.57
L293-4	10	1244	201.0	5	196.5	3.8	51.70

*Not included in kinetic analysis because of volcano effect.

Approximate calculations were used to further insure that the growth process for the experimental conditions given in Table 11 was kinetically limited. From Fick's first law, the diffusion rate can be expressed as follows:

$$J_{dif} = -D\frac{\Delta C_{MTS}}{\Delta X} \tag{11}$$

where $J_{dif}$is the diffusion rate in mol/cm^2s, D is the diffusion coefficient in cm^2/s, $\Delta C_{MTS}$is the concentration difference between the bulk concentration and the surface concentration

of MTS in mol/cm^3, and $\Delta X$is the approximate boundary layer thickness in cm.

First, assuming for the moment that the reactions are in the diffusion limited regime, the surface concentration of MTS should be close to zero. Then the concentration difference ΔC_{MTS}would approach the bulk MTS concentration, which was 3.06E-7 $mole/cm^3$, corresponding to the experimental condition of H_2/MTS=10 at a pressure of 67 KPa. Similarly, for a H_2/MTS ratio of 20 the concentration difference is 1.60E-7 $mole/cm^3$. The value of the diffusion coefficient D for MTS was previously calculated to be 1.79 cm^2/s at 1000^{o}C. [76] The thickness of the boundary layer was assumed to be 1 mm. [68], [74] The calculated diffusion rates for the two sets of experiments were 5.5E-5 and 2.9E-5 mol/cm^2s. These rates correspond to linear growth rates of 410 and 214 $\mu m/min$ for the H_2/MTS ratios of 10 and 20, respectively.

Comparison of these growth rates with the experimentally observed growth rates shown in Table 11, for each set of experiments, reveals that the calculated diffusion-based values are more than 10 times higher than the observed growth rates. This indicates that the process is kinetically limited. Further evidence that the deposition process was operating in the kinetic regime is the fact that the diffusion coefficient used in the calculation was for 1000°C while the actual growth temperatures were higher than 1000°C. At these higher actual temperatures, diffusion and the predicted fiber growth would be even faster. Also, one-dimensional diffusion, instead of three-dimensional diffusion, was assumed for the calculations. This also would cause the calculated diffusion rates to be lower than actual three-dimensional diffusion. With all the factors considered, it is reasonable to assume that the growth process was kinetically limited for the conditions given in Table 11.

For the kinetically limited regime, the SiC growth rate from MTS and H_2 can be expressed by equation (11), if a simple reaction mechanism involving MTS is assumed.

$$J = kC_{MTS}^n \tag{12}$$

Here, J is the deposition rate in $mole/cm^2s$; k is the rate constant in cm/s; C_{MTS} is the concentration of MTS in $mole/cm^3$; and n is the apparent order of the reaction. The rate

constant can be expressed by the Arrhenius relationship shown in equation (12).

$$k = k_0 e^{(-Q/RT)} \tag{13}$$

Here k_0 is the pre-exponential constant, Q is the apparent activation energy in KJ/mol, R is the gas constant, and T is the temperature in K. Substituting equation (12) into equation (11), yields equation (13).

$$J = k_0 e^{(-Q/RT)} C_{MTS}^n \tag{14}$$

Taking the natural logarithm of equation (13) converts it to a form which is amendable to multiple regression analysis.

$$ln(J) = ln(k_0) + nln(C_{MTS}) - \frac{Q}{R}(\frac{1}{T}) \tag{15}$$

By performing the multiple regression analysis using Statgraphics, the values of the apparent activation energy Q, the apparent order of reaction n, and the constant k_0 for the LCVD of SiC fibers were determined.

The growth rates given in Table 11 were obtained by dividing the central steady state heights of the SiC fibers with the steady state growth time and the corresponding growth temperatures were captured by measuring the maximum central temperatures of the laser spot. Fibers exhibiting the volcano effect were not used in this analysis. Typical SiC fibers without volcanoes for the two set of experiments with different H_2 to MTS ratio are shown in Figure 54. It was assumed that the peak temperature was always at the center of the fiber and the fiber steady state height at the center of the fiber was used in the kinetic analysis. The logarithm of the deposition rates were plotted in Figure 54 as a function of reciprocal temperatures for H_2/MTS ratios of 10 and 20. The two broken straight lines are the least squares fit for the two different sets of experimental data.

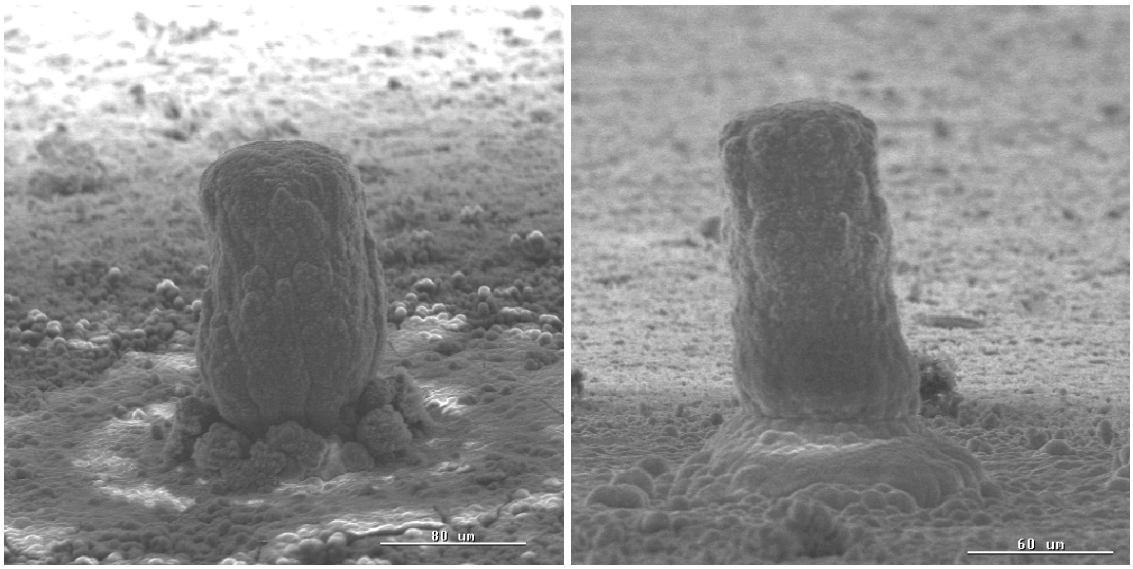

(a) L284-9, H_2/MTS=20, T_{max} =1107 ˚ C (b) L292-12, H_2/MTS =10, T_{max} = 1155 ˚ C

Figure 54: LCVD-SiC fibers without volcano effects.

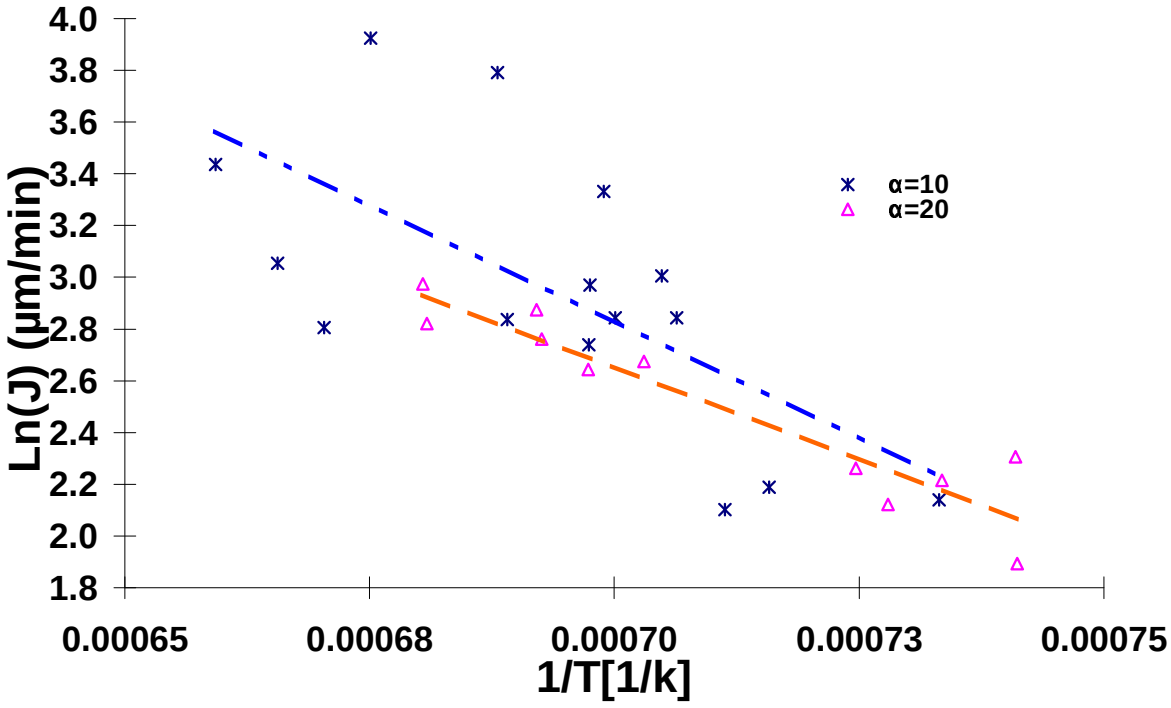

Figure 55: Deposition rate vs. reciprocal temperature for SiC fiber growth process.

Table 12: SiC from MTS and H_2 Multi-Regression Fitting Results

Parameter	*Fitted value*	*90% Confidence Intervals*
$Q(KJ/mol)$	163	122 to 204
n	0.36	0.03 to 0.69
K_0	216	2 to 21.7E+3

The multiple regression results from fitting of Equation (13) are displayed in Table 12. The fitted apparent activation energy of 163 KJ/mol falls within the range of literature values of 40 to 400 KJ/mol for the CVD of SiC. [60] The apparent order of reaction was determined to be 0.36, much less than one. The statistical analysis showed that the MTS concentration and the reciprocal temperature were both statistically significant at the 90% confidence level. Results from past attempts to determine the kinetics of the CVD of SiC from MTS and H_2 ranged widely with apparent activation energies between 40 and 400 KJ/mol and reaction orders between 0 and 2.5 depending on the experimental parameters. [60], [77]. Our kinetics data are within those ranges.

Therefore, the experimental relationship of the LCVD-SiC deposition rate and the MTS concentration and the deposition temperatures using the Georgia Tech LCVD system is the one shown in equation (15). The LCVD-SiC deposition rate can be predicted by given the concentration of the MTS and the deposition temperature using the equation (15). But the values of the MTS concentration and deposition temperatures must be within the ranges of those MTS concentration and deposition temperatures used in the kinetic analysis.

$$J = 216e^{(-163/RT)}C_{MTS}^{0.36} \tag{16}$$

5.4 Characterization of Deposits

The deposits were characterized using light and scanning electron microscopy. Mechanically grounded and polished samples were examined. The SEM micrographs in Figure 55 display the typical morphologies of SiC fibers fabricated at temperatures below 1250^oC for either H_2/MTS ratio. Small and large crystals are faintly visible in Figures 56 (a) and (b), respectively. As shown later, etching more clearly revealed the grain size. The grain size increased from about 2 μm for a deposition temperature of 1101^oC to 50 μm at 1161^oC.

This typical phenomenon can be explained by higher processing temperature increasing the surface mobility and diffusion of the adsorbed chemical species.

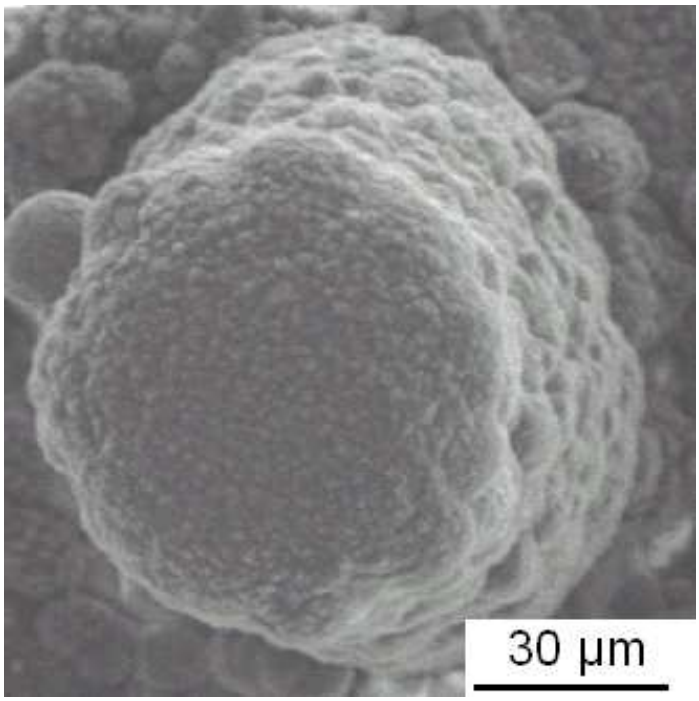

(a) L284-8, T_{max}=1101^{o}C, H_2/MTS=20

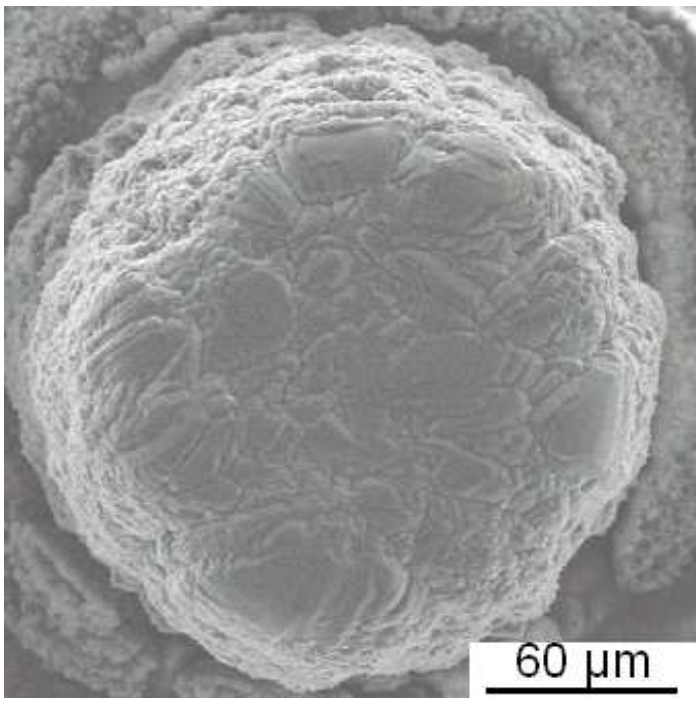

(b) L285-5, T_{max}=1161^{o}C, H_2/MTS=20

Figure 56: SEM micrographs of the general morphologies of SiC fibers.

Figures 57 and 58 show the transverse and longitudinal polished sections of uneteched SiC fibers. The SiC grains could be observed by utilizing high-magnification optical microscopy and the back-scattered SEM technique. The back scattered micrographs are shown in Figures 57 (b), (d) and 58 (b), (d). Importantly, the fibers are revealed to be dense and crack free, dissimilar to LCVD carbon fibers. [78] Also, the processing condition used for growth of fiber L293-4 yielded a fiber with rather uniform diameter along its length. This morphology is desirable for deposition of three dimensional structures as in rapid prototyping.

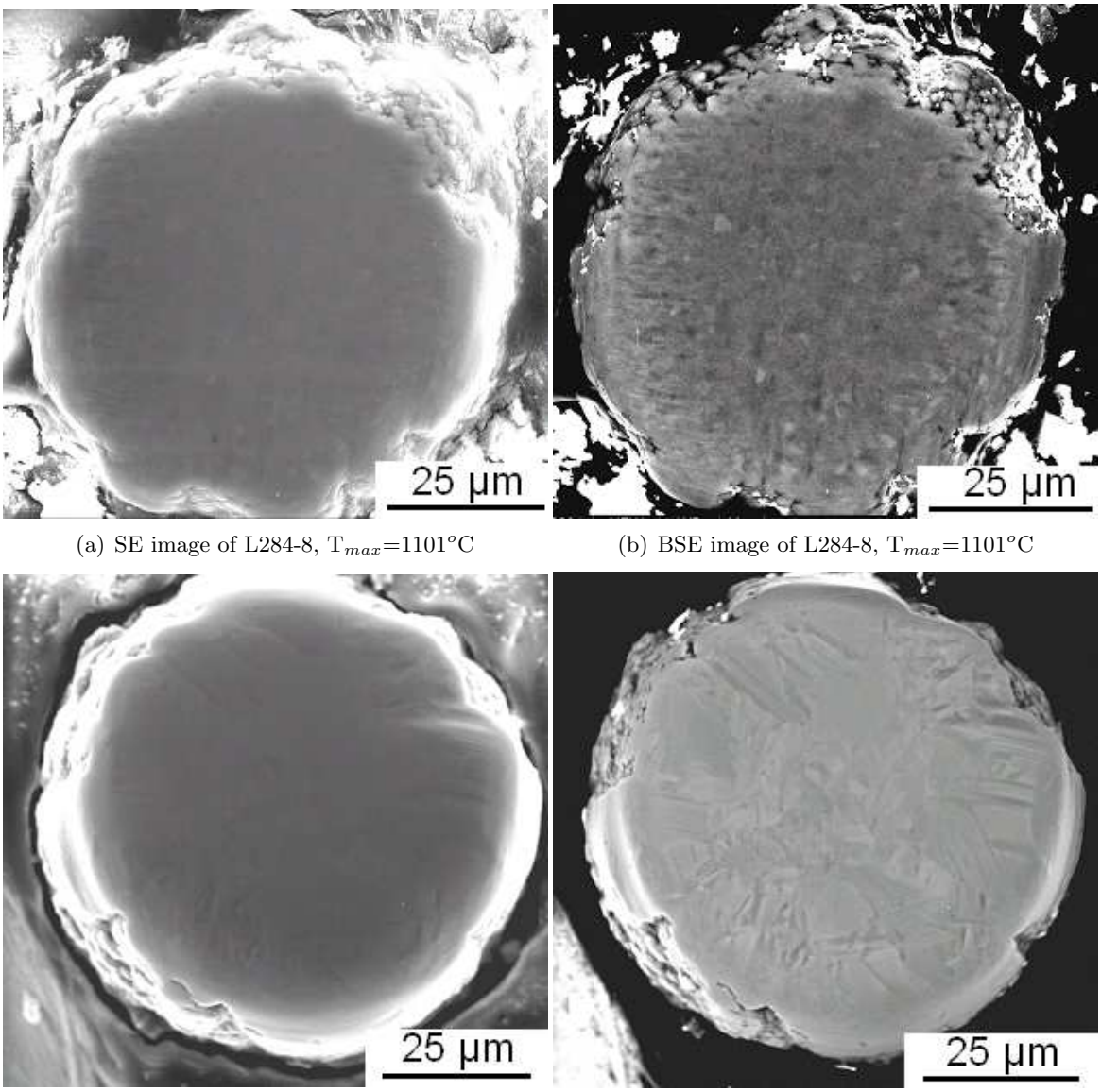

(a) SE image of L284-8, T_{max}=1101^{o}C

(b) BSE image of L284-8, T_{max}=1101^{o}C

(c) SE image of L285-5, T_{max}=1161^{o}C

(d) BSE image of L285-5, T_{max}=1161^{o}C

Figure 57: Secondary and Back-scattered SEM micrographs of transverse sectioned polished SiC fibers.

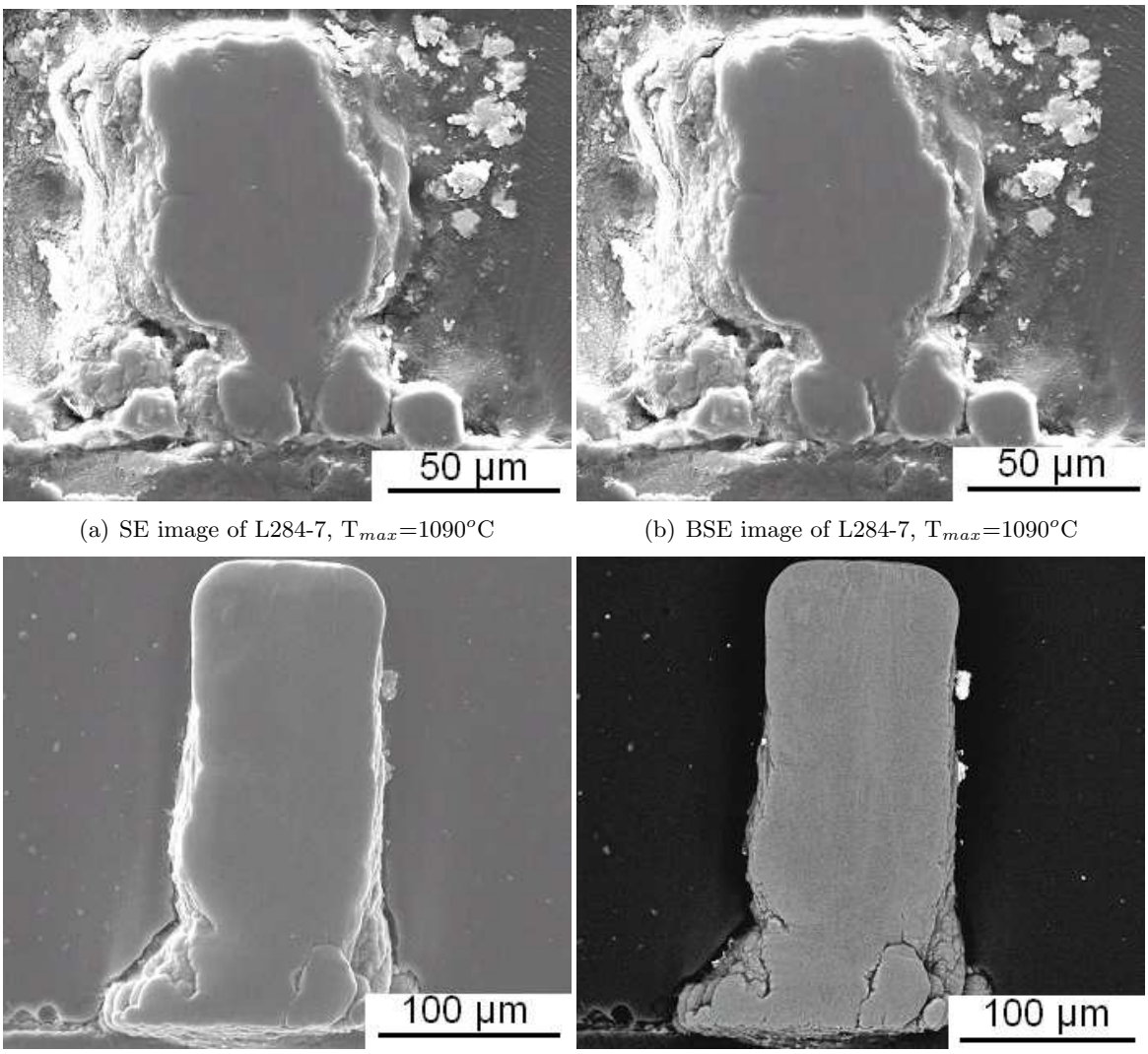

(a) SE image of L284-7, T_{max}=1090^{o}C

(b) BSE image of L284-7, T_{max}=1090^{o}C

(c) SE image of L293-4, T_{max}=1244^{o}C

(d) BSE image of L293-4, T_{max}=1244^{o}C

Figure 58: Secondary and Back-scattered SEM micrographs of polished longitudinal section of SiC fibers.

To delineate the grain structures of the SiC fibers, polished samples were chemically etched by boiling in Murakami's solution with $K_3Fe(CN)_6/NaOH/H_2O$ =1/1/2.5 for 40 minutes. [75] The etched cross-sections of the same fibers are shown in Figures 59 and 60. After etching, the grains were clearly revealed. Figure 59 (b) shows the etched microstructure of the same fiber previously shown in Figure 56 (b), and it is confirmed that the growth features seen in Figure 56 (b) are grains.

The grain size is clearly larger for the higher average growth temperature as shown by comparing Figures 59 (a) and (b). The grains for the lower growth temperature are 1-2 μm in size. For fiber L285-5 shown in Figure 58 (b), the grain size at the fiber periphery, is larger (50 μm) than at the center (3 μm) despite the fact that the center of the fiber was hotter during growth. An increase in grain size from the center of the fiber to the periphery was observed for other fibers, without exception, where the temperature was high enough to cause the volcano effect as shown in Figure 52 (c). Thus, for fibers grown at low temperatures, grain size increases with temperature, but for fibers grown at very high temperatures, the grain size is larger at the cooler periphery. Whatever is responsible for the lower deposition rate at the center of fibers exhibiting the volcano effect may also be responsible for the reduced grain size. Or perhaps grain size and growth rate are simply directly correlated.

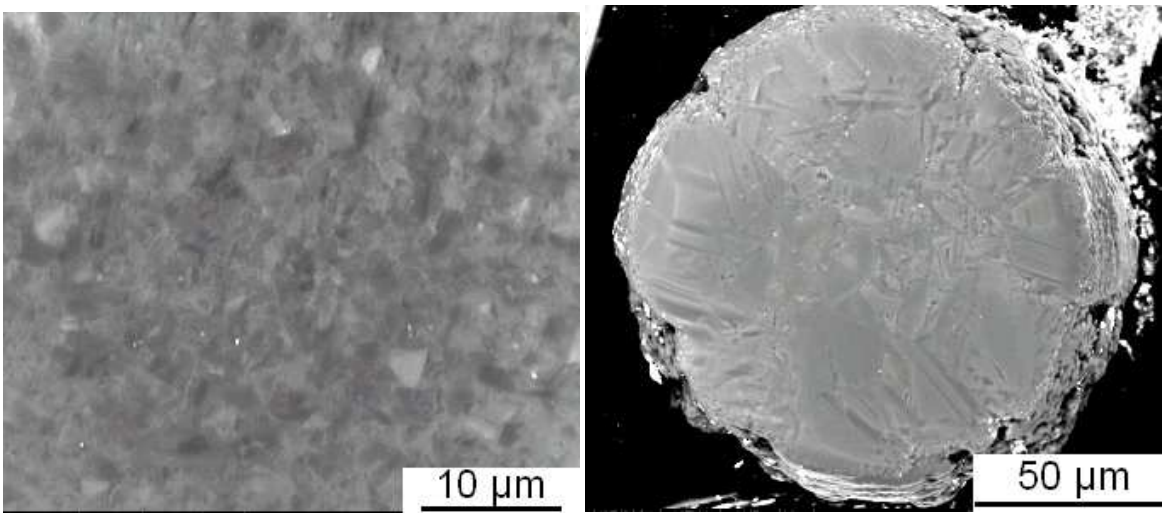

(a) BSE image of L284-8, T_{max}=1101^{o}C (b) BSE image of L285-5, T_{max}=1161^{o}C

Figure 59: Back-scattered SEM micrographs of transverse sectioned polished and etched SiC fibers.

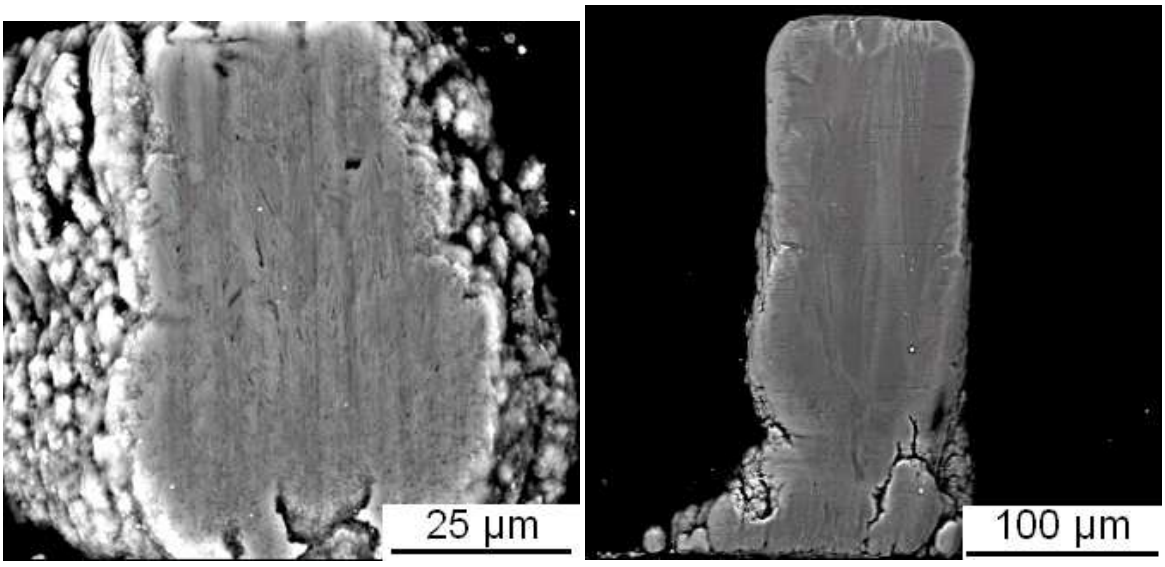

(a) BSE image of L284-7, T_{max}=1090^{o}C (b) BSE image of L293-4, T_{max}=1244^{o}C

Figure 60: Back-scattered SEM micrographs of longitudinal sectioned polished and etched section of SiC fibers.

X-Ray Diffraction (XRD) technique was used to detect the crystal structure of the deposited SiC fibers. Due to the small size of the deposits, about 20 fibers were grown under the same conditions. Those fibers were collected by taking them off the substrates and were examined by a high precision XRD equipment. This equipment is applicable for power samples of small amount. Figure 61 shows the results of the XRD examination. By comparing this figure with the standards of XRD figures of SiC, it is found out that 3C-SiC (β-SiC) is the only crystal structure that is detected from the deposited fibers. This means that the SiC fibers fabricated with the Georgia Tech LCVD system under normal conditions are β-SiC, which is the only one cubic crystal structure of SiCs.

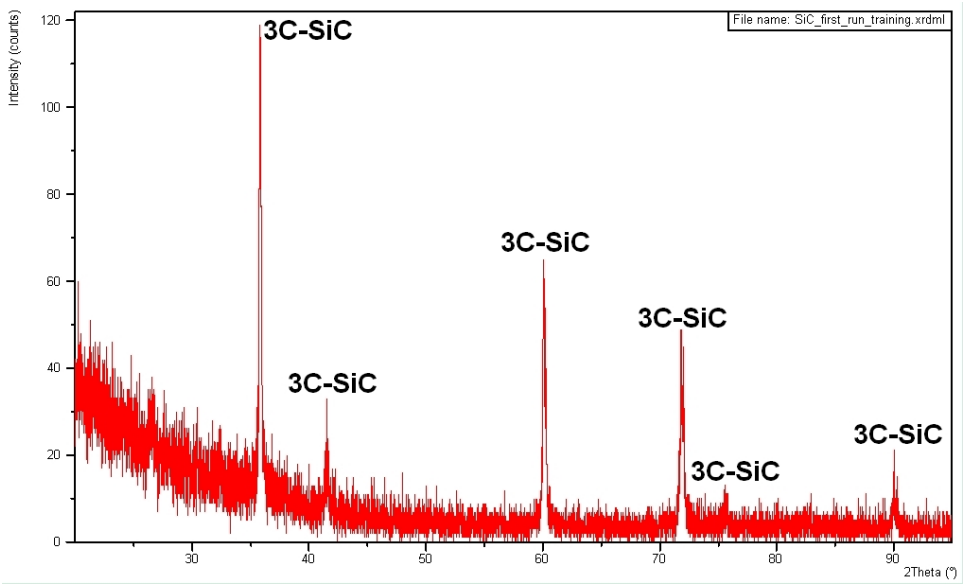

Figure 61: XRD figure for LCVD-SiC fibers.

Energy Dispersive X-ray Spectroscopy (EDS) was utilized to find out the chemical composition of the deposited SiC fibers. Figure 62 is the EDS figure for fiber, L284-8. The quantitative analysis result is shown in Appendix A. It is indicated that the deposits are SiC materials. And the atomic ratio of Si to C is close to one. Normally, the composition results detected by EDS technique might not be very accurate. This is due to the limitation of the EDS technique itself.

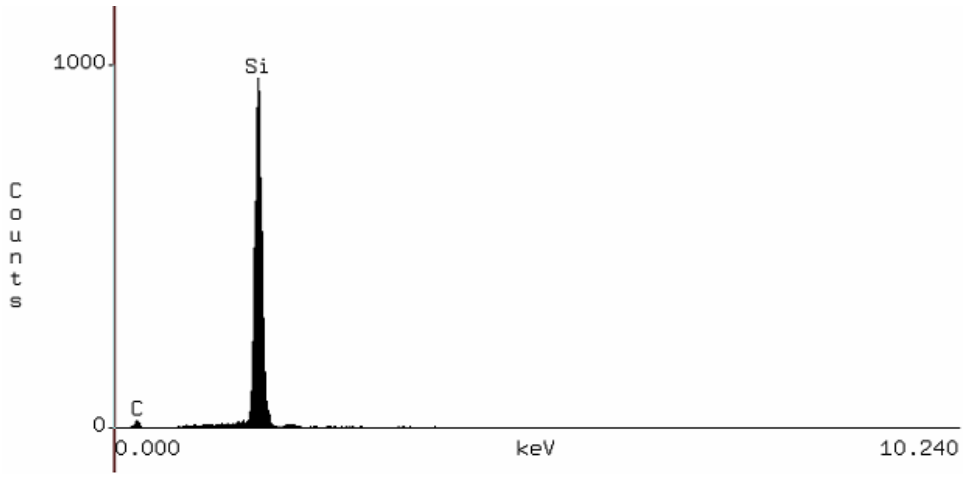

Figure 62: EDS figure of LCVD-SiC fiber, L284-8.

5.5 Summary of SiC Fiber Deposition

SiC fibers were fabricated by laser CVD from MTS and H_2 and conditions conducive to the growth of dense, uniform fibers were identified. Comparing the results of thermodynamic calculations described in Chapter IV and the actual deposited SiC fibers, it is indicated that the lower deposition rates at high temperatures, which was predicted by thermodynamic calculations, causes the occurance of a volcano-like depression in the center of fibers grown at the higher temperatures.

A kinetic model, based on the experimental measurements of fiber heights, permitted determination of the apparent activation energy and the apparent order of reaction under the growth conditions investigated. These values were 163 KJ/mol and 0.36, respectively. Chemical etching was employed to reveal grain size. Elongated grains were formed with their long axis parallel to the growth direction, i.e., the fiber axis. Grain diameters increased from 2 to 50 μm as the average deposition temperature increased from 1076 to 1244^oC. Surprisingly, for fibers grown at higher temperatures, grain diameters were smaller in the central portion of the fiber, even though the deposition temperatures were significantly higher there.

XRD and EDS techniques were used to examine the crystal structure and chemical composition of the deposits. It is revealed that the SiC fibers deposited at normal conditions are β-SiC. The result of EDS detection confirmed that the deposits are SiC materials.

CHAPTER VI

SIC LINE DEPOSITION

SiC lines were fabricated using the Georgia Tech LCVD system. MTS and H_2 were the reagents for the deposition process. In this chapter, a set of one-layer lines was fabricated first. The outcomes of these one-layer lines helped us to determine the processing conditions of the first layer, when multiple layers of lines were deposited. Then surface response experiments and analysis were performed to determine the relationships between different characteristics of the lines and the processing conditions. Finally, material characterization was performed for the deposited lines.

6.1 One-Layer Lines

SiC lines are fabricated layer by layer by moving the substrate forward and backward. In order to deposit SiC lines having good shape, the first layer of the line must be as good as possible, which means that the thickness and width of the first layer should be uniform. Because after the first layer is finished, it serves as the substrate for the second layer and so on. The topograph of the first layer is very important for the deposition process afterwards. Without a good shaped first layer, it is very difficult to fabricate a line with multiple layers.

Among the processing parameters, laser power and scan speed of the laser are the most influential factors for line deposition. Seven sets of experiments were performed by executing the one-layer line deposition in which one fixed laser power is applied for each set and in each set 11 different scan speeds were used. Table 12 lists the laser powers and scan speeds applied for this one-layer line study. A total of 77 one-layer lines were deposited.

During the deposition process, the one-layer lines were deposited on SK-85 graphite substrates. The total upper chamber pressure was 500 torr and the H_2/MTS ratio was 20. The gas-jet was not used during the entire process. The mixture of MTS and H_2 was flown through the side port of the upper chamber.

Table 12 The laser powers and the laser scan speeds for the one-layer lines.

Set #	Laser Power (V)
1	8
2	7
3	6
4	5
5	4
6	3
7	2

Scan Speed (in/min)
0.01
0.05
0.1
0.15
0.2
0.25
0.3
0.35
0.4
0.45
0.5

The micrographs in Figures 63-67 display the one-layer lines grown under different laser powers and scan speeds. As shown in Figures 63 and 64, when the laser power was equal to or larger than 6 V, the lower the scan speed, the worse the volcano effect. The high energy laser powers etched off the material in the center of the lines. Also, lower scan speed generates much more material, as shown in Figure 63 (a) and 64 (a). Generally speaking, laser power that is equal to or larger than 6 V is not suitable for the first layer deposition of multiple-layer lines.

When the laser power was lower than 6 V, i.e., 5, 4, or 3 V, the effect of the scan speed on the outcome of one-layer lines was similar to those with 6 V laser power applied. But the level of the volcano effect is less than the lines deposited at 6 V. By examining and comparing all of the lines in Figures 65-67, it seems that when the laser power was 5 V, scan speeds of 0.3 or 0.35 in/min produced better shaped one-layer lines. If the laser power is changed to 4 V, scan speeds of 0.1 to 0.5 in/min seems to generate relatively similar outcomes, which are better than for the scan speeds of 0.01 or 0.05 in/min. With a 3 V laser power, good shaped one-layer lines were deposited by using scan speeds from 0.05 to 0.3 in/min. In addition, the outcome of 3 V laser power seems better than those of 4 or 5 V laser powers.

When the laser power becomes 2 V or even lower, it seems that those laser power are

too low for first layer deposition. Because most of the time, there is very little SiC material deposited on the substrate no matter how slow the laser scan speed. Also, it is difficult to be examined by the SEM technique.

Therefore, based on the comprehensive one-layer line study, it is recommended that a laser power of 3 V be used with scan speeds of 0.05 to 0.3 in/min to deposit the first layer of the lines. The following surface response experiments for SiC lines utilized these processing conditions initially.

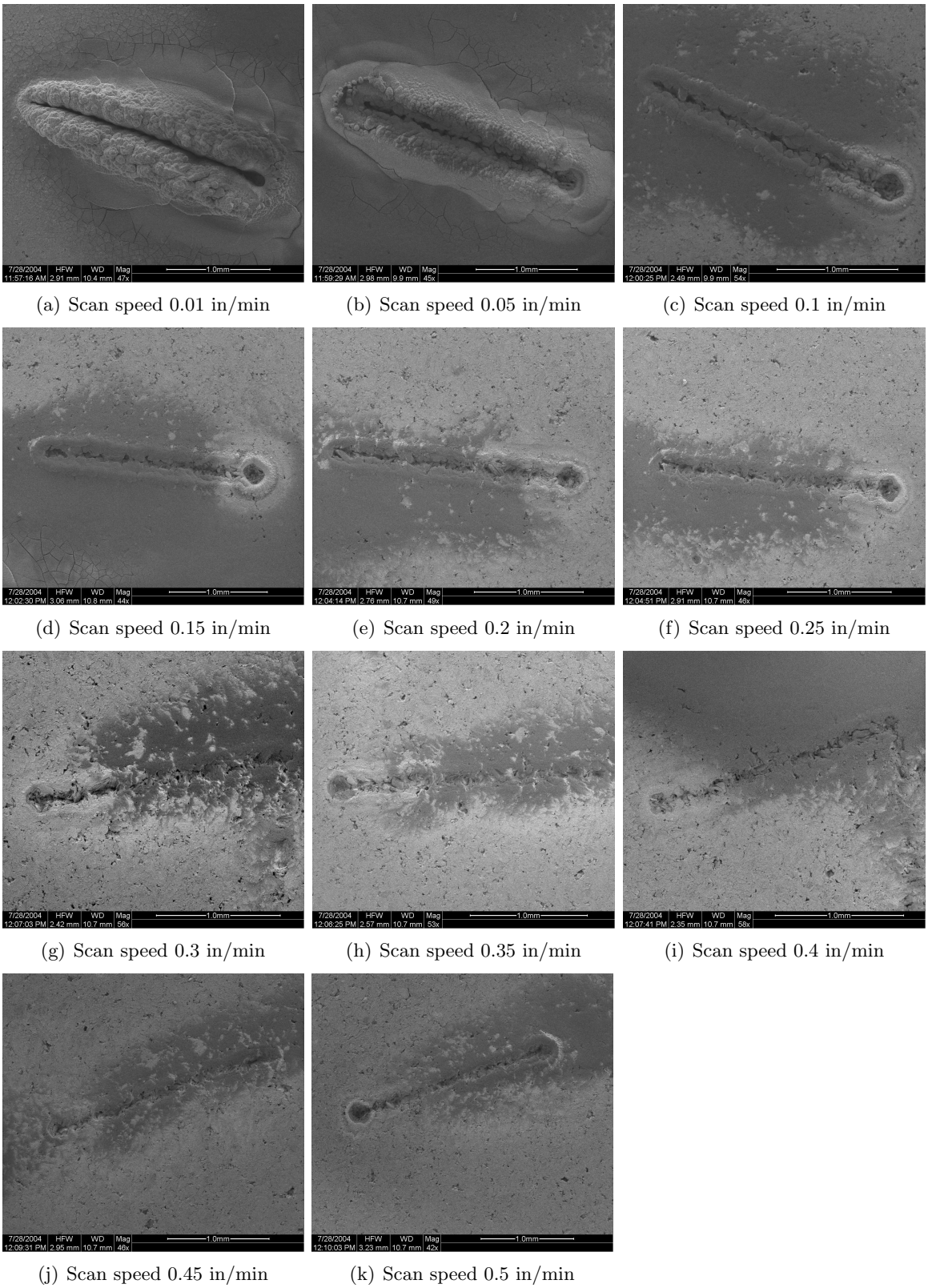

(a) Scan speed 0.01 in/min (b) Scan speed 0.05 in/min (c) Scan speed 0.1 in/min

(d) Scan speed 0.15 in/min (e) Scan speed 0.2 in/min (f) Scan speed 0.25 in/min

(g) Scan speed 0.3 in/min (h) Scan speed 0.35 in/min (i) Scan speed 0.4 in/min

(j) Scan speed 0.45 in/min (k) Scan speed 0.5 in/min

Figure 63: SEM micrographs of one-layer lines deposited with laser power of 8 V.

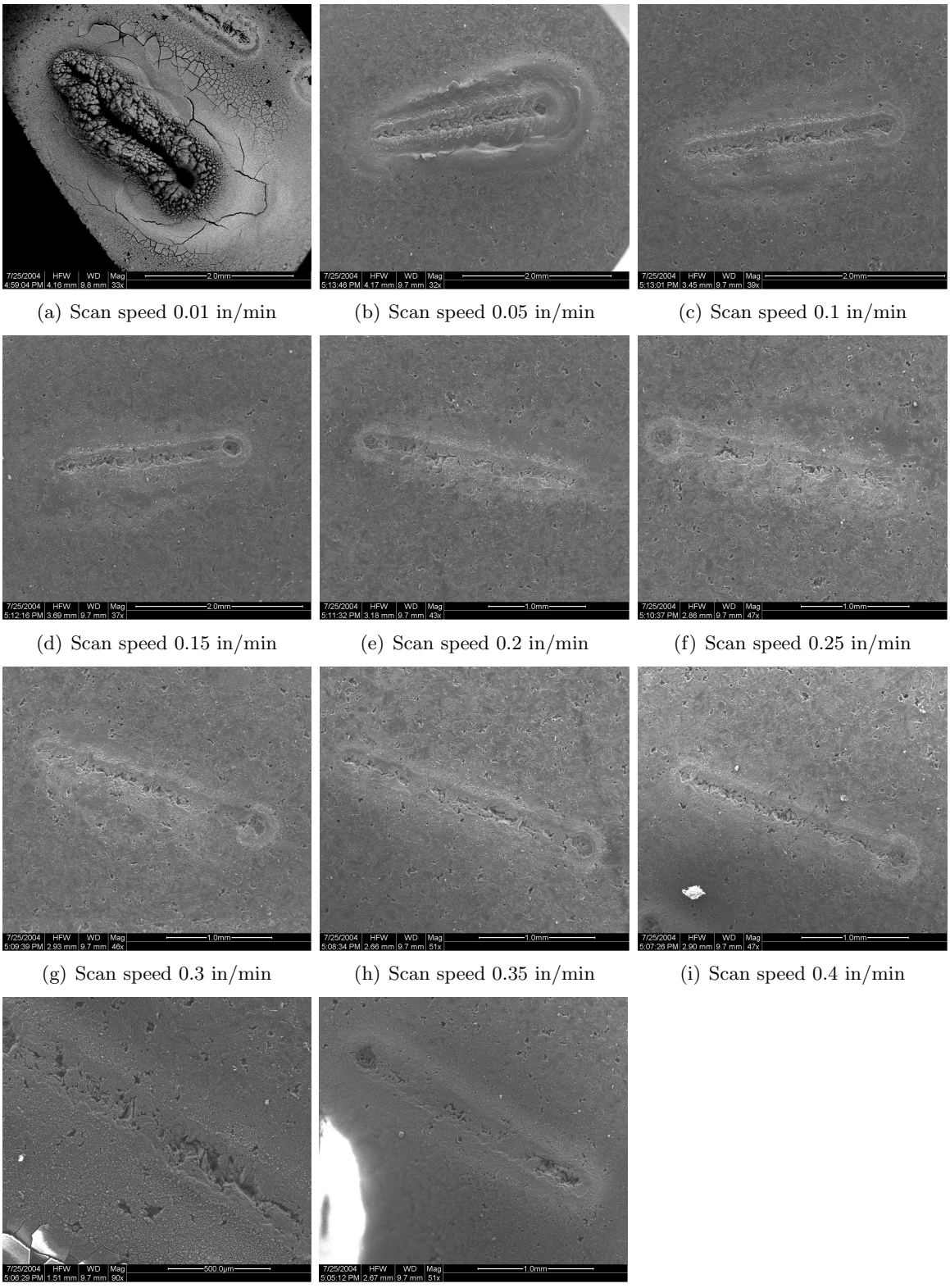

(a) Scan speed 0.01 in/min (b) Scan speed 0.05 in/min (c) Scan speed 0.1 in/min

(d) Scan speed 0.15 in/min (e) Scan speed 0.2 in/min (f) Scan speed 0.25 in/min

(g) Scan speed 0.3 in/min (h) Scan speed 0.35 in/min (i) Scan speed 0.4 in/min

(j) Scan speed 0.45 in/min (k) Scan speed 0.5 in/min

Figure 64: SEM micrographs of one-layer lines deposited with laser power of 6 V.

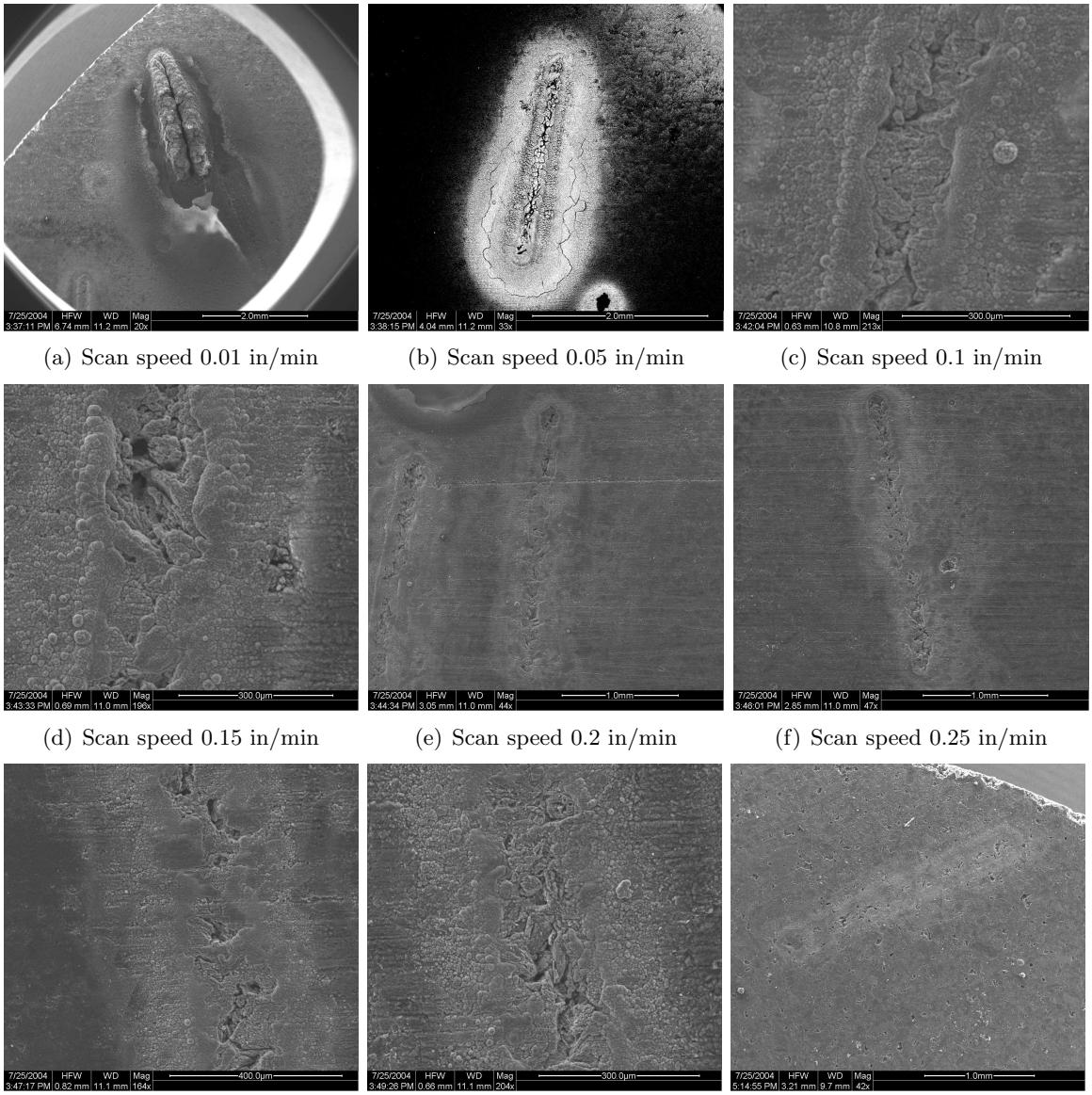

(a) Scan speed 0.01 in/min (b) Scan speed 0.05 in/min (c) Scan speed 0.1 in/min

(d) Scan speed 0.15 in/min (e) Scan speed 0.2 in/min (f) Scan speed 0.25 in/min

(g) Scan speed 0.3 in/min (h) Scan speed 0.35 in/min (i) Scan speed 0.4 in/min

Figure 65: SEM micrographs of one-layer lines deposited with laser power of 5 V.

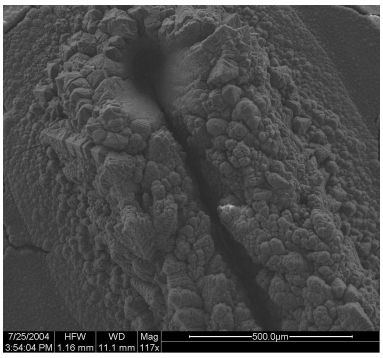

(a) Scan speed 0.01 in/min

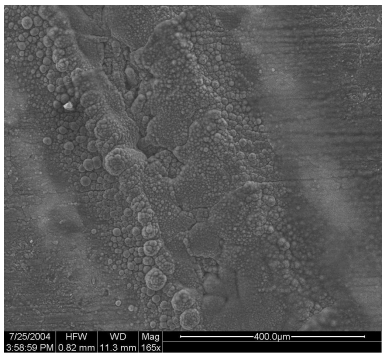

(b) Scan speed 0.05 in/min

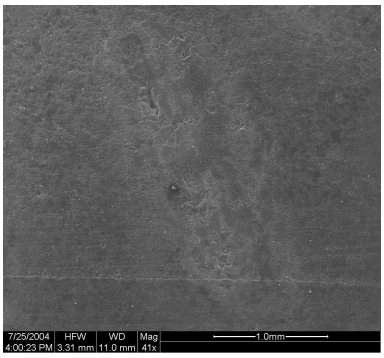

(c) Scan speed 0.1 in/min

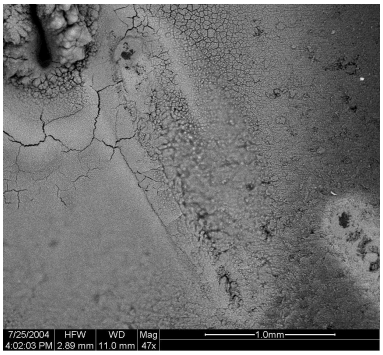

(d) Scan speed 0.15 in/min

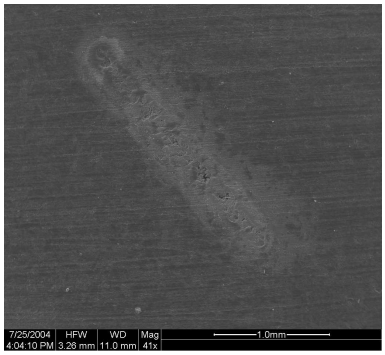

(e) Scan speed 0.2 in/min

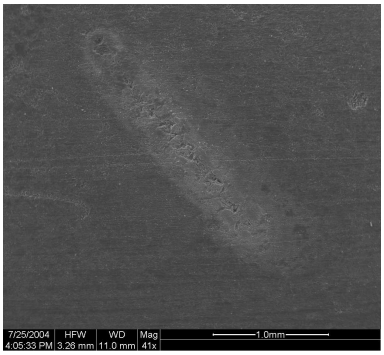

(f) Scan speed 0.25 in/min

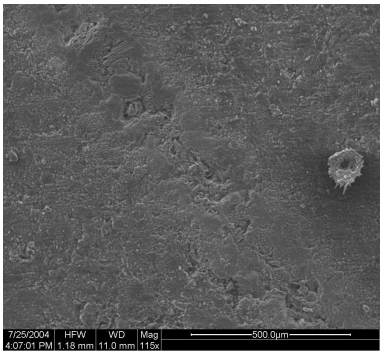

(g) Scan speed 0.3 in/min

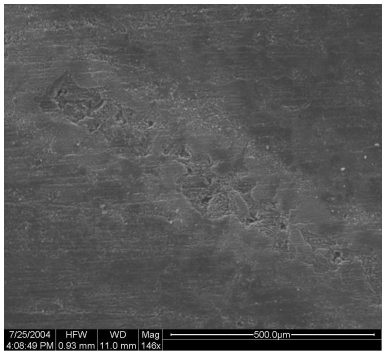

(h) Scan speed 0.35 in/min

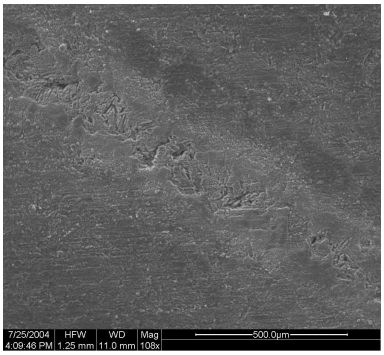

(i) Scan speed 0.4 in/min

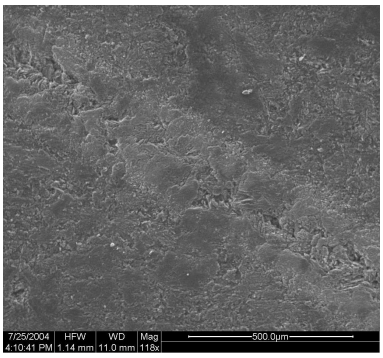

(j) Scan speed 0.45 in/min

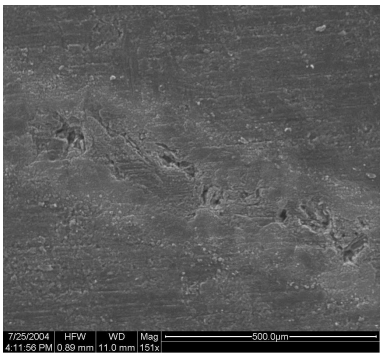

(k) Scan speed 0.5 in/min

Figure 66: SEM micrographs of one-layer lines deposited with laser power of 4 V.

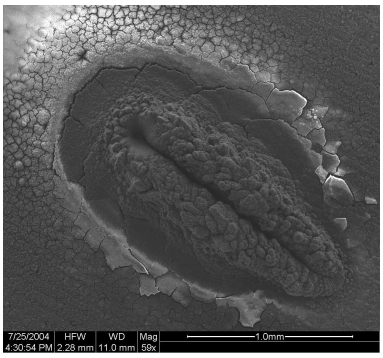

(a) Scan speed 0.01 in/min

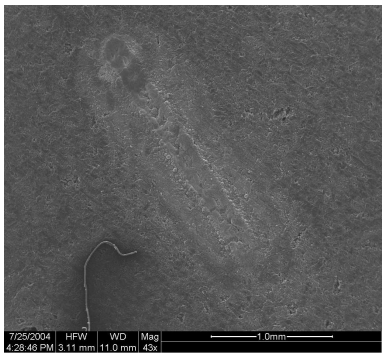

(b) Scan speed 0.05 in/min

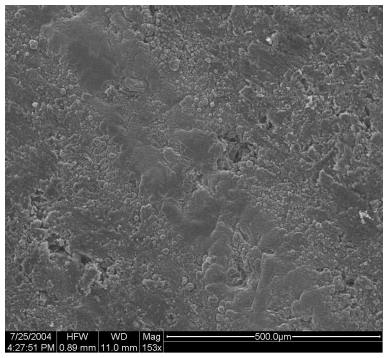

(c) Scan speed 0.1 in/min

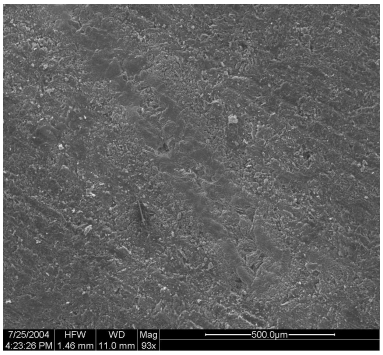

(d) Scan speed 0.15 in/min

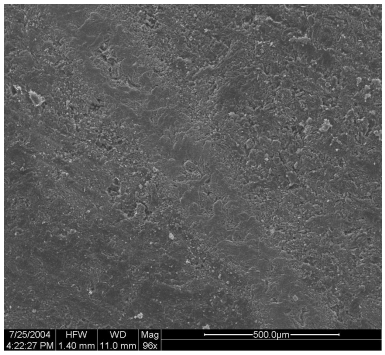

(e) Scan speed 0.2 in/min

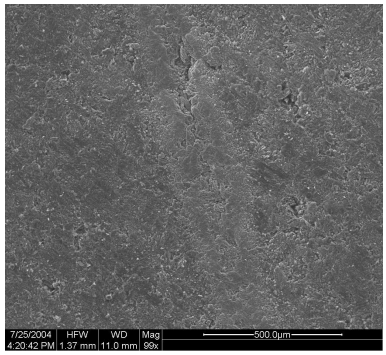

(f) Scan speed 0.25 in/min

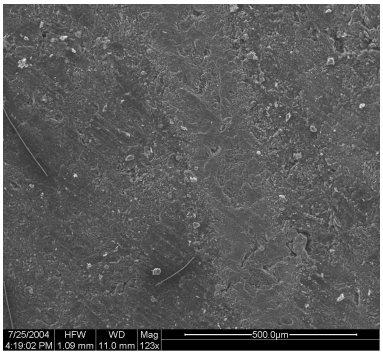

(g) Scan speed 0.3 in/min

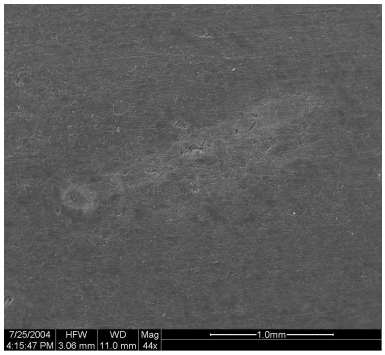

(h) Scan speed 0.35 in/min

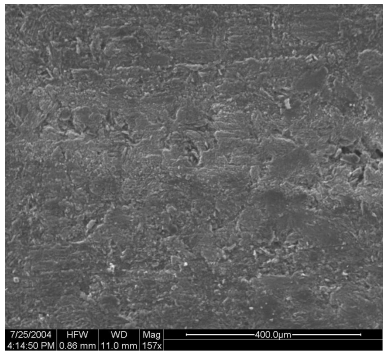

(i) Scan speed 0.4 in/min

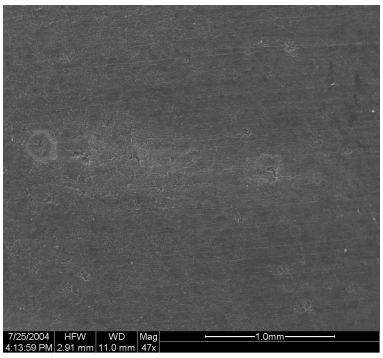

(j) Scan speed 0.45 in/min

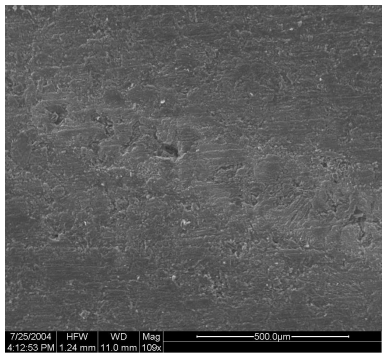

(k) Scan speed 0.5 in/min

Figure 67: SEM micrographs of one-layer lines deposited with laser power of 3 V.

6.2 Surface Response Experiments

6.2.1 Surface Response Experimental Procedure

Through preliminary experiments, it was determined that the most important processing parameters for LCVD-SiC line deposition were laser power (deposition temperature), scan speed, and MTS concentration. Surface response experiments were performed to determine experimentally the relationships between SiC line characteristics and those three processing parameters. Three responses were considered. They were volcano level, line thickness, and porosity present in the lines. The surface response experiment was a rotatable box design with four center point experiments, giving a total of 18 experiments. Figure 68 shows the surface response experiments schematically, where A, B, and C represent processing parameters, i.e., average deposition temperature, laser scan speed, and H_2/MTS. Each of the three factors was varied at 5 levels according to the design. Table 13 lists the processing conditions the 18 SiC lines.

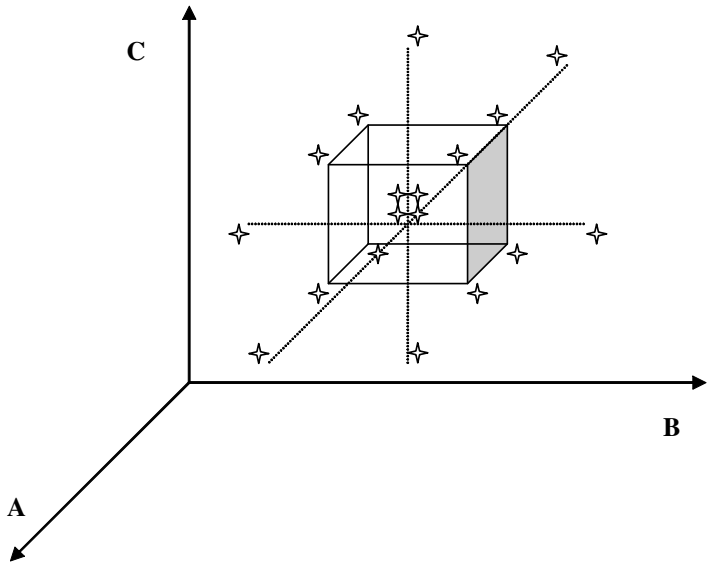

Figure 68: Schematic of LCVD-SiC line surface response experiment.

As it was described in Chapter V, the average temperature over a certain size of circle was measured and controlled during the deposition process. This surface response experiment considered 5 different average temperatures over a circle of 100 pixels in diameter. The

Table 13: Factors and levels for LCVD-SiC line surface response experiment.

Level	T_{avg} (^oC)	H_2/MTS	*Laser Scan Speed (in/min)*
1	1320	10	0.05
2	1340	20	0.1
3	1380	40	0.2
4	1420	60	0.3
5	1440	70	0.35

concentration of MTS is given as a ratio of H_2 to MTS. For all lines, the flow rate of MTS was 25 sccm. The flow rate of H_2 was adjusted line by line according to the desired ratio of H_2 to MTS. For all experiments, the total pressure of the reaction chamber was maintained at 500 torr. All lines were 0.1 inch long and 4 passes were used.

To save time, the order of the experiments was not completely randomized. Experiments having the same MTS concentration were run at the same time. Alos, the order of the experiments was from high MTS concentration to low MTS concentration. Before each set of depositions under the same MTS concentration, the chamber was evacuated completely and then filled with the mixture of MTS and H_2 having appropriate ratio. The flow was continue at least 6 minutes before the line deposition process was started. This purge and fill cycle ensured an accurate MTS concentration for each line experiment.

Table 14 list the deposited lines and the three outcomes of the deposited lines. The volcano level, the thickness, and the porosity of the lines were estimated using the SEM technique. The higher the volcano level value, the worse the volcano effect. The higher the porosity value, the more pores present in the lines. The values of those three line responses are for comparison purposes, and are not very accurate. But those values help us to generate the experimental relationships between the outcomes of LCVD-SiC lines and processing conditions. These relationships further our understanding of the deposition process and help us control the processing conditions for a specific purpose.

6.2.2 Surface Response Experimental Results

Figure 69 shows an example of a SiC line deposited from run 1. Figure 69 (a) displays the SiC line magnified at 45x. The white border material around the line may be some SiC powers deposited while fabricating the line. Figure 69 (b) shows the same line magnified

Table 14: Results of LCVD-SiC line surface response experiment.

Run	T_{avg} (^oC)	T_{max} (^oC)	H_2/MTS	*Ls-SS (in/min)*	*Volcano*	*Thickness*	*Porosity*
1	1361.6	1603.4	10	0.2	1.5	2	0.5
2	1354.3	1605.1	20	0.1	1.7	1.6	0.5
3	1340.1	1590.4	20	0.3	2.2	0.8	2.2
4	1420.4	1712.8	20	0.1	1	1.8	0.4
5	1393.7	1664.3	20	0.3	2	1	1.6
6	1376.3	1681.3	40	0.05	2.5	0.7	2.3
7	1369.1	1645.7	40	0.2	1.9	0.8	2.0
8	1382.8	1687.5	40	0.2	1.9	0.8	2.0
9	1377.8	1673.6	40	0.2	1.9	0.8	2.0
10	1377.7	1675.3	40	0.2	1.9	0.8	2.0
11	1375.1	1666.0	40	0.35	2	0.6	2.2
12	1334.2	1580.1	40	0.2	1.9	0.9	2.1
13	1438.9	1752.9	40	0.2	2.1	0.8	2.1
14	1337.3	1609.2	60	0.1	2.3	0.5	2.3
15	1340.5	1640.3	60	0.3	2.3	0.5	2.3
16	1420.2	1762.0	60	0.1	2.3	0.5	2.3
17	1419.4	1748.1	60	0.3	2.3	0.5	2.3
18	1380.9	1704.9	70	0.2	2.3	0.5	2.3

at 167x. It is observed from these micrographs that the line has little porosity. There is a slight volcano effect present in the line. The thickness of the line is not very small.

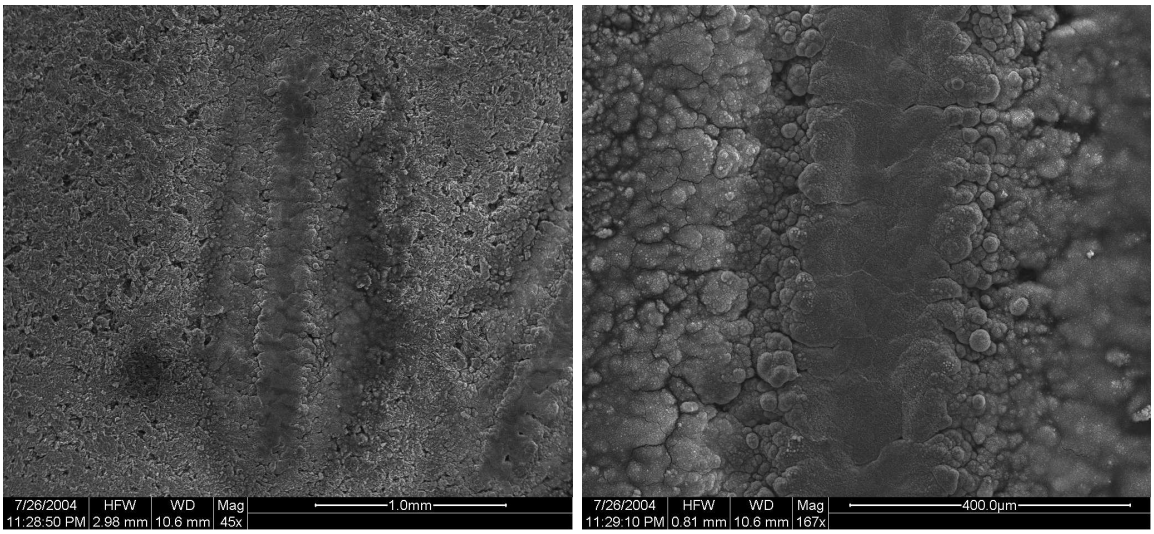

(a) run 1 at 45X

(b) run 1 at 167X

Figure 69: SEM micrographs of SiC line of run 1 from the surface response experiment.

The surface response experiment was analyzed using a commercial software called Statgraphics. The surfaces of volcano response versus T_{max}, laser scan speed, and H_2/MTS ratio are shown in Figure 70. Figure 71 displays the analysis results of the effects of those three factors on the volcano levels of SiC lines. Among those figures, H_2 stands for the ratio of H_2/MTS.

As shown in Figure 71 (a), the ratio of H_2/MTS was the only significant factor at the 95% confidence level. Lower H_2/MTS ratios produced lines with less of the volcano effect. The interaction effects of any two factors on the volcano level is revealed in Figure 71 (b). No interactions were significant at the 95% confidence level. Figure 71 (c) indicates the main effects of those three factors alone on the volcano effects of SiC lines. Appendix B contains more detail on the statistical analysis of the surface response experiments for volcano level of lines.

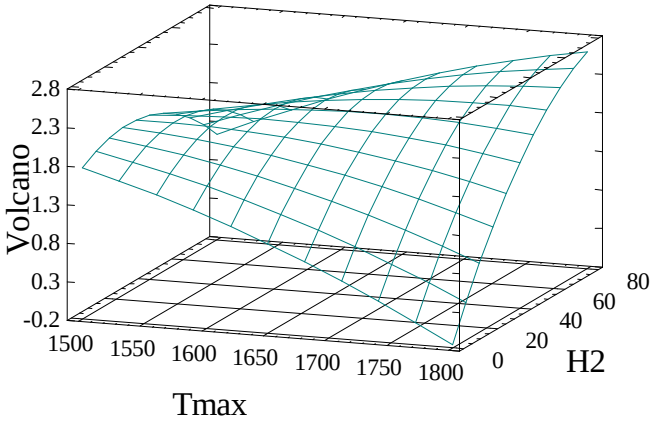

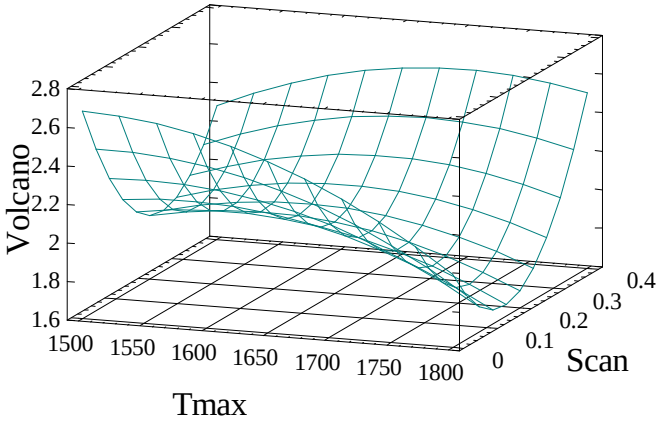

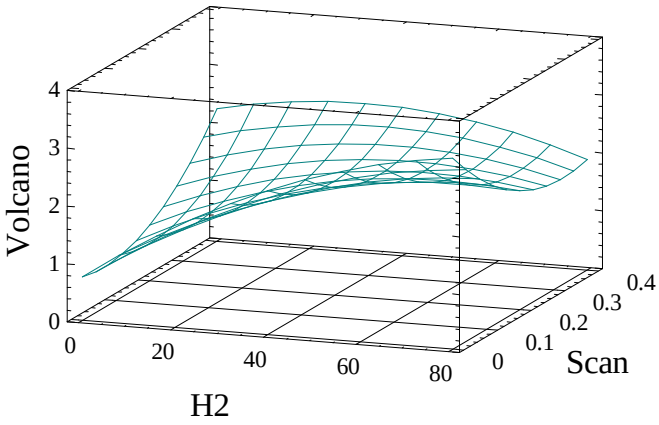

(c) Volcano vs. H_2/MTS and Scan Speed

Figure 70: Response surface of volcano level.

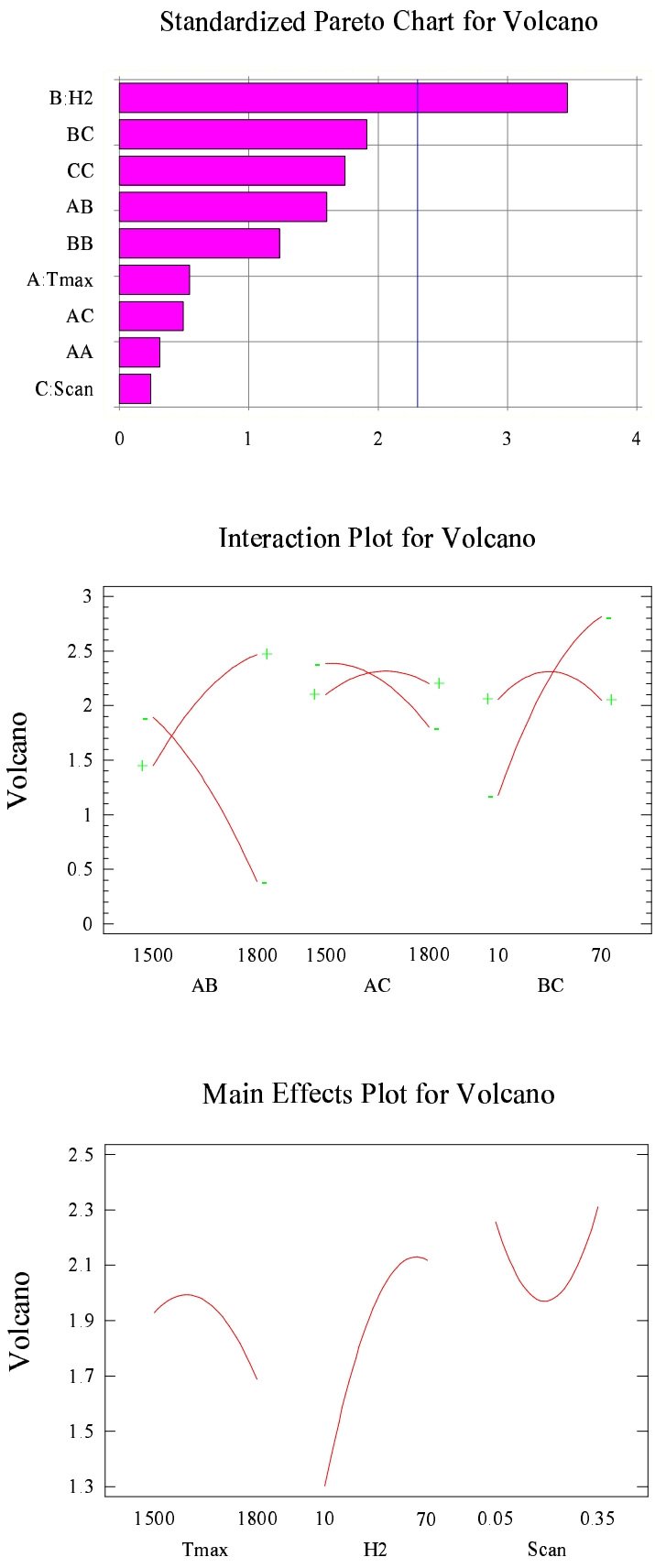

Figure 71: Analysis of surface response of volcano level.

As shown in Figure 70 (a) and (b) and Figure 71 (c), it seems that lower T_{max} favors the formation of volcano effect, which is opposite from the conclusion we got from the SiC fiber deposition experiments. We do not believe this conclusion due to two reasons. One is that lots of the lines deposited for the surface response experiment are very thin, and thus it was very difficult to measure the level of the volcano effect of each line accurately. Second is under the given deposition conditions for the surface response experiment, the factor of the deposition time is not significant at all. Therefore, we think even for lines, lower deposition should minimize the formation of volcanos. Actually, this is confirmed with further line experiments, which will be described later in this chapter.

As the only significant factor on volcano level, the H_2/MTS ratio plays a dominant role in the formation of volcanos. It is indicated that the higher the H_2/MTS ratio, the worse the volcano effect. This means lower concentration of MTS favors the formation of volcano effect in SiC lines according to this study. As for the scan speed effect on the volcano level, as shown in Figure 71 (c), scan speed of 0.2 in/min is the best one for preventing the volcano effect in SiC lines.

The results of the surface response of thickness and porosity of SiC lines are displayed in Figures 72-75. The details of those statistical analysis are listed in Appendix C and D. As for the responses of porosity and thickness of the SiC lines, the significant factors with 95% confidence level are shown in Figures 72 (a) and 74 (a). They are MTS concentration, a quadratic effect of MTS concentration, combination effect of MTS concentration and laser scan speed, and laser scan speed.

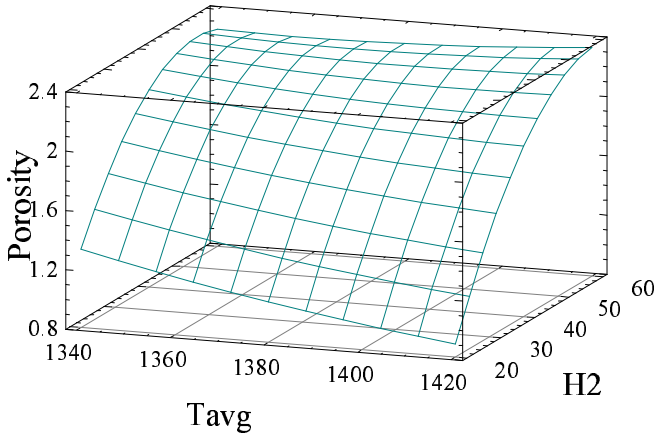

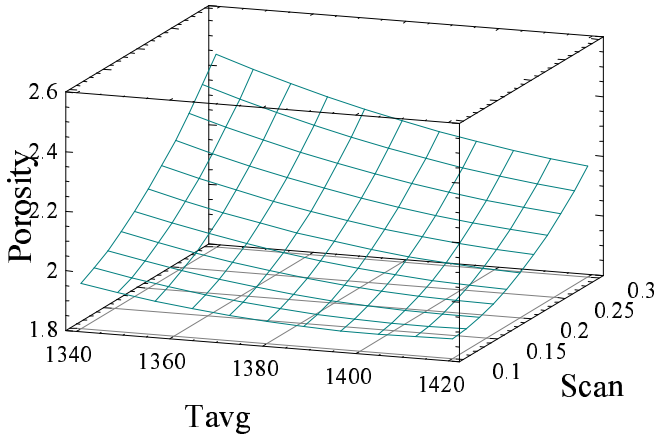

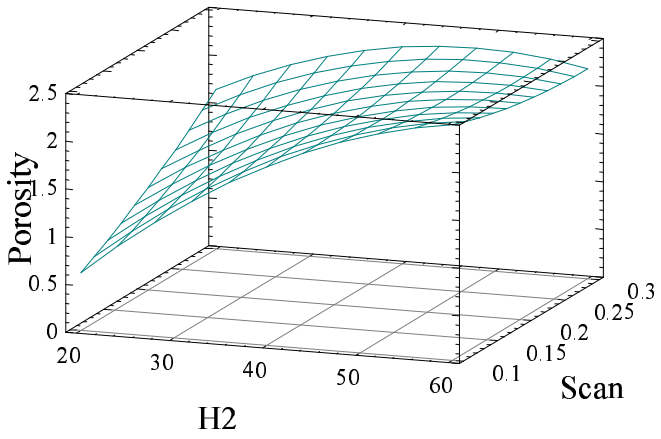

(c) Porosity vs. H_2/MTS and Scan Speed

Figure 72: Response surface of porosity level.

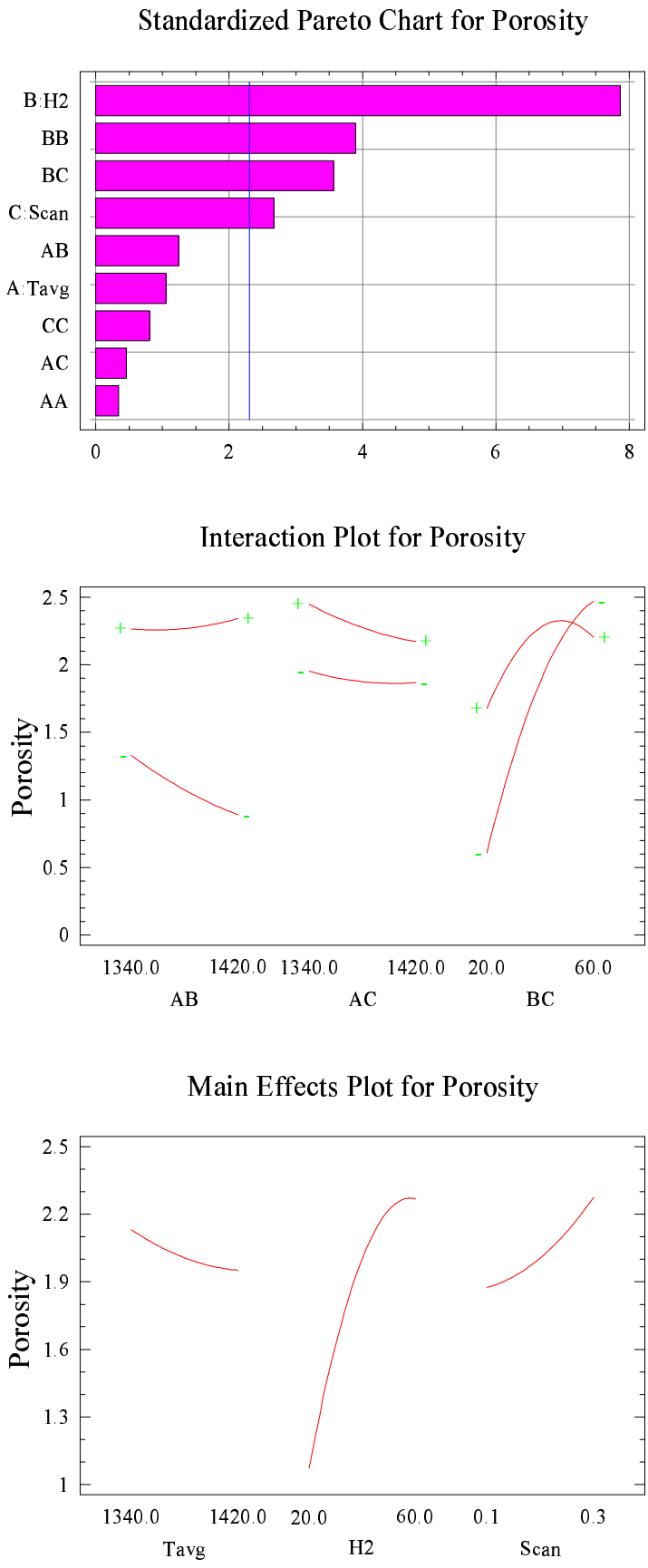

Figure 73: Analysis of surface response of porosity level.

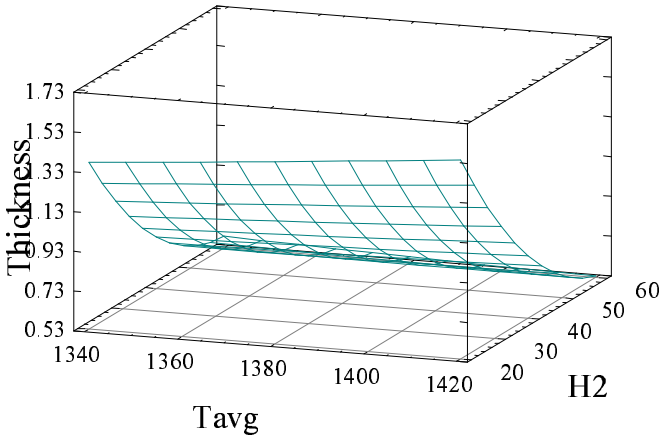

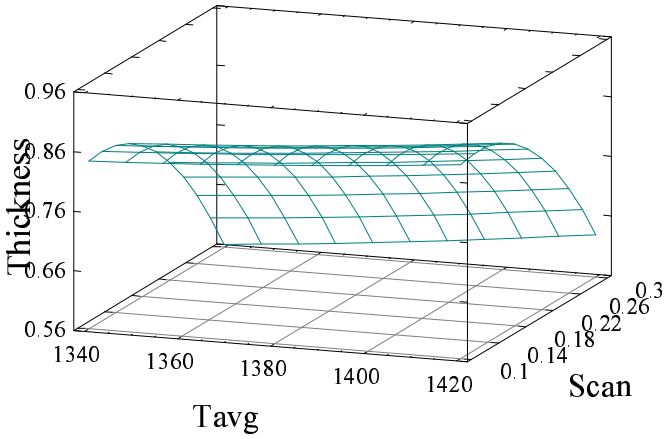

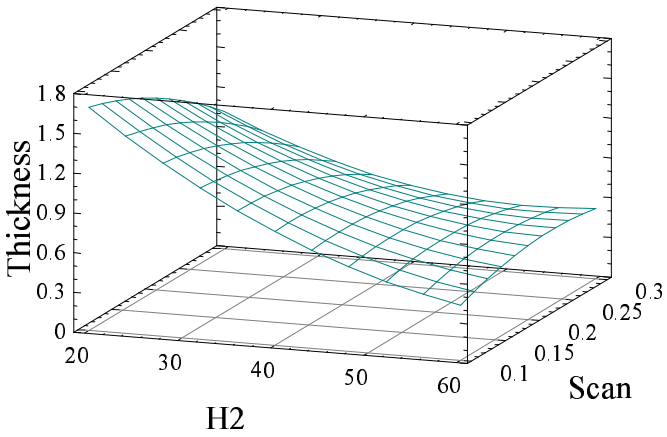

(c) Thicknessvs. H_2/MTS and Scan Speed

Figure 74: Response surface of thickness level.

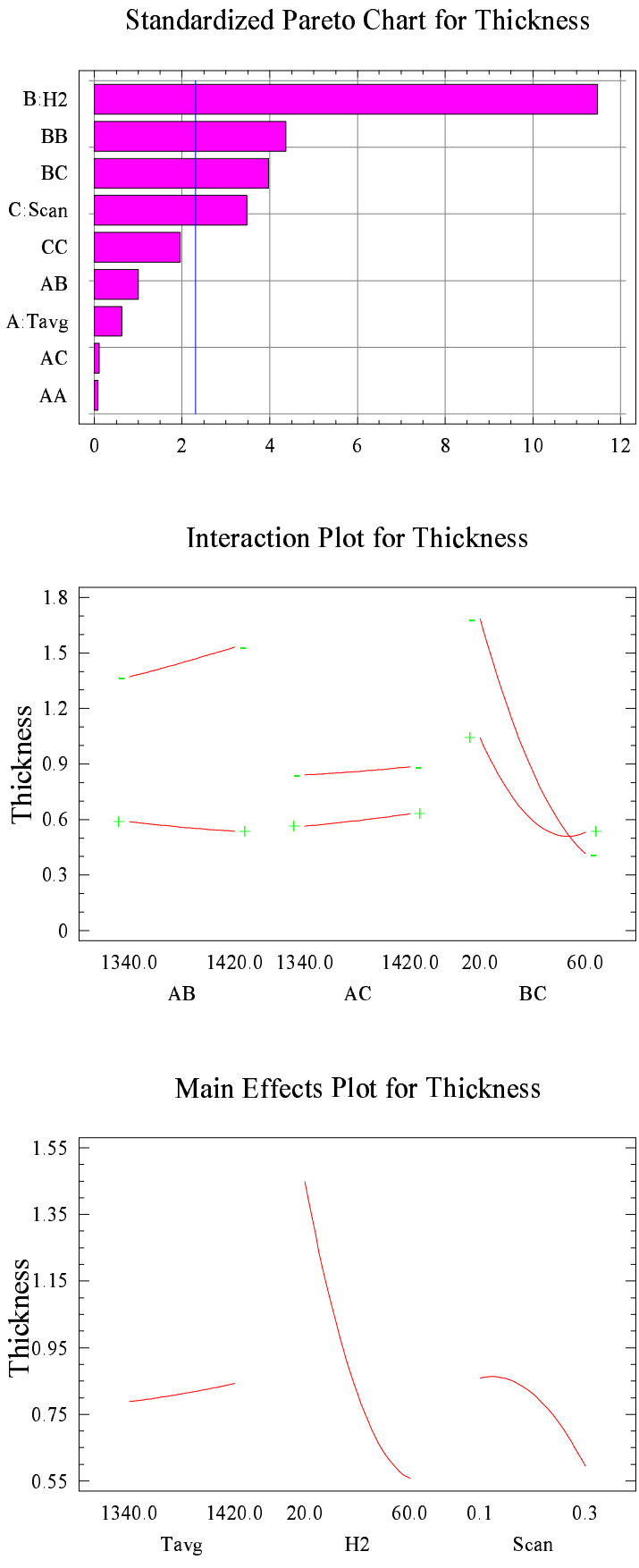

Figure 75: Analysis of surface response of thickness level.

6.2.3 Refined SiC Line deposition

Efforts were made to deposit SiC lines without the volcano effect using different processing conditions. The processing conditions, under which SiC lines without the volcano effect were deposited, are listed in Table 15. Figure 76 shows some of the SiC lines without a volcano effect.

As shown in Table 15, the deposition temperatures and the concentrations of MTS for lines without the volcano effect are relatively low. This confirms the hypothesized effect of deposition temperature that we mentioned in the surface response experiment above. The effect of MTS concentration on the volcano effect were consistent with the conclusion we got from the surface response experiment. The scan speeds in Table 15 are relatively lower than what we got from the surface response experiments, which is about 0.2 in/min. This is because when the deposition temperature is high, the speed of the laser movement is important for the formation of volcano shape. But when the deposition temperature is low, slow laser moving speed is beneficial for fabricating SiC lines having good shape.

Table 15: Processing conditions of LCVD-SiC lines without volcano effect.

Sample No.	*passes*	T_{avg} (^oC)	*Ls-SS (in/min)*	H_2/MTS
L437-2	2.5	1060.0	0.060	13.2
L437-4	5.5	1060.0	0.060	13.2
L437-5	2.5	1020.0	0.040	20.0
L437-6	5.5	1020.0	0.040	20.0
L437-7	2.5	1100.0	0.040	20.0
L437-8	5.5	1100.0	0.040	20.0
L437-9	2.5	1020.0	0.080	20.0
L437-10	5.5	1020.0	0.080	20.0
L437-11	2.5	1100.0	0.080	20.0
L437-12	5.5	1100.0	0.080	20.0
L437-13	2.5	1020.0	0.040	20.0
L437-14	2.5	1060.0	0.060	30.0

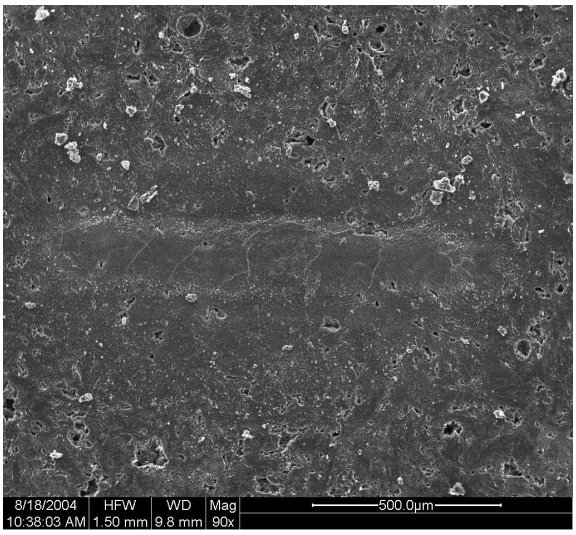

(a) L437-8 at 90x

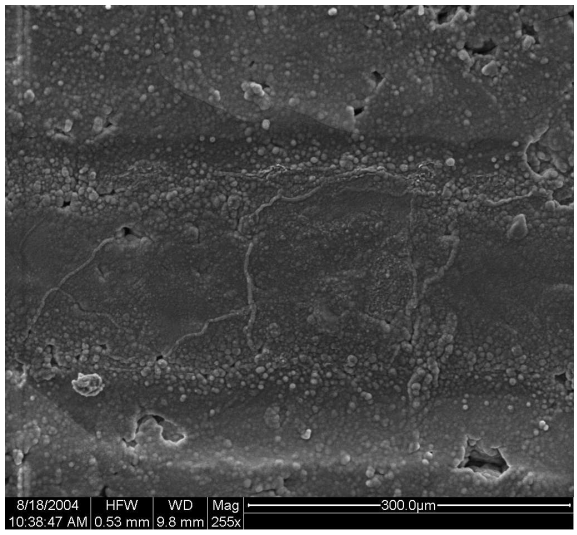

(b) L437-8 at 255x

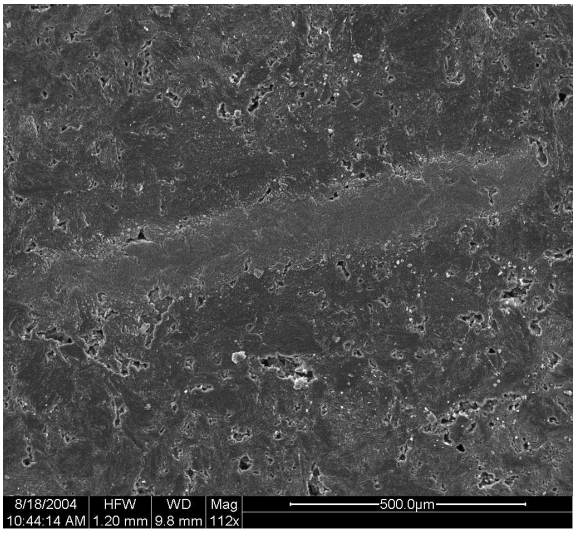

(c) L437-11 at 112x

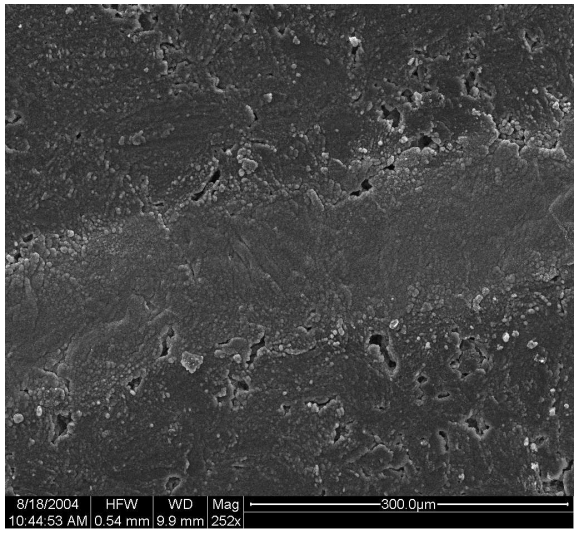

(d) L437-11 at 252x

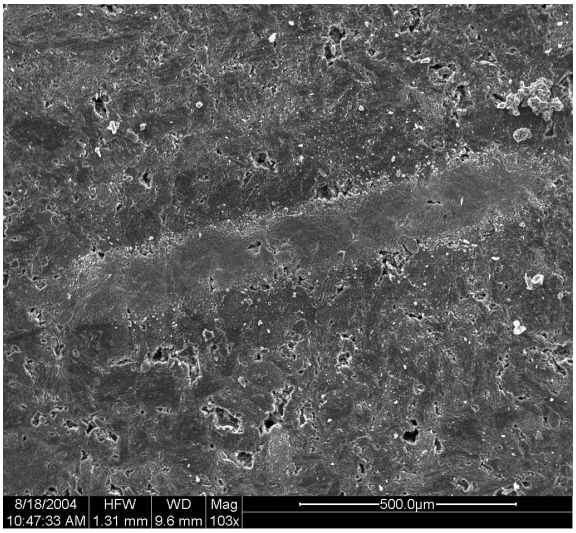

(e) L437-13 at 103x

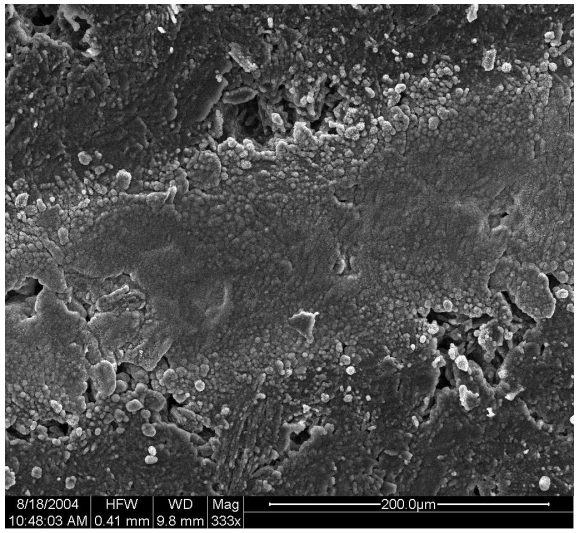

(f) L437-13 at 333x

Figure 76: SEM micrographs of SiC lines without volcano effect.

6.3 Characterization of Deposits

While examining the morphology of the one-layer lines, some interesting shaped crystal were observed to be present at the periphery area of some of the lines. Figure 77 displays the crystal features at the periphery of a one-layer line, which was deposited under 3 V laser power and at laser scan speed of 0.01 in/min. It is clear that the size and the shape of the crystals are different in different regions, as revealed in Figure 77. During the deposition process, the temperature of the different region are very different. Because the scan speed is very slow, the deposition process is very similar to a fiber deposition process. Temperature is the most influential factor for controlling the shape and size of the crystals.

In order to study the microstructure of deposited SiC lines, several lines were mounted in epoxy and then were grounded and polished to reveal their cross sections. The SEM technique was then applied. Figures 78 and 79 are the micrographs of the cross sections of two SiC lines, L416-5 and L418-6. Figures 78 (a) and 79 (a) are the entire cross section of the lines at lower magnification, and Figure 78 (b) and 79 (b) display small regions of those cross sections shown in Figures 78 (a) and 79 (a).

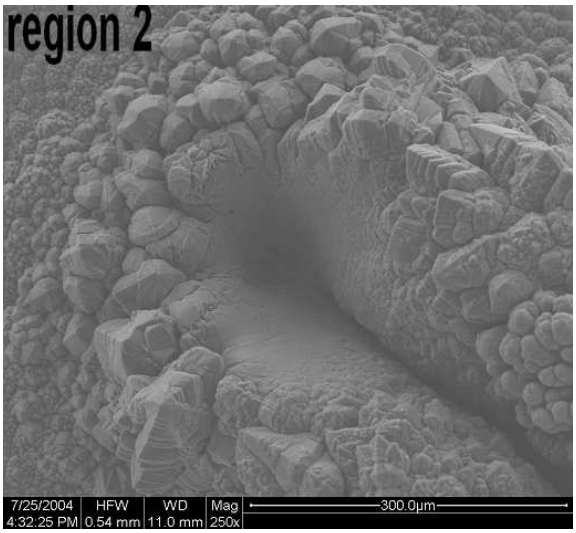

(a) region 1

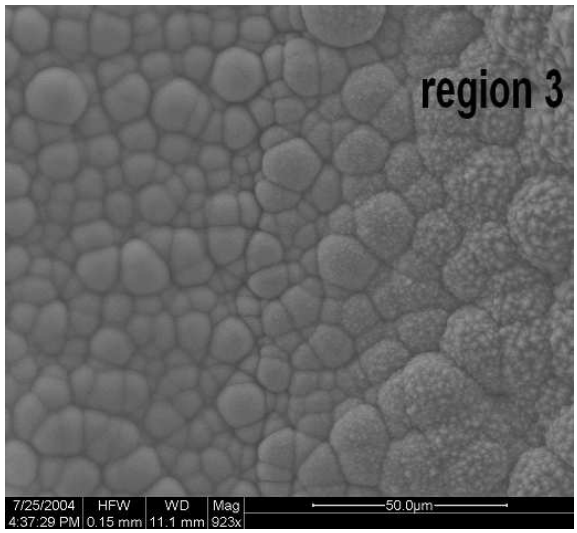

(b) region 2

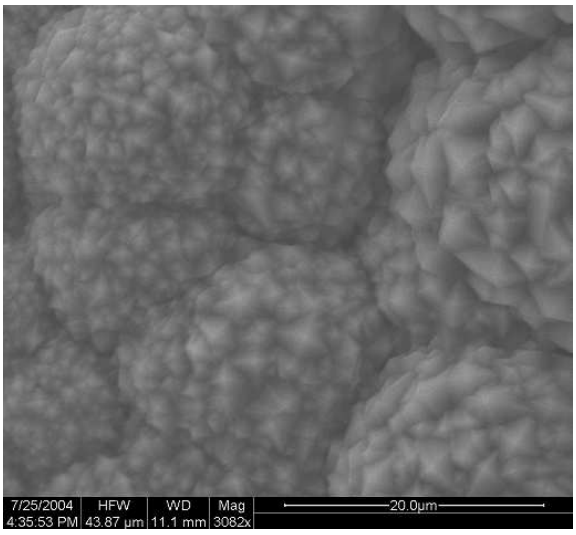

(c) region 3

Figure 77: SEM micrographs of the periphery area of one-layer line deposited with laser power of 3 V and scan speed of 0.01 in/min.

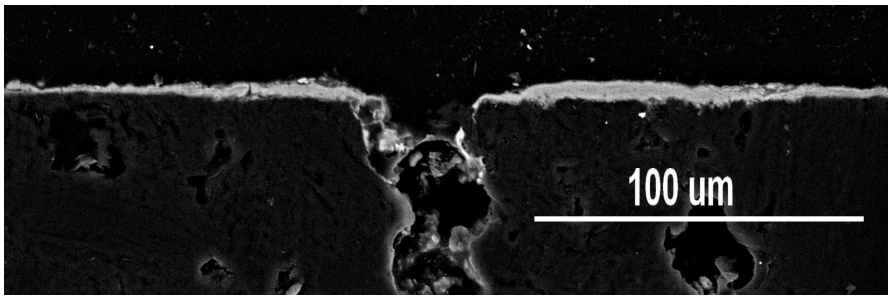

(a) 519x

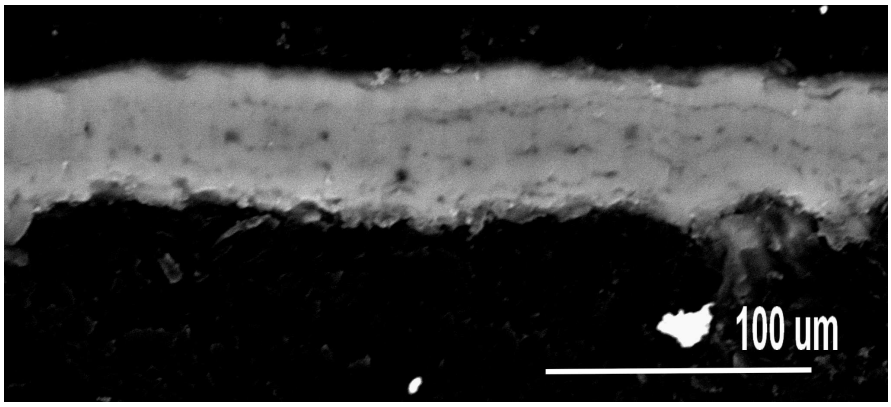

(b) 3964x

Figure 78: Back scattered SEM micrographs of cross section of SiC line, L416-5.

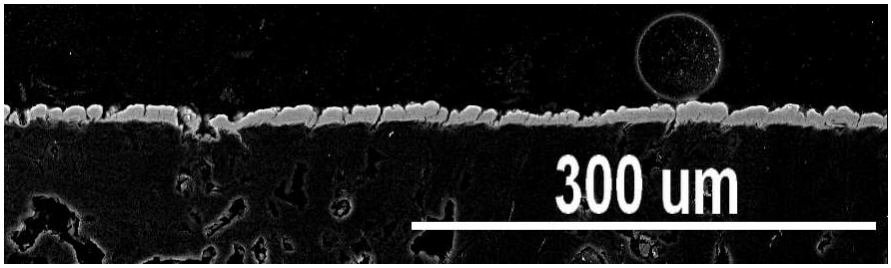

(a) 209x

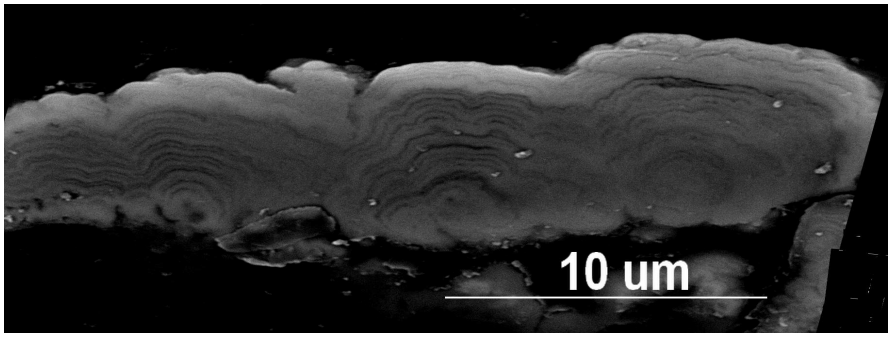

(b) 3696x

Figure 79: Back scattered SEM micrographs of cross section of SiC lines, L418-6.

L416-5 is a SiC line with a volcano effect. The volcano effect is very obvious, as shown in Figure 78 (a). L418-6 is a SiC line without any volcano effect. The thickness of the line was relatively constant, as shown in Figure 79 (a). The deposited lines are not as dense as SiC fibers. The layer interfaces are clearly seen in both Figure 78 (b) and 79 (b).

6.4 Summary of Line Deposition

In order to determine the initial deposition conditions for the first layer of SiC lines, a comprehensive set of one-layer lines was deposited and analyzed. It was shown that a laser power of 3 V together with scan speeds of 0.1 to 0.3 in/min are the good processing conditions that will generate relatively uniform first layers of a SiC line.

A surface response experiment of SiC lines was performed. Three processing factors with five different levels were considered in this study. Those three factors were deposition temperature, MTS concentration, and laser scan speed. It was indicated that high MTS concentration and medium scan speed minimize the formation of volcanos. Further experiments were performed to correct and confirm the conclusions of the surface response experiment. The SEM technique was applied to examine the microstructure of SiC lines. It

turned out that the material of SiC line is not as dense as that of SiC fibers. The interfaces of each layer are clearly seen by the aid of SEM.

CHAPTER VII

THERMAL RESIDUAL STRESS SIMULATION

The high temperature gradient within the deposits during the deposition process, which is introduced by the laser Gaussian energy profile, might induce high thermal stress and strain within the deposits. Some of the thermally induced stress could persist after cooling and thus affect the mechanical properties of the deposits. If the thermal stress is large enough, the deposits might be damaged and cracked. Considering the future applications of the deposits manufactured by LCVD, the thermal stress present within the deposits must be studied. The objectives of this study is to calculate the magnitude and locations of the stress during the deposition process and after cooling, as well as to understand how the stress changes with time during the deposition process and the cooling process.

With those objectives, a coupled thermal and structural model for LCVD SiC fiber deposition on graphite substrate was developed. The strategy to accomplish this is to simulate the temperature distributions of a SiC fiber at three heights, corresponding to three different time points during the deposition process. Then those temperature distributions for fibers with different heights were applied as body force loads to the structural models, which have the same geometry and meshing with those of the thermal model. Given the strain and stress free reference temperatures and boundary conditions, the thermal strain and stress within the fiber at different heights can be determined. After that, a uniform 300 K temperature load was applied to the structural model of the fiber in full length as the body force. This case represents the process of cooling the deposited fiber down to room temperature. Finally, the permanent thermal residual stresses present in the fiber were obtained.

7.1 Model Geometry and Meshing

The geometries and boundary conditions for the thermal analysis are shown in Figure 80. A SiC fiber was positioned coaxially on a substrate with a thickness of 2540 μm and a radius of 9525 μm. This configuration represents typical SiC fibers deposited using the LCVD technique. In order to study the thermal residual stress during the deposition process, three different heights of fibers, 14 μm, 49 μm, and 175 μm, are considered. Those three fibers with different heights represent three "snapshots" during the deposition process.

The thermal residual stress simulation is based on two assumptions. One is that the material is stress and strain free right after it is deposited. This means that the strain and stress free temperatures for the deposits are their deposition temperatures. The second assumption is that the deposition temperature for the entire fiber is constant in the longitudinal direction, which is reasonable because during the deposition process the deposition temperature is maintained constant all the time. Given those two assumptions, the strain free reference temperature in the structural model is radially location dependent. In order to specify different strain and stress free reference temperature at different radial location, the main body of the fiber was divided into eight separate parts. The dimensions of those eight parts are shown in Figure 81.

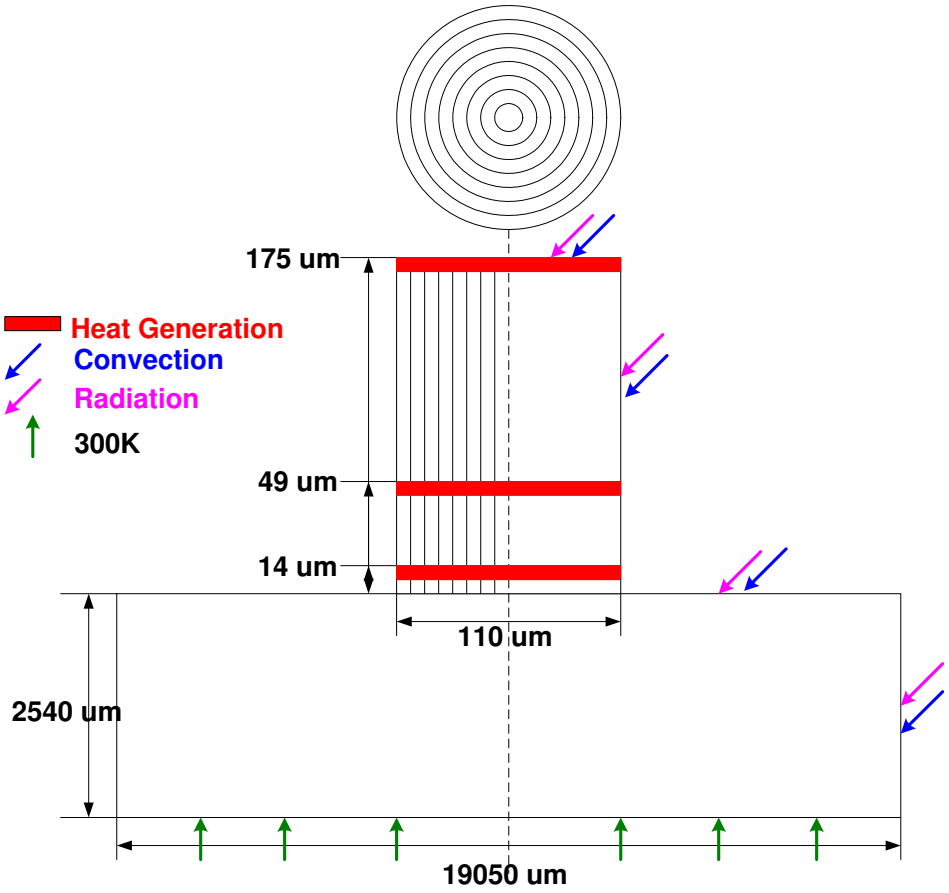

Figure 80: Geometries and boundary conditions used in the thermal analysis

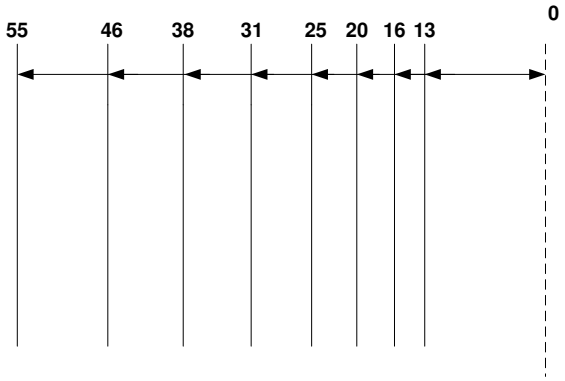

Figure 81: Dimensions of the eight separate parts of the main body of fiber.

Element types of PLANE77 and SOLID90 were used for the thermal analysis. PLANE77 is 2-D 8 nodes element with one degree of freedom, temperature, at each node. SOLID90 is 3-D 20 nodes element with one degree of freedom, temperature, at each node. PLANE82 and SOLID 95 were the element types that were used in the structural analysis. PLANE82 is 2-D 8 nodes element, having two degrees of freedom at each node: translations in the nodal x and y directions. It provides more accurate results for mixed (quadrilateral-triangular) automatic meshes and can tolerate irregular shapes without as much loss of accuracy. SOLID95 is 3-D 20 nodes element, having three degrees of freedom per node: translations in the nodal x, y, and z directions. It can tolerate irregular shapes without as much loss of accuracy.

Because of the sharp temperature gradient observed within the fiber, much finer mesh was applied to the fiber with a mapped meshing method. The substrate was free meshed with smart size of 4. Because the volumetric heat generation was applied to the top layer of the elements, to ensure that the total heat generation within the top layer elements equals the total energy provided by the laser, through some calculations, the element size in the longitudinal direction has to be 7 μm. In order to maintain the meshing consistency, which makes the overlaps of those three fibers have exactly the same meshes, therefore, all of the elements of the fiber have the fixed 7 μm size in the longitudinal direction. In the circular direction of the eight parts of the fibers, 32 elements were evenly specified, which makes finer mesh in the center of the fiber and the element size in the circular direction lower than 11 μm. The configuration of the number of elements is shown in Figure 82. The mesh of

the full fiber with 175 μm in height is shown in Figure 83.

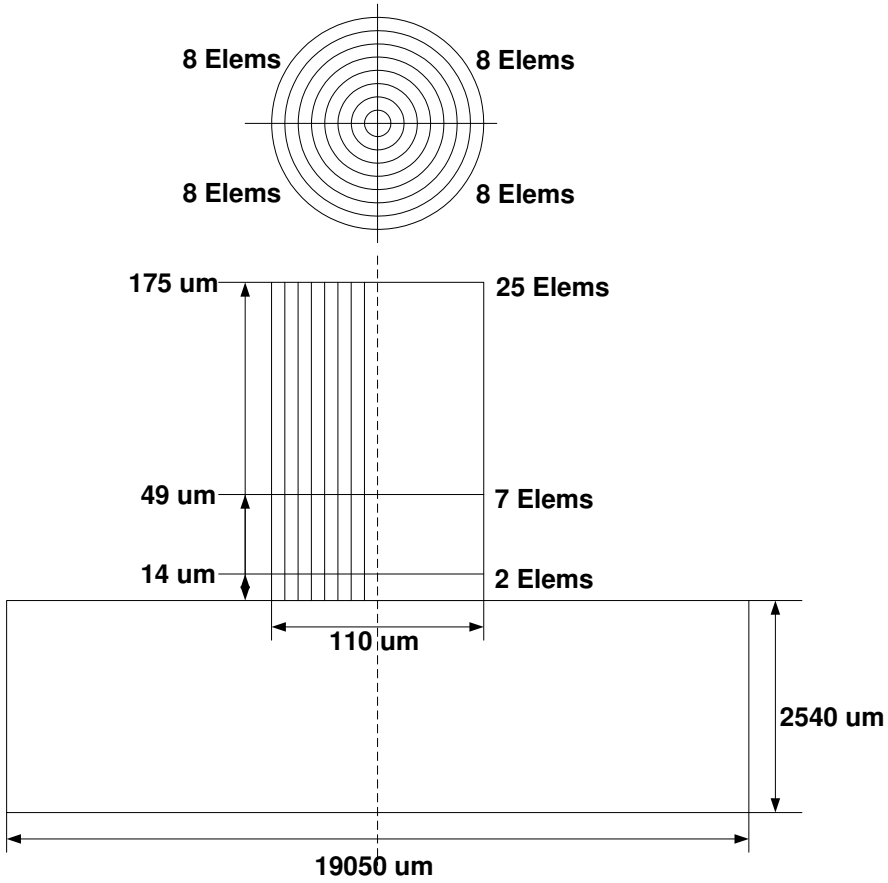

Figure 82: Element numbers specified for both the thermal and structural analysis.

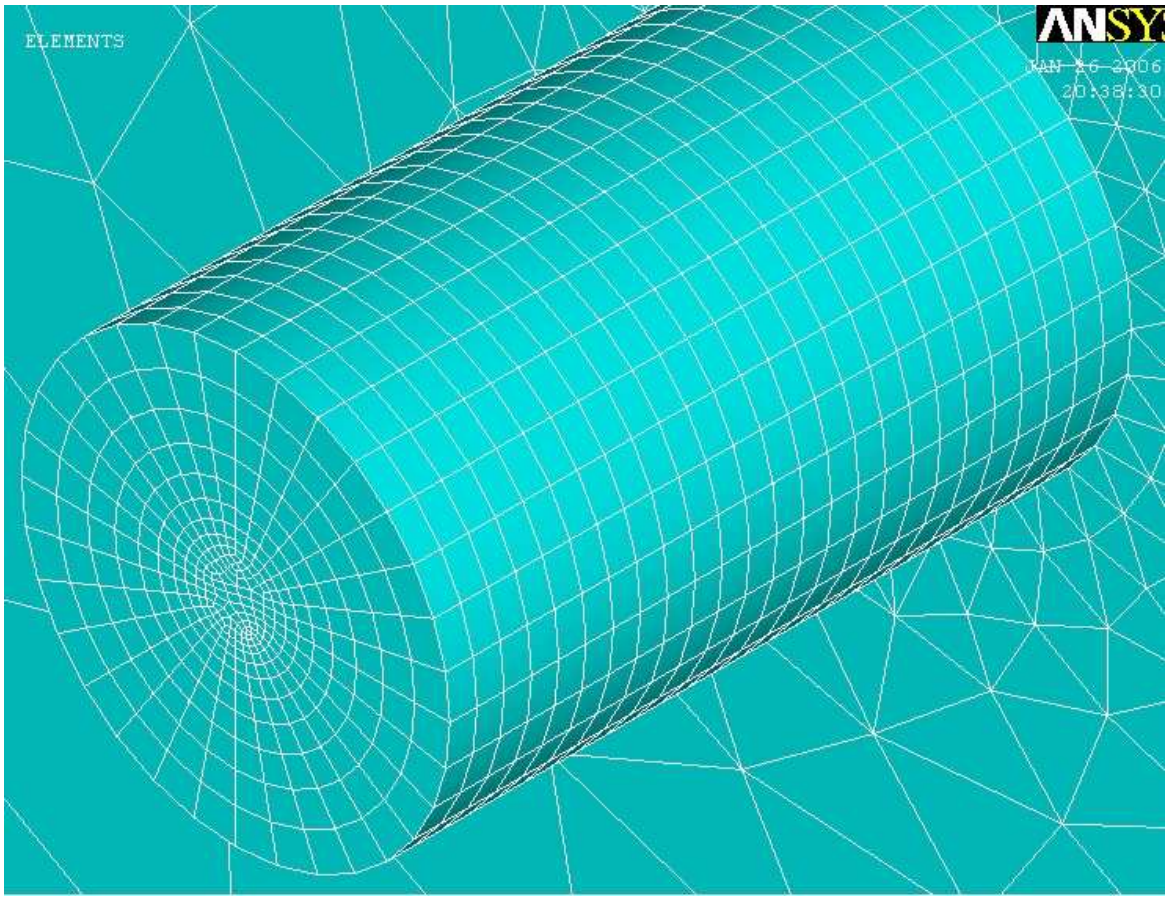

Figure 83: The mesh of the 175um fiber.

In order to ensure the solution is mesh independent, a mesh convergence check was performed. Due to requirements of the volumetric heat generation, the element size in the longitudinal direction has to be 7 μm. Therefore, only the element size in the circular direction is changed to do the mesh convergence check. Table 13 lists four cases of meshing and the results of maximum temperatures within the fibers. The temperatures are extremely stable for all of the four different cases, which is much below the typical 5% criteria for satisfactory mesh independence. Due to the high temperature gradients and stress gradients within the fiber, the highest resolution mesh was used for the thermal residual stress simulation.

Table 16: Thermal model mesh convergence check cases

Circular elements	*Maximum temperature (^oC)*	*Change from low resolution*
32	1423	0.07%
20	1424	0.07%
16	1423	0.07%
12	1424	0.07%

7.2 Material Properties

The material properties needed for the LCVD thermal analysis include density ρ, specific heat capacity C_p, thermal conductivity k, emissivity ϵ, and reflectivity $\rho_{10.59}$ of SiC fiber and graphite substrate. Among these, both C_p and k were defined as temperature dependent, and the rest of those were defined as a constant, independent of temperature. The material properties of the graphite substrate were those of ATJ graphite. The density is 1.76e-15 $kg/\mu m^3$, and the emissivity is 0.9. The density of SiC fiber is 3.2e-15 $kg/\mu m^3$, the emissivity of SiC is 0.85, [79] and the reflectivity of SiC, $\rho_{10.59}$, is defined to be 0.453 which is the average value of several data taken from different handbooks. [80] The temperature dependent properties of thermal conductivity and specific heat capacity of both materials are shown in Tables 14 and 15.

Table 17: Specific heat capacity and thermal conductivity of graphite substrate

T (K)	C_p *(pJ/Kg) [81]*	*T (K)*	*K (pW/μK) [82]*
273	8.29e+14	298.2	1.18e+8
366	9.965e+14	516.5	7.93e+7
478	1.177e+15	518.2	8.58e+7
589	1.331e+15	519.3	1e+8
700	1.47e+15	524.3	7.33e+7
811	1.583e+15	608.7	7.493e+7
922	1.675e+15	614.3	7.28e+7
1033	1.746e+15	836.5	5.13e+7
1144	1.792e+15	840.4	6.29e+7
1255	1.821e+15	856.5	5.05e+7
1366	1.826e+15	1133.7	3.03e+7
1477	1.846e+15	1142.1	3.29e+7
1676	1.913e+15	1147.6	2.94e+7
1694	2.052e+15	1157.1	4.04e+7
1839	2.052e+15	1159.8	3.95e+7
1868	2.014e+15	1260.9	3.55e+7
2103	2.056e+15	1272.1	3.3e+7
2232	2.056e+15	1580.4	3.94e+7
2278	1.901e+15	1583.2	4.1e+7
2555	2.1311e+15	1585.9	3.63e+7
2722	2.198e+15	1594.3	3.26e+7
2778	2.19e+15	1602.6	3.46e+7
3000	2.152e+15	1811	3.52e+7
		1813.7	3.45e+7
		1991.5	2.86e+7
		2091.5	1.76e+7
		2102.6	1.95e+7
		2108.2	2.52e+7
		2236	1.89e+7
		2238.7	2.02e+7
		2244.3	1.72e+7
		2247	2.03e+7
		2358.2	2.71e+7
		2369.3	2.03e+7
		2622	1.72e+7
		2641.5	1.6e+7
		2972.1	1.33e+7
		3002.6	1.23e+7

Table 18: Specific heat capacity and thermal conductivity of SiC fiber

T (K)	C_p *(pJ/Kg) [83]*	*T (K)*	*K (pW/μK) [84]*
286.2	6.402e+14	195	1.35e+8
296.36	6.615e+14	300	1.35e+8
298.15	6.674e+14	888.8	1.04e+8
300	6.729e+14	889.8	1.03e+8
400	8.789e+14	1130	6.7e+7
500	9.848e+14	1133.2	6.66e+7
600	1.052e+15	1388.7	3.95e+7
700	1.1e+15	1389.6	3.95e+7
800	1.138e+15	1414.6	3.6e+7
900	1.171e+15	1528.3	2.49e+7
1000	1.27e+15	1528.6	2.51e+7
1100	1.297e+15	1800	1.32e+7
1200	1.32e+15	1800.5	1.32e+7
1300	1.34e+15	1801.1	1.35e+7
1400	1.357e+15		
1500	1.371e+15		
1600	1.384e+15		
1700	1.395e+15		
1800	1.405e+15		
1900	1.414e+15		
2000	1.422e+15		
2100	1.429e+15		
2200	1.436e+15		
2300	1.442e+15		
2400	1.447e+15		
2500	1.452e+15		
2600	1.457e+15		
2700	1.461e+15		
2800	1.465e+15		
2900	1.469e+15		

The material properties needed for the structural model are Youngs modulus E, coefficient of thermal expansion CTE or α, and Poisson's ratio r. Those properties of the graphite substrate are defined as constant for the structural model. The Youngs modulus of graphite is reported between 1.4 to 34.5 GPa, the value of CTE is reported as 0.1 - 19.4e-6 $1/K$, and the Poisson's ratio is reported ranging from 0.07 to 0.22. [79] Values used in the structural model is taken as some median values in those ranges, where 20 GPa for Youngs modulus, 10e-6 $1/K$ for CTE, and 0.2 is the Poisson's ratio. The Poisson's ratio for the SiC fiber is a constant value throughout the simulation, which is 0.19. [79] The remainder of the

Table 19: Youngs modulus and coefficient of thermal expansion of SiC fiber

T (K)	*E (MPa) [85]*	*T (K)*	*α (1/K) [86]*
273	4.8e+5	293	3.3e-6
297	4.2e+5	300	3.4e-6
1210	3.7e+5	400	4.0e-6
1490	3.4e+5	500	4.2e-6
1670	2.7e+5	600	4.5e-6
		700	4.7e-6
		800	4.9e-6
		900	5.1e-6
		1000	5.3e-6
		1200	5.6e-6
		1400	6.0e-6
		1600	6.2e-6
		1800	6.5e-6
		2000	6.7e-6
		2200	6.9e-6
		2400	7.0e-6
		2600	7.1e-6
		2800	7.1e-6

material properties for the SiC fiber were specified as temperature dependent, as shown in Table 16.

7.3 Thermal Model

7.3.1 Boundary Conditions

The boundary conditions applied in the thermal analysis were shown in Figure 80. Heat convection and radiation were applied to all of the outer surfaces except the bottom one of the graphite substrate. Instead, the bottom surface of the substrate was constrained to 300 K all the time, which represents the cooling effects of the sample holder and the stage shaft. Because ANSYS prohibits applying heat flux and heat convection on the same surface, in order to specify the energy input from the CO_2 laser, the volumetric heat generation is applied on the top surface of the fiber instead, shown as the small red rectangle in Figure 80.

The governing equation for the thermal model was the general form of the heat conduction equation, shown in equation (15), where t is time, ρ is density, h is specific enthalpy, $\overrightarrow{\nu}$ is the velocity of the solid if moving, k is the thermal conductivity, T is the temperature,

and S_h is volumetric heat generation rate. For the steady state case, the time dependent term on the left side of Equation (15) does not apply. The model geometry was stationary, which eliminates the second term on the left hand side of the Equation (15). The remaining governing equation includes the conductivity term represented by the first term on the right and the volumetric heat generation represented by S_h. For transient analysis, the first term on the left will apply in addition to the terms included in the steady state.

$$\frac{\partial}{\partial t}(\rho h) + \nabla \cdot (\overrightarrow{\nu}\rho h) = \nabla \cdot (k\nabla T) + S_h \tag{17}$$

The laser energy input is simulated as a volumetric heat generation specified in the thin top layer elements within the radius of the laser beam. The equation used to calculate the necessary heat generation value within each element is shown in Equation (16), where P_0 is the norminal laser power, $\rho_{10.59}$ is the reflectivity of SiC fiber at the laser wavelength of 10.59 μm, R_0 is the radius of the laser beam, d is the thickness of the mesh element, and r is the radial distance from the center of the laser spot. The method for applying the volumetric heat generation rate to the top surface of the SiC fiber is to define a function which is exactly in the format of Equation (16) in GUI of ANSYS, then load and apply this function as a tabular boundary condition in the ANSYS environment, after that, simply copy and paste the corresponding text files of those operations into the final text files. Figure 84 shows the contour of the heat generation rate specified as a function boundary condition on the top layer of elements of SiC fiber.

$$P(r) = \frac{2P_0(1-\rho_{10.59})}{\pi {R_0}^2 d} exp(\frac{-2r^2}{{R_0}^2}) \tag{18}$$

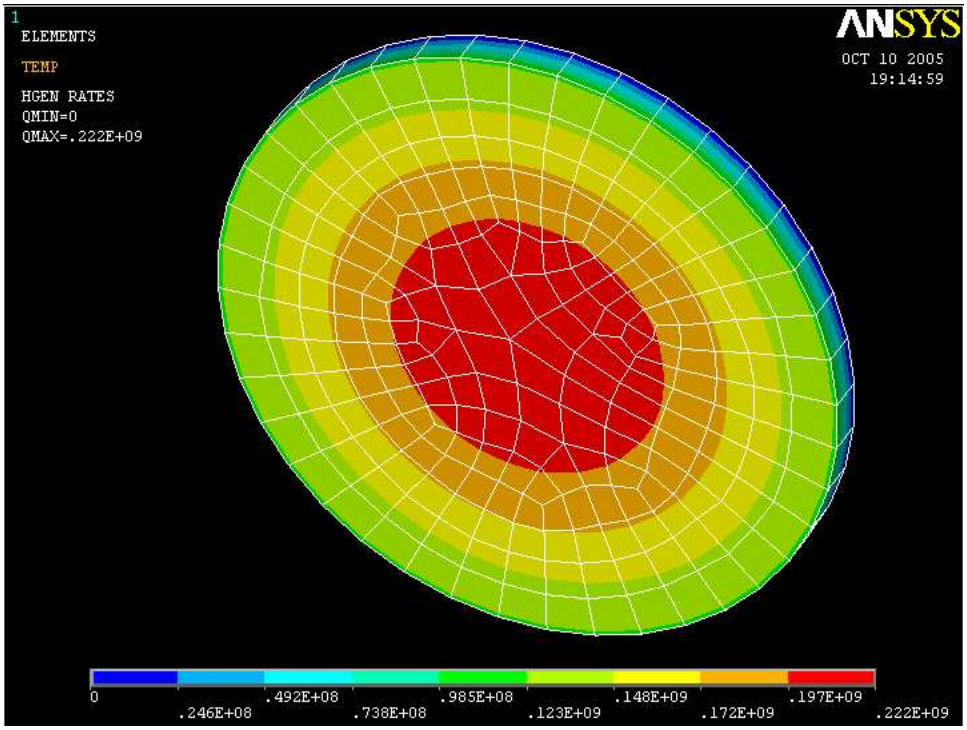

Figure 84: The heat generation rate applied in the thermal model within the top layer element of the fiber.

Convective heat transfer was applied on all of the outer surfaces of the model except the bottom surface of the substrate, which always perfectly sits on the sample holder inside the reaction chamber. Because there is no fluid motion involved, only natural convection is considered. The heat convection boundary condition is given by Newton's law of cooling, as shown in Equation (17), where q'' is the local heat flux, h is the local convection coefficient, T_s is the temperature of the boundary surface, and T_∞ is the free stream temperature of the fluid. The total heat transfer rate is obtained by integrating Equation (17) over the entire outer surface. Assuming isothermal conditions, the total heat transfer can be written as Equation (18), where $\overline{h}$ is the average convection coefficient over the surface, and A_s is the area of the surface. For all of the cases, T_∞ is specified to be 300 K.

$$q'' = h(T_s - T_\infty) \tag{19}$$

$$q = \overline{h} A_s (T_s - T_\infty) \tag{20}$$

Values of $\overline{h}$ for the boundary surfaces were computed using empirical correlations for external free convection flow. For the vertical surface of the fiber, the equations used for Nusselt number were shown as Equations (19)-(24), [87] where L is the length of the fiber, D is the diameter of the fiber, g is the gravity accelerator, β is the volume coefficient of expansion, $\triangle T$ is the difference between T_s and T_∞ , ν is the kinematic viscosity, and α is the thermal diffusivity. The average convection coefficient, h_{V-F}, was related to the Nusselt number by Equation (24), where k is the thermal conductivity of the fiber material. All of the material properties required to calculate the average convection coefficient, h_{V-F}, were chosen to be the values at a temperature of T_f, which is the average of T_s and T_∞ .

$$Nu_c = \frac{1.8L/D}{ln\{1 + 1.8/[\overline{C_l}(Ra^*)^{1/4}]\}} \tag{21}$$

$$\overline{C_l} = \frac{4}{3}C_l \tag{22}$$

$$C_l = \frac{0.503}{[1 + (0.492/P_r)^{9/16}]^{4/9}} \tag{23}$$

$$P_r = \nu/2 \tag{24}$$

$$Ra^* = \frac{g\beta\triangle TD^4}{\nu\alpha L} \tag{25}$$

$$Nu_c = \frac{\overline{h}_{V-F}L}{l} \tag{26}$$

Similarly, for the vertical surface of the substrate, Equations (25) - (30) [87] were used to calculate the average convection coefficient, h_{V-S}.

$$Nu_c = \frac{0.9\xi N\mu_p}{ln(1 + 0.9\xi)} \tag{27}$$

$$\xi = \frac{2L/D}{{Nu_p}^T} \tag{28}$$

$$Nu_p{}^T = \overline{C}_l Ra^{1/4} \tag{29}$$

$$Nu_p = \frac{2.8}{ln(1 + 2.8/Nu^T)} \tag{30}$$

$$Ra = \frac{g\beta \triangle T L^3}{\alpha\nu} \tag{31}$$

$$Nu_c = \frac{\overline{h}_{V-S}}{k} \tag{32}$$

For the horizontal top surfaces of the fiber and substrate, the average convention coefficients were calculated using Equations (31) - (35) [88] as shown below. All of the calculated convection coefficients for boundary surfaces are shown in Table 17 below, where h_{V-F} and h_{T-F} are those for the vertical and horizontal top surfaces of the SiC fiber, and h_{V-S} and h_{T-S} are those for the vertical and horizontal top surfaces of the graphite substrate, respectively.

$$Nu^T = 0.835\overline{C}_l Ra^{1/4} \tag{33}$$

$$Nu_l = \frac{1.4}{ln(1 + 1.4/Nu^T)} \tag{34}$$

$$Nu_t = C_t{}^H Ra^{1/3} \tag{35}$$

$$Nu = [(Nu_l)^m + (Nu_t)^m]^{1/m}, m = 10 \tag{36}$$

$$Nu = \frac{\overline{h}_T L}{k} \tag{37}$$

Table 20: Average convection coefficients for boundary surfaces

T_s (K)	T_∞ (K)	T_f (K)	h_{V-F}	h_{T-F}	h_{V-S}	h_{T-S}
301	300	300.5	682.7	1778.85	115.83	33.76
400	300	350	975.78	2437.64	163.79	66.53
500	300	400	1088.38	2715.56	183.08	74.88
600	300	450	1179.88	2948.22	197.97	80.30
700	300	500	1254.99	3142.95	209.82	84.02
800	300	550	1326.61	3330.36	221.02	87.23
900	300	600	1399.73	3522.82	232.44	90.33
1000	300	650	1390.83	3508.02	230.40	88.30
1100	300	700	1528.64	3865.21	252.63	95.26
1200	300	750	1532.99	3883.71	252.98	94.14
1300	300	800	1649.70	4188.66	271.89	99.62
1400	300	850	1671.19	4250.58	275.24	99.59
1500	300	900	1760.99	4487.25	289.91	103.47
1600	300	950	1806.37	4610.60	297.36	104.78
1700	300	1000	1877.83	4800.84	309.19	107.57
1800	300	1050	1939.10	4964.99	319.44	109.79
1900	300	1100	2008.38	5150.39	331.11	112.35
2000	300	1150	2069.75	5314.59	341.54	114.65

For all of the thermal analysis cases, nonlinear radiation was considered. The radiation boundary condition was accomplished using the radiosity solver in ANSYS environment, which calculated the radiation heat transfer between the boundary surfaces and the free surface using Equation (36), where q'' is heat flux, ϵ is the average hemispherical emissivity over the entire spectral range, σ is the Stefan-Boltzman constant, T_s is the radiating surface temperature, and T_{ref} is the temperature of the remote surface. T_{ref} was assigned to be 300 K for all of the analyses to simulate the radiation effects of the inner surface of the reaction chamber. Also the bottom surface of the graphite substrate was always constrained to be 300 K for all of the cases, which is used to simulate the heat conduction away from the substrate to the cold sample holder and the shaft of the stages.

$$q'' = \epsilon\sigma({T_s}^4 - {T_{ref}}^4) \tag{38}$$

7.3.2 Solutions

The internal scripting language, APDL, of ANSYS was used to perform the entire thermal simulations, where a single text file accomplished the building geometry, defining material

properties, meshing the entire model, applying boundary conditions and loads, executing the calculations, and controlling results output. For reference, the APDL codes for the thermal analysis were listed in Appendix E.

The thermal analysis was run using a typical SiC fiber deposition conditions, i.e., the height and diameter of the fiber is 175 μm and 55 μm, respectively, and the maximum deposition temperatures at different time points is maintained constant at 1150 ^oC, all of which are similar to the real SiC fiber deposition process.

The nodal temperature data within the fiber at three different time points are shown in Figure 85. Figure 85 (a) is the temperatures within the fiber at the time point 1 (t_1) when the fiber has grown to 14 μm high. Figure 85 (b) is the temperatures within the fiber at the time point 2 (t_2) when the fiber is 49 μm high. Figure 85 (c) is the temperatures within the fiber at the time point 3 (t_3) when the fiber has grown to the full 175 μm high. Those temperature data were exported for later use as body force loads of the structural models.

The temperature distribution for all of the three time points are reasonable with high temperature at the center and lower temperatures at the edge of the fiber. The temperatures are symmetric about the axis of the fiber as we observed during the experiment. And the temperatures of most of the region of the substrate are 300 K, except the region directly underneath the fiber, which has relatively high temperature compared to the rest of the substrate.

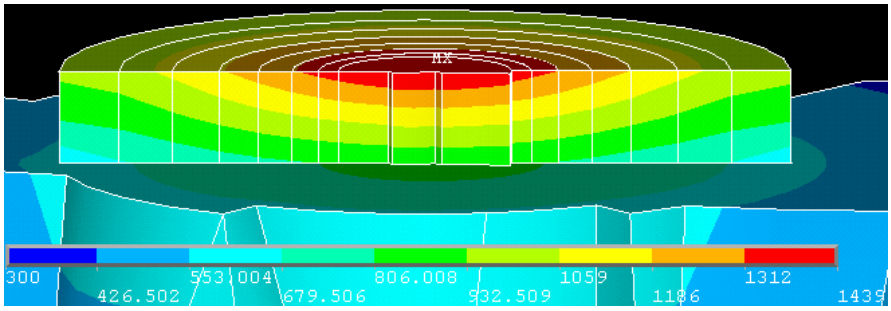

(a) t_1

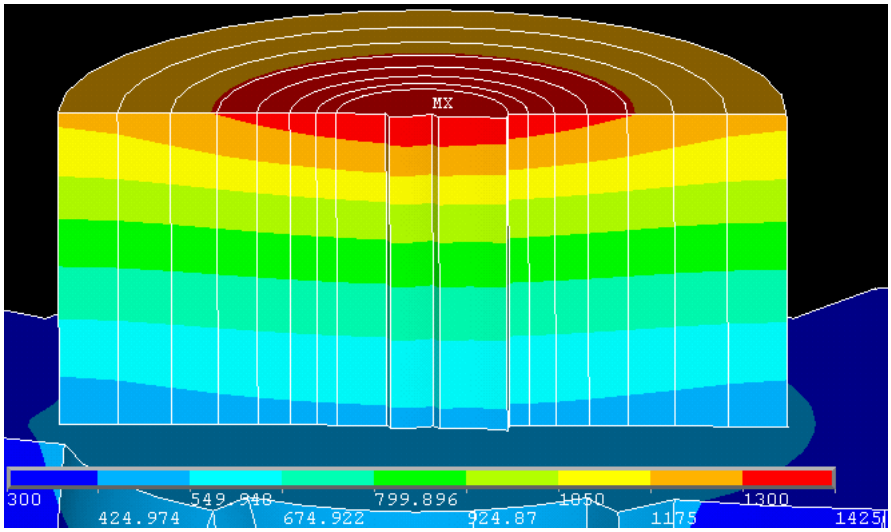

(b) t_2

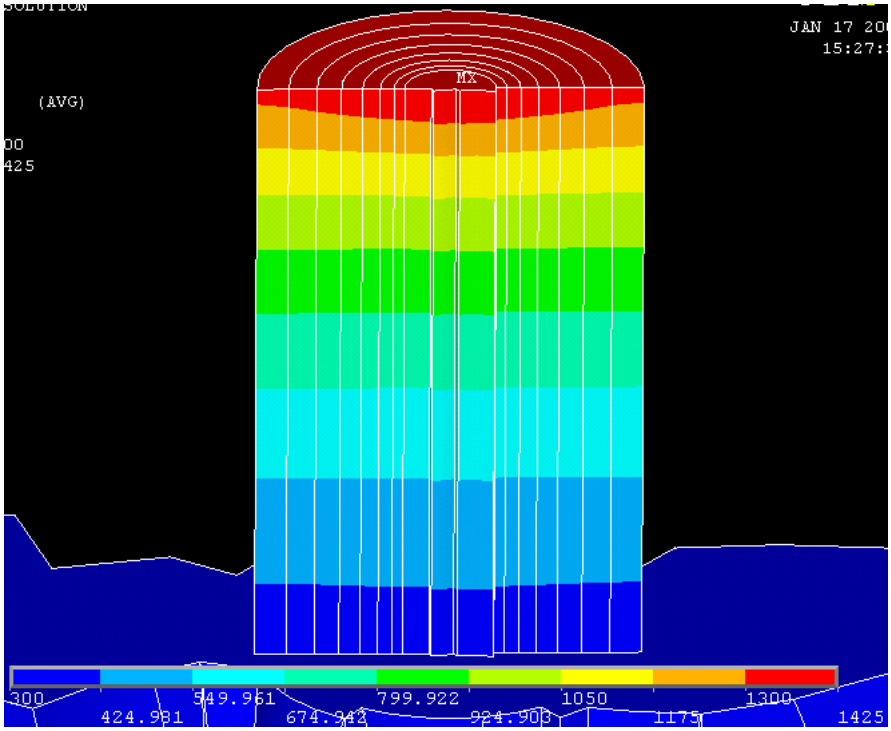

(c) t_3

Figure 85: Temperature (K) distributions within the fiber at three different time points.

The temperatures of different locations at different time points are plotted in Figure 86. Time point 4 t_4 simply represents that the fiber is cooling down to the uniform room temperature, 300 K. Figure 86 (a) is the temperatures for the line from the center of the fiber to the edge at the interface between the fiber and the substrate, representing by h = 0 μm where h is the height of the line from the top surface of the substrate. Figure 86 (b), (c), and (d) are for the lines from the center of the fiber to the edge of the fiber at heights of 14 μm, 49 μm, and 175 μm, respectively.

As shown in Figure 86, right after the deposits are finished, the temperatures vary radially, higher in the center and lower at the edge of the fiber. As the deposition process continues, the temperatures of previously deposited material decrease with time as more material is deposited on this initial layer and finally it will be cooled down to the uniform room temperature. It was indicated by both Figures 85 and 86 that the temperature gradients in the radial directions right after the material is deposited are very high. The value is around 8 $^oC/\mu m$. While in the longitudinal direction, the situation is even worse, where the temperature gradient is as high as 43 $^oC/\mu m$, as shown in Figure 86. With those high temperature gradients present in the deposits, it is obvious that thermal residual stress will be generated.

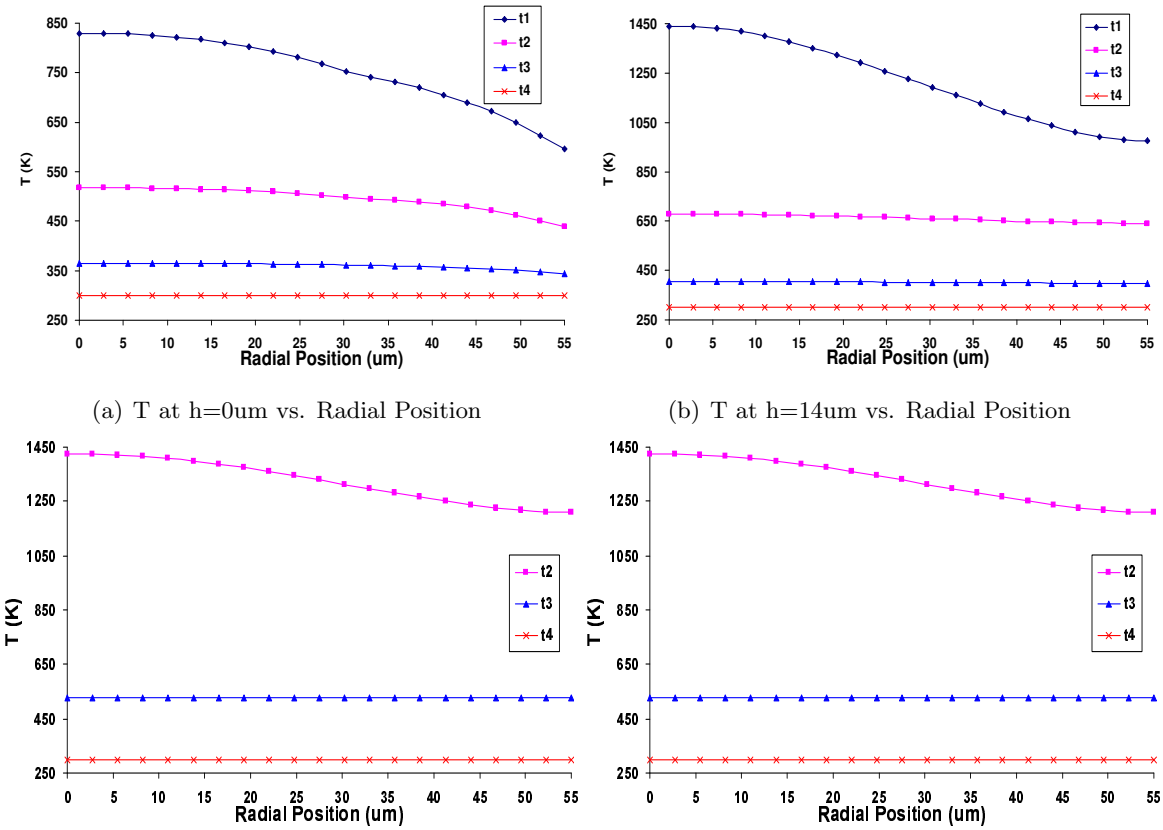

(a) T at h=0um vs. Radial Position

(b) T at h=14um vs. Radial Position

(c) T at h=49um vs. Radial Position

(d) T at h=175um vs. Radial Position

Figure 86: Temperature (K) distributions from the center to the edge of the fiber at four different heights at four time points.

7.4 Structural Model

The structural analysis has the same geometries as those of the thermal model. Four sets of temperature distributions are applied as the body force to the structural model with different heights of fibers. The first three temperature loads are those obtained from the thermal analysis, as shown in Figure 85, and the last one is just a uniform room temperature, 300 K. Those first three sets of temperature distributions are applied to the model with fiber heights of 14 μm, 49 μm, and 175 μm, respectively, which are aimed to determine the thermal residual stress within the fiber due to the temperature change at three different time points during the deposition process. The last uniform room temperature load is applied as the body force load to the structural model to calculate how much thermal residual stress will remain in the fiber after the entire geometry is cooled down to uniform room temperature.

7.4.1 Boundary Conditions

The governing equation of the relationship of stress and strain for the thermal residual stress simulation is shown in Equation 37, where $\overline{\sigma}$ is the stress vector, D is the stiffness matrix or stress-strain matrix, $\overline{\epsilon}$ is the total strain vector, and $\overline{\epsilon}^{th}$ is the thermal strain vector. The thermal strain vector is defined as Equation 38, where the $\alpha' s$ are the coefficient of thermal expansion in x, y, and z directions, T is the current temperature at the point in question, and T_{ref} is the strain-free reference temperature.

$$\overline{\sigma} = D(\overline{\epsilon} - \overline{\epsilon}^{th}) \tag{39}$$

$$\overline{\epsilon}^{th} = \triangle T[\alpha_x, \alpha_y, \alpha_z, 0, 0, 0,]^T, \triangle T = T - T_{ref} \tag{40}$$

During the stress calculation process, zero displacement boundary condition was imposed on the bottom surface of the substrate to simulate the situation that the substrate is fixed to the sample holder during the deposition process. The rest of the geometries in the structural model are set free to move, which is similar to the real case.

7.4.2 Strain Free Reference Temperatures

Since we assumed that the strain-free reference temperature is the actual deposition temperature, and the deposition temperature in the longitudinal direction is constant, therefore the way we determine the strain - free reference temperatures is to average the surface temperatures on each top surface of those eight separate parts of the fiber right after the top surface is deposited. The deposition temperatures for the eight parts are shown in Figure 87. Actually this is the temperatures of the top surface of the fiber when the 49 μm portion has just been finished. The final strain - free reference temperatures for those eight parts are listed in Table 18.

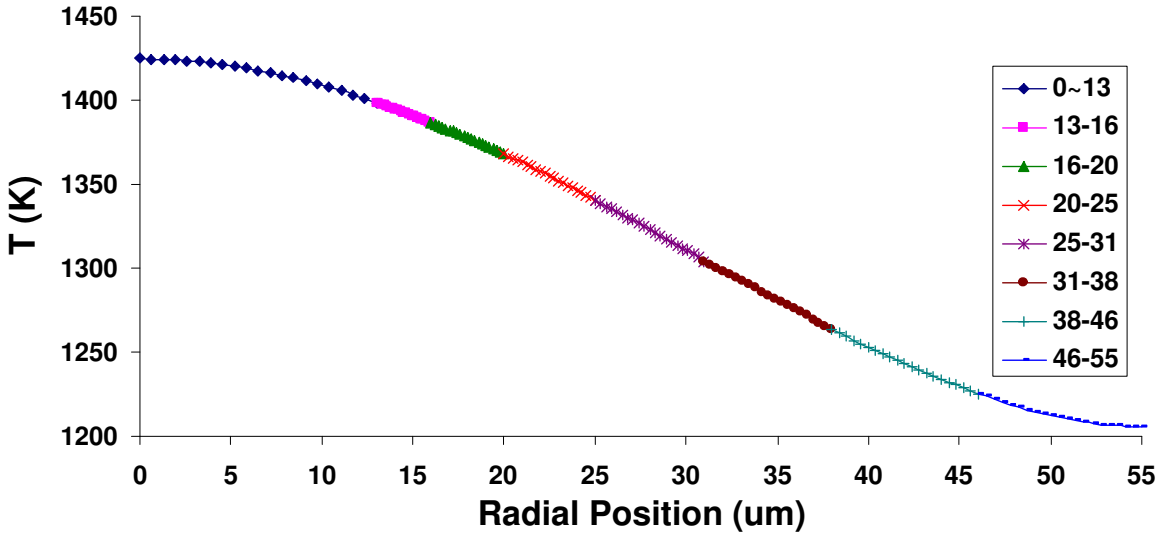

Figure 87: The deposition temperatures (K) along the radial direction.

Table 21: The reference temperatures for different portions

Portion (μm)	0-13	13-16	16-20	20-25	25-31	31-38	38-46	46-55
Ref.T (K)	1343	1334	1328	1319	1307	1292	1276	1263

7.4.3 Solutions

Similarly to the thermal analysis, the APDL code of ANSYS was used to accomplish the whole stress simulation. The codes for the stress simulation files are listed in Appendix F.

Because SiC is a brittle material, the most critical stress that may cause cracks or fracture is the first principal stress. Figure 88 is the distribution of the first principal stress of the fiber at the four time points. The maximum principal stress for the fiber at the four time points are listed in Table 19. It was indicated by Figure 88 that the first principal stress has similar distribution during the deposition process and cooling process. The first principal stress keeps increasing during the deposition process and gets released a little during the cooling process to room temperature, as shown in Table 19.

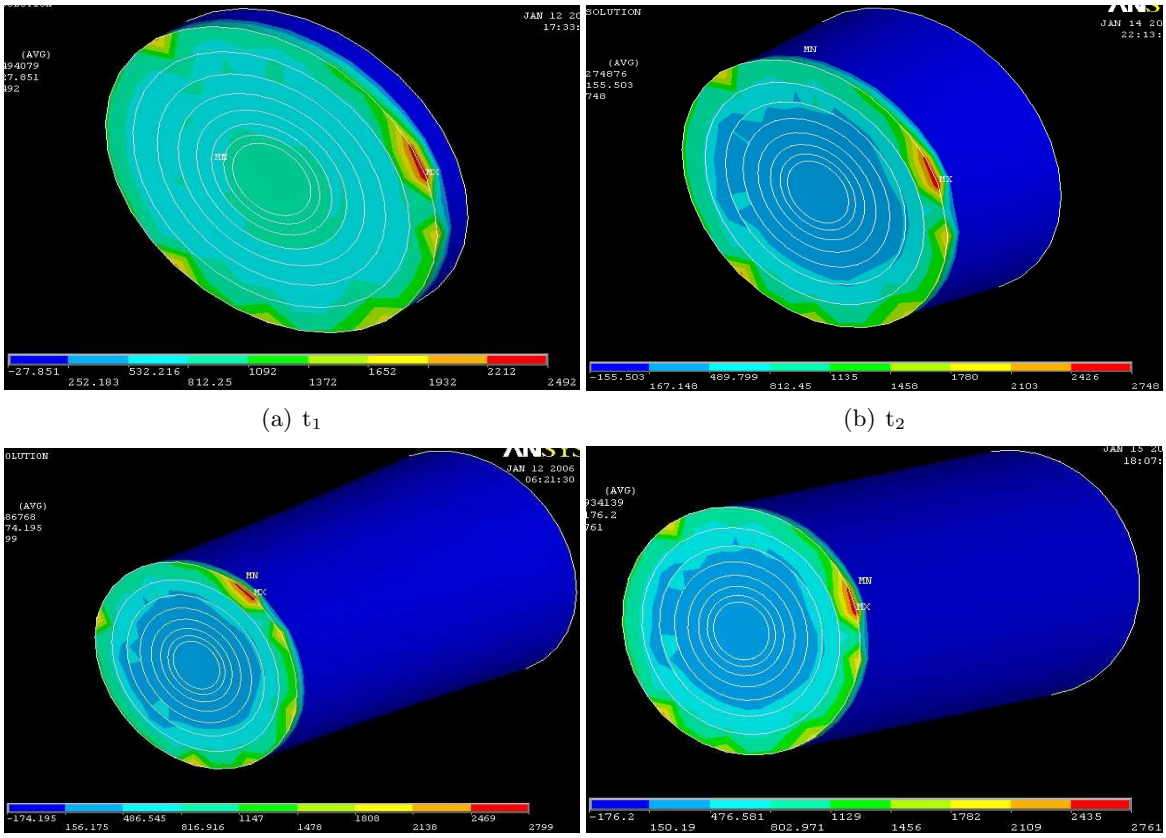

(a) t_1 (b) t_2

(c) t_3 (d) t_4

Figure 88: The first principal stress (MPa) of the fiber at four time points.

Table 22: The maximum principal stresses of the fiber at four time points in MPa

Time	σ_1	σ_2	σ_3
t_1 *(h=14μm)*	2492	1160	-541
t_2 *(h=49μm)*	2748	656	-868
t_3 *(h=175μm)*	2799	600	-968
t_1^* *(h=175μm)*	2761	576	-720

* Fiber is cooled to RT (300 K)

In addition, the value of the first principal stress during both the deposition process and the cooling process is much higher than the reported rupture strength of SiC, which is 1 GPa. [79] But this is not sufficient to conclude that the fiber will experience damage. One reason is that this critical first principal stress on the bottom edge of the fiber might be caused by some calculation error, i.e., singular points in the entire model, which could be due to the unsymmetric meshing or the sharp corner at the interface of the fiber and the substrate. A 2-D axisymmetric simulation was generated to check the effects of the unsymmetric meshing on the thermal residual stresses. This model will be presented later in this chapter. Even the high thermal residual stress value is reasonable, the critical principal stress is just always present on a small region near the bottom edge of the fiber. What about the stresses inside the main body of the fiber? Will the main body of the fiber be damaged by the thermal stress?

7.4.3.1 Stress without the bottom 7 μm layer

By cutting off the bottom 7 μm layer, the distribution of the first principal stress at the four time points and the way that the first principal stress changes with time are shown in Figure 89. The maximum principal stresses within the main body at four time points are listed in Table 20. It was indicated by Figure 89 that the first principal stress at the four time points is much lower than the rupture strength of the SiC material, which means that the main body of the fiber will not be damaged either during the deposition process or the cooling process according to our calculations. This was verified by examining the cross section of LCVD-SiC fibers deposited at similar conditions as the model used. It turned out the cross sections show high dense and integrity without any cracks being detected by the SEM technique, as shown in Figure 90.

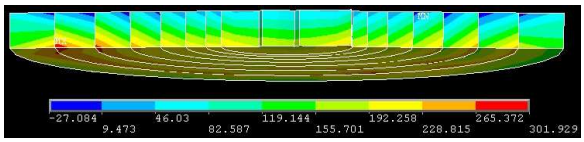

(a) t_1

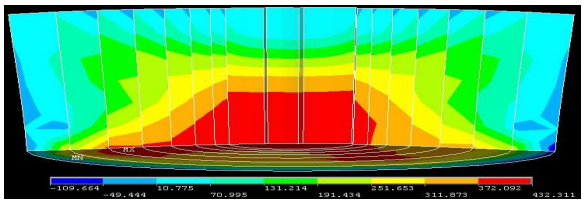

(b) t_2

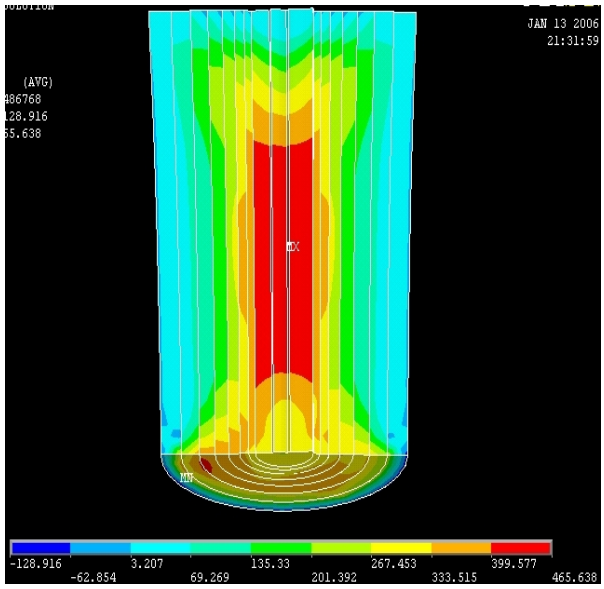

(c) t_3

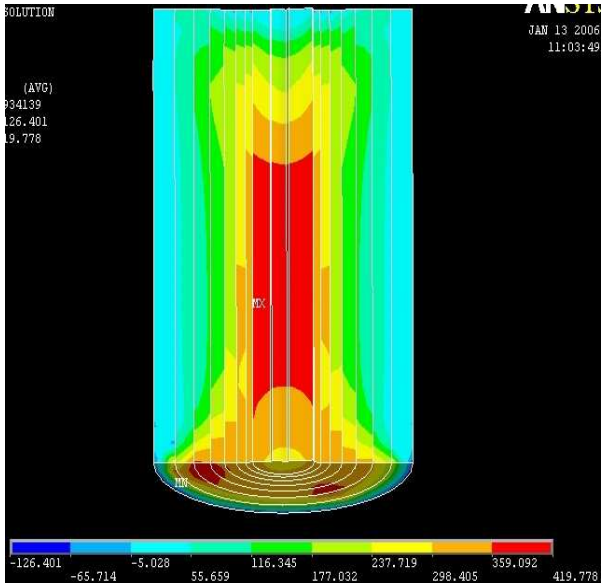

(d) t_4

Figure 89: The first principal stress (MPa) of the fiber without the bottom 7 μm layer at four different time points.

Table 23: The maximum principal stresses of the fiber without the bottom 7 μm layer at four time points in MPa

Time	σ_1	σ_2	σ_3
t_1 *(h=14μm*	321	230	-493
t_2 *(h=49μm*	456	393	-685
t_3 *(h=175μm*	465	293	-578
t_1^* *(h=175μm*	427	299	-548

* Fiber is cooled to RT (300 K)

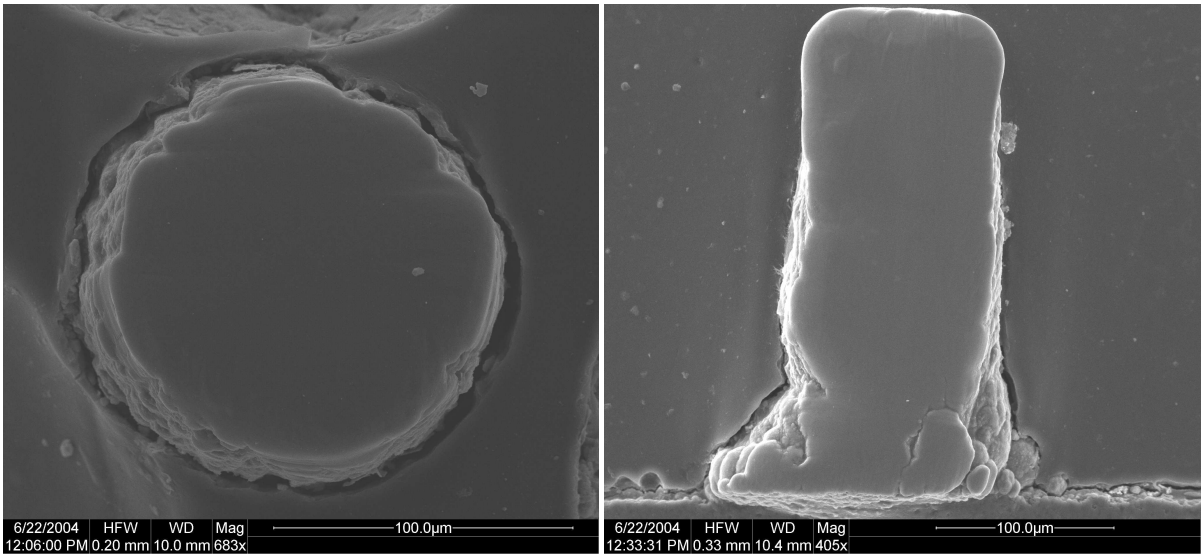

(a) L285-5, T_{max}=1160 ^oC (b) L293-4, T_{max}=1243 ^oC

Figure 90: SEM figures of cross section of SiC fibers.

The first principal stresses inside the main body of the fiber without the bottom 7 μm layer shows a similar pattern of change as for the entire fiber. The value of the first principal stress slightly keeps increasing slightly as the deposition process continues and then reduces a little during the final cooling process, as shown in Table 20. This means that the most dangerous thermal stress within the SiC fiber seems to follow this changing pattern with time.

7.4.3.2 Principal Stress vs. time

An important question is how do the first principal stresses change with time during the deposition and cooling processes? In order to answer that, the entire fiber was divided into three portions: from 7 to 14 μm, from 14 to 49 μm, and from 49 to 175 μm. The first

principal stress of each portion at different time points during the processes of deposition and cooling are shown in Figures 91 - 93. The values of the maximum first principal stresses within each portion at different time are listed in Table 21.

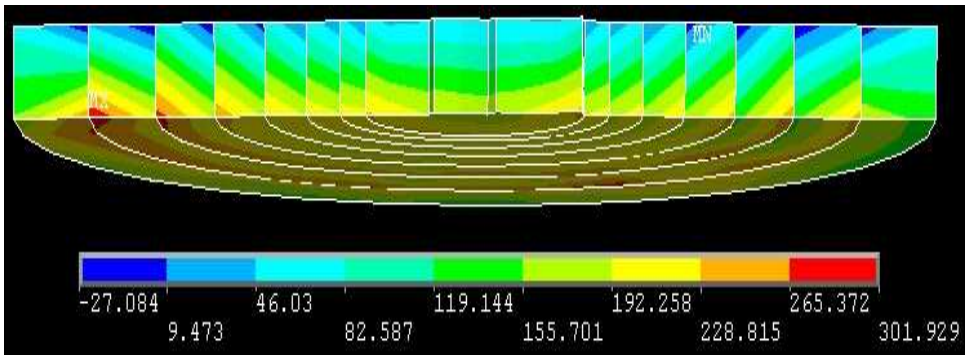

(a) t_1

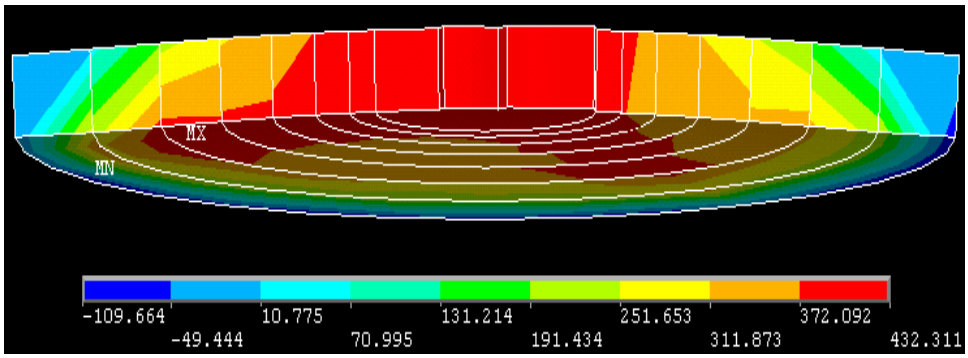

(b) t_2

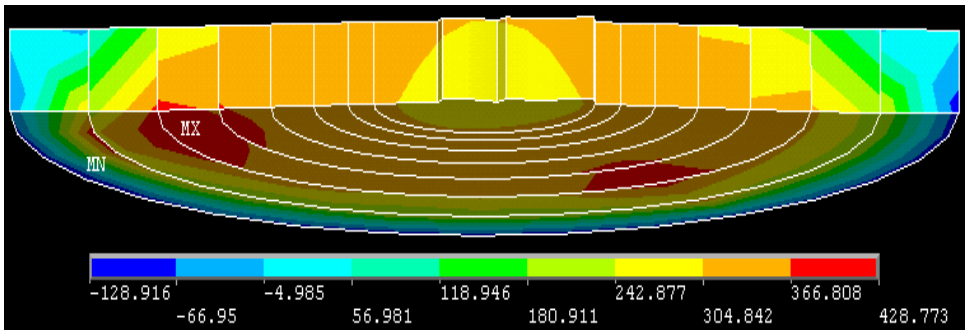

(c) t_3

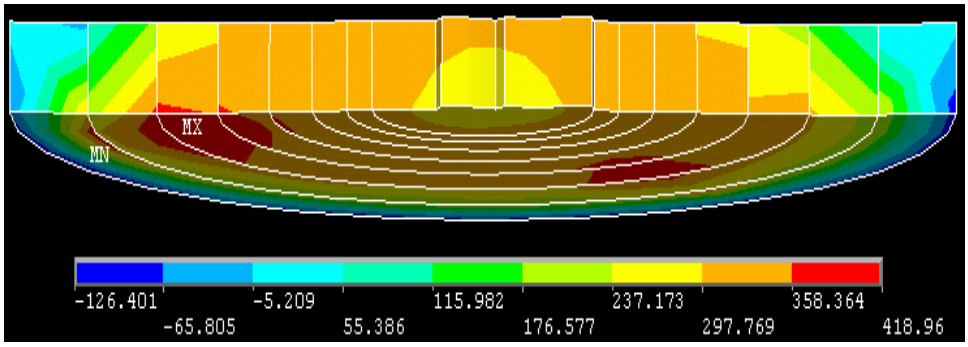

(d) t_4

Figure 91: The first principal stress (MPa) of the region from 7 μm to 14 μm of the fiber at four different time point.

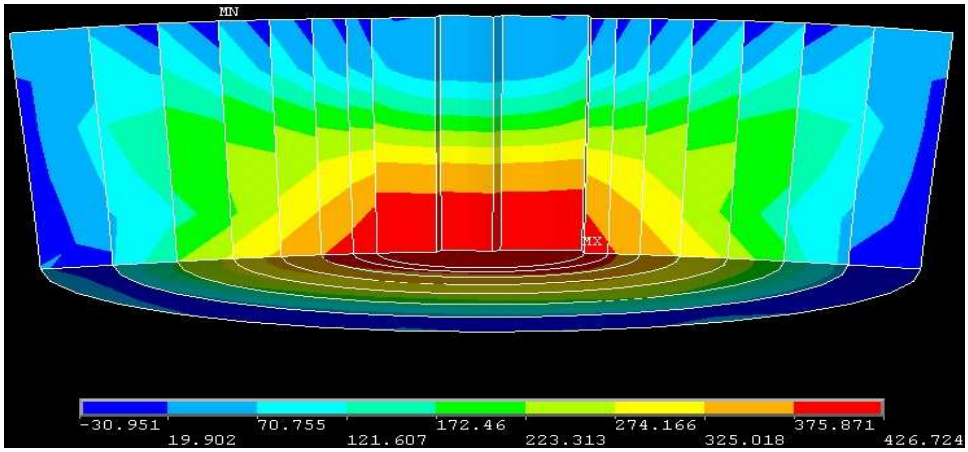

(a) t_2

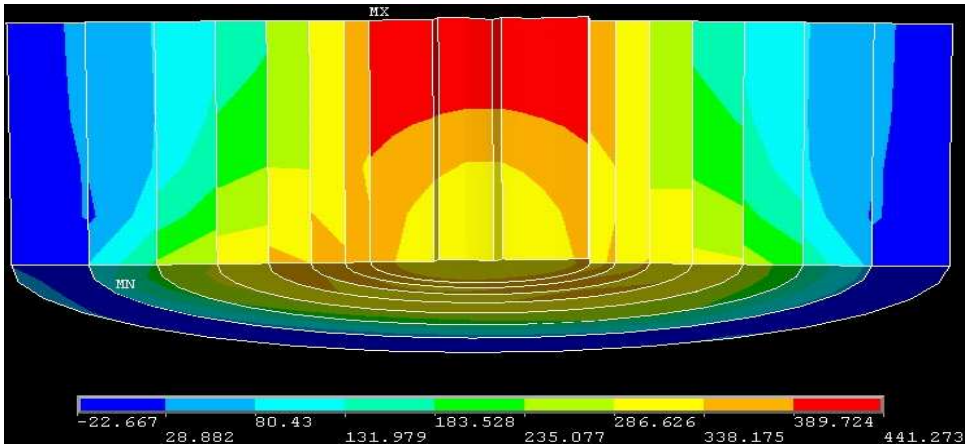

(b) t_3

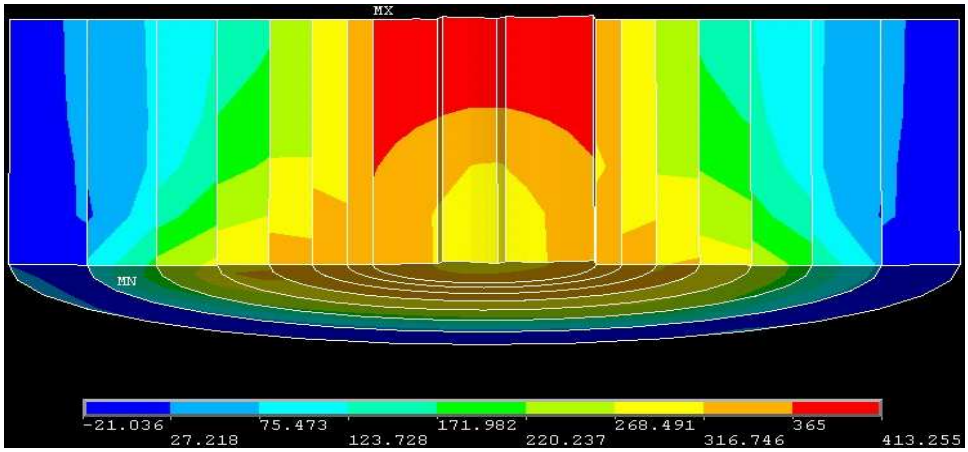

(c) t_4

Figure 92: The first principal stress (MPa) of the region from 14 μm to 49 μm of the fiber at three different time point.

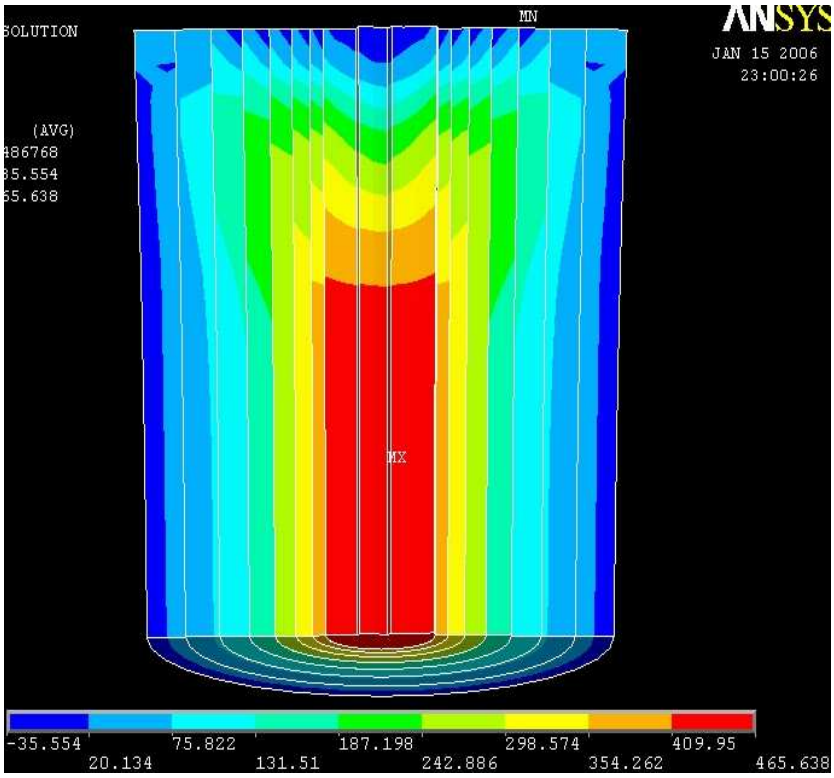

(a) t_3

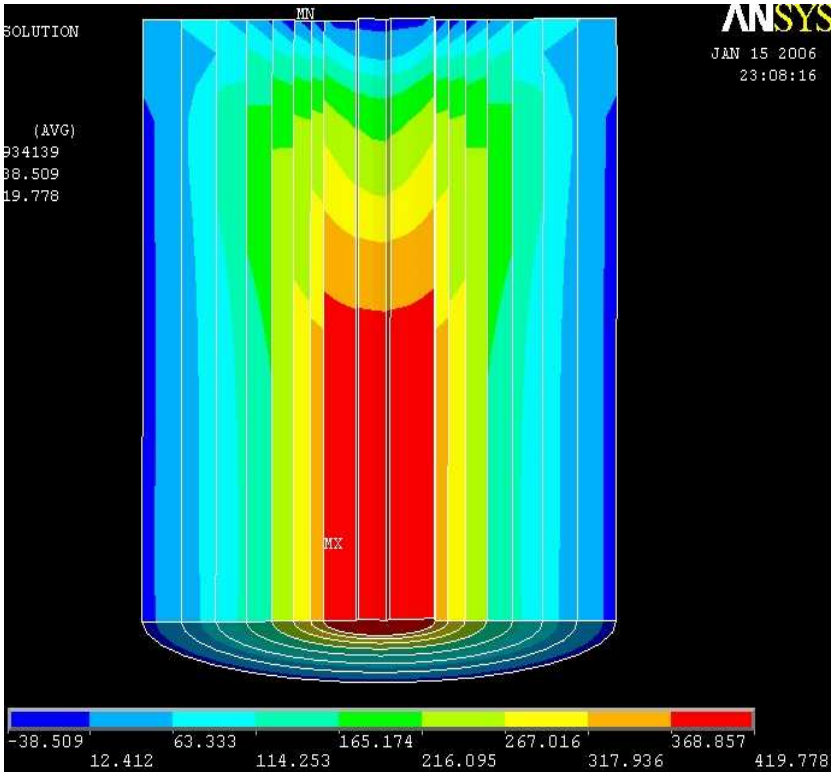

(b) t_4

Figure 93: The first principal stress (MPa) of the region from 49 μm to 175 μm of the fiber at two different time point.

Table 24: First principal stresses of different portions of fiber at different time in MPa

Time	$7 \sim 14\mu m$	$14 \sim 49\mu m$	$49 \sim 175\mu m$
t_1 *(h=14μm)*	301	\	\
t_2 *(h=49μm)*	432	426	\
t_3 *(h=175μm)*	428	441	465
t_4 *(h=175μm, RT)*	418	413	419

For each portion, as the deposition process proceeds, the first principal stress increases in the beginning, reaches a maximum value, and then decreases. On cooling to room temperature the stress decreases further. Therefore, the most dangerous thermal stress will be generated during the deposition process at some time point, which is different for different portions of the fiber. The final cooling process will not generate the most dangerous thermal residual stress in the main body of the fiber. This changing pattern of principal stresses is true for the entire fiber case, the fiber without the bottom 7 μm layer, and those three different portions of the fiber.

Therefore, in order to decrease the most dangerous thermal residual stress of the fiber or prevent from cracking, efforts should be made to decrease the temperature gradients within the fiber during the deposition process. How the fiber is cooled is not important. To decrease the radial temperature gradient within a fiber, a non-Gaussian laser might be used instead. Due to the lower heat transfer rate in the center than at the edge, a laser with lower energy in the center and higher energy at the edge could be a better choice. In this way, a relatively constant temperature radially might be obtained during the deposition process.

7.5 2-D Axisymmetric Thermal Residual Stress Simulation

As shown in Figure 88, there was extremely high first principal stress present in a small region at the bottom edge of the SiC fiber at all of the four time points. We suspect that those high stress values are not correct. They might be due to the slightly unsymmetric meshing of the fiber shown in Figure 83. Therefore, a 2-D axisymmetric coupled thermal and structural model was developed to check the effects of the mesh.

7.5.1 Model Geometry and Meshing

The geometry of the new axisymmetric model is shown in Figure 94. It has the exact same size of the 3-D simulation. Eight separate portions composed the body of the entire fiber, with the same dimensions as the 3-D model, as shown in Figure 81. Fiber with three heights, 14 μm, 49 μm, and 175 μm, were considered, which are the same as those of the 3-D model.

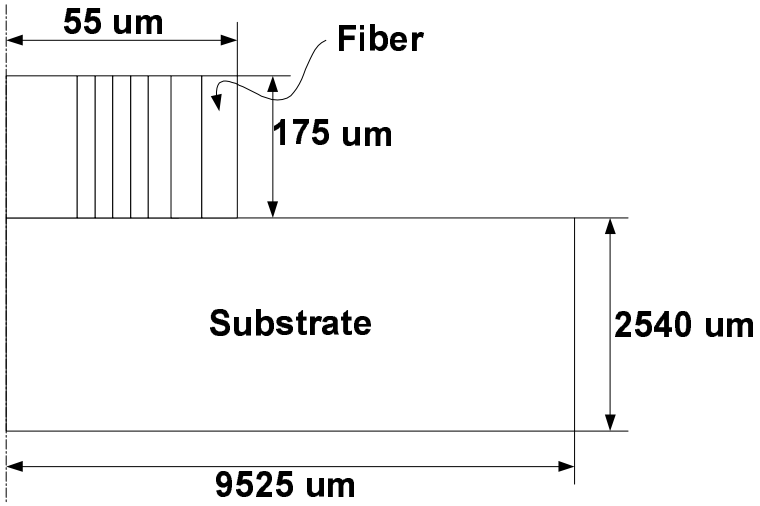

Figure 94: The geometry of the 2-D axisymmetric coupled thermal and stress model.

The way that the 2-D axisymmetric model is meshed ensures that the meshes of the 2-D geometry are as close as possible to that of the 3-D model. In the radial direction of the 2-D fiber, one element is specified for all of the parts except the one in the center, which has a length of 13 μm. Four elements are assigned to the center part. In the longitudinal direction of the fiber, uniform 7 μm element sizes are defined. The substrate is free meshed with a smart size of 4. The element types used in the 2-D axisymmetric model are PLANE77 and PLANE82, same with those used in the 3-D model. The mesh of the 2-D axisymmetric model is shown in Figure 95.

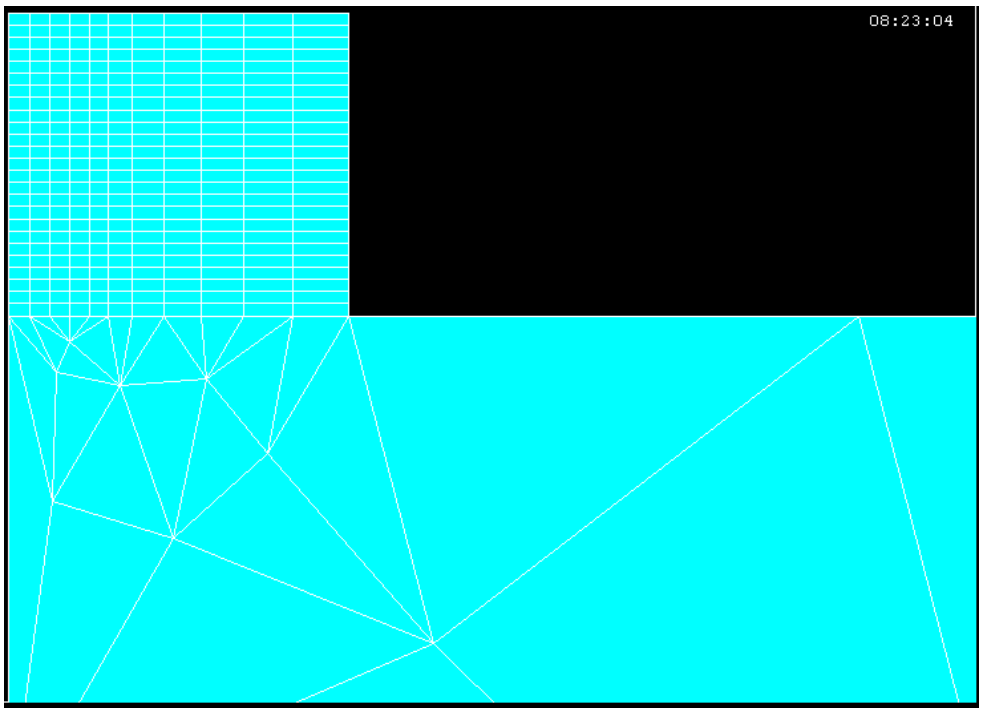

Figure 95: The mesh of the 2-D axisymmetric coupled thermal and stress model.

7.5.2 Model Procedure and Solutions

APDL code was used to developed the 2-D axisymmetric model in ANSYS environment. Appendix G and H are the lists of the text files for the entire simulation. For both the thermal and structural analyses, the governing equations, the material properties, the boundary conditions, the way to specify loads, and the simulation situations are same as those of the 3-D model.

The temperature distributions at three time points during the deposition process are shown in Figure 96. As before, the maximum deposition temperature is maintained around 1150 ^oC. The calculated first principal stresses of the fiber at four time points are shown in Figure 97. Time point 1, t_1, represents when the fiber is 14 μm high, time point 2, t_2, is the time when the fiber grew to 49 μm, time point 3, t_3, is when the fiber deposited to its full height, 175 μm, and time point 4, t_4, represents cooling down the deposited fiber to room temperature, 300 K. The values of the maximum first principal stresses for the four time points are listed in Table 22.

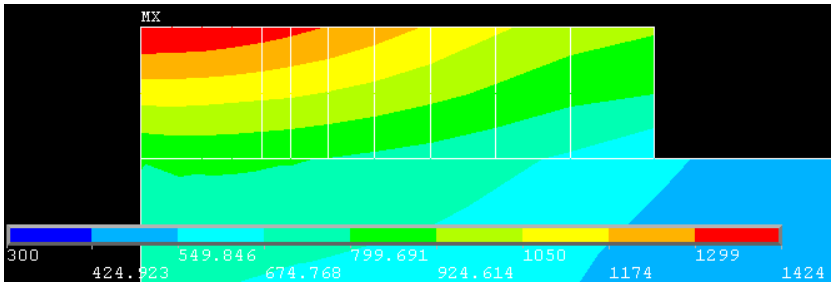

(a) t_1

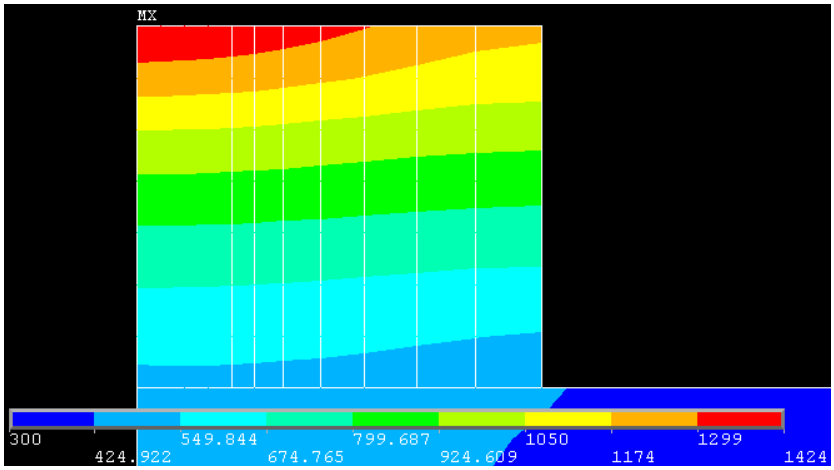

(b) t_2

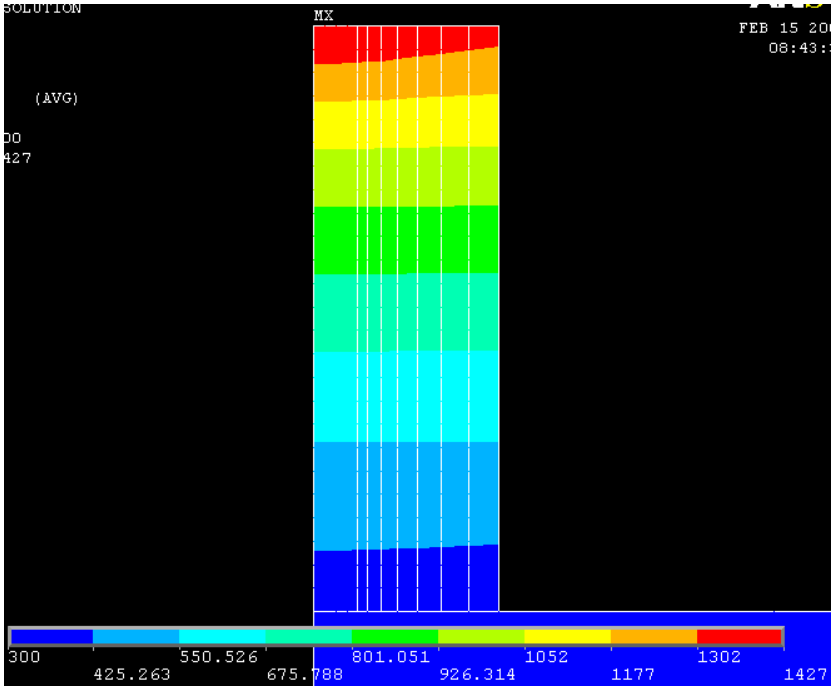

(c) t_3

Figure 96: The temperature (K) distributions of fiber at three time points.

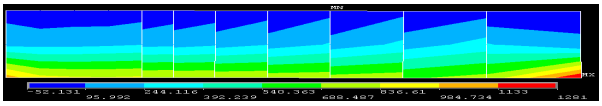

(a) t_1

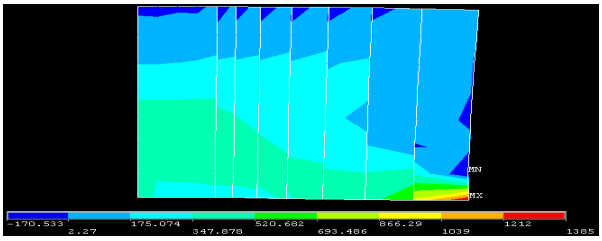

(b) t_2

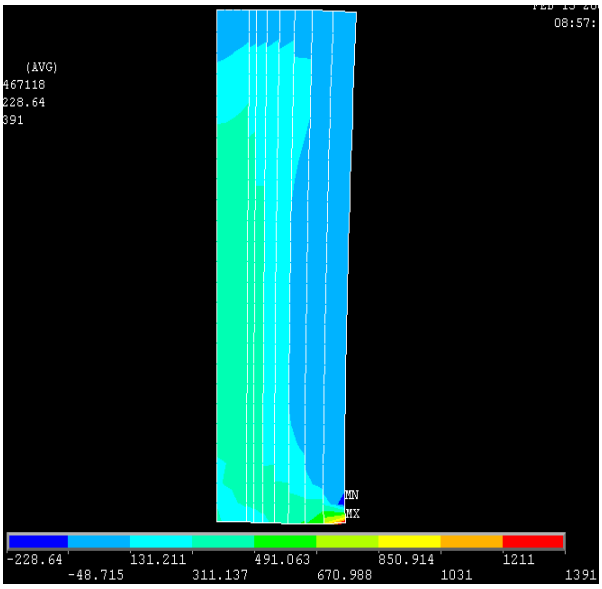

(c) t_3

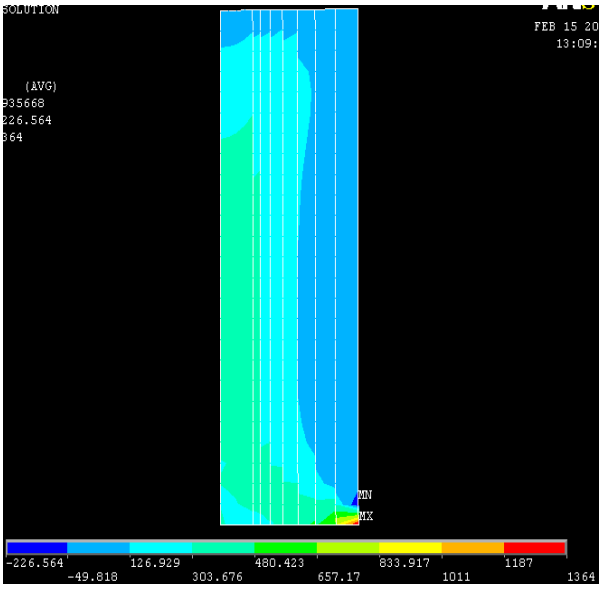

(d) t_4

Figure 97: The first principal stress (MPa) distributions of fiber at four time points from 2-D axisymmetric model.

Table 25: Maximum first principal stresses of the fiber at different time

$Time$	t_1	t_2	t_3	t_4
σ_{1max} (MPa)	1281	1385	1391	1364

It was indicated by Figure 97 that the maximum first principal stress always occurs at the circumference of the bottom surface of the fiber for all of the four time points. The values of the maximum principal stress are around 1 GPa for all of the four time points, which are significantly lower than those for the 3-D simulation as shown in Figure 88 and Table 19. Considering the first principal stresses shown in Figure 88, if we cut off the spot which has the most dangerous first principal stress, the rest of the first principal stress values along the circumference of the bottom surface of the fiber are very similar to those obtained from this 2-D axisymmetric model. This indicates that it is very likely that those highest first principal stresses at the circumference of the bottom surface of the fiber occur due to the unsymmetric meshing. Therefore, we probably can just neglect those extremely high stress values in the 3-D thermal stress simulations.

7.6 Summary of Thermal Residual Stress Simulation

A 3-D coupled thermal and structural model was developed to calculate the thermal residual stress induced during the LCVD-SiC fiber deposition process and to study the how the thermal residual stresses change during the deposition process and the final cooling process. During both the deposition and the cooling processes, the highest first principal stresses always occur at a specific spot on the circumference of the bottom surface of the fiber. The values of the maximum first principal stresses are beyond 2 GPa, which are larger than the reported rupture strength of CVD-SiC material, 1GPa.

By cutting off the very bottom layer material of the fiber, the maximum principal stresses within the main body of the fiber were revealed. The values of those maximum first principal stresses were about 450 MPa for all of the four time points. These values are lower than the reported tensile strength for CVD-SiC. Therefore, according to these calculations, no cracks will be generated within the main body of the fiber during either the deposition process or the final cooling to room temperature.

In order to study how the thermal residual stresses change during the deposition and cooling processes, the entire SiC fiber was divided into three portions, according to those three deposition time points. The thermal residual stresses within each portion at different time points were studied. It was shown that the thermal residual stress tends to increase during the deposition process until a maximum value is reached, then decreases during further deposition. A further decrease occurs during the process of cooling to room temperature. Therefore, if the fiber is going to be damaged by the thermal residual stress, it would occur at some point during the deposition process, not during cooling the hot fiber to room temperature.

A 2-D axisymmetric coupled thermal and structural model was developed to check the effect of the unsymmetric meshing of the fiber on the thermal residual stress. The 2-D model results showed that the extremely high thermal stresses at the specific spot on the circumference of the bottom surface of the fiber were inaccurate. Most likely, those points are just the singular ones present in the entire 3-D simulation work. The maximum first principal thermal residual stresses still occur at the circumference of the bottom surface of the fiber, but the values are about 1 GPa, according to both the 3-D simulation and the 2-D axisymmetrc model.

CHAPTER VIII

LASER HEATING SIMULATION OF LCVD SIC PROCESS

The Georgia Tech LCVD system utilizes a CO_2 laser to locally heat up the substrate. When the local temperatures are high enough, it initializes the chemical reactions, which make the solid deposition occur. Therefore, temperature is the most important parameter of the LCVD process. It will help the researcher to better understand the actual deposition process if the way the temperature changes with time right after the laser power is applied is available.

It is observed from the actual deposition of a fiber that as the deposition continues, the power of the CO_2 laser needs to be decreased if a constant deposition temperature is desired for the entire fiber. If a constant laser power is applied for the entire fiber deposition process, the deposition temperature will become higher and higher as the fiber continues growing. Most of the time, the deposition temperature will become extremely high, and the entire fiber is burned out by the laser. Therefore, in order to fabricate fibers with good shape, the way to decrease the laser power during the deposition process has to be studied.

This chapter presents two models related to CO_2 laser heating. One is a transient heat transfer study based on two geometries. The two geometries were a graphite substrate alone and the other is a SiC fiber together with the substrate. This study helps us to know how fast the laser will heat up the substrate or the underlying fiber material. The second model is a steady state heat transfer simulation for SiC fibers of different heights. By adjusting the input laser power, a constant maximum temperature will be obtained for the substrate alone situation and five fibers of different heights. The relationships between those laser powers and the fiber heights were obtained by combining the results of those six different geometry models. In return, a graph of applied laser power, which generated relatively constant deposition temperatures, versus the corresponding height of the fiber is achieved.

This curve indicates, theoretically, how to control the the laser power during the deposition process to achieve constant deposition temperature throughout the entire fiber deposition process.

8.1 Transient Heat Transfer Study

8.1.1 Geometry, Mesh, Material Properties, and Boundary Conditions

The transient heat transfer model has similar geometry and boundary conditions as the thermal model descried in chapter VI. The geometries of the model are shown in Figure 98. Two geometries were considered for the transient heat transfer model. One is a long fiber of 171 μm high, and the other is simply a graphite substrate, shown in Figure 98. These two geometries were included to study the transient behaviors of laser heating on a fiber and on a substrate, which represent two typical laser heating situations of the actual experiments.

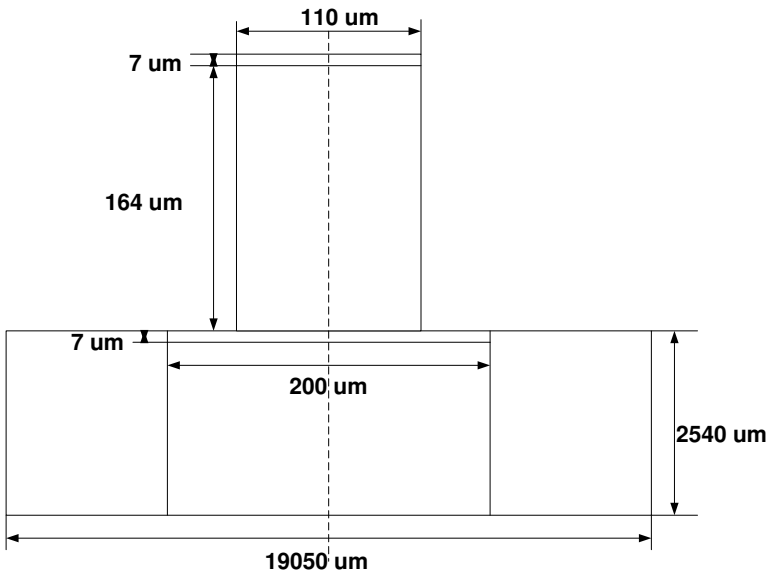

Figure 98: Geometry of transient heat transfer study of LCVD-SiC fiber.

The boundary conditions and material properties of these transient models are exactly the same as those of the thermal analysis described in chapter VI. All of the outer surfaces are subjected to heat convection and radiation, except for the bottom one of the substrate, which is constrained to a constant 300 K during the entire simulation. Because ANSYS dose not allow heat convection and another heat flux applied to the same surface, the laser heating was simulated as a volumetric heat generation within a specific volume, which is

the same as that described in chapter VI.

The dimension of the specific volume, which is used to specify the volumetric heat generation, is designed to ensure that the effects of those two types of energy input are as close as possible. The volumetric heat generation input requires that the thickness of the layer of the elements, where the volumetric heat generation is applied, must be 7 μm. Therefore, the long fiber geometry is composed of two parts, a short cylinder of 7 μm thick and 110 μm in diameter, and a long cylinder, which represents the remainder of the fiber, shown in Figure 98. The volumetric heat generation rate was applied to the top small cylinder. For the substrate case, three parts are included, a short cylinder with 7 μm in thickness and 200 μm in diameter, a long cylinder with the same diameter as the upper one, which is right underneath the short one, and a hollow cylinder next to those two. The diameter of this thin cylinder is the same as the diameter of the CO_2 laser beam, 200 μm. The volumetric heat generation rate for the substrate case is applied to this 7 μm cylinder on the top center of the substrate. This ensures that the heat energy input within the model is close to the actual case.

PLANE55 and SOLID70 are the two element types used in this simulation work. For each geometry, 1 element is specified in the longitudinal direction of the short 7 μm cylinder, which ensures the amount of the heat generation input equals the actual laser energy. For the long fiber case, 14 elements with 0.2 spacing ratio were assigned to the remainder of the fiber in the longitudinal direction. The spacing ratio of 0.2 ensures fine elements on the top and coarse elements at the bottom of the fiber. In the circular direction, 40 elements were specified evenly for the entire fiber. The graphite substrate is free meshed with a smart size of 6. For the substrate case, 20 elements with a spacing ratio of 2 were assigned to the cylinder underneath the thin 7 μm cylinder in the longitudinal direction. A total of 24 elements were specified evenly in the circular direction of both cylinders. The outer hollow cylinder was free meshed with smart size of 6. Figure 99 shows the meshes of both geometries.

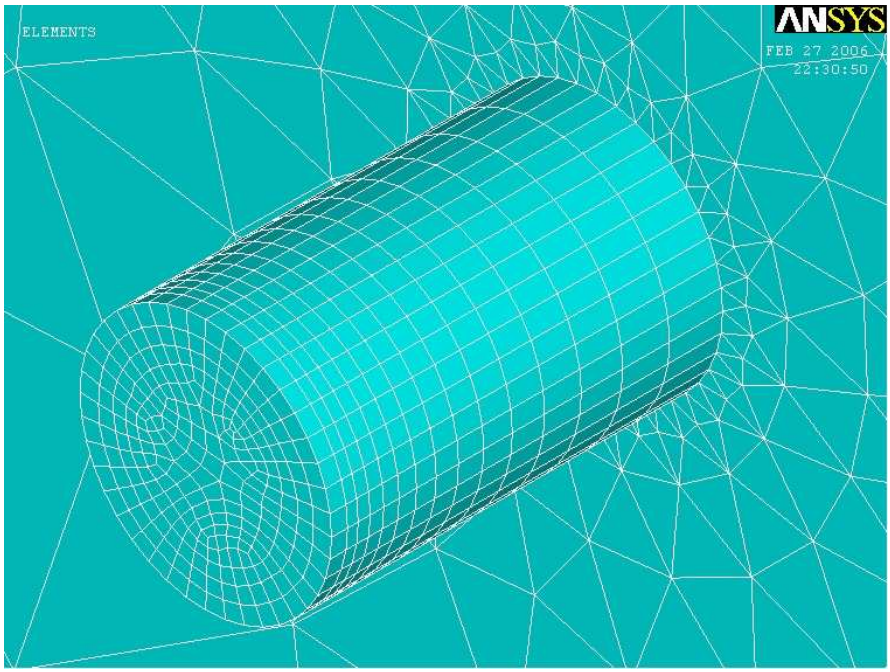

(a) Mesh of the fiber

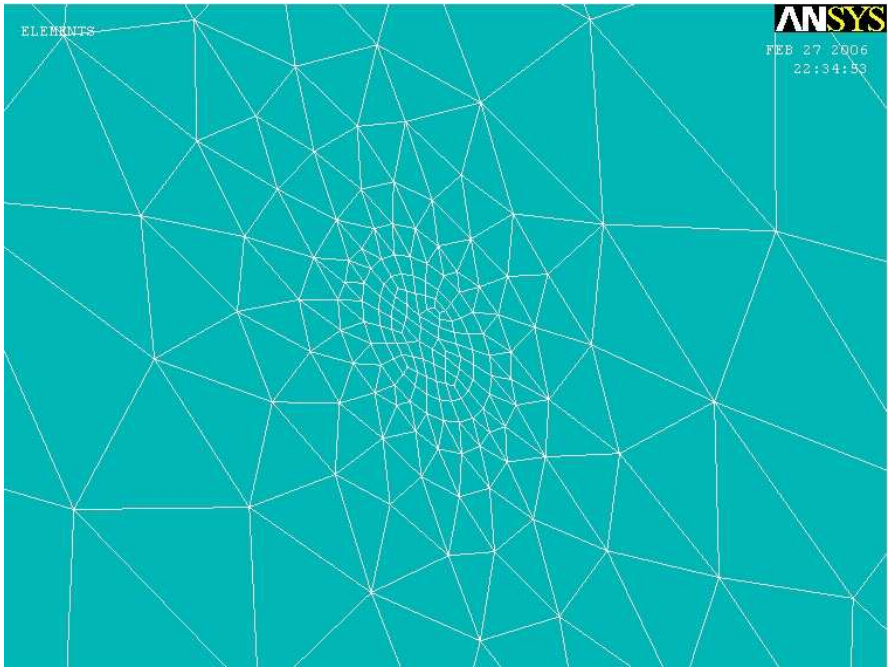

(b) Mesh of the pure substrate

Figure 99: Meshes of the two geometries for transient heat transfer study.

8.1.2 Solutions

8.1.2.1 Temperatures vs. Time for the Fiber Case

As with the coupled thermal and structural model, the APDL language was used to accomplish the entire simulation in the ANSYS environment. The text file of the simulation is listed in Appendix I. Given the material properties for both the fiber and the substrate and the meshes of both geometry cases, as well as with the boundary conditions specified, the temperature distributions within the geometries and the temperature changes right after the laser power is applied on the top surface were obtained. The temperatures versus time for several nodes of the geometries were plotted. The behaviors of the entire temperature distributions of the geometry versus time are similar to the nodal behaviors. For the long fiber case, temperatures of two typical nodes were plotted versus time. Those two nodes are located at the center (node 47) and the bottom circumference (node 491) of the top 7 μm cylinder, shown in Figure 100.

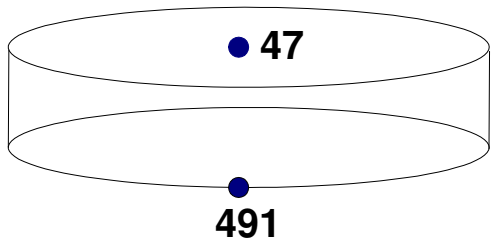

Figure 100: The locations of nodes 47 and 491 in the small top 7 μm cylinder in the fiber.

Figure 101 exhibits the temperatures of nodes 47 and 491 versus time when the initial temperatures for the SiC fiber and the graphite substrate are uniformly 300 K. Figure 102 shows a plot of the temperatures of nodes 47 and 491 versus time when the initial temperatures for the SiC fiber are uniformly 1000 K and the initial temperatures for the graphite substrate are uniformly 500 K. Figure 103 displays the temperatures of the same two nodes when the initial temperatures are uniformly 1000 K for both the SiC fiber and the graphite substrate. It can be seen from Figures 101-103 that after 0.1 second, for the first two cases, the temperatures almost reach the steady state results, but the temperatures

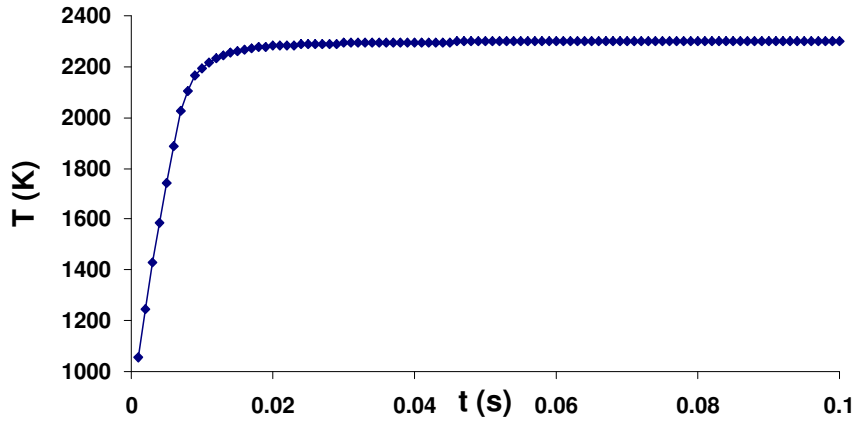

(a) Temperatures of node 47 in the fiber

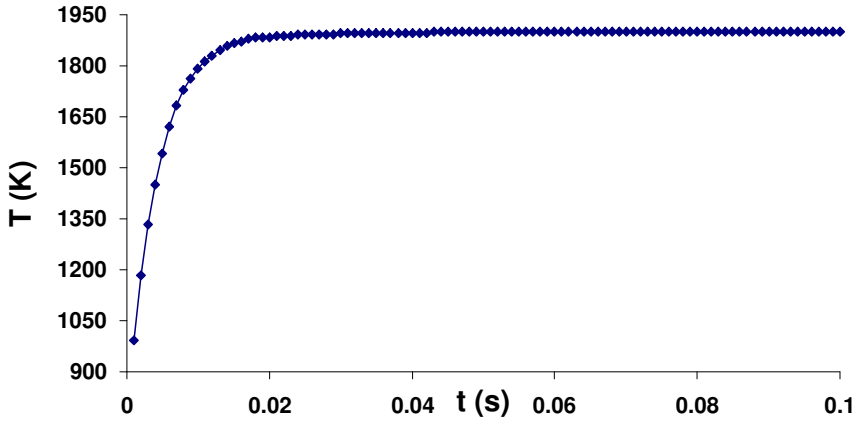

(b) Temperatures of node 491 in the fiber

Figure 101: The relationship between fiber node temperature and time when the initial temperatures are uniformly 300 K for the entire model.

of the third case are still much higher than the steady state temperatures. These implies that the higher the initial temperatures, the longer it takes for the model to reach its steady state.

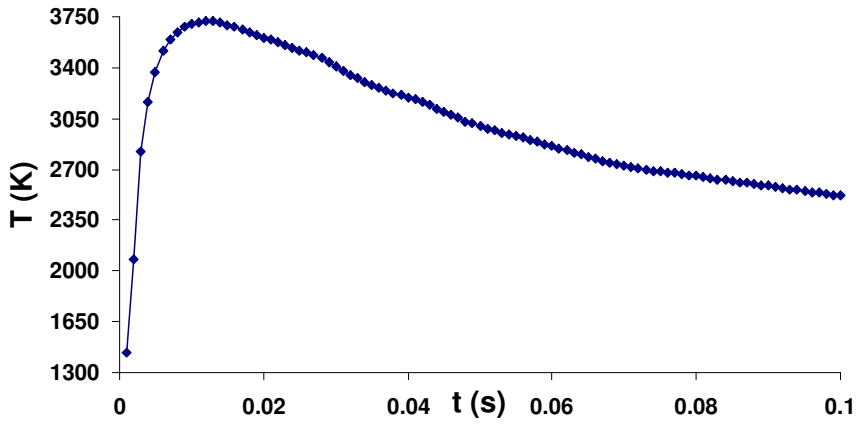

(a) Temperatures of node 47 in the fiber

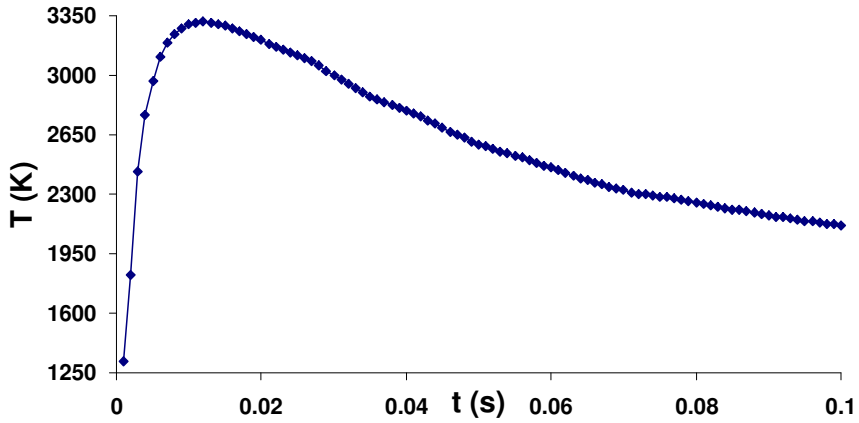

(b) Temperatures of node 491 in the fiber

Figure 102: The relationship between fiber node temperature and time when the initial temperatures are uniformly 1000 K for the fiber and 500 K for the substrate.

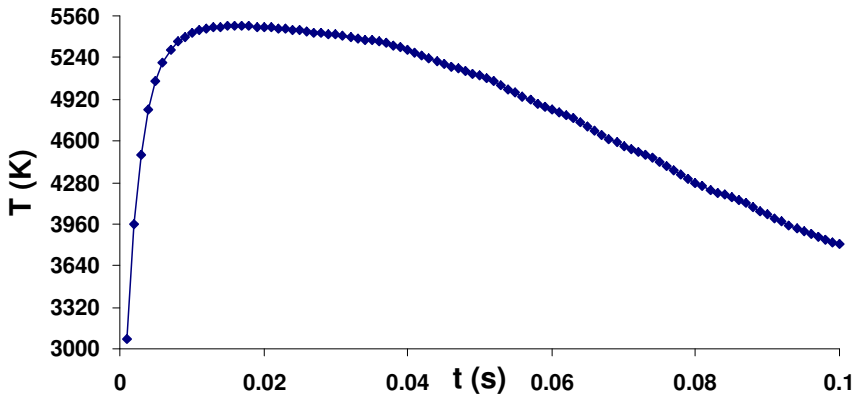

(a) Temperatures of node 47 in the fiber

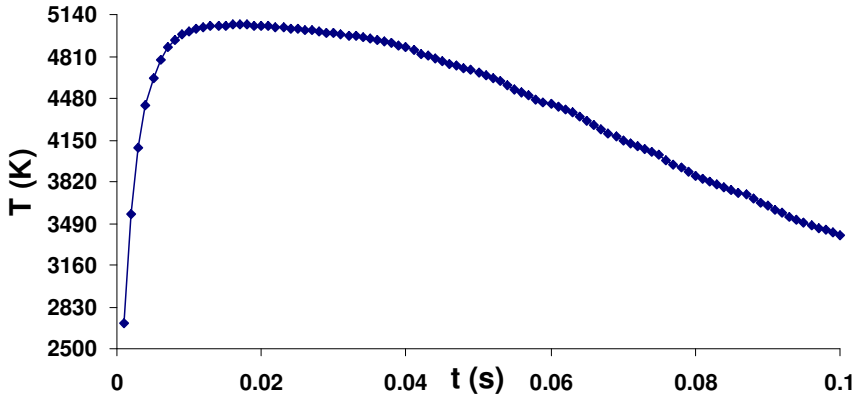

(b) Temperatures of node 491 in the fiber

Figure 103: The relationship between fiber node temperature and time when the initial temperatures are uniformly 1000 K for the entire model.

The manner in which the temperature changes with time is strongly affected by the initial temperature. As shown in Figure 101, if the initial temperature is low, the temperatures of the nodes will keep increasing until reaching their maximum values. Actually, these maximum temperatures are the steady temperatures. On the contrary, with high enough initial temperatures specified, the temperatures of the nodes will increase in the beginning, then reach the maximum values which are much higher than the steady temperatures, and then decrease with time until reaching the steady state temperatures as shown in Figures 102 and 103.

This phenomena is very important for controlling the deposition temperatures during the actual experiments. As discussed in chapter V, high deposition temperatures will either

damage the deposits that has been grown or cause volcano-like depressions at the end of the fibers. Therefore, if the there is high initial temperature present on the substrate, lower laser power should be applied in the beginning to avoid extremely high temperatures, which might damage the substrate in the beginning or cause poor deposition. In the manufacture of a part, when it is desired to deposit on top of previously deposited material, if the temperatures of the underlying material are still high, attention must be paid to the initial laser power. Laser power lower than the usual value might be applied first, and then adjusted to achieve the desired temperatures. Also, the underlying geometry can be damaged by the high temperatures.

8.1.2.2 Temperatures vs. Time for the Substrate Case

For the substrate alone case, the temperature distributions within the substrate and the temperature changes with time within the geometry were obtained through the transient heat transfer modeling. The temperatures of two nodes within the top center 7 μm cylinder were plotted versus time. The locations of those two nodes (25 and 188) in the small central top cylinder are shown in Figure 104.

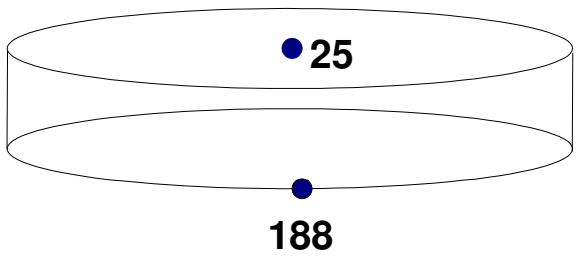

Figure 104: The locations of nodes 25 and 188 in the small top 7 μm cylinder in the substrate.

Figure 105 displays the temperatures of nodes 25 and 188 versus time when the initial temperature of the graphite substrate was uniformly 300 K. Figure 106 shows the temperatures of nodes 25 and 188 versus time when the initial temperatures are uniformly 500 K for the graphite substrate. It is observed that about 0.1 second later, the substrate reaches its steady state, achieving relatively constant temperatures. The effects of the initial temperatures on the temperature change pattern with time are similar to the fiber case. This

means that if the initial temperatures are low, the temperatures within the substrate will keep increasing with time until they reach the maximum values, which are the temperatures at steady state. But if the initial temperatures present in the substrate are high enough, the temperatures within the substrate will increase with time in the beginning, then reach the maximum values very shortly, after that the temperatures will decrease until reaching the steady state temperatures. In addition, for the high initial temperature cases, it takes longer to reach steady state temperatures. Thsi behavior was also observed for the fiber transient heat transfer as well.

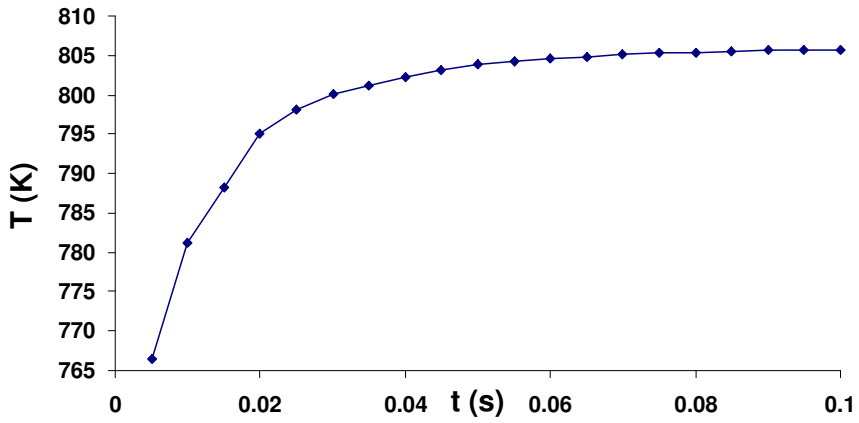

(a) Temperatures of node 25 in the substrate

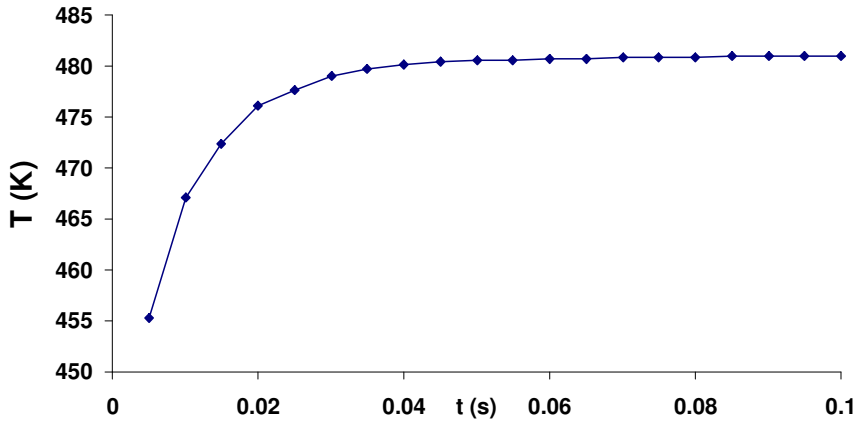

(b) Temperatures of node 188 in the substrate

Figure 105: The relationship between substrate node temperature (K) and time when the initial temperatures are uniformly 300 K for the entire model.

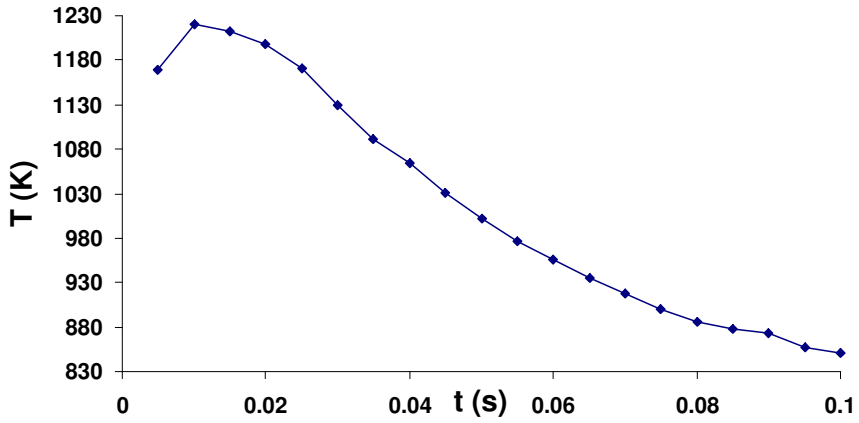

(a) Temperatures of node 25 in the substrate

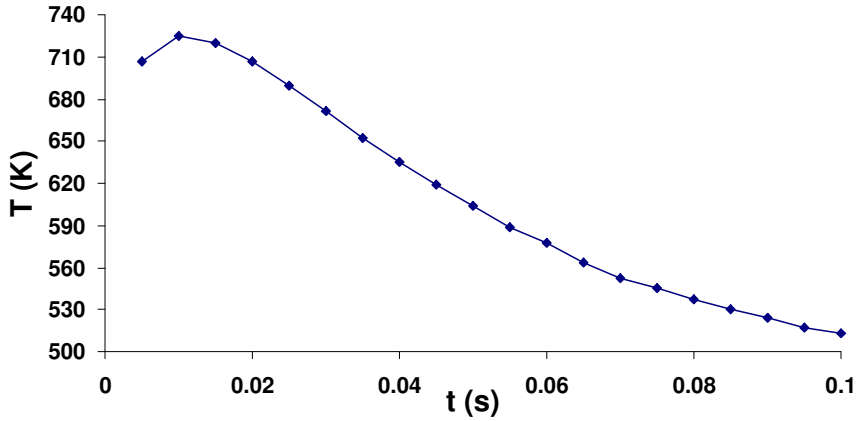

(b) Temperatures of node 188 in the substrate

Figure 106: The relationship between substrate node temperature (K) and time when the initial temperatures are uniformly 500 K for the entire model.

The two transient heat transfer models infer that the transient effect of the laser heating process is very short. After about 0.1 second, steady state will be reached for different geometries. This means that during the actual deposition process, the temperatures that we monitored and measured are the steady state temperatures. This also demonstrates that it is accurate to use steady state analysis for the thermal residual stress simulation presented in chapter VII.

It was also found that the initial temperature specified for each model played an important role in controlling the relationship between temperature and time. If the initial temperatures are high enough, the temperatures within the geometry might reach extremely large

values, much higher than the steady state temperatures, as shown in Figures 102, 103, and 106. This phenomenon was also observed during the actual LCVD deposition experiments. When depositing lots of fibers on one graphite substrate, if the subsequent fiber was located very close to the previous one, or the previous fiber had a very high deposition temperature, the small region of the subsequent fiber on the substrate might have been heated to very high temperatures. In these cases, the initial laser power for the subsequent fiber must be adjusted to lower values than usual, otherwise the temperatures of the subsequent fiber will become extremely high. A hole instead of a fiber will be drilled. This is very much due to the initial temperature effect.

8.2 Curve of Laser Power vs. Fiber Height

In order to fabricate SiC fibers with good shape and relatively uniform composition, the deposition temperatures must be maintained constant throughout the entire deposition process. Due to the nature of the CO_2 laser energy profile, it is impossible to obtain uniform deposition temperature radially. But the laser power can be manipulated to achieve relatively constant deposition temperature in the longitudinal direction. Since the maximum temperature present in the center of the fiber is the most critical parameter for eliminating the volcano effect of the deposits, normally, during the actual SiC deposition experiments, efforts were made to obtain relatively constant maximum temperatures at the center of the fiber. It was observed that in order to obtain relatively constant maximum deposition temperature, the laser power has to be decreased during the entire deposition process. Therefore, to get the relationship between the laser power and the height of the SiC fiber theoretically, a thermal model involving laser heating of SiC fibers of different heights was developed.

8.2.1 Geometry, Mesh, Material Properties, and Boundary Conditions

Six different geometries were included in this model. They are a simple substrate case and five fibers of different heights, which are 7, 49, 91, 133, and 175 μm. Figure 107 displays the configuration of those six geometries. The pure substrate geometry consists of five parts. They are a top center small cylinder of 110 μm in diameter and 7 μm in length, a long

cylinder of the same diameter beneath it, two hollow cylinders next to those two center ones of the same outer diameter of 200 μm and the same thickness with those at the center, and a big hollow cylinder of 19050 μm in diameter and 2540 μm in length. Those two 7 μm thick parts are created to specify the volumetric heat generation, which represents the local laser heating. The remaining five geometries are five fibers of different heights, together with the same graphite substrate as before.

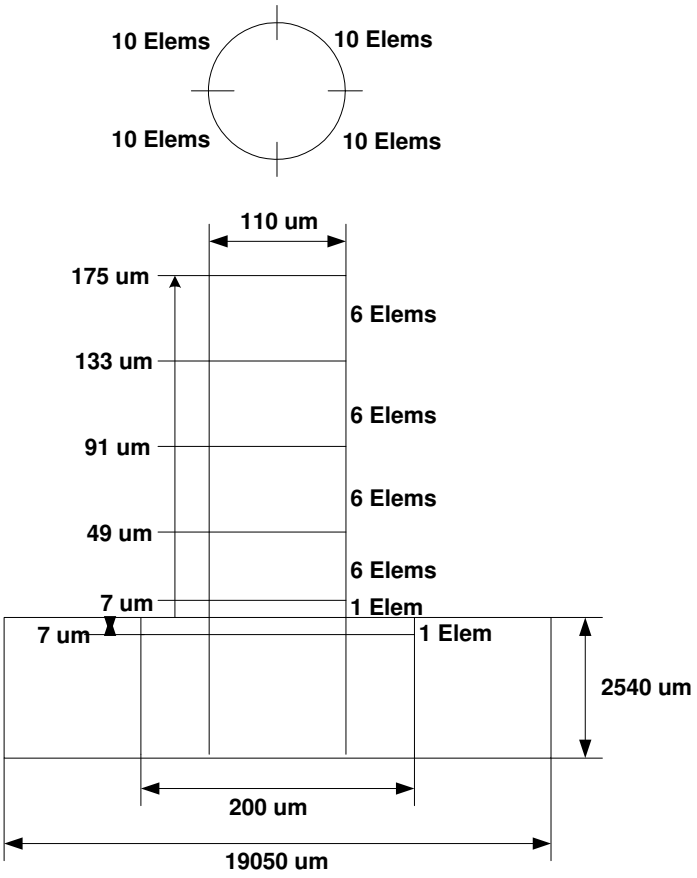

Figure 107: The geometries for simulating the curve of laser power and fiber height.

PLANE55 and SOLID70 are the two element types used in this simulation work. The way the five geometries are meshed is shown in Figure 107. The fibers and the two small parts of 7 μm in thickness at the top of the substrate were mapped meshed. The rest of the geometries were free meshed with a smart size of 8. A total of 40 elements were specified evenly in the circular direction of the fibers and the two thin top 7 μm parts of the substrate. In the longitudinal direction of the fibers and the two top thin parts of the substrate, the

element size was specified as a constant 7 μm. The way that the elements were specified ensures the mesh consistency for the overlaps of different geometries. Without this, the relationship between the laser power and different geometries might not be accurate. Since the mesh difference will induce a large change in the results. The mesh of a fiber with a full length of 175 μm is shown in Figure 108.

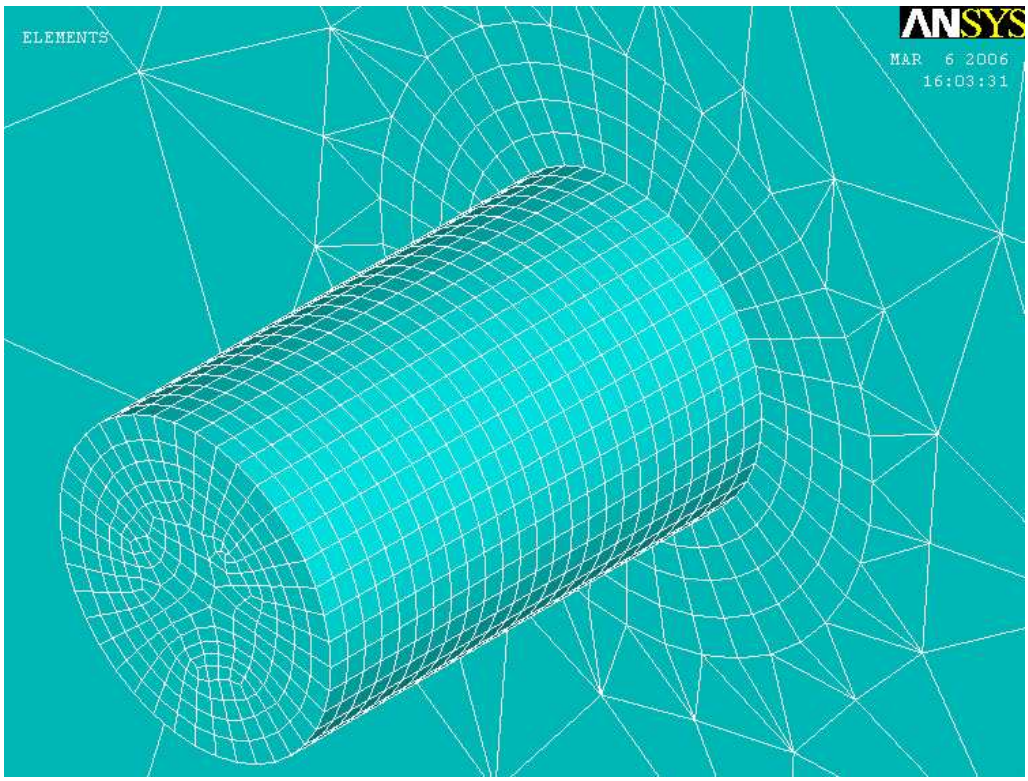

Figure 108: The mesh of a 175 μm high fiber and the substrate for simulating the curve of laser power and fiber height.

Material properties and boundary conditions for the six geometries were the same as those for the thermal analysis described in chapter VI.

8.2.2 Solutions

As before, a single text file was used to accomplish the entire modeling process. Appendix J lists the text files for the entire simulation.

For each geometry, the entire calculation is a steady state heat transfer with laser heating on the top. To obtain the relationship of the laser power and different geometries, for each geometry case, the laser power applied was manipulated manually until the maximum

temperature of the geometry, or the top surface of the model, was the desired. The laser powers were plotted versus the heights of the fibers. A height of zero represents the substrate alone case.

There are two different ways of specifying the laser heating energy. One is that only the center 7 μm cylinder with 110 μm in diameter is supplied with the volumetric heat generation rate. The other is that both the center 7 μm cylinder and the 7 μm hollow cylinder on the top of the substrate are applied with the volumetric heat generation rate. The first case simulated that the laser only heats on the circular region of 110 μm in diameter, which is the same area as the laser heating on the top surface of the fiber. The second one represents that the laser heating is applied on a circular region with a diameter of 200 μm. This diameter is the same as the actual CO_2 laser beam diameter.

Figure 109 shows the plots of the laser power versus the fiber height for maintaining constant maximum temperatures of 1200 and 1000^oC. For Figure 109, the laser is applied on a region of 110 μm in diameter on the substrate alone case. Figure 110 displays the same relationships of laser power and fiber height. But this time, the laser is applied on a region of 200 μm in diameter for the simple substrate case.

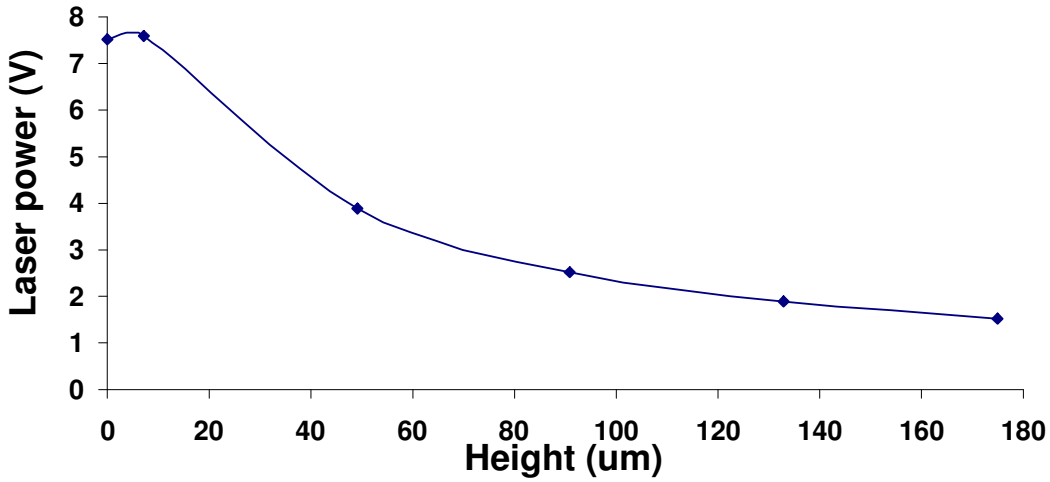

(a) Constant $T_{max} = 1200^oC$

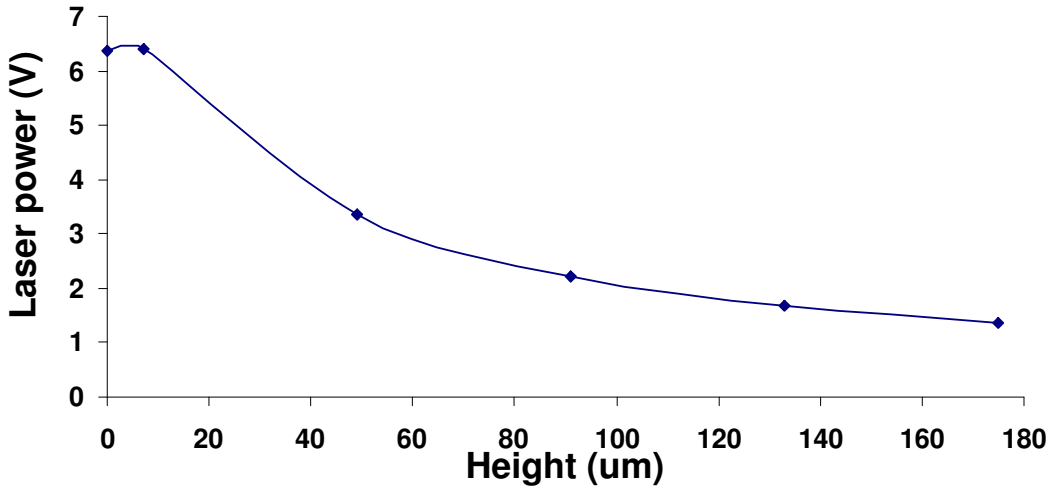

(b) Constant $T_{max} = 1000^oC$

Figure 109: The relationship of laser power and the fiber height for maintaining a constant T_{max} when the laser application region is 110 μm in diameter for the pure substrate case.

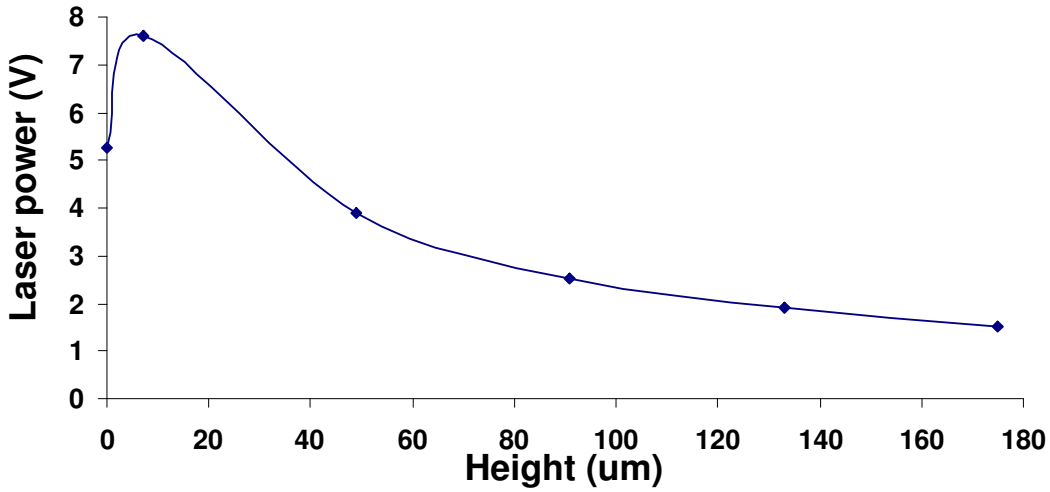

(a) Constant $T_{max} = 1200^{o}C$

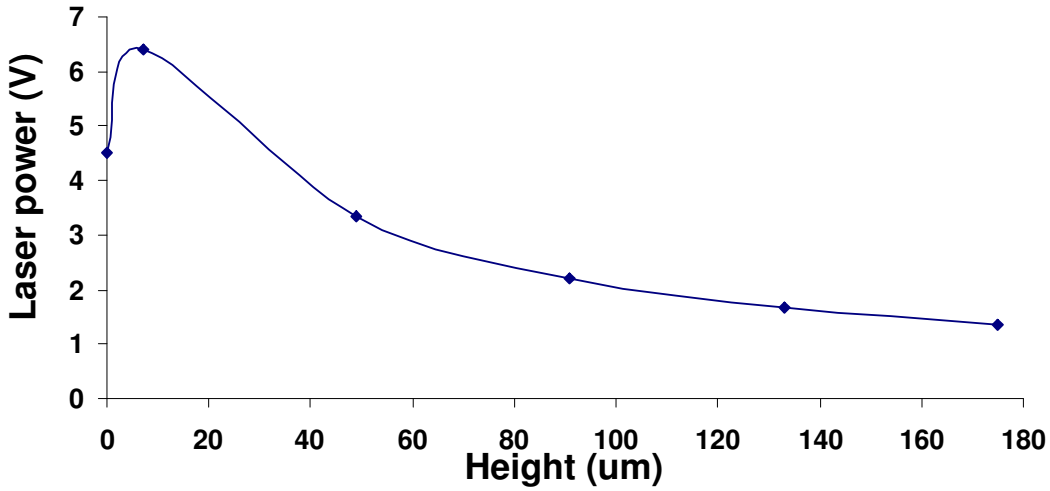

(b) Constant $T_{max} = 1000^{o}C$

Figure 110: The relationship of laser power and the fiber height for maintaining a constant T_{max} when the laser application region is 200 μm in diameter for the pure substrate case.

As shown in Figures 109 and 110, as the fiber deposition continues, the laser power must be decreased to maintain relatively constant maximum temperatures. This is due to the fact that the higher the previously deposited fiber, the higher the heat transfer resistance for heat transferring from the top of the fiber to the substrate.

But there is a big difference between these two figures in the early stage of the deposition process, i.e., there is no fiber deposited yet. If the laser power is applied in a region of 200 μm in diameter on the substrate, the laser powers required to generate a constant maximum temperature is much lower than those when the laser is applied on a region of 110 μm in diameter on the substrate. The reason is very obvious. The larger the region of laser application, the higher the energy input. The CO_2 laser of the Georgia Tech LCVD system has a diameter of $200\mu m$. This diameter is the $1/e^2$ diameter, which means that the energy at a position 100 μm away from the center of the laser spot is $1/e^2$ of that energy at the center of the laser. If the diameter of a fiber is smaller than the diameter of the laser, Figure 110 represents the relationship between the laser power and the height of a fiber during the deposition process, while Figure 109 displays the relationship between the laser power and the height of a fiber during the deposition process if the fiber diameter is the same as that of the laser.

Two typical experimental relationships of the applied laser power versus time are shown in Figure 111. Since the fiber height is proportional to time, the relationships of the laser power versus the height of a fiber during the actual deposition process should be the same as those shown in Figure 111.

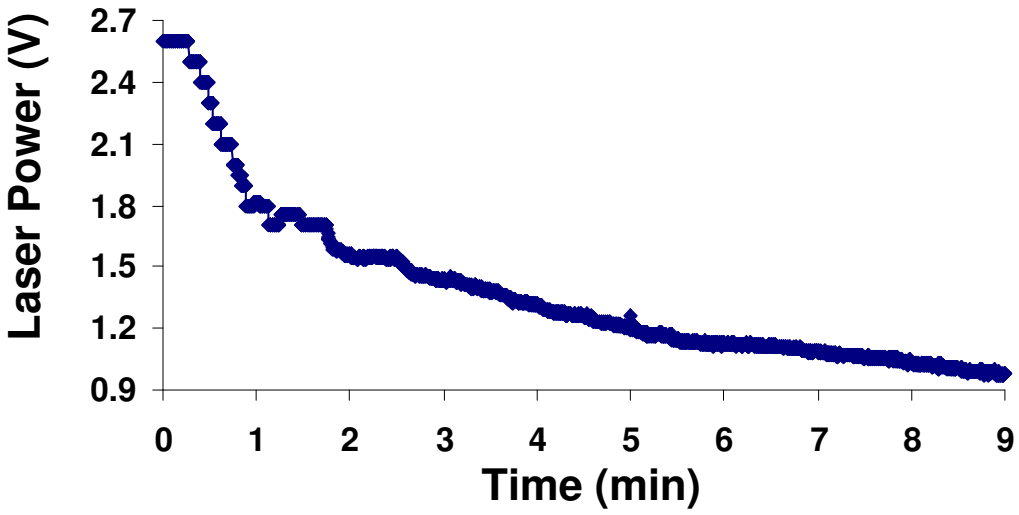

(a) L292-11, T_{max}=1143^oC

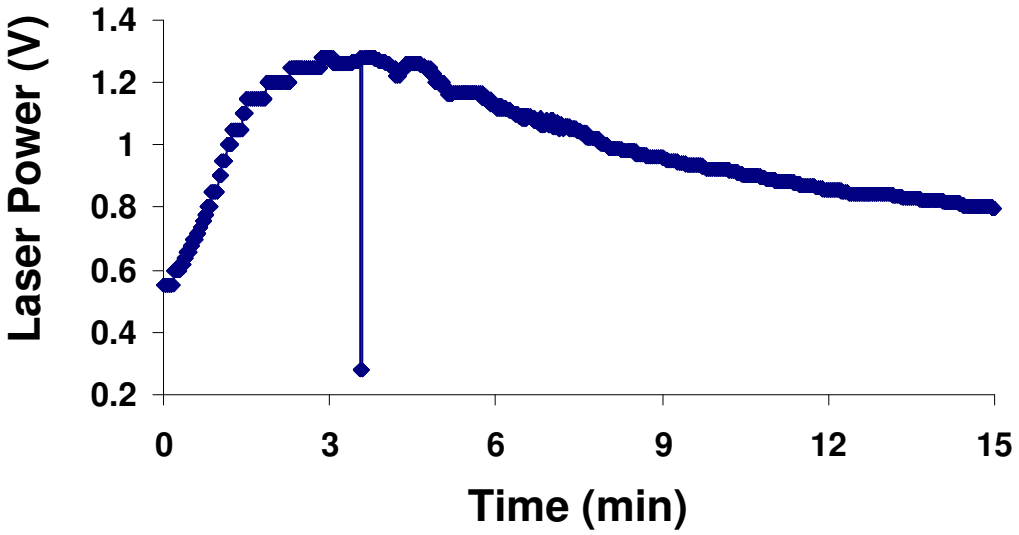

(b) L285-4, T_{max} = 1150^oC

Figure 111: The actual relationship of laser power and the fiber height during the deposition process for maintaining a constant T_{max}.

Comparing Figures 109 and 111 (a), it is observed that the manner in which the laser power changes with time, or height of a fiber, shown in those figures are very similar to each other. The similar change of the laser power versus the time, or height of a fiber, exists for both Figures 110 and 111 (b).

The SEM images of those two fibers are shown in Figure 112. Notice that the diameter of the bottom region of the fiber L292-11 is more than 400 μm. It is much larger than the diameter of the CO_2 laser, which is 200 μm. The reason that a larger diameter fiber could be fabricated was that the initial laser power was very high. The high laser power makes the temperatures of the region which is out of the range of the laser beam diameter high enough to cause the chemical deposition reaction to occur. This situation is similar to applying the laser power on the same size area as both the substrate and the fiber. Therefore, the way the laser power changes in Figures 109 and 111 (a) are similar to each other during the early deposition process.

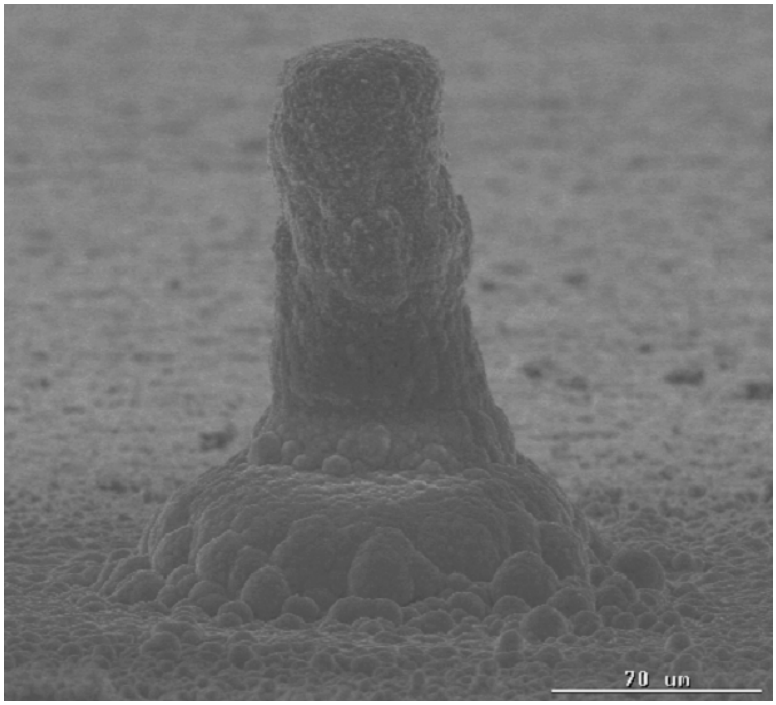

(a) L292-11, T_{max}=1143^oC, H_2/MTS=10

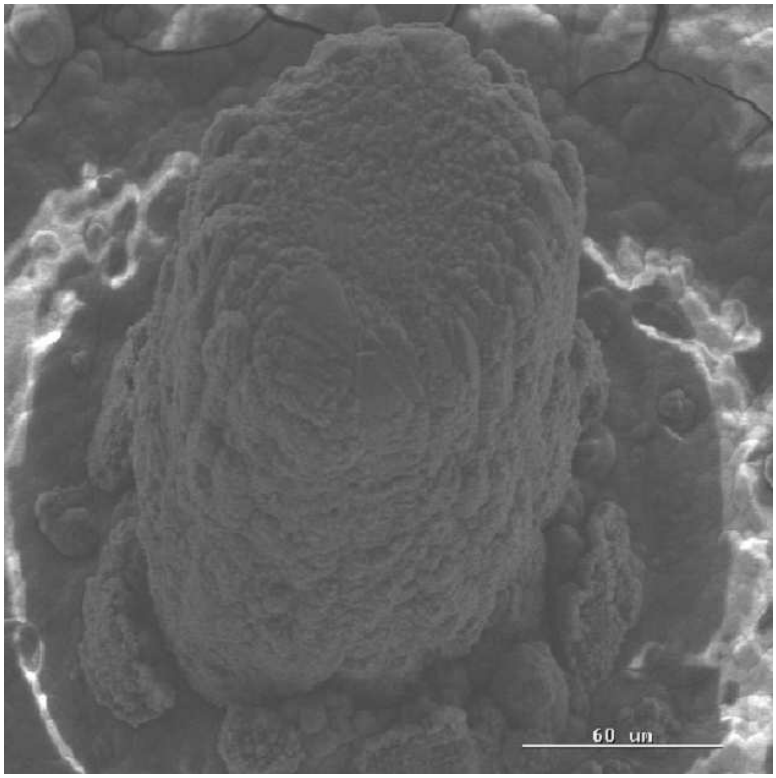

(b) L285-4, T_{max} = 1150^oC, H_2/MTS=20

Figure 112: The SEM figures of fibers L292-11 and L285-4.

The fiber (L285-4) displayed in Figure 111 (b) has relatively constant diameter throughout its entire length. Its diameter is about 110 μm, which is the same as the diameter of the fiber in the current model. Figures 110 and 111 (b) reveal similar patterns of laser power change during the deposition process. That is the laser power begins to increase very quickly, reaches a maximum value, then starts to decrease as the deposition process continues. A relatively low laser power is needed to heat the pure substrate and thus generates a constant maximum temperature in the center of the laser application zone. For the actual fiber deposition case, such as the fabrication of fiber L285-4, the maximum temperature in the center of the laser spot might be even higher than the one of the fiber subsequently deposited.

The relatively low laser power in the beginning of the deposition process is due to the fact that the area affected by the laser heating on the pure substrate is larger than that of the subsequent laser heating on the previously deposited fiber. Because there is more energy input from the larger laser heating region, lower laser power might generate the same or even higher temperatures on the substrate surface. Therefore, these two situations presented in Figures 109 and 110 help to explain the two different patterns of laser power change during the actual SiC fiber deposition process.

Comparing Figures 109, 110, and 111, it is observed that to generate the same maximum temperature, much higher laser power is needed according to our simulation than that required during the actual fiber deposition process. One reason for this big discrepancy is the fact that, actually, the fiber and the substrate are not perfectly bonded, which will make less heat transferred from the top the fiber to the bottom of the substrate. Another reason is that since the diameter of the CO_2 laser is 200 μm, in our simulation, the laser heating effect is simulated as the heat generation within the exactly same area of 200 μm in diameter and the total energy input applied to that region is the same as total energy of the laser within a circular region in diameter of 200 μm. The fact is that the diameter of the CO_2 laser, actually, is the $1/e^2$ Gaussian half-width of the beam spot. Note that when r equals the diameter of the laser, the energy input at that location equals to $1/e^2$ times the energy input in the center of the laser beam, which is about 0.13534 of the center energy

input. Also the actual energy input out of the $1/e^2$ Gaussian half-width of the beam spot is not zero. Because the laser energy at the center of the laser beam is very high, the total actual energy input out of the region of 200 μm in diameter is significant too. Therefore, during the actual deposition process, more laser heating energy is applied to the top surface of either the substrate or the fiber. Also, the differences between the values of material properties applied in the simulation and those of the actual materials would contribute to the discrepancy between the actual and the simulation results.

8.3 Summary of Laser Heating Simulations

Two transient heat transfer models were created to study the effects of the laser heating on a SiC fiber and on a graphite substrate. The simulations showed that how the temperature changes with time right after the laser is turn on. It turned out that for both geometries, a fiber and a substrate, about 0.1 second is needed for the model to reach the steady state. The initial temperatures of the geometries have an important effect on how temperatures change with time. It also affects the time needed for the model to reach the steady state. The higher the initial temperature, the longer the time needed for the model to reach its steady state.

The relationships of laser power versus time, or in another words, the height of a fiber for maintaining constant maximum deposition temperature were obtained. Applying the laser energy either on a region with the same diameter as the fiber or on another region whose diameter is the same as the diameter of the CO_2 laser on the substrate, yielded two different laser power changing patterns. Factoring in the nature of the laser heating the results explained why two typical manners of laser power change with time occur during the actual deposition process.

CHAPTER IX

CONCLUSIONS AND RECOMMENDATIONS

The conclusions of each subject of this research have been presented in each chapter. This chapter briefly summarizes them and discuss the some recommendations for future studies.

9.1 Conclusions

The research reported here furthers the understanding of the thermodynamics and kinetics of the LCVD of SiC from methyltrichlorosilane (MTS or CH_3SiCl_3) hydrogen mixtures and identified processing conditions that produce short, crack free fibers which do not display the volcano-like morphology often observed in LCVD deposits.

The thermodynamics of the Chemical Vapor Deposition (CVD) of SiC from MTS and H_2 have been studied extensively. The results of thermodynamic calculations are applicable for the LCVD process. However, most of the previous studies emphasized the condensed phase diagram and the concentrations of the gaseous species. In this thesis, a set of thermodynamic calculations was carried out to predict the actual amount of SiC that would be deposited at equilibrium, which offers guidance for deposition of SiC fibers by the LCVD technique. Because of the large temperature gradient across the laser spot, deposition rates vary radially within the region heated by the laser and knowledge of this variation, obtained from the thermodynamic predictions, permits identifying processing conditions which minimize the variation in deposition rate and thus permits growth of flat-topped deposits, as opposed to those having a volcano-like shape. Thermodynamic calculations suggested the use of lower processing temperatures which experimentally proved advantageous for avoiding the volcano effect. A kinetic study determined that apparent activation energy of LCVD-SiC was 163 KJ/mol and its order of reaction with respect to the concentration of MTS was 0.36.

A coupled thermal and structural model was created to simulate the thermal residual

stress present in the SiC deposits. SiC fiber was the simulated geometry. There were four "snapshots" were considered during the entire fiber deposition process. The temperature distribution at each time point was obtained by applying appropriate laser power, which will generate the same maximum deposition temperature at the tip of the fibers of different heights. Then those temperature distributions were applied as the load for the structural models, which are the fibers of different heights. It was indicated by these simulations that the maximum thermal residual stress was present at the circumference of the bottom surface of the fiber. The value of the maximum thermal stress was about 1 Gpa. This value is close to the lowest reported tensile strength of CVD-SiC. Except the bottom surface of the fiber, the maximum thermal residual stress within the main body of the SiC fiber was predicted to be about 500 MPa. This value is much smaller than the reported tensile strength of CVD-SiC. This means that there should be no cracks generated within in the main body of the LCVD-SiC fibers, which was verified by the experiments very well.

In addition to this coupled thermal and stress model, two simulations about laser heating process were created. The transient laser heating model simulated the temperature distribution right after the laser beam was turned on. The study of the curve of laser power versus fiber height helped us to explained two different experimental laser power changing patterns.

9.2 Recommendations

9.2.1 Heat and Mass Transport Model

Comprehensive heat and mass transport models of LCVD carbon have been created by Dr. Chad Duty and Dr. Ryan Johnson. Most of the conclusions are applicable for SiC deposition. But it would be beneficial if a similar simulation of LCVD-SiC from MTS and H_2 were created. At least, this could confirm the conclusions of those earlier models.

9.2.2 Stability of the LCVD Equipment

Due to the complex nature of the LCVD process, it is very difficult to design, manufacture, and assembly the equipment. In return, performance of the equipment is not very stable. Sometimes, even two "identical" processing conditions failed to produce the same outcomes.

One reason for this is the leakage of the system. If possible, future researchers might need to improve the methods of sealing the system.

Another reason for the unstable performance of LCVD process is the temperature control system. Currently, the temperature control system is helpful, but the adjustment according to the temperature feedback is not fast enough. This causes the temperature control performance to be very sensitive to the pre-existing conditions including the current temperature, the surface finish of the substrate or previously deposited material, or even the laser power either initially or during the deposition process. Also, the accuracy of the temperature control is relatively low. This makes deposition occur over a range of temperature rather than at a desired set point. If the performance of the automatic temperature control function can be improved, it will benefit the LCVD deposition process significantly.

9.2.3 Material Properties of Deposits

Currently, it is very difficult to test the material properties of LCVD deposits due to their small size. But in order to apply those deposits into the actual applications, it is necessary to develop suitable characterization methods.

When the the material properties of those tiny geometries are available, the processing conditions can be adjusted accordingly to fabricate various materials with desirable material properties for the applications. In addition, the lack of the material properties of LCVD deposits also influences the accuracy of the simulations of the LCVD process. Currently, for most of the LCVD modeling, the material properties are all those of the bulk materials fabricated by the conventional methods. This limits the accuracy of the results of the simulation significantly.

9.2.4 Fabrication of Complex Geometries

In order to commercialized the LCVD technique, it has to be able to fabricate real parts. Since the simple shapes of LCVD deposits have been accomplished, the next step will be targeting at fabrication of complex geometries. This will need improvement of the performance of the current equipment as discussed above. The addition of extra lasers might also be needed.

APPENDIX A

EDS QUANTITATIVE ANALYSIS OF L284-8

Accelerating Voltage: 15 KeV
Live Time: 30 seconds

Take Off Angle: 39.6197°
Dead Time: 8.729

```
Quantitative Analysis

Fri Jun 25 15:18:59 2004

L284-8

Filter Fit Method
Chi-sqd = 1.72     Livetime = 30.0 Sec.
Standardless Analysis
Element   Relative      Error         Net       Error
          k-ratio     (1-Sigma)     Counts   (1-Sigma)
  C -K    0.04191 +/- 0.00349         133 +/-     11
  Si-K    0.95809 +/- 0.01031        9851 +/-    106

Adjustment Factors            K            L            M
  Z-Balance:              0.00000      0.00000      0.00000
  Shell:                  1.00000      1.00000      1.00000

PROZA Correction  Acc.Volt.= 15 kV  Take-off Angle=39.62 deg   Tilt = 30 deg
Number of Iterations = 6

Element  k-ratio     ZAF    Atom %  Element  Wt % Err.
         (calc.)                     Wt %    (1-Sigma)
  C -K    0.0299   8.942    46.09    26.78     +/- 2.23
  Si-K    0.6846   1.070    53.91    73.22     +/- 0.79
  Total                    100.00   100.00
```

APPENDIX B

VOLCANO ANALYSIS OF SIC LINES

```
Analysis Summary
----------------
File name: volcano-Tmax4.sfx

Estimated effects for Volcano
------------------------------------------------------------------------------
average = 1.97054   +/- 0.116726
A:Tmax  = -0.241155 +/- 0.443531
B:H2    = 0.815963  +/- 0.235525
C:Scan  = 0.0556678 +/- 0.2289
AA      = -0.323096 +/- 1.03499
AB      = 1.26111   +/- 0.787053
AC      = 0.342177  +/- 0.696048
BB      = -0.520798 +/- 0.420874
BC      = -0.824105 +/- 0.430575
CC      = 0.626321  +/- 0.359162
------------------------------------------------------------------------------
Standard errors are based on total error with 8 d.f.


The StatAdvisor
---------------
   This table shows each of the estimated effects and interactions.
Also shown is the standard error of each of the effects, which
measures their sampling error.  To plot the estimates in decreasing
order of importance, select Pareto Charts from the list of Graphical
Options.  To test the statistical significance of the effects, select
ANOVA Table from the list of Tabular Options.  You can then remove
insignificant effects by pressing the alternate mouse button,
selecting Analysis Options, and pressing the Exclude button.
```

Regression coeffs. for Volcano

constant	= -5.71278		
A:Tmax		= 0.0157641	
B:H2		= -0.176145	
C:Scan		= -14.2655	
AA	= -0.00000717991		
AB	= 0.000140124		
AC	= 0.00760392		
BB	= -0.000289332		
BC	= -0.0915672		
CC	= 13.9182		

The StatAdvisor

This pane displays the regression equation which has been fitted to the data. The equation of the fitted model is

Volcano = -5.71278 + 0.0157641*Tmax - 0.176145*H2 - 14.2655*Scan - 0.00000717991*Tmax^2 + 0.000140124*Tmax*H2 + 0.00760392*Tmax*Scan - 0.000289332*H2^2 - 0.0915672*H2*Scan + 13.9182*Scan^2

where the values of the variables are specified in their original units. To have STATGRAPHICS evaluate this function, select Predictions from the list of Tabular Options. To plot the function, select Response Plots from the list of Graphical Options.

Analysis of Variance for Volcano

Source	Sum of Squares	Df	Mean Square	F-Ratio	P-Value
A:Tmax	0.0172304	1	0.0172304	0.30	0.6015
B:H2	0.699551	1	0.699551	12.00	0.0085
C:Scan	0.00344722	1	0.00344722	0.06	0.8140
AA	0.00567988	1	0.00567988	0.10	0.7629
AB	0.149642	1	0.149642	2.57	0.1478
AC	0.0140855	1	0.0140855	0.24	0.6362
BB	0.0892454	1	0.0892454	1.53	0.2510
BC	0.21351	1	0.21351	3.66	0.0920
CC	0.177241	1	0.177241	3.04	0.1193
Total error	0.466274	8	0.0582842		
Total (corr.)	2.14	17			

R-squared = 78.2115 percent
R-squared (adjusted for d.f.) = 53.6994 percent
Standard Error of Est. = 0.241421
Mean absolute error = 0.121536
Durbin-Watson statistic = 2.39843

The StatAdvisor

The ANOVA table partitions the variability in Volcano into separate pieces for each of the effects. It then tests the statistical significance of each effect by comparing the mean square against an estimate of the experimental error. In this case, 1 effects have P-values less than 0.05, indicating that they are significantly different from zero at the 95.0% confidence level.

The R-Squared statistic indicates that the model as fitted explains 78.2115% of the variability in Volcano. The adjusted R-squared statistic, which is more suitable for comparing models with different numbers of independent variables, is 53.6994%. The standard error of the estimate shows the standard deviation of the residuals to be 0.241421. The mean absolute error (MAE) of 0.121536 is the average value of the residuals. The Durbin-Watson (DW) statistic tests the residuals to determine if there is any significant correlation based on the order in which they occur in your data file. Since the DW value is greater than 1.4, there is probably not any serious autocorrelation in the residuals.

Influential Points

Row	Leverage	Mahalanobis Distance	DFITS
4	0.7969	61.8376	-5.24848
6	0.614128	24.5234	3.62477
11	0.538448	17.7245	-2.64439
13	0.545123	18.2332	2.32378
14	0.877289	113.446	-2.10026
15	0.679719	33.0149	2.77965
16	0.762685	50.4797	-3.03209

Average leverage of single data point = 0.555556

The StatAdvisor

The table of influential data points lists all observations which have leverage values greater than 3 times that of an average data point, or which have an unusually large value of DFITS. Leverage is a statistic which measures how influential each observation is in determining the coefficients of the estimated model. DFITS is a statistic which measures how much the estimated coefficients would change if each observation was removed from the data set. In this case, an average data point would have a leverage value equal to 0.555556. There are no data points with more than 3 times the average leverage. There are 7 data points with unusually large values of DFITS.

APPENDIX C

THICKNESS ANALYSIS OF SIC LINES

Analysis Summary

File name: Poro-Tavg.sfx

Estimated effects for Thickness

average	= 0.811561	+/- 0.0633391
A:Tavg	= 0.0548351	+/- 0.0873976
B:H2	= -0.88923	+/- 0.0774498
C:Scan	= -0.265333	+/- 0.0763521
AA	= 0.00793267	+/- 0.105882
AB	= -0.105877	+/- 0.106155
AC	= 0.0112315	+/- 0.106037
BB	= 0.382991	+/- 0.0877363
BC	= 0.379414	+/- 0.0954719
CC	= -0.169637	+/- 0.0866895

Standard errors are based on total error with 8 d.f.

The StatAdvisor

This table shows each of the estimated effects and interactions. Also shown is the standard error of each of the effects, which measures their sampling error. To plot the estimates in decreasing order of importance, select Pareto Charts from the list of Graphical Options. To test the statistical significance of the effects, select ANOVA Table from the list of Tabular Options. You can then remove insignificant effects by pressing the alternate mouse button, selecting Analysis Options, and pressing the Exclude button.

Regression coeffs. for Thickness

constant	= 3.66142		
A:Tavg		=	-0.00379036
B:H2		=	0.0118182
C:Scan		=	-3.6655
AA	= 0.00000247896		
AB	= -0.000066173		
AC	= 0.00140394		
BB	= 0.000478739		
BC	= 0.0948535		
CC	= -8.48187		

The StatAdvisor

This pane displays the regression equation which has been fitted to the data. The equation of the fitted model is

Thickness = 3.66142 - 0.00379036*Tavg + 0.0118182*H2 - 3.6655*Scan + 0.00000247896*Tavg^2 - 0.000066173*Tavg*H2 + 0.00140394*Tavg*Scan + 0.000478739*H2^2 + 0.0948535*H2*Scan - 8.48187*Scan^2

where the values of the variables are specified in their original units. To have STATGRAPHICS evaluate this function, select Predictions from the list of Tabular Options. To plot the function, select Response Plots from the list of Graphical Options.

Analysis of Variance for Thickness

Source	Sum of Squares	Df	Mean Square	F-Ratio	P-Value
A:Tavg	0.0068738	1	0.0068738	0.39	0.5479
B:H2	2.30179	1	2.30179	131.82	0.0000
C:Scan	0.210872	1	0.210872	12.08	0.0084
AA	0.0000980097	1	0.0000980097	0.01	0.9421
AB	0.0173698	1	0.0173698	0.99	0.3478
AC	0.000195905	1	0.000195905	0.01	0.9183
BB	0.332733	1	0.332733	19.06	0.0024
BC	0.275774	1	0.275774	15.79	0.0041
CC	0.0668634	1	0.0668634	3.83	0.0861
Total error	0.139691	8	0.0174614		
Total (corr.)	3.505	17			

R-squared = 96.0145 percent
R-squared (adjusted for d.f.) = 91.5309 percent
Standard Error of Est. = 0.132141
Mean absolute error = 0.0697557
Durbin-Watson statistic = 1.7907

The StatAdvisor

The ANOVA table partitions the variability in Thickness into separate pieces for each of the effects. It then tests the statistical significance of each effect by comparing the mean square against an estimate of the experimental error. In this case, 4 effects have P-values less than 0.05, indicating that they are significantly different from zero at the 95.0% confidence level.

The R-Squared statistic indicates that the model as fitted explains 96.0145% of the variability in Thickness. The adjusted R-squared statistic, which is more suitable for comparing models with different numbers of independent variables, is 91.5309%. The standard error of the estimate shows the standard deviation of the residuals to be 0.132141. The mean absolute error (MAE) of 0.0697557 is the average value of the residuals. The Durbin-Watson (DW) statistic tests the residuals to determine if there is any significant correlation based on the order in which they occur in your data file. Since the DW value is greater than 1.4, there is probably not any serious autocorrelation in the residuals.

Influential Points

Row	Leverage	Mahalanobis Distance	DFITS
1	0.553428	18.8873	1.97193
3	0.655627	29.5201	-3.82517
6	0.580983	21.2434	-1.74046
11	0.557851	19.2457	3.21933
14	0.834404	79.6797	1.86916
16	0.753818	48.0514	3.44499

Average leverage of single data point = 0.555556

The StatAdvisor

The table of influential data points lists all observations which have leverage values greater than 3 times that of an average data point, or which have an unusually large value of DFITS. Leverage is a statistic which measures how influential each observation is in determining the coefficients of the estimated model. DFITS is a statistic which measures how much the estimated coefficients would change if each observation was removed from the data set. In this case, an average data point would have a leverage value equal to 0.555556. There are no data points with more than 3 times the average leverage. There are 6 data points with unusually large values of DFITS.

APPENDIX D

POROSITY ANALYSIS OF SIC LINES

Analysis Summary

File name: C:\SiC\L-S Res\L428-429-Mar16\L428-429.sfx

Estimated effects for Porosity

average	= 2.00608	+/- 0.124175
A:Tavg	= -0.180685	+/- 0.171341
B:H2	= 1.19455	+/- 0.151839
C:Scan	= 0.399645	+/- 0.149687
AA	= 0.0703413	+/- 0.20758
AB	= 0.25783	+/- 0.208115
AC	= -0.0950973	+/- 0.207882
BB	= -0.670877	+/- 0.172005
BC	= -0.667909	+/- 0.187171
CC	= 0.137076	+/- 0.169953

Standard errors are based on total error with 8 d.f.

The StatAdvisor

This table shows each of the estimated effects and interactions. Also shown is the standard error of each of the effects, which measures their sampling error. To plot the estimates in decreasing order of importance, select Pareto Charts from the list of Graphical Options. To test the statistical significance of the effects, select ANOVA Table from the list of Tabular Options. You can then remove insignificant effects by pressing the alternate mouse button, selecting Analysis Options, and pressing the Exclude button.

Regression coeffs. for Porosity

constant	= 48.6014		
A:Tavg		= -0.0669963	
B:H2		= -0.0920311	
C:Scan		= 22.3401	
AA	= 0.0000219817		
AB	= 0.000161143		
AC	= -0.0118872		
BB	= -0.000838596		
BC	= -0.166977		
CC	= 6.85381		

The StatAdvisor

This pane displays the regression equation which has been fitted to the data. The equation of the fitted model is

Porosity = 48.6014 - 0.0669963*Tavg - 0.0920311*H2 + 22.3401*Scan + 0.0000219817*Tavg^2 + 0.000161143*Tavg*H2 - 0.0118872*Tavg*Scan - 0.000838596*H2^2 - 0.166977*H2*Scan + 6.85381*Scan^2

where the values of the variables are specified in their original units. To have STATGRAPHICS evaluate this function, select Predictions from the list of Tabular Options. To plot the function, select Response Plots from the list of Graphical Options.

Analysis of Variance for Porosity

Source	Sum of Squares	Df	Mean Square	F-Ratio	P-Value
A:Tavg	0.0746316	1	0.0746316	1.11	0.3224
B:H2	4.1538	1	4.1538	61.89	0.0000
C:Scan	0.478394	1	0.478394	7.13	0.0284
AA	0.00770641	1	0.00770641	0.11	0.7434
AB	0.103005	1	0.103005	1.53	0.2505
AC	0.0140444	1	0.0140444	0.21	0.6595
BB	1.02095	1	1.02095	15.21	0.0045
BC	0.854598	1	0.854598	12.73	0.0073
CC	0.0436585	1	0.0436585	0.65	0.4432
Total error	0.536898	8	0.0671123		
Total (corr.)	7.48444	17			

R-squared = 92.8265 percent
R-squared (adjusted for d.f.) = 84.7563 percent
Standard Error of Est. = 0.25906
Mean absolute error = 0.122979
Durbin-Watson statistic = 2.40368

The StatAdvisor

The ANOVA table partitions the variability in Porosity into separate pieces for each of the effects. It then tests the statistical significance of each effect by comparing the mean square against an estimate of the experimental error. In this case, 4 effects have P-values less than 0.05, indicating that they are significantly different from zero at the 95.0% confidence level.

The R-Squared statistic indicates that the model as fitted explains 92.8265% of the variability in Porosity. The adjusted R-squared statistic, which is more suitable for comparing models with different numbers of independent variables, is 84.7563%. The standard error of the estimate shows the standard deviation of the residuals to be 0.25906. The mean absolute error (MAE) of 0.122979 is the average value of the residuals. The Durbin-Watson (DW) statistic tests the residuals to determine if there is any significant correlation based on the order in which they occur in your data file. Since the DW value is greater than 1.4, there is probably not any serious autocorrelation in the residuals.

Influential Points

Row	Leverage	Mahalanobis Distance	DFITS
2	0.567058	20.0153	-1.67122
3	0.655627	29.5201	2.21676
6	0.580983	21.2434	7.42616
11	0.557851	19.2457	-2.09089
14	0.834404	79.6797	-2.57815
16	0.753818	48.0514	-6.28192

Average leverage of single data point = 0.555556

The StatAdvisor

The table of influential data points lists all observations which have leverage values greater than 3 times that of an average data point, or which have an unusually large value of DFITS. Leverage is a statistic which measures how influential each observation is in determining the coefficients of the estimated model. DFITS is a statistic which measures how much the estimated coefficients would change if each observation was removed from the data set. In this case, an average data point would have a leverage value equal to 0.555556. There are no data points with more than 3 times the average leverage. There are 6 data points with unusually large values of DFITS.

APPENDIX E

THERMAL ANALYSIS OF 3-D MODEL

```
finish
    /clear,nostart
    /filname,Th-175um,1
    /prep7
    h1=2715
    !substrate
    cylind,0,9525,0,2540,0,360
    !175um
    cylind,13,0,2540,2715,0,360
    cylind,16,13,2540,2715,0,360
    cylind,16,20,2540,2715,0,360
    cylind,20,25,2540,2715,0,360
    cylind,25,31,2540,2715,0,360
    cylind,31,38,2540,2715,0,360
    cylind,46,38,2540,2715,0,360
    cylind,46,55,2540,2715,0,360
    ET, 1, PLANE77
    ET, 2, SOLID90
    !defining graphite substrate material properties
    mp,dens,1,1.76e-15,,,,,
    mptemp,1,298.2,516.5,518.2,519.3,524.3,608.7
    mpdata,kxx,1,1,1.180E+08,7.930E+07,8.580E+07,1.000E+08,7.330E+07,7.430E+07
    mptemp,7,614.3,836.5,840.4,856.5,1133.7,1142.1
    mpdata,kxx,1,7,7.280E+07,5.130E+07,6.290E+07,5.050E+07,3.030E+07,3.290E+07
    mptemp,13,1147.6,1157.1,1159.8,1260.9,1272.1,1580.4
    mpdata,kxx,1,13,2.940E+07,4.040E+07,3.950E+07,3.550E+07,3.300E+07,3.940E+07
    mptemp,19,1583.2,1585.9,1594.3,1602.6,1811,1813.7
    mpdata,kxx,1,19,4.100E+07,3.630E+07,3.260E+07,3.460E+07,3.520E+07,3.450E+07
    mptemp,25,1991.5,2091.5,2102.6,2108.2,2236,2238.7
    mpdata,kxx,1,25,2.860E+07,1.760E+07,1.950E+07,2.520E+07,1.890E+07,2.020E+07
    mptemp,31,2244.3,2247,2358.2,2369.3,2622,2641.5
    mpdata,kxx,1,31,1.720E+07,2.030E+07,2.710E+07,2.030E+07,1.720E+07,1.600E+07
    mptemp,37,2972.1,3002.6,3022.1
    mpdata,kxx,1,37,1.330E+07,1.230E+07,1.770E+07
    MPTEMP,,,,,,,,
    mptemp,1,298.2,516.5,518.2,519.3,524.3,608.7
    mpdata,kyy,1,1,1.180E+08,7.930E+07,8.580E+07,1.000E+08,7.330E+07,7.430E+07
    mptemp,7,614.3,836.5,840.4,856.5,1133.7,1142.1
    mpdata,kyy,1,7,7.280E+07,5.130E+07,6.290E+07,5.050E+07,3.030E+07,3.290E+07
    mptemp,13,1147.6,1157.1,1159.8,1260.9,1272.1,1580.4
```

mpdata,kyy,1,13,2.940E+07,4.040E+07,3.950E+07,3.550E+07,3.300E+07,3.940E+07
mptemp,19,1583.2,1585.9,1594.3,1602.6,1811,1813.7
mpdata,kyy,1,19,4.100E+07,3.630E+07,3.260E+07,3.460E+07,3.520E+07,3.450E+07
mptemp,25,1991.5,2091.5,2102.6,2108.2,2236,2238.7
mpdata,kyy,1,25,2.860E+07,1.760E+07,1.950E+07,2.520E+07,1.890E+07,2.020E+07
mptemp,31,2244.3,2247,2358.2,2369.3,2622,2641.5
mpdata,kyy,1,31,1.720E+07,2.030E+07,2.710E+07,2.030E+07,1.720E+07,1.600E+07
mptemp,37,2972.1,3002.6,3022.1
mpdata,kyy,1,37,1.330E+07,1.230E+07,1.770E+07
MPTEMP,,,,,,,,
mptemp,1,298.2,516.5,518.2,519.3,524.3,608.7
mpdata,kzz,1,1,1.180E+08,7.930E+07,8.580E+07,1.000E+08,7.330E+07,7.430E+07
mptemp,7,614.3,836.5,840.4,856.5,1133.7,1142.1
mpdata,kzz,1,7,7.280E+07,5.130E+07,6.290E+07,5.050E+07,3.030E+07,3.290E+07
mptemp,13,1147.6,1157.1,1159.8,1260.9,1272.1,1580.4
mpdata,kzz,1,13,2.940E+07,4.040E+07,3.950E+07,3.550E+07,3.300E+07,3.940E+07
mptemp,19,1583.2,1585.9,1594.3,1602.6,1811,1813.7
mpdata,kzz,1,19,4.100E+07,3.630E+07,3.260E+07,3.460E+07,3.520E+07,3.450E+07
mptemp,25,1991.5,2091.5,2102.6,2108.2,2236,2238.7
mpdata,kzz,1,25,2.860E+07,1.760E+07,1.950E+07,2.520E+07,1.890E+07,2.020E+07
mptemp,31,2244.3,2247,2358.2,2369.3,2622,2641.5
mpdata,kzz,1,31,1.720E+07,2.030E+07,2.710E+07,2.030E+07,1.720E+07,1.600E+07
mptemp,37,2972.1,3002.6,3022.1
mpdata,kzz,1,37,1.330E+07,1.230E+07,1.770E+07 !mp,c,1,710e12
MPTEMP,,,,,,,,
mptemp,1,273,366,478,589,700,811
mpdata,c,1,1,8.290E+14,9.965E+14,1.177E+15,1.331E+15,1.470E+15,1.583E+15
mptemp,7,922,1033,1144,1255,1366,1447
mpdata,c,1,7,1.675E+15,1.746E+15,1.792E+15,1.821E+15,1.826E+15,1.846E+15
mptemp,13,1676,1694,1839,1868,2103,2232
mpdata,c,1,13,1.913E+15,2.052E+15,2.052E+15,2.014E+15,2.056E+15,2.056E+15
mptemp,19,2278,2555,2722,2778,3000,3077
mpdata,c,1,19,1.901E+15,2.131E+15,2.198E+15,2.190E+15,2.152E+15,1.800E+15
mptemp,25,3198,3221,3525,3656,3711,3719
mpdata,c,1,25,2.123E+15,2.114E+15,2.311E+15,2.500E+15,2.512E+15,2.341E+15
mptemp,31,3739,3767,3818,3905
mpdata,c,1,31,2.445E+15,2.755E+15,2.939E+15,3.203E+15
!defining SiC fiber material properties
!Thermal conductivity
!Material 2
MPTEMP,,,,,,,,
mptemp,1,185,270,413.2,483.2,573.2,598.2
mpdata,kxx,2,1,8.360E+07,6.550E+07,4.180E+07,3.870E+07,3.510E+07,3.390E+07
mptemp,7,683.2,783.2,883.2,963.2,1063.2,1168.2
mpdata,kxx,2,7,3.050E+07,2.720E+07,2.430E+07,2.300E+07,1.950E+07,1.800E+07
mptemp,13,1302.1,1582.1,1673.2
mpdata,kxx,2,13,1.440E+07,1.180E+07,1.090E+07
MPTEMP,,,,,,,,

mptemp,1,185,270,413.2,483.2,573.2,598.2
mpdata,kyy,2,1,8.360E+07,6.550E+07,4.180E+07,3.870E+07,3.510E+07,3.390E+07
mptemp,7,683.2,783.2,883.2,963.2,1063.2,1168.2
mpdata,kyy,2,7,3.050E+07,2.720E+07,2.430E+07,2.300E+07,1.950E+07,1.800E+07
mptemp,13,1302.1,1582.1,1673.2
mpdata,kyy,2,13,1.440E+07,1.180E+07,1.090E+07
MPTEMP,,,,,,,,
mptemp,1,185,270,413.2,483.2,573.2,598.2
mpdata,kzz,2,1,8.360E+07,6.550E+07,4.180E+07,3.870E+07,3.510E+07,3.390E+07
mptemp,7,683.2,783.2,883.2,963.2,1063.2,1168.2
mpdata,kzz,2,7,3.050E+07,2.720E+07,2.430E+07,2.300E+07,1.950E+07,1.800E+07
mptemp,13,1302.1,1582.1,1673.2
mpdata,kzz,2,13,1.440E+07,1.180E+07,1.090E+07
MPTEMP,,,,,,,,
mptemp,1,286.2,296.36,298.15,300,400,500
mpdata,c,2,1,6.402E+14,6.615E+14,6.674E+14,6.729E+14,8.789E+14,9.848E+14
mptemp,7,600,700,800,900,1000,1100
mpdata,c,2,7,1.052E+15,1.100E+15,1.138E+15,1.171E+15,1.270E+15,1.297E+15
mptemp,13,1200,1300,1400,1500,1600,1700
mpdata,c,2,13,1.320E+15,1.340E+15,1.357E+15,1.371E+15,1.384E+15,1.395E+15
mptemp,19,1800,1900,2000,2100,2200,2300
mpdata,c,2,19,1.405E+15,1.414E+15,1.422E+15,1.429E+15,1.436E+15,1.442E+15
mptemp,25,2400,2500,2600,2700,2800,2900
mpdata,c,2,25,1.447E+15,1.452E+15,1.457E+15,1.461E+15,1.465E+15,1.469E+15
!Material 3
MPTEMP,,,,,,,,
mptemp,1,185,270,413.2,483.2,573.2,598.2
mpdata,kxx,3,1,8.360E+07,6.550E+07,4.180E+07,3.870E+07,3.510E+07,3.390E+07
mptemp,7,683.2,783.2,883.2,963.2,1063.2,1168.2
mpdata,kxx,3,7,3.050E+07,2.720E+07,2.430E+07,2.300E+07,1.950E+07,1.800E+07
mptemp,13,1302.1,1582.1,1673.2
mpdata,kxx,3,13,1.440E+07,1.180E+07,1.090E+07
MPTEMP,,,,,,,,
mptemp,1,185,270,413.2,483.2,573.2,598.2
mpdata,kyy,3,1,8.360E+07,6.550E+07,4.180E+07,3.870E+07,3.510E+07,3.390E+07
mptemp,7,683.2,783.2,883.2,963.2,1063.2,1168.2
mpdata,kyy,3,7,3.050E+07,2.720E+07,2.430E+07,2.300E+07,1.950E+07,1.800E+07
mptemp,13,1302.1,1582.1,1673.2
mpdata,kyy,3,13,1.440E+07,1.180E+07,1.090E+07
MPTEMP,,,,,,,,
mptemp,1,185,270,413.2,483.2,573.2,598.2
mpdata,kzz,3,1,8.360E+07,6.550E+07,4.180E+07,3.870E+07,3.510E+07,3.390E+07
mptemp,7,683.2,783.2,883.2,963.2,1063.2,1168.2
mpdata,kzz,3,7,3.050E+07,2.720E+07,2.430E+07,2.300E+07,1.950E+07,1.800E+07
mptemp,13,1302.1,1582.1,1673.2
mpdata,kzz,3,13,1.440E+07,1.180E+07,1.090E+07
MPTEMP,,,,,,,,
mptemp,1,286.2,296.36,298.15,300,400,500

mpdata,c,3,1,6.402E+14,6.615E+14,6.674E+14,6.729E+14,8.789E+14,9.848E+14
mptemp,7,600,700,800,900,1000,1100
mpdata,c,3,7,1.052E+15,1.100E+15,1.138E+15,1.171E+15,1.270E+15,1.297E+15
mptemp,13,1200,1300,1400,1500,1600,1700
mpdata,c,3,13,1.320E+15,1.340E+15,1.357E+15,1.371E+15,1.384E+15,1.395E+15
mptemp,19,1800,1900,2000,2100,2200,2300
mpdata,c,3,19,1.405E+15,1.414E+15,1.422E+15,1.429E+15,1.436E+15,1.442E+15
mptemp,25,2400,2500,2600,2700,2800,2900
mpdata,c,3,25,1.447E+15,1.452E+15,1.457E+15,1.461E+15,1.465E+15,1.469E+15
!Material 4
MPTEMP,,,,,,,,
mptemp,1,185,270,413.2,483.2,573.2,598.2
mpdata,kxx,4,1,8.360E+07,6.550E+07,4.180E+07,3.870E+07,3.510E+07,3.390E+07
mptemp,7,683.2,783.2,883.2,963.2,1063.2,1168.2
mpdata,kxx,4,7,3.050E+07,2.720E+07,2.430E+07,2.300E+07,1.950E+07,1.800E+07
mptemp,13,1302.1,1582.1,1673.2
mpdata,kxx,4,13,1.440E+07,1.180E+07,1.090E+07
MPTEMP,,,,,,,,
mptemp,1,185,270,413.2,483.2,573.2,598.2
mpdata,kyy,4,1,8.360E+07,6.550E+07,4.180E+07,3.870E+07,3.510E+07,3.390E+07
mptemp,7,683.2,783.2,883.2,963.2,1063.2,1168.2
mpdata,kyy,4,7,3.050E+07,2.720E+07,2.430E+07,2.300E+07,1.950E+07,1.800E+07
mptemp,13,1302.1,1582.1,1673.2
mpdata,kyy,4,13,1.440E+07,1.180E+07,1.090E+07
MPTEMP,,,,,,,,
mptemp,1,185,270,413.2,483.2,573.2,598.2
mpdata,kzz,4,1,8.360E+07,6.550E+07,4.180E+07,3.870E+07,3.510E+07,3.390E+07
mptemp,7,683.2,783.2,883.2,963.2,1063.2,1168.2
mpdata,kzz,4,7,3.050E+07,2.720E+07,2.430E+07,2.300E+07,1.950E+07,1.800E+07
mptemp,13,1302.1,1582.1,1673.2
mpdata,kzz,4,13,1.440E+07,1.180E+07,1.090E+07
MPTEMP,,,,,,,,
mptemp,1,286.2,296.36,298.15,300,400,500
mpdata,c,4,1,6.402E+14,6.615E+14,6.674E+14,6.729E+14,8.789E+14,9.848E+14
mptemp,7,600,700,800,900,1000,1100
mpdata,c,4,7,1.052E+15,1.100E+15,1.138E+15,1.171E+15,1.270E+15,1.297E+15
mptemp,13,1200,1300,1400,1500,1600,1700
mpdata,c,4,13,1.320E+15,1.340E+15,1.357E+15,1.371E+15,1.384E+15,1.395E+15
mptemp,19,1800,1900,2000,2100,2200,2300
mpdata,c,4,19,1.405E+15,1.414E+15,1.422E+15,1.429E+15,1.436E+15,1.442E+15
mptemp,25,2400,2500,2600,2700,2800,2900
mpdata,c,4,25,1.447E+15,1.452E+15,1.457E+15,1.461E+15,1.465E+15,1.469E+15
!Material 5
MPTEMP,,,,,,,,
mptemp,1,185,270,413.2,483.2,573.2,598.2
mpdata,kxx,5,1,8.360E+07,6.550E+07,4.180E+07,3.870E+07,3.510E+07,3.390E+07
mptemp,7,683.2,783.2,883.2,963.2,1063.2,1168.2
mpdata,kxx,5,7,3.050E+07,2.720E+07,2.430E+07,2.300E+07,1.950E+07,1.800E+07

mptemp,13,1302.1,1582.1,1673.2
mpdata,kxx,5,13,1.440E+07,1.180E+07,1.090E+07
MPTEMP,,,,,,,,
mptemp,1,185,270,413.2,483.2,573.2,598.2
mpdata,kyy,5,1,8.360E+07,6.550E+07,4.180E+07,3.870E+07,3.510E+07,3.390E+07
mptemp,7,683.2,783.2,883.2,963.2,1063.2,1168.2
mpdata,kyy,5,7,3.050E+07,2.720E+07,2.430E+07,2.300E+07,1.950E+07,1.800E+07
mptemp,13,1302.1,1582.1,1673.2
mpdata,kyy,5,13,1.440E+07,1.180E+07,1.090E+07
MPTEMP,,,,,,,,
mptemp,1,185,270,413.2,483.2,573.2,598.2
mpdata,kzz,5,1,8.360E+07,6.550E+07,4.180E+07,3.870E+07,3.510E+07,3.390E+07
mptemp,7,683.2,783.2,883.2,963.2,1063.2,1168.2
mpdata,kzz,5,7,3.050E+07,2.720E+07,2.430E+07,2.300E+07,1.950E+07,1.800E+07
mptemp,13,1302.1,1582.1,1673.2
mpdata,kzz,5,13,1.440E+07,1.180E+07,1.090E+07
MPTEMP,,,,,,,,
mptemp,1,286.2,296.36,298.15,300,400,500
mpdata,c,5,1,6.402E+14,6.615E+14,6.674E+14,6.729E+14,8.789E+14,9.848E+14
mptemp,7,600,700,800,900,1000,1100
mpdata,c,5,7,1.052E+15,1.100E+15,1.138E+15,1.171E+15,1.270E+15,1.297E+15
mptemp,13,1200,1300,1400,1500,1600,1700
mpdata,c,5,13,1.320E+15,1.340E+15,1.357E+15,1.371E+15,1.384E+15,1.395E+15
mptemp,19,1800,1900,2000,2100,2200,2300
mpdata,c,5,19,1.405E+15,1.414E+15,1.422E+15,1.429E+15,1.436E+15,1.442E+15
mptemp,25,2400,2500,2600,2700,2800,2900
mpdata,c,5,25,1.447E+15,1.452E+15,1.457E+15,1.461E+15,1.465E+15,1.469E+15
!Material 6
MPTEMP,,,,,,,,
mptemp,1,185,270,413.2,483.2,573.2,598.2
mpdata,kxx,6,1,8.360E+07,6.550E+07,4.180E+07,3.870E+07,3.510E+07,3.390E+07
mptemp,7,683.2,783.2,883.2,963.2,1063.2,1168.2
mpdata,kxx,6,7,3.050E+07,2.720E+07,2.430E+07,2.300E+07,1.950E+07,1.800E+07
mptemp,13,1302.1,1582.1,1673.2
mpdata,kxx,6,13,1.440E+07,1.180E+07,1.090E+07
MPTEMP,,,,,,,,
mptemp,1,185,270,413.2,483.2,573.2,598.2
mpdata,kyy,6,1,8.360E+07,6.550E+07,4.180E+07,3.870E+07,3.510E+07,3.390E+07
mptemp,7,683.2,783.2,883.2,963.2,1063.2,1168.2
mpdata,kyy,6,7,3.050E+07,2.720E+07,2.430E+07,2.300E+07,1.950E+07,1.800E+07
mptemp,13,1302.1,1582.1,1673.2
mpdata,kyy,6,13,1.440E+07,1.180E+07,1.090E+07
MPTEMP,,,,,,,,
mptemp,1,185,270,413.2,483.2,573.2,598.2
mpdata,kzz,6,1,8.360E+07,6.550E+07,4.180E+07,3.870E+07,3.510E+07,3.390E+07
mptemp,7,683.2,783.2,883.2,963.2,1063.2,1168.2
mpdata,kzz,6,7,3.050E+07,2.720E+07,2.430E+07,2.300E+07,1.950E+07,1.800E+07
mptemp,13,1302.1,1582.1,1673.2

mpdata,kzz,6,13,1.440E+07,1.180E+07,1.090E+07
MPTEMP,,,,,,,,
mptemp,1,286.2,296.36,298.15,300,400,500
mpdata,c,6,1,6.402E+14,6.615E+14,6.674E+14,6.729E+14,8.789E+14,9.848E+14
mptemp,7,600,700,800,900,1000,1100
mpdata,c,6,7,1.052E+15,1.100E+15,1.138E+15,1.171E+15,1.270E+15,1.297E+15
mptemp,13,1200,1300,1400,1500,1600,1700
mpdata,c,6,13,1.320E+15,1.340E+15,1.357E+15,1.371E+15,1.384E+15,1.395E+15
mptemp,19,1800,1900,2000,2100,2200,2300
mpdata,c,6,19,1.405E+15,1.414E+15,1.422E+15,1.429E+15,1.436E+15,1.442E+15
mptemp,25,2400,2500,2600,2700,2800,2900
mpdata,c,6,25,1.447E+15,1.452E+15,1.457E+15,1.461E+15,1.465E+15,1.469E+15
!Material 7
MPTEMP,,,,,,,,
mptemp,1,185,270,413.2,483.2,573.2,598.2
mpdata,kxx,7,1,8.360E+07,6.550E+07,4.180E+07,3.870E+07,3.510E+07,3.390E+07
mptemp,7,683.2,783.2,883.2,963.2,1063.2,1168.2
mpdata,kxx,7,7,3.050E+07,2.720E+07,2.430E+07,2.300E+07,1.950E+07,1.800E+07
mptemp,13,1302.1,1582.1,1673.2
mpdata,kxx,7,13,1.440E+07,1.180E+07,1.090E+07
MPTEMP,,,,,,,,
mptemp,1,185,270,413.2,483.2,573.2,598.2
mpdata,kyy,7,1,8.360E+07,6.550E+07,4.180E+07,3.870E+07,3.510E+07,3.390E+07
mptemp,7,683.2,783.2,883.2,963.2,1063.2,1168.2
mpdata,kyy,7,7,3.050E+07,2.720E+07,2.430E+07,2.300E+07,1.950E+07,1.800E+07
mptemp,13,1302.1,1582.1,1673.2
mpdata,kyy,7,13,1.440E+07,1.180E+07,1.090E+07
MPTEMP,,,,,,,,
mptemp,1,185,270,413.2,483.2,573.2,598.2
mpdata,kzz,7,1,8.360E+07,6.550E+07,4.180E+07,3.870E+07,3.510E+07,3.390E+07
mptemp,7,683.2,783.2,883.2,963.2,1063.2,1168.2
mpdata,kzz,7,7,3.050E+07,2.720E+07,2.430E+07,2.300E+07,1.950E+07,1.800E+07
mptemp,13,1302.1,1582.1,1673.2
mpdata,kzz,7,13,1.440E+07,1.180E+07,1.090E+07
MPTEMP,,,,,,,,
mptemp,1,286.2,296.36,298.15,300,400,500
mpdata,c,7,1,6.402E+14,6.615E+14,6.674E+14,6.729E+14,8.789E+14,9.848E+14
mptemp,7,600,700,800,900,1000,1100
mpdata,c,7,7,1.052E+15,1.100E+15,1.138E+15,1.171E+15,1.270E+15,1.297E+15
mptemp,13,1200,1300,1400,1500,1600,1700
mpdata,c,7,13,1.320E+15,1.340E+15,1.357E+15,1.371E+15,1.384E+15,1.395E+15
mptemp,19,1800,1900,2000,2100,2200,2300
mpdata,c,7,19,1.405E+15,1.414E+15,1.422E+15,1.429E+15,1.436E+15,1.442E+15
mptemp,25,2400,2500,2600,2700,2800,2900
mpdata,c,7,25,1.447E+15,1.452E+15,1.457E+15,1.461E+15,1.465E+15,1.469E+15
!Material 8
MPTEMP,,,,,,,,
mptemp,1,185,270,413.2,483.2,573.2,598.2

mpdata,kxx,8,1,8.360E+07,6.550E+07,4.180E+07,3.870E+07,3.510E+07,3.390E+07
mptemp,7,683.2,783.2,883.2,963.2,1063.2,1168.2
mpdata,kxx,8,7,3.050E+07,2.720E+07,2.430E+07,2.300E+07,1.950E+07,1.800E+07
mptemp,13,1302.1,1582.1,1673.2
mpdata,kxx,8,13,1.440E+07,1.180E+07,1.090E+07
MPTEMP,,,,,,,,
mptemp,1,185,270,413.2,483.2,573.2,598.2
mpdata,kyy,8,1,8.360E+07,6.550E+07,4.180E+07,3.870E+07,3.510E+07,3.390E+07
mptemp,7,683.2,783.2,883.2,963.2,1063.2,1168.2
mpdata,kyy,8,7,3.050E+07,2.720E+07,2.430E+07,2.300E+07,1.950E+07,1.800E+07
mptemp,13,1302.1,1582.1,1673.2
mpdata,kyy,8,13,1.440E+07,1.180E+07,1.090E+07
MPTEMP,,,,,,,,
mptemp,1,185,270,413.2,483.2,573.2,598.2
mpdata,kzz,8,1,8.360E+07,6.550E+07,4.180E+07,3.870E+07,3.510E+07,3.390E+07
mptemp,7,683.2,783.2,883.2,963.2,1063.2,1168.2
mpdata,kzz,8,7,3.050E+07,2.720E+07,2.430E+07,2.300E+07,1.950E+07,1.800E+07
mptemp,13,1302.1,1582.1,1673.2
mpdata,kzz,8,13,1.440E+07,1.180E+07,1.090E+07
MPTEMP,,,,,,,,
mptemp,1,286.2,296.36,298.15,300,400,500
mpdata,c,8,1,6.402E+14,6.615E+14,6.674E+14,6.729E+14,8.789E+14,9.848E+14
mptemp,7,600,700,800,900,1000,1100
mpdata,c,8,7,1.052E+15,1.100E+15,1.138E+15,1.171E+15,1.270E+15,1.297E+15
mptemp,13,1200,1300,1400,1500,1600,1700
mpdata,c,8,13,1.320E+15,1.340E+15,1.357E+15,1.371E+15,1.384E+15,1.395E+15
mptemp,19,1800,1900,2000,2100,2200,2300
mpdata,c,8,19,1.405E+15,1.414E+15,1.422E+15,1.429E+15,1.436E+15,1.442E+15
mptemp,25,2400,2500,2600,2700,2800,2900
mpdata,c,8,25,1.447E+15,1.452E+15,1.457E+15,1.461E+15,1.465E+15,1.469E+15
!Material 9
MPTEMP,,,,,,,,
mptemp,1,185,270,413.2,483.2,573.2,598.2
mpdata,kxx,9,1,8.360E+07,6.550E+07,4.180E+07,3.870E+07,3.510E+07,3.390E+07
mptemp,7,683.2,783.2,883.2,963.2,1063.2,1168.2
mpdata,kxx,9,7,3.050E+07,2.720E+07,2.430E+07,2.300E+07,1.950E+07,1.800E+07
mptemp,13,1302.1,1582.1,1673.2
mpdata,kxx,9,13,1.440E+07,1.180E+07,1.090E+07
MPTEMP,,,,,,,,
mptemp,1,185,270,413.2,483.2,573.2,598.2
mpdata,kyy,9,1,8.360E+07,6.550E+07,4.180E+07,3.870E+07,3.510E+07,3.390E+07
mptemp,7,683.2,783.2,883.2,963.2,1063.2,1168.2
mpdata,kyy,9,7,3.050E+07,2.720E+07,2.430E+07,2.300E+07,1.950E+07,1.800E+07
mptemp,13,1302.1,1582.1,1673.2
mpdata,kyy,9,13,1.440E+07,1.180E+07,1.090E+07
MPTEMP,,,,,,,,
mptemp,1,185,270,413.2,483.2,573.2,598.2
mpdata,kzz,9,1,8.360E+07,6.550E+07,4.180E+07,3.870E+07,3.510E+07,3.390E+07

mptemp,7,683.2,783.2,883.2,963.2,1063.2,1168.2
mpdata,kzz,9,7,3.050E+07,2.720E+07,2.430E+07,2.300E+07,1.950E+07,1.800E+07
mptemp,13,1302.1,1582.1,1673.2
mpdata,kzz,9,13,1.440E+07,1.180E+07,1.090E+07
MPTEMP,,,,,,,,
mptemp,1,286.2,296.36,298.15,300,400,500
mpdata,c,9,1,6.402E+14,6.615E+14,6.674E+14,6.729E+14,8.789E+14,9.848E+14
mptemp,7,600,700,800,900,1000,1100
mpdata,c,9,7,1.052E+15,1.100E+15,1.138E+15,1.171E+15,1.270E+15,1.297E+15
mptemp,13,1200,1300,1400,1500,1600,1700
mpdata,c,9,13,1.320E+15,1.340E+15,1.357E+15,1.371E+15,1.384E+15,1.395E+15
mptemp,19,1800,1900,2000,2100,2200,2300
mpdata,c,9,19,1.405E+15,1.414E+15,1.422E+15,1.429E+15,1.436E+15,1.442E+15
mptemp,25,2400,2500,2600,2700,2800,2900
mpdata,c,9,25,1.447E+15,1.452E+15,1.457E+15,1.461E+15,1.465E+15,1.469E+15
vsel,all
vglue,all
numcmp,area
numcmp,volu
numcmp,line
∗SET,incc,1e-4
!mapped mesh fiber on the substrate
type,1
!mapped mesh the top surface of the fiber
lsel,s,loc,z,2715-incc,2715+incc
lesize,all,,,8,,,,
asel,s,area,,5
aatt,2
amesh,all
asel,s,area,,23
aatt,3
amesh,all
asel,s,area,,25
aatt,4
amesh,all
asel,s,area,,27
aatt,5
amesh,all
asel,s,area,,29
aatt,6
amesh,all
asel,s,area,,31
aatt,7
amesh,all
asel,s,area,,33
aatt,8
amesh,all
asel,s,area,,35

```
aatt,9
amesh,all
!175um
lsel,s,loc,z,2540+incc,2715-incc
lesize,all,,,25
vsel,s,volu,,1
vatt,2
vsweep,all
vsel,s,volu,,2
vatt,3
vsweep,all
vsel,s,volu,,3
vatt,4
vsweep,all
vsel,s,volu,,4
vatt,5
vsweep,all
vsel,s,volu,,5
vatt,6
vsweep,all
vsel,s,volu,,6
vatt,7
vsweep,all
vsel,s,volu,,7
vatt,8
vsweep,all
vsel,s,volu,,8
vatt,9
vsweep,all
!Free Mesh the graphite substrate
type,2
mat,1
smrt,4
mshape,1,3d
mshkey,0
vsel,s,loc,z,incc,2540-incc
vmesh,all
!clear the mesh of the top surface of fiber
asel,s,loc,z,2715-incc,2715+incc
aclear,all
!Specify BCs
* DEL,_FNCNAME
* DEL,FNCMTID
* SET,FNCNAME, 'laserpw'
* DIM,%FNCNAME%,TABLE,6,17,1
!
! Begin of equation: 3.24e8*exp(-2*M0/10000)
%_FNCNAME%(0,0,1)= 0.0, -999
```

%_FNCNAME%(2,0,1)= 0.0
%_FNCNAME%(3,0,1)= 0.0
%_FNCNAME%(4,0,1)= 0.0
%_FNCNAME%(5,0,1)= 0.0
%_FNCNAME%(6,0,1)= 0.0
%_FNCNAME%(0,1,1)= 1.0, -1, 0, 0, 0, 0, 0
%_FNCNAME%(0,2,1)= 0.0, -2, 0, 1, 0, 0, -1
%_FNCNAME%(0,3,1)= 0, -3, 0, 1, -1, 2, -2
%_FNCNAME%(0,4,1)= 0.0, -1, 0, 2, 0, 0, -3
%_FNCNAME%(0,5,1)= 0.0, -2, 0, 1, -3, 3, -1
%_FNCNAME%(0,6,1)= 0.0, -1, 0, 2, 0, 0, 2
%_FNCNAME%(0,7,1)= 0.0, -3, 0, 1, 2, 17, -1
%_FNCNAME%(0,8,1)= 0.0, -1, 0, 2, 0, 0, 3
%_FNCNAME%(0,9,1)= 0.0, -4, 0, 1, 3, 17, -1
%_FNCNAME%(0,10,1)= 0.0, -1, 0, 1, -3, 1, -4
%_FNCNAME%(0,11,1)= 0.0, -3, 0, 1, -2, 3, -1
%_FNCNAME%(0,12,1)= 0.0, -1, 0, 10000, 0, 0, -3
%_FNCNAME%(0,13,1)= 0.0, -2, 0, 1, -3, 4, -1
%_FNCNAME%(0,14,1)= 0.0, -1, 7, 1, -2, 0, 0
%_FNCNAME%(0,15,1)= 0.0, -2, 0, 7.099e7, 0, 0, -1
%_FNCNAME%(0,16,1)= 0.0, -3, 0, 1, -2, 3, -1
%_FNCNAME%(0,17,1)= 0.0, 99, 0, 1, -3, 0, 0
! End of equation: 3.24e8∗exp(-2∗M0/10000) !–¿
∗dim,topf,table,19,1,1,temp
∗set,topf(1,0),301,400,500,600,700,800,900,1000,1100,1200
∗set,topf(1,1),1778.85,2437.64,2715.56,2948.22,3142.95,3330.36,3522.82,3508.02,3865.21,3883.71
∗set,topf(11,0),1300,1400,1500,1600,1700,1800,1900,2000,2100
∗set,topf(11,1),4188.66,4250.58,4487.25,4610.60,4800.84,4964.99,5150.39,5314.59,5495.84
∗dim,sidef,table,19,1,1,temp
∗set,sidef(1,0),301,400,500,600,700,800,900,1000,1100,1200
∗set,sidef(1,1),682.74,975.78,1088.38,1179.88,1254.99,1326.61,1399.73,1390.83,1528.64,1532.99
∗set,sidef(11,0),1300,1400,1500,1600,1700,1800,1900,2000,2100
∗set,sidef(11,1),1649.70,1671.19,1760.99,1806.37,1877.83,1939.10,2008.38,2069.75,2137.19
∗dim,tops,table,19,1,1,temp
∗set,tops(1,0),301,400,500,600,700,800,900,1000,1100,1200
∗set,tops(1,1),33.76,66.53,74.88,80.30,84.02,87.23,90.33,88.30,95.26,94.14
∗set,tops(11,0),1300,1400,1500,1600,1700,1800,1900,2000,2100
∗set,tops(11,1),99.62,99.59,103.47,104.78,107.57,109.79,112.35,114.65,117.03
∗dim,sides,table,19,1,1,temp
∗set,sides(1,0),301,400,500,600,700,800,900,1000,1100,1200
∗set,sides(1,1),115.83,163.79,183.08,197.97,209.82,221.02,232.44,230.40,252.63,252.98
∗set,sides(11,0),1300,1400,1500,1600,1700,1800,1900,2000,2100
∗set,sides(11,1),271.89,275.24,289.91,297.36,309.19,319.44,331.11,341.54,353.12
FINISH
/SOLU
vsel,s,loc,z, -incc,h1+incc
cm,laserspot,node
outres,nsol,all,laserspot

```
kbc,1
time,3
nsubst,3
bcsoption,,incore,1200
!Specify BCs of fiber
asel,s,loc,z, h1-incc,h1+incc
bfa,all,hgen,%laserpw%
SFA,all,1,CONV, %topf% ,300
SFA,all, ,rdsf,.85, 1
asel,s,loc,z,2540+incc,h1-incc
sfa,all,1,conv,%sidef%,300
SFA,all, ,rdsf,.85, 2
!BCs of substrate
asel,s,area,,36
SFA,all,1,CONV, %tops% ,300
SFA,all, ,rdsf,.9, 3
asel,s,loc,z,incc,2540-incc
SFA,all,1,CONV, %sides% ,300
SFA,all, ,rdsf,.9, 4
asel,s,loc,z,-incc,incc
da,all,temp,300
STEF,0.567E-07
radopt,.0,.0001,0,1000,.1,.1
spctemp,1,300
spctemp,2,300
spctemp,3,300
spctemp,4,300
hemiopt,10
v2dopt,0,,0,200
allsel,all
solve
save,Th-175um-db,db,,all
FINISH
```

APPENDIX F

STRUCTURAL ANALYSIS OF 3-D MODEL

```
finish
    /clear,nostart
    /filname,Struc-175um-2ls,1
    /prep7
    h1=2715
    !substrate
    cylind,0,9525,0,2540,0,360
    !175um
    cylind,13,0,2540,2715,0,360
    cylind,16,13,2540,2715,0,360
    cylind,16,20,2540,2715,0,360
    cylind,20,25,2540,2715,0,360
    cylind,25,31,2540,2715,0,360
    cylind,31,38,2540,2715,0,360
    cylind,46,38,2540,2715,0,360
    cylind,46,55,2540,2715,0,360
    ET, 1, PLANE82
    ET, 2, SOLID95
    !defining graphite substrate material properties
    mp,dens,1,2.21e-15
    mp,ctex,1,10e-6
    mp,ctey,1,10e-6
    mp,ctez,1,10e-6
    mp,ex,1,2e4
    mp,prxy,1,0.2
    mp,reft,1,300
    !defining SiC fiber material properties
    !Material 2
    mp,dens,3,3.21e-15
    !Thermal expansion
    MPTEMP,,,,,,,,
    mptemp,1,200,250,293,300,400,500
    mpdata,ctex,2,1,1.5E-06,2.8E-06,3.3E-06,3.4E-06,4.0E-06,4.2E-06
    mptemp,7,600,700,800,900,1000,1200
    mpdata,ctex,2,7,4.5E-06,4.7E-06,4.9E-06,5.1E-06,5.3E-06,5.6E-06
    mptemp,13,1400,1600,1800,2000,2200,2400
    mpdata,ctex,2,13,6.0E-06,6.2E-06,6.5E-06,6.7E-06,6.9E-06,7.0E-06
    mptemp,19,2600,2800 mpdata,ctex,2,19,7.1E-06,7.1E-06
    MPTEMP,,,,,,,,
    mptemp,1,200,250,293,300,400,500
```

mpdata,ctey,2,1,1.5E-06,2.8E-06,3.3E-06,3.4E-06,4.0E-06,4.2E-06
mptemp,7,600,700,800,900,1000,1200
mpdata,ctey,2,7,4.5E-06,4.7E-06,4.9E-06,5.1E-06,5.3E-06,5.6E-06
mptemp,13,1400,1600,1800,2000,2200,2400
mpdata,ctey,2,13,6.0E-06,6.2E-06,6.5E-06,6.7E-06,6.9E-06,7.0E-06
mptemp,19,2600,2800
mpdata,ctey,2,19,7.1E-06,7.1E-06
MPTEMP,,,,,,,,
mptemp,1,200,250,293,300,400,500
mpdata,ctez,2,1,1.5E-06,2.8E-06,3.3E-06,3.4E-06,4.0E-06,4.2E-06
mptemp,7,600,700,800,900,1000,1200
mpdata,ctez,2,7,4.5E-06,4.7E-06,4.9E-06,5.1E-06,5.3E-06,5.6E-06
mptemp,13,1400,1600,1800,2000,2200,2400
mpdata,ctez,2,13,6.0E-06,6.2E-06,6.5E-06,6.7E-06,6.9E-06,7.0E-06
mptemp,19,2600,2800
mpdata,ctez,2,19,7.1E-06,7.1E-06
!Young's modulus !mp,ex,2,2.9e5
MPTEMP,,,,,,,,
mptemp,1,273,297,1210,1490,1670
mpdata,ex,2,1,4.8E+05,4.2E+05,3.7E+05,3.4E+05,2.7E+05
mp,prxy,2,0.19 mp,reft,2,1415
!Material 3
mp,dens,3,3.21e-15
!Thermal expansion
MPTEMP,,,,,,,,
mptemp,1,200,250,293,300,400,500
mpdata,ctex,3,1,1.5E-06,2.8E-06,3.3E-06,3.4E-06,4.0E-06,4.2E-06
mptemp,7,600,700,800,900,1000,1200
mpdata,ctex,3,7,4.5E-06,4.7E-06,4.9E-06,5.1E-06,5.3E-06,5.6E-06
mptemp,13,1400,1600,1800,2000,2200,2400
mpdata,ctex,3,13,6.0E-06,6.2E-06,6.5E-06,6.7E-06,6.9E-06,7.0E-06
mptemp,19,2600,2800
mpdata,ctex,3,19,7.1E-06,7.1E-06
MPTEMP,,,,,,,,
mptemp,1,200,250,293,300,400,500
mpdata,ctey,3,1,1.5E-06,2.8E-06,3.3E-06,3.4E-06,4.0E-06,4.2E-06
mptemp,7,600,700,800,900,1000,1200
mpdata,ctey,3,7,4.5E-06,4.7E-06,4.9E-06,5.1E-06,5.3E-06,5.6E-06
mptemp,13,1400,1600,1800,2000,2200,2400
mpdata,ctey,3,13,6.0E-06,6.2E-06,6.5E-06,6.7E-06,6.9E-06,7.0E-06
mptemp,19,2600,2800
mpdata,ctey,3,19,7.1E-06,7.1E-06
MPTEMP,,,,,,,,
mptemp,1,200,250,293,300,400,500
mpdata,ctez,3,1,1.5E-06,2.8E-06,3.3E-06,3.4E-06,4.0E-06,4.2E-06
mptemp,7,600,700,800,900,1000,1200
mpdata,ctez,3,7,4.5E-06,4.7E-06,4.9E-06,5.1E-06,5.3E-06,5.6E-06
mptemp,13,1400,1600,1800,2000,2200,2400

mpdata,ctez,3,13,6.0E-06,6.2E-06,6.5E-06,6.7E-06,6.9E-06,7.0E-06
mptemp,19,2600,2800
mpdata,ctez,3,19,7.1E-06,7.1E-06
!Young's modulus
MPTEMP,,,,,,,,
mptemp,1,273,297,1210,1490,1670
mpdata,ex,3,1,4.8E+05,4.2E+05,3.7E+05,3.4E+05,2.7E+05
mp,prxy,3,0.19 mp,reft,3,1393
!Material 4
mp,dens,4,3.21e-15
!Thermal expansion
MPTEMP,,,,,,,,
mptemp,1,200,250,293,300,400,500
mpdata,ctex,4,1,1.5E-06,2.8E-06,3.3E-06,3.4E-06,4.0E-06,4.2E-06
mptemp,7,600,700,800,900,1000,1200
mpdata,ctex,4,7,4.5E-06,4.7E-06,4.9E-06,5.1E-06,5.3E-06,5.6E-06
mptemp,13,1400,1600,1800,2000,2200,2400
mpdata,ctex,4,13,6.0E-06,6.2E-06,6.5E-06,6.7E-06,6.9E-06,7.0E-06
mptemp,19,2600,2800 mpdata,ctex,4,19,7.1E-06,7.1E-06
MPTEMP,,,,,,,,
mptemp,1,200,250,293,300,400,500
mpdata,ctey,4,1,1.5E-06,2.8E-06,3.3E-06,3.4E-06,4.0E-06,4.2E-06
mptemp,7,600,700,800,900,1000,1200
mpdata,ctey,4,7,4.5E-06,4.7E-06,4.9E-06,5.1E-06,5.3E-06,5.6E-06
mptemp,13,1400,1600,1800,2000,2200,2400
mpdata,ctey,4,13,6.0E-06,6.2E-06,6.5E-06,6.7E-06,6.9E-06,7.0E-06
mptemp,19,2600,2800
mpdata,ctey,4,19,7.1E-06,7.1E-06
MPTEMP,,,,,,,,
mptemp,1,200,250,293,300,400,500
mpdata,ctez,4,1,1.5E-06,2.8E-06,3.3E-06,3.4E-06,4.0E-06,4.2E-06
mptemp,7,600,700,800,900,1000,1200
mpdata,ctez,4,7,4.5E-06,4.7E-06,4.9E-06,5.1E-06,5.3E-06,5.6E-06
mptemp,13,1400,1600,1800,2000,2200,2400
mpdata,ctez,4,13,6.0E-06,6.2E-06,6.5E-06,6.7E-06,6.9E-06,7.0E-0 6 mptemp,19,2600,2800
mpdata,ctez,4,19,7.1E-06,7.1E-06
!Young's modulus
MPTEMP,,,,,,,,
mptemp,1,273,297,1210,1490,1670
mpdata,ex,4,1,4.8E+05,4.2E+05,3.7E+05,3.4E+05,2.7E+05
mp,prxy,4,0.19
mp,reft,4,1377
!Material 5
mp,dens,5,3.21e-15
!Thermal expansion
MPTEMP,,,,,,,,
mptemp,1,200,250,293,300,400,500
mpdata,ctex,5,1,1.5E-06,2.8E-06,3.3E-06,3.4E-06,4.0E-06,4.2E-06

mptemp,7,600,700,800,900,1000,1200
mpdata,ctex,5,7,4.5E-06,4.7E-06,4.9E-06,5.1E-06,5.3E-06,5.6E-06
mptemp,13,1400,1600,1800,2000,2200,2400
mpdata,ctex,5,13,6.0E-06,6.2E-06,6.5E-06,6.7E-06,6.9E-06,7.0E-06
mptemp,19,2600,2800
mpdata,ctex,5,19,7.1E-06,7.1E-06
MPTEMP,,,,,,,,
mptemp,1,200,250,293,300,400,500
mpdata,ctey,5,1,1.5E-06,2.8E-06,3.3E-06,3.4E-06,4.0E-06,4.2E-06
mptemp,7,600,700,800,900,1000,1200
mpdata,ctey,5,7,4.5E-06,4.7E-06,4.9E-06,5.1E-06,5.3E-06,5.6E-06
mptemp,13,1400,1600,1800,2000,2200,2400
mpdata,ctey,5,13,6.0E-06,6.2E-06,6.5E-06,6.7E-06,6.9E-06,7.0E-06
mptemp,19,2600,2800
mpdata,ctey,5,19,7.1E-06,7.1E-06
MPTEMP,,,,,,,,
mptemp,1,200,250,293,300,400,500
mpdata,ctez,5,1,1.5E-06,2.8E-06,3.3E-06,3.4E-06,4.0E-06,4.2E-06
mptemp,7,600,700,800,900,1000,1200
mpdata,ctez,5,7,4.5E-06,4.7E-06,4.9E-06,5.1E-06,5.3E-06,5.6E-06
mptemp,13,1400,1600,1800,2000,2200,2400
mpdata,ctez,5,13,6.0E-06,6.2E-06,6.5E-06,6.7E-06,6.9E-06,7.0E-06
mptemp,19,2600,2800 mpdata,ctez,5,19,7.1E-06,7.1E-06
!Young's modulus
MPTEMP,,,,,,,,
mptemp,1,273,297,1210,1490,1670
mpdata,ex,5,1,4.8E+05,4.2E+05,3.7E+05,3.4E+05,2.7E+05
mp,prxy,5,0.19
mp,reft,5,1355
!Material 6
mp,dens,6,3.21e-15
!Thermal expansion
MPTEMP,,,,,,,,
mptemp,1,200,250,293,300,400,500
mpdata,ctex,6,1,1.5E-06,2.8E-06,3.3E-06,3.4E-06,4.0E-06,4.2E-06
mptemp,7,600,700,800,900,1000,1200
mpdata,ctex,6,7,4.5E-06,4.7E-06,4.9E-06,5.1E-06,5.3E-06,5.6E-06
mptemp,13,1400,1600,1800,2000,2200,2400
mpdata,ctex,6,13,6.0E-06,6.2E-06,6.5E-06,6.7E-06,6.9E-06,7.0E-06
mptemp,19,2600,2800
mpdata,ctex,6,19,7.1E-06,7.1E-06
MPTEMP,,,,,,,,
mptemp,1,200,250,293,300,400,500
mpdata,ctey,6,1,1.5E-06,2.8E-06,3.3E-06,3.4E-06,4.0E-06,4.2E-06
mptemp,7,600,700,800,900,1000,1200
mpdata,ctey,6,7,4.5E-06,4.7E-06,4.9E-06,5.1E-06,5.3E-06,5.6E-06
mptemp,13,1400,1600,1800,2000,2200,2400
mpdata,ctey,6,13,6.0E-06,6.2E-06,6.5E-06,6.7E-06,6.9E-06,7.0E-06

mptemp,19,2600,2800
mpdata,ctey,6,19,7.1E-06,7.1E-06
MPTEMP,,,,,,,,
mptemp,1,200,250,293,300,400,500
mpdata,ctez,6,1,1.5E-06,2.8E-06,3.3E-06,3.4E-06,4.0E-06,4.2E-06
mptemp,7,600,700,800,900,1000,1200
mpdata,ctez,6,7,4.5E-06,4.7E-06,4.9E-06,5.1E-06,5.3E-06,5.6E-06
mptemp,13,1400,1600,1800,2000,2200,2400
mpdata,ctez,6,13,6.0E-06,6.2E-06,6.5E-06,6.7E-06,6.9E-06,7.0E-06
mptemp,19,2600,2800
mpdata,ctez,6,19,7.1E-06,7.1E-06
!Young's modulus
MPTEMP,,,,,,,,
mptemp,1,273,297,1210,1490,1670
mpdata,ex,6,1,4.8E+05,4.2E+05,3.7E+05,3.4E+05,2.7E+05
mp,prxy,6,0.19
mp,reft,6,1323
!Material 7
mp,dens,7,3.21e-15
!Thermal expansion
MPTEMP,,,,,,,,
mptemp,1,200,250,293,300,400,500
mpdata,ctex,7,1,1.5E-06,2.8E-06,3.3E-06,3.4E-06,4.0E-06,4.2E-06
mptemp,7,600,700,800,900,1000,1200
mpdata,ctex,7,7,4.5E-06,4.7E-06,4.9E-06,5.1E-06,5.3E-06,5.6E-06
mptemp,13,1400,1600,1800,2000,2200,2400
mpdata,ctex,7,13,6.0E-06,6.2E-06,6.5E-06,6.7E-06,6.9E-06,7.0E-06
mptemp,19,2600,2800
mpdata,ctex,7,19,7.1E-06,7.1E-06
MPTEMP,,,,,,,,
mptemp,1,200,250,293,300,400,500
mpdata,ctey,7,1,1.5E-06,2.8E-06,3.3E-06,3.4E-06,4.0E-06,4.2E-06
mptemp,7,600,700,800,900,1000,1200
mpdata,ctey,7,7,4.5E-06,4.7E-06,4.9E-06,5.1E-06,5.3E-06,5.6E-06
mptemp,13,1400,1600,1800,2000,2200,2400
mpdata,ctey,7,13,6.0E-06,6.2E-06,6.5E-06,6.7E-06,6.9E-06,7.0E-06
mptemp,19,2600,2800 mpdata,ctey,7,19,7.1E-06,7.1E-06
MPTEMP,,,,,,,,
mptemp,1,200,250,293,300,400,500
mpdata,ctez,7,1,1.5E-06,2.8E-06,3.3E-06,3.4E-06,4.0E-06,4.2E-06
mptemp,7,600,700,800,900,1000,1200
mpdata,ctez,7,7,4.5E-06,4.7E-06,4.9E-06,5.1E-06,5.3E-06,5.6E-06
mptemp,13,1400,1600,1800,2000,2200,2400
mpdata,ctez,7,13,6.0E-06,6.2E-06,6.5E-06,6.7E-06,6.9E-06,7.0E-06
mptemp,19,2600,2800
mpdata,ctez,7,19,7.1E-06,7.1E-06
!Young's modulus
MPTEMP,,,,,,,,

```
mptemp,1,273,297,1210,1490,1670
mpdata,ex,7,1,4.8E+05,4.2E+05,3.7E+05,3.4E+05,2.7E+05
mp,prxy,7,0.19
mp,reft,7,1284
!Material 8
mp,dens,8,3.21e-15
!Thermal expansion
MPTEMP,,,,,,,,
mptemp,1,200,250,293,300,400,500
mpdata,ctex,8,1,1.5E-06,2.8E-06,3.3E-06,3.4E-06,4.0E-06,4.2E-06
mptemp,7,600,700,800,900,1000,1200
mpdata,ctex,8,7,4.5E-06,4.7E-06,4.9E-06,5.1E-06,5.3E-06,5.6E-06
mptemp,13,1400,1600,1800,2000,2200,2400
mpdata,ctex,8,13,6.0E-06,6.2E-06,6.5E-06,6.7E-06,6.9E-06,7.0E-06
mptemp,19,2600,2800
mpdata,ctex,8,19,7.1E-06,7.1E-06
MPTEMP,,,,,,,,
mptemp,1,200,250,293,300,400,500
mpdata,ctey,8,1,1.5E-06,2.8E-06,3.3E-06,3.4E-06,4.0E-06,4.2E-06
mptemp,7,600,700,800,900,1000,1200
mpdata,ctey,8,7,4.5E-06,4.7E-06,4.9E-06,5.1E-06,5.3E-06,5.6E-06
mptemp,13,1400,1600,1800,2000,2200,2400
mpdata,ctey,8,13,6.0E-06,6.2E-06,6.5E-06,6.7E-06,6.9E-06,7.0E-06
mptemp,19,2600,2800
mpdata,ctey,8,19,7.1E-06,7.1E-06
MPTEMP,,,,,,,,
mptemp,1,200,250,293,300,400,500
mpdata,ctez,8,1,1.5E-06,2.8E-06,3.3E-06,3.4E-06,4.0E-06,4.2E-06
mptemp,7,600,700,800,900,1000,1200
mpdata,ctez,8,7,4.5E-06,4.7E-06,4.9E-06,5.1E-06,5.3E-06,5.6E-06
mptemp,13,1400,1600,1800,2000,2200,2400
mpdata,ctez,8,13,6.0E-06,6.2E-06,6.5E-06,6.7E-06,6.9E-06,7.0E-06
mptemp,19,2600,2800
mpdata,ctez,8,19,7.1E-06,7.1E-06
!Young's modulus
MPTEMP,,,,,,,,
mptemp,1,273,297,1210,1490,1670
mpdata,ex,8,1,4.8E+05,4.2E+05,3.7E+05,3.4E+05,2.7E+05
mp,prxy,8,0.19
mp,reft,8,1244
!Material 9
mp,dens,6,3.21e-15
!Thermal expansion
MPTEMP,,,,,,,,
mptemp,1,200,250,293,300,400,500
mpdata,ctex,9,1,1.5E-06,2.8E-06,3.3E-06,3.4E-06,4.0E-06,4.2E-06
mptemp,7,600,700,800,900,1000,1200
mpdata,ctex,9,7,4.5E-06,4.7E-06,4.9E-06,5.1E-06,5.3E-06,5.6E-06
```

```
mptemp,13,1400,1600,1800,2000,2200,2400
mpdata,ctex,9,13,6.0E-06,6.2E-06,6.5E-06,6.7E-06,6.9E-06,7.0E-06
mptemp,19,2600,2800
mpdata,ctex,9,19,7.1E-06,7.1E-06
MPTEMP,,,,,,,,
mptemp,1,200,250,293,300,400,500
mpdata,ctey,9,1,1.5E-06,2.8E-06,3.3E-06,3.4E-06,4.0E-06,4.2E-06
mptemp,7,600,700,800,900,1000,1200
mpdata,ctey,9,7,4.5E-06,4.7E-06,4.9E-06,5.1E-06,5.3E-06,5.6E-06
mptemp,13,1400,1600,1800,2000,2200,2400
mpdata,ctey,9,13,6.0E-06,6.2E-06,6.5E-06,6.7E-06,6.9E-06,7.0E-06
mptemp,19,2600,2800
mpdata,ctey,9,19,7.1E-06,7.1E-06
MPTEMP,,,,,,,,
mptemp,1,200,250,293,300,400,500
mpdata,ctez,9,1,1.5E-06,2.8E-06,3.3E-06,3.4E-06,4.0E-06,4.2E-06
mptemp,7,600,700,800,900,1000,1200
mpdata,ctez,9,7,4.5E-06,4.7E-06,4.9E-06,5.1E-06,5.3E-06,5.6E-06
mptemp,13,1400,1600,1800,2000,2200,2400
mpdata,ctez,9,13,6.0E-06,6.2E-06,6.5E-06,6.7E-06,6.9E-06,7.0E-06
mptemp,19,2600,2800
mpdata,ctez,9,19,7.1E-06,7.1E-06
!Young's modulus
MPTEMP,,,,,,,,
mptemp,1,273,297,1210,1490,1670
mpdata,ex,9,1,4.8E+05,4.2E+05,3.7E+05,3.4E+05,2.7E+05
mp,prxy,9,0.19
mp,reft,9,1213
vsel,all
vglue,all
numcmp,area
numcmp,volu
numcmp,line
*SET,incc,1e-4
!mapped mesh fiber on the substrate
type,1
!mapped mesh the top surface of the fiber
lsel,s,loc,z,2715-incc,2715+incc
lesize,all,,,8,,,,
asel,s,area,,5
aatt,2
amesh,all
asel,s,area,,23
aatt,3
amesh,all
asel,s,area,,25
aatt,4
amesh,all
```

```
asel,s,area,,27
aatt,5
amesh,all
asel,s,area,,29
aatt,6
amesh,all
asel,s,area,,31
aatt,7
amesh,all
asel,s,area,,33
aatt,8
amesh,all
asel,s,area,,35
aatt,9
amesh,all
!175um
lsel,s,loc,z,2540+incc,2715-incc
lesize,all,,,25
vsel,s,volu,,1
vatt,2
vsweep,all
vsel,s,volu,,2
vatt,3
vsweep,all
vsel,s,volu,,3
vatt,4
vsweep,all
vsel,s,volu,,4
vatt,5
vsweep,all
vsel,s,volu,,5
vatt,6
vsweep,all
vsel,s,volu,,6
vatt,7
vsweep,all
vsel,s,volu,,7
vatt,8
vsweep,all
vsel,s,volu,,8
vatt,9
vsweep,all
!Free Mesh the graphite substrate
type,2
mat,1
smrt,4
mshape,1,3d
mshkey,0
```

```
vsel,s,loc,z,
incc,2540-incc
vmesh,all
!clear the mesh of the top surface of fiber
asel,s,loc,z,2715-incc,2715+incc
aclear,all
/SOLU
antype,0
kbc,0
time,1
nsubst,3
ldread,temp,1,,,,'Th-175umentire-Jan11-onepart','rth',''
asel,s,loc,z,-incc,incc
da,all,all,0
outres,all,last
allsel,all
solve
save,Struc-49-1ls-db
/status,solu finish
```

APPENDIX G

THERMAL ANALYSIS OF 2-D MODEL

```
finish
    /clear,nostart
    /filname,Th-175um,1
    /prep7
    h1=2715
    !substrate
    rectng,0,9525,0,2540
    !175um
    rectng,0,13,2540,h1
    rectng,13,16,2540,h1
    rectng,16,20,2540,h1
    rectng,20,25,2540,h1
    rectng,25,31,2540,h1
    rectng,31,38,2540,h1
    rectng,46,38,2540,h1
    rectng,46,55,2540,h1
    ET, 1, PLANE77,,,1
    !defining graphite substrate material properties
    mp,dens,1,1.76e-15,,,,,
    mptemp,1,298.2,516.5,518.2,519.3,524.3,608.7
    mpdata,kxx,1,1,1.180E+08,7.930E+07,8.580E+07,1.000E+08,7.330E+07,7.430E+07
    mptemp,7,614.3,836.5,840.4,856.5,1133.7,1142.1
    mpdata,kxx,1,7,7.280E+07,5.130E+07,6.290E+07,5.050E+07,3.030E+07,3.290E+07
    mptemp,13,1147.6,1157.1,1159.8,1260.9,1272.1,1580.4
    mpdata,kxx,1,13,2.940E+07,4.040E+07,3.950E+07,3.550E+07,3.300E+07,3.940E+07
    mptemp,19,1583.2,1585.9,1594.3,1602.6,1811,1813.7
    mpdata,kxx,1,19,4.100E+07,3.630E+07,3.260E+07,3.460E+07,3.520E+07,3.450E+07
    mptemp,25,1991.5,2091.5,2102.6,2108.2,2236,2238.7
    mpdata,kxx,1,25,2.860E+07,1.760E+07,1.950E+07,2.520E+07,1.890E+07,2.020E+07
    mptemp,31,2244.3,2247,2358.2,2369.3,2622,2641.5
    mpdata,kxx,1,31,1.720E+07,2.030E+07,2.710E+07,2.030E+07,1.720E+07,1.600E+07
    mptemp,37,2972.1,3002.6,3022.1
    mpdata,kxx,1,37,1.330E+07,1.230E+07,1.770E+07
    MPTEMP,,,,,,,,
    mptemp,1,298.2,516.5,518.2,519.3,524.3,608.7
    mpdata,kyy,1,1,1.180E+08,7.930E+07,8.580E+07,1.000E+08,7.330E+07,7.430E+07
    mptemp,7,614.3,836.5,840.4,856.5,1133.7,1142.1
    mpdata,kyy,1,7,7.280E+07,5.130E+07,6.290E+07,5.050E+07,3.030E+07,3.290E+07
    mptemp,13,1147.6,1157.1,1159.8,1260.9,1272.1,1580.4
    mpdata,kyy,1,13,2.940E+07,4.040E+07,3.950E+07,3.550E+07,3.300E+07,3.940E+07
```

mptemp,19,1583.2,1585.9,1594.3,1602.6,1811,1813.7
mpdata,kyy,1,19,4.100E+07,3.630E+07,3.260E+07,3.460E+07,3.520E+07,3.450E+07
mptemp,25,1991.5,2091.5,2102.6,2108.2,2236,2238.7
mpdata,kyy,1,25,2.860E+07,1.760E+07,1.950E+07,2.520E+07,1.890E+07,2.020E+07
mptemp,31,2244.3,2247,2358.2,2369.3,2622,2641.5
mpdata,kyy,1,31,1.720E+07,2.030E+07,2.710E+07,2.030E+07,1.720E+07,1.600E+07
mptemp,37,2972.1,3002.6,3022.1
mpdata,kyy,1,37,1.330E+07,1.230E+07,1.770E+07
MPTEMP,,,,,,,,
mptemp,1,298.2,516.5,518.2,519.3,524.3,608.7
mpdata,kzz,1,1,1.180E+08,7.930E+07,8.580E+07,1.000E+08,7.330E+07,7.430E+07
mptemp,7,614.3,836.5,840.4,856.5,1133.7,1142.1
mpdata,kzz,1,7,7.280E+07,5.130E+07,6.290E+07,5.050E+07,3.030E+07,3.290E+07
mptemp,13,1147.6,1157.1,1159.8,1260.9,1272.1,1580.4
mpdata,kzz,1,13,2.940E+07,4.040E+07,3.950E+07,3.550E+07,3.300E+07,3.940E+07
mptemp,19,1583.2,1585.9,1594.3,1602.6,1811,1813.7
mpdata,kzz,1,19,4.100E+07,3.630E+07,3.260E+07,3.460E+07,3.520E+07,3.450E+07
mptemp,25,1991.5,2091.5,2102.6,2108.2,2236,2238.7
mpdata,kzz,1,25,2.860E+07,1.760E+07,1.950E+07,2.520E+07,1.890E+07,2.020E+07
mptemp,31,2244.3,2247,2358.2,2369.3,2622,2641.5
mpdata,kzz,1,31,1.720E+07,2.030E+07,2.710E+07,2.030E+07,1.720E+07,1.600E+07
mptemp,37,2972.1,3002.6,3022.1
mpdata,kzz,1,37,1.330E+07,1.230E+07,1.770E+07 !mp,c,1,710e12
MPTEMP,,,,,,,,
mptemp,1,273,366,478,589,700,811
mpdata,c,1,1,8.290E+14,9.965E+14,1.177E+15,1.331E+15,1.470E+15,1.583E+15
mptemp,7,922,1033,1144,1255,1366,1447
mpdata,c,1,7,1.675E+15,1.746E+15,1.792E+15,1.821E+15,1.826E+15,1.846E+15
mptemp,13,1676,1694,1839,1868,2103,2232
mpdata,c,1,13,1.913E+15,2.052E+15,2.052E+15,2.014E+15,2.056E+15,2.056E+15
mptemp,19,2278,2555,2722,2778,3000,3077
mpdata,c,1,19,1.901E+15,2.131E+15,2.198E+15,2.190E+15,2.152E+15,1.800E+15
mptemp,25,3198,3221,3525,3656,3711,3719
mpdata,c,1,25,2.123E+15,2.114E+15,2.311E+15,2.500E+15,2.512E+15,2.341E+15
mptemp,31,3739,3767,3818,3905
mpdata,c,1,31,2.445E+15,2.755E+15,2.939E+15,3.203E+15
!defining SiC fiber material properties
!Thermal conductivity
!Material 2
MPTEMP,,,,,,,,
mptemp,1,185,270,413.2,483.2,573.2,598.2
mpdata,kxx,2,1,8.360E+07,6.550E+07,4.180E+07,3.870E+07,3.510E+07,3.390E+07
mptemp,7,683.2,783.2,883.2,963.2,1063.2,1168.2
mpdata,kxx,2,7,3.050E+07,2.720E+07,2.430E+07,2.300E+07,1.950E+07,1.800E+07
mptemp,13,1302.1,1582.1,1673.2
mpdata,kxx,2,13,1.440E+07,1.180E+07,1.090E+07
MPTEMP,,,,,,,,
mptemp,1,185,270,413.2,483.2,573.2,598.2

mpdata,kyy,2,1,8.360E+07,6.550E+07,4.180E+07,3.870E+07,3.510E+07,3.390E+07
mptemp,7,683.2,783.2,883.2,963.2,1063.2,1168.2
mpdata,kyy,2,7,3.050E+07,2.720E+07,2.430E+07,2.300E+07,1.950E+07,1.800E+07
mptemp,13,1302.1,1582.1,1673.2
mpdata,kyy,2,13,1.440E+07,1.180E+07,1.090E+07
MPTEMP,,,,,,,,
mptemp,1,185,270,413.2,483.2,573.2,598.2
mpdata,kzz,2,1,8.360E+07,6.550E+07,4.180E+07,3.870E+07,3.510E+07,3.390E+07
mptemp,7,683.2,783.2,883.2,963.2,1063.2,1168.2
mpdata,kzz,2,7,3.050E+07,2.720E+07,2.430E+07,2.300E+07,1.950E+07,1.800E+07
mptemp,13,1302.1,1582.1,1673.2
mpdata,kzz,2,13,1.440E+07,1.180E+07,1.090E+07
MPTEMP,,,,,,,,
mptemp,1,286.2,296.36,298.15,300,400,500
mpdata,c,2,1,6.402E+14,6.615E+14,6.674E+14,6.729E+14,8.789E+14,9.848E+14
mptemp,7,600,700,800,900,1000,1100
mpdata,c,2,7,1.052E+15,1.100E+15,1.138E+15,1.171E+15,1.270E+15,1.297E+15
mptemp,13,1200,1300,1400,1500,1600,1700
mpdata,c,2,13,1.320E+15,1.340E+15,1.357E+15,1.371E+15,1.384E+15,1.395E+15
mptemp,19,1800,1900,2000,2100,2200,2300
mpdata,c,2,19,1.405E+15,1.414E+15,1.422E+15,1.429E+15,1.436E+15,1.442E+15
mptemp,25,2400,2500,2600,2700,2800,2900
mpdata,c,2,25,1.447E+15,1.452E+15,1.457E+15,1.461E+15,1.465E+15,1.469E+15
!Material 3
MPTEMP,,,,,,,,
mptemp,1,185,270,413.2,483.2,573.2,598.2
mpdata,kxx,3,1,8.360E+07,6.550E+07,4.180E+07,3.870E+07,3.510E+07,3.390E+07
mptemp,7,683.2,783.2,883.2,963.2,1063.2,1168.2
mpdata,kxx,3,7,3.050E+07,2.720E+07,2.430E+07,2.300E+07,1.950E+07,1.800E+07
mptemp,13,1302.1,1582.1,1673.2
mpdata,kxx,3,13,1.440E+07,1.180E+07,1.090E+07
MPTEMP,,,,,,,,
mptemp,1,185,270,413.2,483.2,573.2,598.2
mpdata,kyy,3,1,8.360E+07,6.550E+07,4.180E+07,3.870E+07,3.510E+07,3.390E+07
mptemp,7,683.2,783.2,883.2,963.2,1063.2,1168.2
mpdata,kyy,3,7,3.050E+07,2.720E+07,2.430E+07,2.300E+07,1.950E+07,1.800E+07
mptemp,13,1302.1,1582.1,1673.2
mpdata,kyy,3,13,1.440E+07,1.180E+07,1.090E+07
MPTEMP,,,,,,,,
mptemp,1,185,270,413.2,483.2,573.2,598.2
mpdata,kzz,3,1,8.360E+07,6.550E+07,4.180E+07,3.870E+07,3.510E+07,3.390E+07
mptemp,7,683.2,783.2,883.2,963.2,1063.2,1168.2
mpdata,kzz,3,7,3.050E+07,2.720E+07,2.430E+07,2.300E+07,1.950E+07,1.800E+07
mptemp,13,1302.1,1582.1,1673.2
mpdata,kzz,3,13,1.440E+07,1.180E+07,1.090E+07
MPTEMP,,,,,,,,
mptemp,1,286.2,296.36,298.15,300,400,500
mpdata,c,3,1,6.402E+14,6.615E+14,6.674E+14,6.729E+14,8.789E+14,9.848E+14

mptemp,7,600,700,800,900,1000,1100
mpdata,c,3,7,1.052E+15,1.100E+15,1.138E+15,1.171E+15,1.270E+15,1.297E+15
mptemp,13,1200,1300,1400,1500,1600,1700
mpdata,c,3,13,1.320E+15,1.340E+15,1.357E+15,1.371E+15,1.384E+15,1.395E+15
mptemp,19,1800,1900,2000,2100,2200,2300
mpdata,c,3,19,1.405E+15,1.414E+15,1.422E+15,1.429E+15,1.436E+15,1.442E+15
mptemp,25,2400,2500,2600,2700,2800,2900
mpdata,c,3,25,1.447E+15,1.452E+15,1.457E+15,1.461E+15,1.465E+15,1.469E+15
!Material 4
MPTEMP,,,,,,,,
mptemp,1,185,270,413.2,483.2,573.2,598.2
mpdata,kxx,4,1,8.360E+07,6.550E+07,4.180E+07,3.870E+07,3.510E+07,3.390E+07
mptemp,7,683.2,783.2,883.2,963.2,1063.2,1168.2
mpdata,kxx,4,7,3.050E+07,2.720E+07,2.430E+07,2.300E+07,1.950E+07,1.800E+07
mptemp,13,1302.1,1582.1,1673.2
mpdata,kxx,4,13,1.440E+07,1.180E+07,1.090E+07
MPTEMP,,,,,,,,
mptemp,1,185,270,413.2,483.2,573.2,598.2
mpdata,kyy,4,1,8.360E+07,6.550E+07,4.180E+07,3.870E+07,3.510E+07,3.390E+07
mptemp,7,683.2,783.2,883.2,963.2,1063.2,1168.2
mpdata,kyy,4,7,3.050E+07,2.720E+07,2.430E+07,2.300E+07,1.950E+07,1.800E+07
mptemp,13,1302.1,1582.1,1673.2
mpdata,kyy,4,13,1.440E+07,1.180E+07,1.090E+07
MPTEMP,,,,,,,,
mptemp,1,185,270,413.2,483.2,573.2,598.2
mpdata,kzz,4,1,8.360E+07,6.550E+07,4.180E+07,3.870E+07,3.510E+07,3.390E+07
mptemp,7,683.2,783.2,883.2,963.2,1063.2,1168.2
mpdata,kzz,4,7,3.050E+07,2.720E+07,2.430E+07,2.300E+07,1.950E+07,1.800E+07
mptemp,13,1302.1,1582.1,1673.2
mpdata,kzz,4,13,1.440E+07,1.180E+07,1.090E+07
MPTEMP,,,,,,,,
mptemp,1,286.2,296.36,298.15,300,400,500
mpdata,c,4,1,6.402E+14,6.615E+14,6.674E+14,6.729E+14,8.789E+14,9.848E+14
mptemp,7,600,700,800,900,1000,1100
mpdata,c,4,7,1.052E+15,1.100E+15,1.138E+15,1.171E+15,1.270E+15,1.297E+15
mptemp,13,1200,1300,1400,1500,1600,1700
mpdata,c,4,13,1.320E+15,1.340E+15,1.357E+15,1.371E+15,1.384E+15,1.395E+15
mptemp,19,1800,1900,2000,2100,2200,2300
mpdata,c,4,19,1.405E+15,1.414E+15,1.422E+15,1.429E+15,1.436E+15,1.442E+15
mptemp,25,2400,2500,2600,2700,2800,2900
mpdata,c,4,25,1.447E+15,1.452E+15,1.457E+15,1.461E+15,1.465E+15,1.469E+15
!Material 5
MPTEMP,,,,,,,,
mptemp,1,185,270,413.2,483.2,573.2,598.2
mpdata,kxx,5,1,8.360E+07,6.550E+07,4.180E+07,3.870E+07,3.510E+07,3.390E+07
mptemp,7,683.2,783.2,883.2,963.2,1063.2,1168.2
mpdata,kxx,5,7,3.050E+07,2.720E+07,2.430E+07,2.300E+07,1.950E+07,1.800E+07
mptemp,13,1302.1,1582.1,1673.2

mpdata,kxx,5,13,1.440E+07,1.180E+07,1.090E+07
MPTEMP,,,,,,,,
mptemp,1,185,270,413.2,483.2,573.2,598.2
mpdata,kyy,5,1,8.360E+07,6.550E+07,4.180E+07,3.870E+07,3.510E+07,3.390E+07
mptemp,7,683.2,783.2,883.2,963.2,1063.2,1168.2
mpdata,kyy,5,7,3.050E+07,2.720E+07,2.430E+07,2.300E+07,1.950E+07,1.800E+07
mptemp,13,1302.1,1582.1,1673.2
mpdata,kyy,5,13,1.440E+07,1.180E+07,1.090E+07
MPTEMP,,,,,,,,
mptemp,1,185,270,413.2,483.2,573.2,598.2
mpdata,kzz,5,1,8.360E+07,6.550E+07,4.180E+07,3.870E+07,3.510E+07,3.390E+07
mptemp,7,683.2,783.2,883.2,963.2,1063.2,1168.2
mpdata,kzz,5,7,3.050E+07,2.720E+07,2.430E+07,2.300E+07,1.950E+07,1.800E+07
mptemp,13,1302.1,1582.1,1673.2
mpdata,kzz,5,13,1.440E+07,1.180E+07,1.090E+07
MPTEMP,,,,,,,,
mptemp,1,286.2,296.36,298.15,300,400,500
mpdata,c,5,1,6.402E+14,6.615E+14,6.674E+14,6.729E+14,8.789E+14,9.848E+14
mptemp,7,600,700,800,900,1000,1100
mpdata,c,5,7,1.052E+15,1.100E+15,1.138E+15,1.171E+15,1.270E+15,1.297E+15
mptemp,13,1200,1300,1400,1500,1600,1700
mpdata,c,5,13,1.320E+15,1.340E+15,1.357E+15,1.371E+15,1.384E+15,1.395E+15
mptemp,19,1800,1900,2000,2100,2200,2300
mpdata,c,5,19,1.405E+15,1.414E+15,1.422E+15,1.429E+15,1.436E+15,1.442E+15
mptemp,25,2400,2500,2600,2700,2800,2900
mpdata,c,5,25,1.447E+15,1.452E+15,1.457E+15,1.461E+15,1.465E+15,1.469E+15
!Material 6
MPTEMP,,,,,,,,
mptemp,1,185,270,413.2,483.2,573.2,598.2
mpdata,kxx,6,1,8.360E+07,6.550E+07,4.180E+07,3.870E+07,3.510E+07,3.390E+07
mptemp,7,683.2,783.2,883.2,963.2,1063.2,1168.2
mpdata,kxx,6,7,3.050E+07,2.720E+07,2.430E+07,2.300E+07,1.950E+07,1.800E+07
mptemp,13,1302.1,1582.1,1673.2
mpdata,kxx,6,13,1.440E+07,1.180E+07,1.090E+07
MPTEMP,,,,,,,,
mptemp,1,185,270,413.2,483.2,573.2,598.2
mpdata,kyy,6,1,8.360E+07,6.550E+07,4.180E+07,3.870E+07,3.510E+07,3.390E+07
mptemp,7,683.2,783.2,883.2,963.2,1063.2,1168.2
mpdata,kyy,6,7,3.050E+07,2.720E+07,2.430E+07,2.300E+07,1.950E+07,1.800E+07
mptemp,13,1302.1,1582.1,1673.2
mpdata,kyy,6,13,1.440E+07,1.180E+07,1.090E+07
MPTEMP,,,,,,,,
mptemp,1,185,270,413.2,483.2,573.2,598.2
mpdata,kzz,6,1,8.360E+07,6.550E+07,4.180E+07,3.870E+07,3.510E+07,3.390E+07
mptemp,7,683.2,783.2,883.2,963.2,1063.2,1168.2
mpdata,kzz,6,7,3.050E+07,2.720E+07,2.430E+07,2.300E+07,1.950E+07,1.800E+07
mptemp,13,1302.1,1582.1,1673.2
mpdata,kzz,6,13,1.440E+07,1.180E+07,1.090E+07

MPTEMP,,,,,,,,
mptemp,1,286.2,296.36,298.15,300,400,500
mpdata,c,6,1,6.402E+14,6.615E+14,6.674E+14,6.729E+14,8.789E+14,9.848E+14
mptemp,7,600,700,800,900,1000,1100
mpdata,c,6,7,1.052E+15,1.100E+15,1.138E+15,1.171E+15,1.270E+15,1.297E+15
mptemp,13,1200,1300,1400,1500,1600,1700
mpdata,c,6,13,1.320E+15,1.340E+15,1.357E+15,1.371E+15,1.384E+15,1.395E+15
mptemp,19,1800,1900,2000,2100,2200,2300
mpdata,c,6,19,1.405E+15,1.414E+15,1.422E+15,1.429E+15,1.436E+15,1.442E+15
mptemp,25,2400,2500,2600,2700,2800,2900
mpdata,c,6,25,1.447E+15,1.452E+15,1.457E+15,1.461E+15,1.465E+15,1.469E+15
!Material 7
MPTEMP,,,,,,,,
mptemp,1,185,270,413.2,483.2,573.2,598.2
mpdata,kxx,7,1,8.360E+07,6.550E+07,4.180E+07,3.870E+07,3.510E+07,3.390E+07
mptemp,7,683.2,783.2,883.2,963.2,1063.2,1168.2
mpdata,kxx,7,7,3.050E+07,2.720E+07,2.430E+07,2.300E+07,1.950E+07,1.800E+07
mptemp,13,1302.1,1582.1,1673.2
mpdata,kxx,7,13,1.440E+07,1.180E+07,1.090E+07
MPTEMP,,,,,,,,
mptemp,1,185,270,413.2,483.2,573.2,598.2
mpdata,kyy,7,1,8.360E+07,6.550E+07,4.180E+07,3.870E+07,3.510E+07,3.390E+07
mptemp,7,683.2,783.2,883.2,963.2,1063.2,1168.2
mpdata,kyy,7,7,3.050E+07,2.720E+07,2.430E+07,2.300E+07,1.950E+07,1.800E+07
mptemp,13,1302.1,1582.1,1673.2
mpdata,kyy,7,13,1.440E+07,1.180E+07,1.090E+07
MPTEMP,,,,,,,,
mptemp,1,185,270,413.2,483.2,573.2,598.2
mpdata,kzz,7,1,8.360E+07,6.550E+07,4.180E+07,3.870E+07,3.510E+07,3.390E+07
mptemp,7,683.2,783.2,883.2,963.2,1063.2,1168.2
mpdata,kzz,7,7,3.050E+07,2.720E+07,2.430E+07,2.300E+07,1.950E+07,1.800E+07
mptemp,13,1302.1,1582.1,1673.2
mpdata,kzz,7,13,1.440E+07,1.180E+07,1.090E+07
MPTEMP,,,,,,,,
mptemp,1,286.2,296.36,298.15,300,400,500
mpdata,c,7,1,6.402E+14,6.615E+14,6.674E+14,6.729E+14,8.789E+14,9.848E+14
mptemp,7,600,700,800,900,1000,1100
mpdata,c,7,7,1.052E+15,1.100E+15,1.138E+15,1.171E+15,1.270E+15,1.297E+15
mptemp,13,1200,1300,1400,1500,1600,1700
mpdata,c,7,13,1.320E+15,1.340E+15,1.357E+15,1.371E+15,1.384E+15,1.395E+15
mptemp,19,1800,1900,2000,2100,2200,2300
mpdata,c,7,19,1.405E+15,1.414E+15,1.422E+15,1.429E+15,1.436E+15,1.442E+15
mptemp,25,2400,2500,2600,2700,2800,2900
mpdata,c,7,25,1.447E+15,1.452E+15,1.457E+15,1.461E+15,1.465E+15,1.469E+15
!Material 8
MPTEMP,,,,,,,,
mptemp,1,185,270,413.2,483.2,573.2,598.2
mpdata,kxx,8,1,8.360E+07,6.550E+07,4.180E+07,3.870E+07,3.510E+07,3.390E+07

mptemp,7,683.2,783.2,883.2,963.2,1063.2,1168.2
mpdata,kxx,8,7,3.050E+07,2.720E+07,2.430E+07,2.300E+07,1.950E+07,1.800E+07
mptemp,13,1302.1,1582.1,1673.2
mpdata,kxx,8,13,1.440E+07,1.180E+07,1.090E+07
MPTEMP,,,,,,,,
mptemp,1,185,270,413.2,483.2,573.2,598.2
mpdata,kyy,8,1,8.360E+07,6.550E+07,4.180E+07,3.870E+07,3.510E+07,3.390E+07
mptemp,7,683.2,783.2,883.2,963.2,1063.2,1168.2
mpdata,kyy,8,7,3.050E+07,2.720E+07,2.430E+07,2.300E+07,1.950E+07,1.800E+07
mptemp,13,1302.1,1582.1,1673.2
mpdata,kyy,8,13,1.440E+07,1.180E+07,1.090E+07
MPTEMP,,,,,,,,
mptemp,1,185,270,413.2,483.2,573.2,598.2
mpdata,kzz,8,1,8.360E+07,6.550E+07,4.180E+07,3.870E+07,3.510E+07,3.390E+07
mptemp,7,683.2,783.2,883.2,963.2,1063.2,1168.2
mpdata,kzz,8,7,3.050E+07,2.720E+07,2.430E+07,2.300E+07,1.950E+07,1.800E+07
mptemp,13,1302.1,1582.1,1673.2
mpdata,kzz,8,13,1.440E+07,1.180E+07,1.090E+07
MPTEMP,,,,,,,,
mptemp,1,286.2,296.36,298.15,300,400,500
mpdata,c,8,1,6.402E+14,6.615E+14,6.674E+14,6.729E+14,8.789E+14,9.848E+14
mptemp,7,600,700,800,900,1000,1100
mpdata,c,8,7,1.052E+15,1.100E+15,1.138E+15,1.171E+15,1.270E+15,1.297E+15
mptemp,13,1200,1300,1400,1500,1600,1700
mpdata,c,8,13,1.320E+15,1.340E+15,1.357E+15,1.371E+15,1.384E+15,1.395E+15
mptemp,19,1800,1900,2000,2100,2200,2300
mpdata,c,8,19,1.405E+15,1.414E+15,1.422E+15,1.429E+15,1.436E+15,1.442E+15
mptemp,25,2400,2500,2600,2700,2800,2900
mpdata,c,8,25,1.447E+15,1.452E+15,1.457E+15,1.461E+15,1.465E+15,1.469E+15
!Material 9
MPTEMP,,,,,,,,
mptemp,1,185,270,413.2,483.2,573.2,598.2
mpdata,kxx,9,1,8.360E+07,6.550E+07,4.180E+07,3.870E+07,3.510E+07,3.390E+07
mptemp,7,683.2,783.2,883.2,963.2,1063.2,1168.2
mpdata,kxx,9,7,3.050E+07,2.720E+07,2.430E+07,2.300E+07,1.950E+07,1.800E+07
mptemp,13,1302.1,1582.1,1673.2
mpdata,kxx,9,13,1.440E+07,1.180E+07,1.090E+07
MPTEMP,,,,,,,,
mptemp,1,185,270,413.2,483.2,573.2,598.2
mpdata,kyy,9,1,8.360E+07,6.550E+07,4.180E+07,3.870E+07,3.510E+07,3.390E+07
mptemp,7,683.2,783.2,883.2,963.2,1063.2,1168.2
mpdata,kyy,9,7,3.050E+07,2.720E+07,2.430E+07,2.300E+07,1.950E+07,1.800E+07
mptemp,13,1302.1,1582.1,1673.2
mpdata,kyy,9,13,1.440E+07,1.180E+07,1.090E+07
MPTEMP,,,,,,,,
mptemp,1,185,270,413.2,483.2,573.2,598.2
mpdata,kzz,9,1,8.360E+07,6.550E+07,4.180E+07,3.870E+07,3.510E+07,3.390E+07
mptemp,7,683.2,783.2,883.2,963.2,1063.2,1168.2

```
mpdata,kzz,9,7,3.050E+07,2.720E+07,2.430E+07,2.300E+07,1.950E+07,1.800E+07
mptemp,13,1302.1,1582.1,1673.2
mpdata,kzz,9,13,1.440E+07,1.180E+07,1.090E+07
MPTEMP,,,,,,,,
mptemp,1,286.2,296.36,298.15,300,400,500
mpdata,c,9,1,6.402E+14,6.615E+14,6.674E+14,6.729E+14,8.789E+14,9.848E+14
mptemp,7,600,700,800,900,1000,1100
mpdata,c,9,7,1.052E+15,1.100E+15,1.138E+15,1.171E+15,1.270E+15,1.297E+15
mptemp,13,1200,1300,1400,1500,1600,1700
mpdata,c,9,13,1.320E+15,1.340E+15,1.357E+15,1.371E+15,1.384E+15,1.395E+15
mptemp,19,1800,1900,2000,2100,2200,2300
mpdata,c,9,19,1.405E+15,1.414E+15,1.422E+15,1.429E+15,1.436E+15,1.442E+15
mptemp,25,2400,2500,2600,2700,2800,2900
mpdata,c,9,25,1.447E+15,1.452E+15,1.457E+15,1.461E+15,1.465E+15,1.469E+15
asel,all
aglue,all
numcmp,area
numcmp,line
*SET,incc,1e-4
!mapped mesh fiber on the substrate
type,1
!mapped mesh the top surface of the fiber
lsel,s,line,,5
lsel,a,line,,13
lesize,all,,,4,,,,
lsel,s,line,,16
lsel,a,line,,15
lesize,all,,,1,,,,
lsel,s,line,,18
lsel,a,line,,17
lesize,all,,,1,,,,
lsel,s,line,,20
lsel,a,line,,19
lesize,all,,,1,,,,
lsel,s,line,,22
lsel,a,line,,21
lesize,all,,,1,,,,
lsel,s,line,,24
lsel,a,line,,23
lesize,all,,,1,,,,
lsel,s,line,,26
lsel,a,line,,25
lesize,all,,,1,,,,
lsel,s,line,,28
lsel,a,line,,27
lesize,all,,,1,,,,
!vertical direction
lsel,s,loc,y,2540+incc,h1-incc
```

lesize,all,,,25
asel,s,area,,1
aatt,2
amesh,all
asel,s,area,,2
aatt,3
amesh,all
asel,s,area,,3
aatt,4
amesh,all
asel,s,area,,4
aatt,5
amesh,all
asel,s,area,,5
aatt,6
amesh,all
asel,s,area,,6
aatt,7
amesh,all
asel,s,area,,7
aatt,8
amesh,all
asel,s,area,,8
aatt,9
amesh,all
!Free Mesh the graphite substrate
type,1
mat,1
smrt,6
mshape,1,2d
mshkey,0
asel,s,loc,y,incc,2540-incc
amesh,all
!Specify BCs
∗DEL,_FNCNAME
∗DEL,_FNCMTID
∗DEL,_FNCCSYS
∗SET,_FNCNAME,'laserpw'
∗SET,_FNCCSYS,0
! /INPUT,laserpw.func
∗DIM,%_FNCNAME%,TABLE,6,18,1,,,,
%_FNCCSYS%
!
! Begin of equation: $3.24 * 10^8 * \exp(-2 * X^2/10000)$
∗SET,%_FNCNAME%(0,0,1), 0.0, -999
∗SET,%_FNCNAME%(2,0,1), 0.0
∗SET,%_FNCNAME%(3,0,1), 0.0
∗SET,%_FNCNAME%(4,0,1), 0.0

*SET,%_FNCNAME%(5,0,1), 0.0
*SET,%_FNCNAME%(6,0,1), 0.0
*SET,%_FNCNAME%(0,1,1), 1.0, -1, 0, 10, 0, 0, 0
*SET,%_FNCNAME%(0,2,1), 0.0, -2, 0, 7, 0, 0, -1
*SET,%_FNCNAME%(0,3,1), 0, -3, 0, 1, -1, 17, -2
*SET,%_FNCNAME%(0,4,1), 0.0, -1, 0, 6.245, 0, 0, -3
*SET,%_FNCNAME%(0,5,1), 0.0, -2, 0, 1, -1, 3, -3
*SET,%_FNCNAME%(0,6,1), 0.0, -1, 0, 0, 0, 0, 0
*SET,%_FNCNAME%(0,7,1), 0.0, -3, 0, 1, 0, 0, -1
*SET,%_FNCNAME%(0,8,1), 0.0, -4, 0, 1, -1, 2, -3
*SET,%_FNCNAME%(0,9,1), 0.0, -1, 0, 2, 0, 0, -4
*SET,%_FNCNAME%(0,10,1), 0.0, -3, 0, 1, -4, 3, -1
*SET,%_FNCNAME%(0,11,1), 0.0, -1, 0, 2, 0, 0, 2
*SET,%_FNCNAME%(0,12,1), 0.0, -4, 0, 1, 2, 17, -1
*SET,%_FNCNAME%(0,13,1), 0.0, -1, 0, 1, -3, 3, -4
*SET,%_FNCNAME%(0,14,1), 0.0, -3, 0, 10000, 0, 0, -1
*SET,%_FNCNAME%(0,15,1), 0.0, -4, 0, 1, -1, 4, -3
*SET,%_FNCNAME%(0,16,1), 0.0, -1, 7, 1, -4, 0, 0
*SET,%_FNCNAME%(0,17,1), 0.0, -3, 0, 1, -2, 3, -1
*SET,%_FNCNAME%(0,18,1), 0.0, 99, 0, 1, -3, 0, 0
! End of equation: $3.24*10^8*\exp(-2*X^2/10000)$
*dim,topf,table,19,1,1,temp
*set,topf(1,0),301,400,500,600,700,800,900,1000,1100,1200
*set,topf(1,1),1778.85,2437.64,2715.56,2948.22,3142.95,3330.36,3522.82,3508.02,3865.21,3883.71
*set,topf(11,0),1300,1400,1500,1600,1700,1800,1900,2000,2100
*set,topf(11,1),4188.66,4250.58,4487.25,4610.60,4800.84,4964.99,5150.39,5314.59,5495.84
*dim,sidef,table,19,1,1,temp
*set,sidef(1,0),301,400,500,600,700,800,900,1000,1100,1200
*set,sidef(1,1),682.74,975.78,1088.38,1179.88,1254.99,1326.61,1399.73,1390.83,1528.64,1532.99
*set,sidef(11,0),1300,1400,1500,1600,1700,1800,1900,2000,2100
*set,sidef(11,1),1649.70,1671.19,1760.99,1806.37,1877.83,1939.10,2008.38,2069.75,2137.19
*dim,tops,table,19,1,1,temp
*set,tops(1,0),301,400,500,600,700,800,900,1000,1100,1200
*set,tops(1,1),33.76,66.53,74.88,80.30,84.02,87.23,90.33,88.30,95.26,94.14
*set,tops(11,0),1300,1400,1500,1600,1700,1800,1900,2000,2100
*set,tops(11,1),99.62,99.59,103.47,104.78,107.57,109.79,112.35,114.65,117.03
*dim,sides,table,19,1,1,temp
*set,sides(1,0),301,400,500,600,700,800,900,1000,1100,1200
*set,sides(1,1),115.83,163.79,183.08,197.97,209.82,221.02,232.44,230.40,252.63,252.98
*set,sides(11,0),1300,1400,1500,1600,1700,1800,1900,2000,2100
*set,sides(11,1),271.89,275.24,289.91,297.36,309.19,319.44,331.11,341.54,353.12
FINISH
/SOLU
asel,s,loc,y, -incc,h1+incc
cm,laserspot,node
outres,nsol,all,laserspot
kbc,1
time,3

```
nsubst,3
!Specify BCs of fiber
lsel,s,loc,y, h1-incc,h1+incc
bfl,all,hgen,%laserpw%
SFl,all,CONV, %topf% ,,300
SFl,all,rdsf,.85,,1
lsel,s,line,,12
sfl,all,conv,%sidef%,,300
SFl,all,rdsf,.85,,2
!BCs of substrate
lsel,s,line,,29
SFl,all,CONV, %tops% ,,300
SFl,all,rdsf,.9,,3
lsel,s,line,,2
SFl,all,CONV, %sides% ,,300
SFl,all,rdsf,.9,,4
lsel,s,loc,y,-incc,incc
dl,all,,temp,300
STEF,0.567E-07
radopt,.0,.0001,0,1000,.1,.1
spctemp,1,300
spctemp,2,300
spctemp,3,300
spctemp,4,300
hemiopt,10
v2dopt,1,,0,200
allsel,all
solve
FINISH
```

APPENDIX H

STRUCTURAL ANALYSIS OF 2-D MODEL

```
finish
    /clear,nostart
    /filname,Coupled-175um,1
    /prep7
    h1=2715
    !substrate
    rectng,0,9525,0,2540
    !175um
    rectng,0,13,2540,h1
    rectng,13,16,2540,h1
    rectng,16,20,2540,h1
    rectng,20,25,2540,h1
    rectng,25,31,2540,h1
    rectng,31,38,2540,h1
    rectng,46,38,2540,h1
    rectng,46,55,2540,h1
    ET, 1, PLANE82,,,1
    !defining graphite substrate material properties
    mp,dens,1,2.21e-15
    mp,ctex,1,10e-6
    mp,ctey,1,10e-6
    mp,ctez,1,10e-6
    mp,ex,1,2e4
    mp,prxy,1,0.2
    mp,reft,1,300
    !defining SiC fiber material properties
    !Material 2
    mp,dens,3,3.21e-15
    !Thermal expansion
    MPTEMP,,,,,,,,
    mptemp,1,200,250,293,300,400,500
    mpdata,ctex,2,1,1.5E-06,2.8E-06,3.3E-06,3.4E-06,4.0E-06,4.2E-06
    mptemp,7,600,700,800,900,1000,1200
    mpdata,ctex,2,7,4.5E-06,4.7E-06,4.9E-06,5.1E-06,5.3E-06,5.6E-06
    mptemp,13,1400,1600,1800,2000,2200,2400
    mpdata,ctex,2,13,6.0E-06,6.2E-06,6.5E-06,6.7E-06,6.9E-06,7.0E-06
    mptemp,19,2600,2800 mpdata,ctex,2,19,7.1E-06,7.1E-06
    MPTEMP,,,,,,,,
    mptemp,1,200,250,293,300,400,500
    mpdata,ctey,2,1,1.5E-06,2.8E-06,3.3E-06,3.4E-06,4.0E-06,4.2E-06
```

mptemp,7,600,700,800,900,1000,1200
mpdata,ctey,2,7,4.5E-06,4.7E-06,4.9E-06,5.1E-06,5.3E-06,5.6E-06
mptemp,13,1400,1600,1800,2000,2200,2400
mpdata,ctey,2,13,6.0E-06,6.2E-06,6.5E-06,6.7E-06,6.9E-06,7.0E-06
mptemp,19,2600,2800
mpdata,ctey,2,19,7.1E-06,7.1E-06
MPTEMP,,,,,,,,
mptemp,1,200,250,293,300,400,500
mpdata,ctez,2,1,1.5E-06,2.8E-06,3.3E-06,3.4E-06,4.0E-06,4.2E-06
mptemp,7,600,700,800,900,1000,1200
mpdata,ctez,2,7,4.5E-06,4.7E-06,4.9E-06,5.1E-06,5.3E-06,5.6E-06
mptemp,13,1400,1600,1800,2000,2200,2400
mpdata,ctez,2,13,6.0E-06,6.2E-06,6.5E-06,6.7E-06,6.9E-06,7.0E-06
mptemp,19,2600,2800
mpdata,ctez,2,19,7.1E-06,7.1E-06
!Young's modulus !mp,ex,2,2.9e5
MPTEMP,,,,,,,,
mptemp,1,273,297,1210,1490,1670
mpdata,ex,2,1,4.8E+05,4.2E+05,3.7E+05,3.4E+05,2.7E+05
mp,prxy,2,0.19 mp,reft,2,1415
!Material 3
mp,dens,3,3.21e-15
!Thermal expansion
MPTEMP,,,,,,,,
mptemp,1,200,250,293,300,400,500
mpdata,ctex,3,1,1.5E-06,2.8E-06,3.3E-06,3.4E-06,4.0E-06,4.2E-06
mptemp,7,600,700,800,900,1000,1200
mpdata,ctex,3,7,4.5E-06,4.7E-06,4.9E-06,5.1E-06,5.3E-06,5.6E-06
mptemp,13,1400,1600,1800,2000,2200,2400
mpdata,ctex,3,13,6.0E-06,6.2E-06,6.5E-06,6.7E-06,6.9E-06,7.0E-06
mptemp,19,2600,2800
mpdata,ctex,3,19,7.1E-06,7.1E-06
MPTEMP,,,,,,,,
mptemp,1,200,250,293,300,400,500
mpdata,ctey,3,1,1.5E-06,2.8E-06,3.3E-06,3.4E-06,4.0E-06,4.2E-06
mptemp,7,600,700,800,900,1000,1200
mpdata,ctey,3,7,4.5E-06,4.7E-06,4.9E-06,5.1E-06,5.3E-06,5.6E-06
mptemp,13,1400,1600,1800,2000,2200,2400
mpdata,ctey,3,13,6.0E-06,6.2E-06,6.5E-06,6.7E-06,6.9E-06,7.0E-06
mptemp,19,2600,2800
mpdata,ctey,3,19,7.1E-06,7.1E-06
MPTEMP,,,,,,,,
mptemp,1,200,250,293,300,400,500
mpdata,ctez,3,1,1.5E-06,2.8E-06,3.3E-06,3.4E-06,4.0E-06,4.2E-06
mptemp,7,600,700,800,900,1000,1200
mpdata,ctez,3,7,4.5E-06,4.7E-06,4.9E-06,5.1E-06,5.3E-06,5.6E-06
mptemp,13,1400,1600,1800,2000,2200,2400
mpdata,ctez,3,13,6.0E-06,6.2E-06,6.5E-06,6.7E-06,6.9E-06,7.0E-06

mptemp,19,2600,2800
mpdata,ctez,3,19,7.1E-06,7.1E-06
!Young's modulus
MPTEMP,,,,,,,,
mptemp,1,273,297,1210,1490,1670
mpdata,ex,3,1,4.8E+05,4.2E+05,3.7E+05,3.4E+05,2.7E+05
mp,prxy,3,0.19 mp,reft,3,1393
!Material 4
mp,dens,4,3.21e-15
!Thermal expansion
MPTEMP,,,,,,,,
mptemp,1,200,250,293,300,400,500
mpdata,ctex,4,1,1.5E-06,2.8E-06,3.3E-06,3.4E-06,4.0E-06,4.2E-06
mptemp,7,600,700,800,900,1000,1200
mpdata,ctex,4,7,4.5E-06,4.7E-06,4.9E-06,5.1E-06,5.3E-06,5.6E-06
mptemp,13,1400,1600,1800,2000,2200,2400
mpdata,ctex,4,13,6.0E-06,6.2E-06,6.5E-06,6.7E-06,6.9E-06,7.0E-06
mptemp,19,2600,2800 mpdata,ctex,4,19,7.1E-06,7.1E-06
MPTEMP,,,,,,,,
mptemp,1,200,250,293,300,400,500
mpdata,ctey,4,1,1.5E-06,2.8E-06,3.3E-06,3.4E-06,4.0E-06,4.2E-06
mptemp,7,600,700,800,900,1000,1200
mpdata,ctey,4,7,4.5E-06,4.7E-06,4.9E-06,5.1E-06,5.3E-06,5.6E-06
mptemp,13,1400,1600,1800,2000,2200,2400
mpdata,ctey,4,13,6.0E-06,6.2E-06,6.5E-06,6.7E-06,6.9E-06,7.0E-06
mptemp,19,2600,2800
mpdata,ctey,4,19,7.1E-06,7.1E-06
MPTEMP,,,,,,,,
mptemp,1,200,250,293,300,400,500
mpdata,ctez,4,1,1.5E-06,2.8E-06,3.3E-06,3.4E-06,4.0E-06,4.2E-06
mptemp,7,600,700,800,900,1000,1200
mpdata,ctez,4,7,4.5E-06,4.7E-06,4.9E-06,5.1E-06,5.3E-06,5.6E-06
mptemp,13,1400,1600,1800,2000,2200,2400
mpdata,ctez,4,13,6.0E-06,6.2E-06,6.5E-06,6.7E-06,6.9E-06,7.0E-0 6 mptemp,19,2600,2800
mpdata,ctez,4,19,7.1E-06,7.1E-06
!Young's modulus
MPTEMP,,,,,,,,
mptemp,1,273,297,1210,1490,1670
mpdata,ex,4,1,4.8E+05,4.2E+05,3.7E+05,3.4E+05,2.7E+05
mp,prxy,4,0.19
mp,reft,4,1377
!Material 5
mp,dens,5,3.21e-15
!Thermal expansion
MPTEMP,,,,,,,,
mptemp,1,200,250,293,300,400,500
mpdata,ctex,5,1,1.5E-06,2.8E-06,3.3E-06,3.4E-06,4.0E-06,4.2E-06
mptemp,7,600,700,800,900,1000,1200

mpdata,ctex,5,7,4.5E-06,4.7E-06,4.9E-06,5.1E-06,5.3E-06,5.6E-06
mptemp,13,1400,1600,1800,2000,2200,2400
mpdata,ctex,5,13,6.0E-06,6.2E-06,6.5E-06,6.7E-06,6.9E-06,7.0E-06
mptemp,19,2600,2800
mpdata,ctex,5,19,7.1E-06,7.1E-06
MPTEMP,,,,,,,,
mptemp,1,200,250,293,300,400,500
mpdata,ctey,5,1,1.5E-06,2.8E-06,3.3E-06,3.4E-06,4.0E-06,4.2E-06
mptemp,7,600,700,800,900,1000,1200
mpdata,ctey,5,7,4.5E-06,4.7E-06,4.9E-06,5.1E-06,5.3E-06,5.6E-06
mptemp,13,1400,1600,1800,2000,2200,2400
mpdata,ctey,5,13,6.0E-06,6.2E-06,6.5E-06,6.7E-06,6.9E-06,7.0E-06
mptemp,19,2600,2800
mpdata,ctey,5,19,7.1E-06,7.1E-06
MPTEMP,,,,,,,,
mptemp,1,200,250,293,300,400,500
mpdata,ctez,5,1,1.5E-06,2.8E-06,3.3E-06,3.4E-06,4.0E-06,4.2E-06
mptemp,7,600,700,800,900,1000,1200
mpdata,ctez,5,7,4.5E-06,4.7E-06,4.9E-06,5.1E-06,5.3E-06,5.6E-06
mptemp,13,1400,1600,1800,2000,2200,2400
mpdata,ctez,5,13,6.0E-06,6.2E-06,6.5E-06,6.7E-06,6.9E-06,7.0E-06
mptemp,19,2600,2800 mpdata,ctez,5,19,7.1E-06,7.1E-06
!Young's modulus
MPTEMP,,,,,,,,
mptemp,1,273,297,1210,1490,1670
mpdata,ex,5,1,4.8E+05,4.2E+05,3.7E+05,3.4E+05,2.7E+05
mp,prxy,5,0.19
mp,reft,5,1355
!Material 6
mp,dens,6,3.21e-15
!Thermal expansion
MPTEMP,,,,,,,,
mptemp,1,200,250,293,300,400,500
mpdata,ctex,6,1,1.5E-06,2.8E-06,3.3E-06,3.4E-06,4.0E-06,4.2E-06
mptemp,7,600,700,800,900,1000,1200
mpdata,ctex,6,7,4.5E-06,4.7E-06,4.9E-06,5.1E-06,5.3E-06,5.6E-06
mptemp,13,1400,1600,1800,2000,2200,2400
mpdata,ctex,6,13,6.0E-06,6.2E-06,6.5E-06,6.7E-06,6.9E-06,7.0E-06
mptemp,19,2600,2800
mpdata,ctex,6,19,7.1E-06,7.1E-06
MPTEMP,,,,,,,,
mptemp,1,200,250,293,300,400,500
mpdata,ctey,6,1,1.5E-06,2.8E-06,3.3E-06,3.4E-06,4.0E-06,4.2E-06
mptemp,7,600,700,800,900,1000,1200
mpdata,ctey,6,7,4.5E-06,4.7E-06,4.9E-06,5.1E-06,5.3E-06,5.6E-06
mptemp,13,1400,1600,1800,2000,2200,2400
mpdata,ctey,6,13,6.0E-06,6.2E-06,6.5E-06,6.7E-06,6.9E-06,7.0E-06
mptemp,19,2600,2800

mpdata,ctey,6,19,7.1E-06,7.1E-06
MPTEMP,,,,,,,,
mptemp,1,200,250,293,300,400,500
mpdata,ctez,6,1,1.5E-06,2.8E-06,3.3E-06,3.4E-06,4.0E-06,4.2E-06
mptemp,7,600,700,800,900,1000,1200
mpdata,ctez,6,7,4.5E-06,4.7E-06,4.9E-06,5.1E-06,5.3E-06,5.6E-06
mptemp,13,1400,1600,1800,2000,2200,2400
mpdata,ctez,6,13,6.0E-06,6.2E-06,6.5E-06,6.7E-06,6.9E-06,7.0E-06
mptemp,19,2600,2800
mpdata,ctez,6,19,7.1E-06,7.1E-06
!Young's modulus
MPTEMP,,,,,,,,
mptemp,1,273,297,1210,1490,1670
mpdata,ex,6,1,4.8E+05,4.2E+05,3.7E+05,3.4E+05,2.7E+05
mp,prxy,6,0.19
mp,reft,6,1323
!Material 7
mp,dens,7,3.21e-15
!Thermal expansion
MPTEMP,,,,,,,,
mptemp,1,200,250,293,300,400,500
mpdata,ctex,7,1,1.5E-06,2.8E-06,3.3E-06,3.4E-06,4.0E-06,4.2E-06
mptemp,7,600,700,800,900,1000,1200
mpdata,ctex,7,7,4.5E-06,4.7E-06,4.9E-06,5.1E-06,5.3E-06,5.6E-06
mptemp,13,1400,1600,1800,2000,2200,2400
mpdata,ctex,7,13,6.0E-06,6.2E-06,6.5E-06,6.7E-06,6.9E-06,7.0E-06
mptemp,19,2600,2800
mpdata,ctex,7,19,7.1E-06,7.1E-06
MPTEMP,,,,,,,,
mptemp,1,200,250,293,300,400,500
mpdata,ctey,7,1,1.5E-06,2.8E-06,3.3E-06,3.4E-06,4.0E-06,4.2E-06
mptemp,7,600,700,800,900,1000,1200
mpdata,ctey,7,7,4.5E-06,4.7E-06,4.9E-06,5.1E-06,5.3E-06,5.6E-06
mptemp,13,1400,1600,1800,2000,2200,2400
mpdata,ctey,7,13,6.0E-06,6.2E-06,6.5E-06,6.7E-06,6.9E-06,7.0E-06
mptemp,19,2600,2800 mpdata,ctey,7,19,7.1E-06,7.1E-06
MPTEMP,,,,,,,,
mptemp,1,200,250,293,300,400,500
mpdata,ctez,7,1,1.5E-06,2.8E-06,3.3E-06,3.4E-06,4.0E-06,4.2E-06
mptemp,7,600,700,800,900,1000,1200
mpdata,ctez,7,7,4.5E-06,4.7E-06,4.9E-06,5.1E-06,5.3E-06,5.6E-06
mptemp,13,1400,1600,1800,2000,2200,2400
mpdata,ctez,7,13,6.0E-06,6.2E-06,6.5E-06,6.7E-06,6.9E-06,7.0E-06
mptemp,19,2600,2800
mpdata,ctez,7,19,7.1E-06,7.1E-06
!Young's modulus
MPTEMP,,,,,,,,
mptemp,1,273,297,1210,1490,1670

mpdata,ex,7,1,4.8E+05,4.2E+05,3.7E+05,3.4E+05,2.7E+05
mp,prxy,7,0.19
mp,reft,7,1284
!Material 8
mp,dens,8,3.21e-15
!Thermal expansion
MPTEMP,,,,,,,,
mptemp,1,200,250,293,300,400,500
mpdata,ctex,8,1,1.5E-06,2.8E-06,3.3E-06,3.4E-06,4.0E-06,4.2E-06
mptemp,7,600,700,800,900,1000,1200
mpdata,ctex,8,7,4.5E-06,4.7E-06,4.9E-06,5.1E-06,5.3E-06,5.6E-06
mptemp,13,1400,1600,1800,2000,2200,2400
mpdata,ctex,8,13,6.0E-06,6.2E-06,6.5E-06,6.7E-06,6.9E-06,7.0E-06
mptemp,19,2600,2800
mpdata,ctex,8,19,7.1E-06,7.1E-06
MPTEMP,,,,,,,,
mptemp,1,200,250,293,300,400,500
mpdata,ctey,8,1,1.5E-06,2.8E-06,3.3E-06,3.4E-06,4.0E-06,4.2E-06
mptemp,7,600,700,800,900,1000,1200
mpdata,ctey,8,7,4.5E-06,4.7E-06,4.9E-06,5.1E-06,5.3E-06,5.6E-06
mptemp,13,1400,1600,1800,2000,2200,2400
mpdata,ctey,8,13,6.0E-06,6.2E-06,6.5E-06,6.7E-06,6.9E-06,7.0E-06
mptemp,19,2600,2800
mpdata,ctey,8,19,7.1E-06,7.1E-06
MPTEMP,,,,,,,,
mptemp,1,200,250,293,300,400,500
mpdata,ctez,8,1,1.5E-06,2.8E-06,3.3E-06,3.4E-06,4.0E-06,4.2E-06
mptemp,7,600,700,800,900,1000,1200
mpdata,ctez,8,7,4.5E-06,4.7E-06,4.9E-06,5.1E-06,5.3E-06,5.6E-06
mptemp,13,1400,1600,1800,2000,2200,2400
mpdata,ctez,8,13,6.0E-06,6.2E-06,6.5E-06,6.7E-06,6.9E-06,7.0E-06
mptemp,19,2600,2800
mpdata,ctez,8,19,7.1E-06,7.1E-06
!Young's modulus
MPTEMP,,,,,,,,
mptemp,1,273,297,1210,1490,1670
mpdata,ex,8,1,4.8E+05,4.2E+05,3.7E+05,3.4E+05,2.7E+05
mp,prxy,8,0.19
mp,reft,8,1244
!Material 9
mp,dens,6,3.21e-15
!Thermal expansion
MPTEMP,,,,,,,,
mptemp,1,200,250,293,300,400,500
mpdata,ctex,9,1,1.5E-06,2.8E-06,3.3E-06,3.4E-06,4.0E-06,4.2E-06
mptemp,7,600,700,800,900,1000,1200
mpdata,ctex,9,7,4.5E-06,4.7E-06,4.9E-06,5.1E-06,5.3E-06,5.6E-06
mptemp,13,1400,1600,1800,2000,2200,2400

```
mpdata,ctex,9,13,6.0E-06,6.2E-06,6.5E-06,6.7E-06,6.9E-06,7.0E-06
mptemp,19,2600,2800
mpdata,ctex,9,19,7.1E-06,7.1E-06
MPTEMP,,,,,,,,
mptemp,1,200,250,293,300,400,500
mpdata,ctey,9,1,1.5E-06,2.8E-06,3.3E-06,3.4E-06,4.0E-06,4.2E-06
mptemp,7,600,700,800,900,1000,1200
mpdata,ctey,9,7,4.5E-06,4.7E-06,4.9E-06,5.1E-06,5.3E-06,5.6E-06
mptemp,13,1400,1600,1800,2000,2200,2400
mpdata,ctey,9,13,6.0E-06,6.2E-06,6.5E-06,6.7E-06,6.9E-06,7.0E-06
mptemp,19,2600,2800
mpdata,ctey,9,19,7.1E-06,7.1E-06
MPTEMP,,,,,,,,
mptemp,1,200,250,293,300,400,500
mpdata,ctez,9,1,1.5E-06,2.8E-06,3.3E-06,3.4E-06,4.0E-06,4.2E-06
mptemp,7,600,700,800,900,1000,1200
mpdata,ctez,9,7,4.5E-06,4.7E-06,4.9E-06,5.1E-06,5.3E-06,5.6E-06
mptemp,13,1400,1600,1800,2000,2200,2400
mpdata,ctez,9,13,6.0E-06,6.2E-06,6.5E-06,6.7E-06,6.9E-06,7.0E-06
mptemp,19,2600,2800
mpdata,ctez,9,19,7.1E-06,7.1E-06
!Young's modulus
MPTEMP,,,,,,,,
mptemp,1,273,297,1210,1490,1670
mpdata,ex,9,1,4.8E+05,4.2E+05,3.7E+05,3.4E+05,2.7E+05
mp,prxy,9,0.19
mp,reft,9,1213
asel,all
aglue,all
numcmp,area
numcmp,line
*SET,incc,1e-4
!mapped mesh fiber on the substrate
type,1
!mapped mesh the top surface of the fiber
lsel,s,line,,5
lsel,a,line,,13
lesize,all,,,4,,,,
lsel,s,line,,16
lsel,a,line,,15
lesize,all,,,1,,,,
lsel,s,line,,18
lsel,a,line,,17
lesize,all,,,1,,,,
lsel,s,line,,20
lsel,a,line,,19
lesize,all,,,1,,,,
lsel,s,line,,22
```

```
lsel,a,line,,21
lesize,all,,,1,,,,
lsel,s,line,,24
lsel,a,line,,23
lesize,all,,,1,,,,
lsel,s,line,,26
lsel,a,line,,25
lesize,all,,,1,,,,
lsel,s,line,,28
lsel,a,line,,27
lesize,all,,,1,,,,
!vertical direction
lsel,s,loc,y,2540+incc,h1-incc
lesize,all,,,25
asel,s,area,,1
aatt,2
amesh,all
asel,s,area,,2
aatt,3
amesh,all
asel,s,area,,3
aatt,4
amesh,all
asel,s,area,,4
aatt,5
amesh,all
asel,s,area,,5
aatt,6
amesh,all
asel,s,area,,6
aatt,7
amesh,all
asel,s,area,,7
aatt,8
amesh,all
asel,s,area,,8
aatt,9
amesh,all
!Free Mesh the graphite substrate
type,1
mat,1
smrt,6
mshape,1,2d
mshkey,0
asel,s,loc,y,incc,2540-incc
amesh,all
/SOLU
antype,0
```

```
kbc,0
time,1
nsubst,3
ldread,temp,1,,,,'Th-175um','rth',"
lsel,s,loc,y,-incc,incc
dl,all,,all,0
outres,all,last
allsel,all
solve
/status,solu
finish
```

APPENDIX I

TRANSIENT HEAT TRANSFER

```
finish
    /clear,nostart
    /prep7
    antype,trans
    cyl4,0,0,9525,,,,2540
    cylind,55,0,2540,2704,0,360
    cylind,55,0,2704,2711,0,360
    ET, 1, PLANE55
    ET, 2, SOLID70
    !defining graphite substrate material properties
    mp,dens,1,1.76e-15,,,,,
    !Thermal conductivity
    mptemp,1,298.2,516.5,518.2,519.3,524.3,608.7
    mpdata,kxx,1,1,1.180E+08,7.930E+07,8.580E+07,1.000E+08,7.330E+07,7.430E+07
    mptemp,7,614.3,836.5,840.4,856.5,1133.7,1142.1
    mpdata,kxx,1,7,7.280E+07,5.130E+07,6.290E+07,5.050E+07,3.030E+07,3.290E+07
    mptemp,13,1147.6,1157.1,1159.8,1260.9,1272.1,1580.4
    mpdata,kxx,1,13,2.940E+07,4.040E+07,3.950E+07,3.550E+07,3.300E+07,3.940E+07
    mptemp,19,1583.2,1585.9,1594.3,1602.6,1811,1813.7
    mpdata,kxx,1,19,4.100E+07,3.630E+07,3.260E+07,3.460E+07,3.520E+07,3.450E+07
    mptemp,25,1991.5,2091.5,2102.6,2108.2,2236,2238.7
    mpdata,kxx,1,25,2.860E+07,1.760E+07,1.950E+07,2.520E+07,1.890E+07,2.020E+07
    mptemp,31,2244.3,2247,2358.2,2369.3,2622,2641.5
    mpdata,kxx,1,31,1.720E+07,2.030E+07,2.710E+07,2.030E+07,1.720E+07,1.600E+07
    mptemp,37,2972.1,3002.6,3022.1
    mpdata,kxx,1,37,1.330E+07,1.230E+07,1.770E+07
    MPTEMP,,,,,,,,
    mptemp,1,298.2,516.5,518.2,519.3,524.3,608.7
    mpdata,kyy,1,1,1.180E+08,7.930E+07,8.580E+07,1.000E+08,7.330E+07,7.430E+07
    mptemp,7,614.3,836.5,840.4,856.5,1133.7,1142.1
    mpdata,kyy,1,7,7.280E+07,5.130E+07,6.290E+07,5.050E+07,3.030E+07,3.290E+07
    mptemp,13,1147.6,1157.1,1159.8,1260.9,1272.1,1580.4
    mpdata,kyy,1,13,2.940E+07,4.040E+07,3.950E+07,3.550E+07,3.300E+07,3.940E+07
    mptemp,19,1583.2,1585.9,1594.3,1602.6,1811,1813.7
    mpdata,kyy,1,19,4.100E+07,3.630E+07,3.260E+07,3.460E+07,3.520E+07,3.450E+07
    mptemp,25,1991.5,2091.5,2102.6,2108.2,2236,2238.7
    mpdata,kyy,1,25,2.860E+07,1.760E+07,1.950E+07,2.520E+07,1.890E+07,2.020E+07
    mptemp,31,2244.3,2247,2358.2,2369.3,2622,2641.5
    mpdata,kyy,1,31,1.720E+07,2.030E+07,2.710E+07,2.030E+07,1.720E+07,1.600E+07
    mptemp,37,2972.1,3002.6,3022.1
```

mpdata,kyy,1,37,1.330E+07,1.230E+07,1.770E+07
MPTEMP,,,,,,,,
mptemp,1,298.2,516.5,518.2,519.3,524.3,608.7
mpdata,kzz,1,1,1.180E+08,7.930E+07,8.580E+07,1.000E+08,7.330E+07,7.430E+07
mptemp,7,614.3,836.5,840.4,856.5,1133.7,1142.1
mpdata,kzz,1,7,7.280E+07,5.130E+07,6.290E+07,5.050E+07,3.030E+07,3.290E+07
mptemp,13,1147.6,1157.1,1159.8,1260.9,1272.1,1580.4
mpdata,kzz,1,13,2.940E+07,4.040E+07,3.950E+07,3.550E+07,3.300E+07,3.940E+07
mptemp,19,1583.2,1585.9,1594.3,1602.6,1811,1813.7
mpdata,kzz,1,19,4.100E+07,3.630E+07,3.260E+07,3.460E+07,3.520E+07,3.450E+07
mptemp,25,1991.5,2091.5,2102.6,2108.2,2236,2238.7
mpdata,kzz,1,25,2.860E+07,1.760E+07,1.950E+07,2.520E+07,1.890E+07,2.020E+07
mptemp,31,2244.3,2247,2358.2,2369.3,2622,2641.5
mpdata,kzz,1,31,1.720E+07,2.030E+07,2.710E+07,2.030E+07,1.720E+07,1.600E+07
mptemp,37,2972.1,3002.6,3022.1
mpdata,kzz,1,37,1.330E+07,1.230E+07,1.770E+07
!Specific heat
MPTEMP,,,,,,,,
mptemp,1,273,366,478,589,700,811
mpdata,c,1,1,8.290E+14,9.965E+14,1.177E+15,1.331E+15,1.470E+15,1.583E+15
mptemp,7,922,1033,1144,1255,1366,1447
mpdata,c,1,7,1.675E+15,1.746E+15,1.792E+15,1.821E+15,1.826E+15,1.846E+15
mptemp,13,1676,1694,1839,1868,2103,2232
mpdata,c,1,13,1.913E+15,2.052E+15,2.052E+15,2.014E+15,2.056E+15,2.056E+15
mptemp,19,2278,2555,2722,2778,3000,3077
mpdata,c,1,19,1.901E+15,2.131E+15,2.198E+15,2.190E+15,2.152E+15,1.800E+15
mptemp,25,3198,3221,3525,3656,3711,3719
mpdata,c,1,25,2.123E+15,2.114E+15,2.311E+15,2.500E+15,2.512E+15,2.341E+15
mptemp,31,3739,3767,3818,3905
mpdata,c,1,31,2.445E+15,2.755E+15,2.939E+15,3.203E+15
!defining SiC fiber material properties
mp,dens,2,3.2e-15,,,,,
!Thermal conductivity
MPTEMP,,,,,,,,
mptemp,1,195,300,888.8,889.8,1130,1133.2
mpdata,kxx,2,1,1.35E+08,1.35E+08,1.04E+08,1.03E+08,6.70E+07,6.66E+07
mptemp,7,1388.7,1389.6,1414.6,1528.3,1528.6,1800
mpdata,kxx,2,7,3.95E+07,3.95E+07,3.60E+07,2.49E+07,2.51E+07,1.32E+07
mptemp,13,1800.5,1801.1 mpdata,kxx,2,13,1.32E+07,1.35E+07
MPTEMP,,,,,,,,
mptemp,1,195,300,888.8,889.8,1130,1133.2
mpdata,kyy,2,1,1.35E+08,1.35E+08,1.04E+08,1.03E+08,6.70E+07,6.66E+07
mptemp,7,1388.7,1389.6,1414.6,1528.3,1528.6,1800
mpdata,kyy,2,7,3.95E+07,3.95E+07,3.60E+07,2.49E+07,2.51E+07,1.32E+07
mptemp,13,1800.5,1801.1
mpdata,kyy,2,13,1.32E+07,1.35E+07
MPTEMP,,,,,,,,
mptemp,1,195,300,888.8,889.8,1130,1133.2

```
mpdata,kzz,2,1,1.35E+08,1.35E+08,1.04E+08,1.03E+08,6.70E+07,6.66E+07
mptemp,7,1388.7,1389.6,1414.6,1528.3,1528.6,1800
mpdata,kzz,2,7,3.95E+07,3.95E+07,3.60E+07,2.49E+07,2.51E+07,1.32E+07
mptemp,13,1800.5,1801.1
mpdata,kzz,2,13,1.32E+07,1.35E+07
!Specific heat
MPTEMP,,,,,,,,
mptemp,1,286.2,296.36,298.15,300,400,500
mpdata,c,2,1,6.402E+14,6.615E+14,6.674E+14,6.729E+14,8.789E+14,9.848E+14
mptemp,7,600,700,800,900,1000,1100
mpdata,c,2,7,1.052E+15,1.100E+15,1.138E+15,1.171E+15,1.270E+15,1.297E+15
mptemp,13,1200,1300,1400,1500,1600,1700
mpdata,c,2,13,1.320E+15,1.340E+15,1.357E+15,1.371E+15,1.384E+15,1.395E+15
mptemp,19,1800,1900,2000,2100,2200,2300
mpdata,c,2,19,1.405E+15,1.414E+15,1.422E+15,1.429E+15,1.436E+15,1.442E+15
mptemp,25,2400,2500,2600,2700,2800,2900
mpdata,c,2,25,1.447E+15,1.452E+15,1.457E+15,1.461E+15,1.465E+15,1.469E+15
vsel,all
vglue,all
*SET,incc,1e-4
!mapped mesh SiC fiber
type,1
mat,2
lsel,s,loc,z,2711-incc,2711+incc
lesize,all,,,10,,,,
lsel,s,loc,z,2704+incc,2711-incc
lesize,all,,,1
lsel,s,loc,z,2540+incc,2704-incc
lesize,all,,,14,.2
asel,s,loc,z,2711-incc,2711+incc
amesh,all
vsel,s,loc,z,2704+incc,2711-incc
vsweep,all
asel,s,loc,z,2711-incc,2711+incc
aclear,all
lsel,s,loc,z,2540+incc,2704-incc l
esize,all,,,10,.2
vsel,s,loc,z,2540-incc,2704+incc
vsweep,all
!free mesh graphite substrate
type,2
mat,1
smrt,6
mshape,1,3d
mshkey,0
vsel,s,loc,z,-incc,2540+incc
vmesh,all
*DEL,_FNCNAME
```

*DEL,_FNCMTID
*SET,_FNCNAME,'laserpw'
*DIM,%_FNCNAME%,TABLE,6,21,1
!
! Begin of equation: $2.22*10^8*\exp(-2*M0/10000)$
*SET,%_FNCNAME%(0,0,1), 0.0, -999
*SET,%_FNCNAME%(2,0,1), 0.0
*SET,%_FNCNAME%(3,0,1), 0.0
*SET,%_FNCNAME%(4,0,1), 0.0
*SET,%_FNCNAME%(5,0,1), 0.0
*SET,%_FNCNAME%(6,0,1), 0.0
*SET,%_FNCNAME%(0,1,1), 1.0, -1, 0, 10, 0, 0, 0
*SET,%_FNCNAME%(0,2,1), 0.0, -2, 0, 8, 0, 0, -1
*SET,%_FNCNAME%(0,3,1), 0, -3, 0, 1, -1, 17, -2
*SET,%_FNCNAME%(0,4,1), 0.0, -1, 0, 2.22, 0, 0, -3
*SET,%_FNCNAME%(0,5,1), 0.0, -2, 0, 1, -1, 3, -3
*SET,%_FNCNAME%(0,6,1), 0.0, -1, 0, 0, 0, 0, 0
*SET,%_FNCNAME%(0,7,1), 0.0, -3, 0, 1, 0, 0, -1
*SET,%_FNCNAME%(0,8,1), 0.0, -4, 0, 1, -1, 2, -3
*SET,%_FNCNAME%(0,9,1), 0.0, -1, 0, 2, 0, 0, -4
*SET,%_FNCNAME%(0,10,1), 0.0, -3, 0, 1, -4, 3, -1
*SET,%_FNCNAME%(0,11,1), 0.0, -1, 0, 2, 0, 0, 2
*SET,%_FNCNAME%(0,12,1), 0.0, -4, 0, 1, 2, 17, -1
*SET,%_FNCNAME%(0,13,1), 0.0, -1, 0, 2, 0, 0, 3
*SET,%_FNCNAME%(0,14,1), 0.0, -5, 0, 1, 3, 17, -1
*SET,%_FNCNAME%(0,15,1), 0.0, -1, 0, 1, -4, 1, -5
*SET,%_FNCNAME%(0,16,1), 0.0, -4, 0, 1, -3, 3, -1
*SET,%_FNCNAME%(0,17,1), 0.0, -1, 0, 10000, 0, 0, -4
*SET,%_FNCNAME%(0,18,1), 0.0, -3, 0, 1, -4, 4, -1
*SET,%_FNCNAME%(0,19,1), 0.0, -1, 7, 1, -3, 0, 0
*SET,%_FNCNAME%(0,20,1), 0.0, -3, 0, 1, -2, 3, -1
*SET,%_FNCNAME%(0,21,1), 0.0, 99, 0, 1, -3, 0, 0
! End of equation: $2.22*10^8*\exp(-2*M0/10000)$
*dim,topf,table,19,1,1,temp
*set,topf(1,0),301,400,500,600,700,800,900,1000,1100,1200
*set,topf(1,1),1778.85,2437.64,2715.56,2948.22,3142.95,3330.36,3522.82,3508.02,3865.21,3883.71
*set,topf(11,0),1300,1400,1500,1600,1700,1800,1900,2000,2100
*set,topf(11,1),4188.66,4250.58,4487.25,4610.60,4800.84,4964.99,5150.39,5314.59,5495.84
*dim,sidef,table,19,1,1,temp
*set,sidef(1,0),301,400,500,600,700,800,900,1000,1100,1200
*set,sidef(1,1),682.74,975.78,1088.38,1179.88,1254.99,1326.61,1399.73,1390.83,1528.64,1532.99
*set,sidef(11,0),1300,1400,1500,1600,1700,1800,1900,2000,2100
*set,sidef(11,1),1649.70,1671.19,1760.99,1806.37,1877.83,1939.10,2008.38,2069.75,2137.19
*dim,tops,table,19,1,1,temp
*set,tops(1,0),301,400,500,600,700,800,900,1000,1100,1200
*set,tops(1,1),33.76,66.53,74.88,80.30,84.02,87.23,90.33,88.30,95.26,94.14
*set,tops(11,0),1300,1400,1500,1600,1700,1800,1900,2000,2100
*set,tops(11,1),99.62,99.59,103.47,104.78,107.57,109.79,112.35,114.65,117.03

```
*dim,sides,table,19,1,1,temp
*set,sides(1,0),301,400,500,600,700,800,900,1000,1100,1200
*set,sides(1,1),115.83,163.79,183.08,197.97,209.82,221.02,232.44,230.40,252.63,252.98
*set,sides(11,0),1300,1400,1500,1600,1700,1800,1900,2000,2100
*set,sides(11,1),271.89,275.24,289.91,297.36,309.19,319.44,331.11,341.54,353.12
/SOLU
kbc,1
deltim,0.001
time,0.1
outres,,all
autots,on
nsel,all
tunif,300
asel,s,loc,z,2711-incc,2711+incc
bfa,all,hgen,%laserpw%
SFA,all,1,CONV, %TOPF% ,300
asel,s,loc,z,2540+incc,2711-incc
sfa,all,1,conv,%sidef%,300
asel,s,area,,9
sfa,all,1,conv,%tops%,300
asel,s,loc,z,incc,2540-incc
sfa,all,1,conv,%sides%,300
asel,s,loc,z,-incc,incc
da,all,temp,300
asel,s,loc,z,2711-incc,2711+incc
SFA,all, ,Rdsf,.85, 1
asel,s,loc,z,2540+incc,2711-incc
SFA,all, ,rdsf,.85,2
asel,s,loc,z,incc,2540-incc
SFA,all, ,rdsf,.9,3
STEF,0.567E-07
radopt,.0,.0001,0,1000,.1,.1
spctemp,1,300
spctemp,2,300
spctemp,3,300
hemiopt,10
v2dopt,0,,0,200
allsel,all
solve
FINISH
/POST26
FILE,'file','rth','.'
/UI,COLL,1
NUMVAR,200 SOLU,191,NCMIT
STORE,MERGE
FILLDATA,191,,,,1,1
REALVAR,191,191
!*
```

```
NSOL,2,47,TEMP,, 1
STORE,MERGE
!*
NSOL,3,51,TEMP,, 2
STORE,MERGE
!*
NSOL,4,61,TEMP,, 3
STORE,MERGE
!*
NSOL,5,7,TEMP,, 4
STORE,MERGE
!*
NSOL,6,491,TEMP,, 5
STORE,MERGE
!*
NSOL,7,492,TEMP,, 6
STORE,MERGE
NSOL,8,795,TEMP,, 7
STORE,MERGE
!*
NSOL,9,800,TEMP,, 8
STORE,MERGE
!*
NSOL,10,989,TEMP,, 9
STORE,MERGE
```

APPENDIX J

LASER POWER VS. FIBER HEIGHT

```
finish
    /clear,nostart
    /filname,175um,1
    /prep7
    h1=2715
    !Substrate
    cylind,55,0,0,2533,0,360
    cylind,55,100,0,2533,0,360
    cylind,55,0,2533,2540,0,360
    cylind,55,100,2533,2540,0,360
    cylind,100,9525,0,2540,0,360
    !Fiber
    !7um
    cylind,55,0,2540,2547,0,360
    !49um
    cylind,55,0,2547,2589,0,360
    !91um
    cylind,55,0,2589,2631,0,360
    !133um
    cylind,55,0,2631,2673,0,360
    !175um
    cylind,55,0,2673,2715,0,360
    ET, 1, PLANE55
    ET, 2, SOLID70
    !defining graphite substrate material properties
    mp,dens,1,1.76e-15,,,,,
    !Thermal conductivity
    mptemp,1,298.2,516.5,518.2,519.3,524.3,608.7
    mpdata,kxx,1,1,1.180E+08,7.930E+07,8.580E+07,1.000E+08,7.330E+07,7.430E+07
    mptemp,7,614.3,836.5,840.4,856.5,1133.7,1142.1
    mpdata,kxx,1,7,7.280E+07,5.130E+07,6.290E+07,5.050E+07,3.030E+07,3.290E+07
    mptemp,13,1147.6,1157.1,1159.8,1260.9,1272.1,1580.4
    mpdata,kxx,1,13,2.940E+07,4.040E+07,3.950E+07,3.550E+07,3.300E+07,3.940E+07
    mptemp,19,1583.2,1585.9,1594.3,1602.6,1811,1813.7
    mpdata,kxx,1,19,4.100E+07,3.630E+07,3.260E+07,3.460E+07,3.520E+07,3.450E+07
    mptemp,25,1991.5,2091.5,2102.6,2108.2,2236,2238.7
    mpdata,kxx,1,25,2.860E+07,1.760E+07,1.950E+07,2.520E+07,1.890E+07,2.020E+07
    mptemp,31,2244.3,2247,2358.2,2369.3,2622,2641.5
    mpdata,kxx,1,31,1.720E+07,2.030E+07,2.710E+07,2.030E+07,1.720E+07,1.600E+07
    mptemp,37,2972.1,3002.6,3022.1
```

mpdata,kxx,1,37,1.330E+07,1.230E+07,1.770E+07
MPTEMP,,,,,,,,
mptemp,1,298.2,516.5,518.2,519.3,524.3,608.7
mpdata,kyy,1,1,1.180E+08,7.930E+07,8.580E+07,1.000E+08,7.330E+07,7.430E+07
mptemp,7,614.3,836.5,840.4,856.5,1133.7,1142.1
mpdata,kyy,1,7,7.280E+07,5.130E+07,6.290E+07,5.050E+07,3.030E+07,3.290E+07
mptemp,13,1147.6,1157.1,1159.8,1260.9,1272.1,1580.4
mpdata,kyy,1,13,2.940E+07,4.040E+07,3.950E+07,3.550E+07,3.300E+07,3.940E+07
mptemp,19,1583.2,1585.9,1594.3,1602.6,1811,1813.7
mpdata,kyy,1,19,4.100E+07,3.630E+07,3.260E+07,3.460E+07,3.520E+07,3.450E+07
mptemp,25,1991.5,2091.5,2102.6,2108.2,2236,2238.7
mpdata,kyy,1,25,2.860E+07,1.760E+07,1.950E+07,2.520E+07,1.890E+07,2.020E+07
mptemp,31,2244.3,2247,2358.2,2369.3,2622,2641.5
mpdata,kyy,1,31,1.720E+07,2.030E+07,2.710E+07,2.030E+07,1.720E+07,1.600E+07
mptemp,37,2972.1,3002.6,3022.1
mpdata,kyy,1,37,1.330E+07,1.230E+07,1.770E+07
MPTEMP,,,,,,,,
mptemp,1,298.2,516.5,518.2,519.3,524.3,608.7
mpdata,kzz,1,1,1.180E+08,7.930E+07,8.580E+07,1.000E+08,7.330E+07,7.430E+07
mptemp,7,614.3,836.5,840.4,856.5,1133.7,1142.1
mpdata,kzz,1,7,7.280E+07,5.130E+07,6.290E+07,5.050E+07,3.030E+07,3.290E+07
mptemp,13,1147.6,1157.1,1159.8,1260.9,1272.1,1580.4
mpdata,kzz,1,13,2.940E+07,4.040E+07,3.950E+07,3.550E+07,3.300E+07,3.940E+07
mptemp,19,1583.2,1585.9,1594.3,1602.6,1811,1813.7
mpdata,kzz,1,19,4.100E+07,3.630E+07,3.260E+07,3.460E+07,3.520E+07,3.450E+07
mptemp,25,1991.5,2091.5,2102.6,2108.2,2236,2238.7
mpdata,kzz,1,25,2.860E+07,1.760E+07,1.950E+07,2.520E+07,1.890E+07,2.020E+07
mptemp,31,2244.3,2247,2358.2,2369.3,2622,2641.5
mpdata,kzz,1,31,1.720E+07,2.030E+07,2.710E+07,2.030E+07,1.720E+07,1.600E+07
mptemp,37,2972.1,3002.6,3022.1
mpdata,kzz,1,37,1.330E+07,1.230E+07,1.770E+07 !mp,c,1,710e12
!Specific heat
MPTEMP,,,,,,,,
mptemp,1,273,366,478,589,700,811
mpdata,c,1,1,8.290E+14,9.965E+14,1.177E+15,1.331E+15,1.470E+15,1.583E+15
mptemp,7,922,1033,1144,1255,1366,1447
mpdata,c,1,7,1.675E+15,1.746E+15,1.792E+15,1.821E+15,1.826E+15,1.846E+15
mptemp,13,1676,1694,1839,1868,2103,2232
mpdata,c,1,13,1.913E+15,2.052E+15,2.052E+15,2.014E+15,2.056E+15,2.056E+15
mptemp,19,2278,2555,2722,2778,3000,3077
mpdata,c,1,19,1.901E+15,2.131E+15,2.198E+15,2.190E+15,2.152E+15,1.800E+15
mptemp,25,3198,3221,3525,3656,3711,3719
mpdata,c,1,25,2.123E+15,2.114E+15,2.311E+15,2.500E+15,2.512E+15,2.341E+15
mptemp,31,3739,3767,3818,3905
mpdata,c,1,31,2.445E+15,2.755E+15,2.939E+15,3.203E+15
vsel,all
vglue,all
numcmp,area

```
numcmp,volu
numcmp,line
*SET,incc,1e-4
!mapped mesh laser spot on sub
type,1
mat,1
!mapped mesh fiber on the substrate
!mapped mesh the top surface of the fiber
lsel,s,loc,z,2715-incc,2715+incc
lesize,all,,,10,,,,
asel,s,loc,z,2715-incc,2715+incc
amesh,all
!175um
lsel,s,loc,z,2673+incc,2715-incc
lesize,all,,,6
vsel,s,loc,z,2673+incc,2715-incc
vsweep,all
!133um
lsel,s,loc,z,2631+incc,2673-incc
lesize,all,,,6
vsel,s,loc,z,2631+incc,2673-incc
vsweep,all
!91um
lsel,s,loc,z,2589+incc,2631-incc
lesize,all,,,6
vsel,s,loc,z,2589+incc,2631-incc
vsweep,all
!49um
lsel,s,loc,z,2547+incc,2589-incc
lesize,all,,,6
vsel,s,loc,z,2547+incc,2589-incc
vsweep,all
!7um
lsel,s,loc,z,2540+incc,2547-incc
lesize,all,,,1
vsel,s,loc,z,2540+incc,2547-incc
vsweep,all
!mapped mesh inner 7um cylinder in the substrate
lsel,s,loc,x, -55-incc,55+incc
lsel,r,loc,z,2533+incc,2540-incc
lesize,all,,,1
vsel,s,volu,,2
vsweep,all
!mapped mesh the outskirts of the 7um cylinder in the substrate
lsel,s,line,,27
lsel,a,line,,25
lsel,a,line,,26
lsel,a,line,,28
```

```
lesize,all,,,10
asel,s,area,,31
amesh,all
vsel,s,volu,,9
vsweep,all
!free mesh the underlying 2533um cylinder of 55um in radius in the substrate
type,2
mat,1
smrt,8
mshape,1,3d
mshkey,0
vsel,s,volu,,1
vmesh,all
!free mesh outskirts of the underlying 2533um cylinder in the substrate
smrt,8
mshape,1,3d
mshkey,0
vsel,s,volu,,8
vmesh,all
!free mesh the rest of the substrate
smrt,8
mshape,1,3d
mshkey,0 vsel,s,volu,,10
vmesh,all
!clear the mesh of the top surface of fiber
asel,s,loc,z,2715-incc,2715+incc
aclear,all
!clear the mapped substrate surfaces of the outskirts of 7um
cylinder asel,s,area,,31
aclear,all
!clear and make 7um fiber
!vsel,s,loc,z,h1-incc,2715+incc
!vclear,all
!vsel,s,loc,z,h1-incc,2715+incc
!vdele,all,,1
!Specify BCs
*DEL,_FNCNAME
*DEL,_FNCMTID
*SET,_FNCNAME,'laserpw'
*DIM,%_FNCNAME%,TABLE,6,17,1
!
! Begin of equation: 3.24e8*exp(-2*M0/10000)
%_FNCNAME%(0,0,1)= 0.0, -999
%_FNCNAME%(2,0,1)= 0.0
%_FNCNAME%(3,0,1)= 0.0
%_FNCNAME%(4,0,1)= 0.0
%_FNCNAME%(5,0,1)= 0.0
%_FNCNAME%(6,0,1)= 0.0
```

%_FNCNAME%(0,1,1)= 1.0, -1, 0, 0, 0, 0, 0
%_FNCNAME%(0,2,1)= 0.0, -2, 0, 1, 0, 0, -1
%_FNCNAME%(0,3,1)= 0, -3, 0, 1, -1, 2, -2
%_FNCNAME%(0,4,1)= 0.0, -1, 0, 2, 0, 0, -3
%_FNCNAME%(0,5,1)= 0.0, -2, 0, 1, -3, 3, -1
%_FNCNAME%(0,6,1)= 0.0, -1, 0, 2, 0, 0, 2
%_FNCNAME%(0,7,1)= 0.0, -3, 0, 1, 2, 17, -1
%_FNCNAME%(0,8,1)= 0.0, -1, 0, 2, 0, 0, 3
%_FNCNAME%(0,9,1)= 0.0, -4, 0, 1, 3, 17, -1
%_FNCNAME%(0,10,1)= 0.0, -1, 0, 1, -3, 1, -4
%_FNCNAME%(0,11,1)= 0.0, -3, 0, 1, -2, 3, -1
%_FNCNAME%(0,12,1)= 0.0, -1, 0, 10000, 0, 0, -3
%_FNCNAME%(0,13,1)= 0.0, -2, 0, 1, -3, 4, -1
%_FNCNAME%(0,14,1)= 0.0, -1, 7, 1, -2, 0, 0
%_FNCNAME%(0,15,1)= 0.0, -2, 0, 2.22e8, 0, 0, -1
%_FNCNAME%(0,16,1)= 0.0, -3, 0, 1, -2, 3, -1
%_FNCNAME%(0,17,1)= 0.0, 99, 0, 1, -3, 0, 0
! End of equation: 3.24e8∗exp(-2∗M0/10000) !–¿
∗dim,topf,table,19,1,1,temp
∗set,topf(1,0),301,400,500,600,700,800,900,1000,1100,1200
∗set,topf(1,1),1778.85,2437.64,2715.56,2948.22,3142.95,3330.36,3522.82,3508.02,3865.21,3883.71
∗set,topf(11,0),1300,1400,1500,1600,1700,1800,1900,2000,2100
∗set,topf(11,1),4188.66,4250.58,4487.25,4610.60,4800.84,4964.99,5150.39,5314.59,5495.84
∗dim,sidef,table,19,1,1,temp
∗set,sidef(1,0),301,400,500,600,700,800,900,1000,1100,1200
∗set,sidef(1,1),682.74,975.78,1088.38,1179.88,1254.99,1326.61,1399.73,1390.83,1528.64,1532.99
∗set,sidef(11,0),1300,1400,1500,1600,1700,1800,1900,2000,2100
∗set,sidef(11,1),1649.70,1671.19,1760.99,1806.37,1877.83,1939.10,2008.38,2069.75,2137.19
∗dim,tops,table,19,1,1,temp
∗set,tops(1,0),301,400,500,600,700,800,900,1000,1100,1200
∗set,tops(1,1),33.76,66.53,74.88,80.30,84.02,87.23,90.33,88.30,95.26,94.14
∗set,tops(11,0),1300,1400,1500,1600,1700,1800,1900,2000,2100
∗set,tops(11,1),99.62,99.59,103.47,104.78,107.57,109.79,112.35,114.65,117.03
∗dim,sides,table,19,1,1,temp
∗set,sides(1,0),301,400,500,600,700,800,9 00,1000,1100,1200
∗set,sides(1,1),115.83,163.79,183.08,197.97,209.82,221.02,232.44,230.40,252.63,252.98
∗set,sides(11,0),1300,1400,1500,1600,1700,1800,1900,2000,2100
∗set,sides(11,1),271.89,275.24,289.91,297.36,309.19,319.44,331.11,341.54,353.12
FINISH
/SOLU
kbc,1
time,3
nsubst,3
!Specify BCs of fiber
asel,s,loc,z, h1-incc,h1+incc
bfa,all,hgen,%laserpw%
SFA,all,1,CONV, %topf% ,300
SFA,all, ,rdsf,.85, 1

```
asel,s,loc,z,2540+incc,h1-incc
sfa,all,1,conv,%sidef%,300
SFA,all, ,rdsf,.85, 2
!BCs of substrate
asel,s,area,,31
asel,a,area,,33
SFA,all,1,CONV, %tops% ,300
SFA,all, ,rdsf,.9, 3
asel,s,area,,8
asel,a,area,,9
SFA,all,1,CONV, %sides% ,300
SFA,all, ,rdsf,.9, 4
asel,s,loc,z,-incc,incc
da,all,temp,300
STEF,0.567E-07
radopt,.0,.0001,0,1000,.1,.1
spctemp,1,300
spctemp,2,300
spctemp,3,300
spctemp,4,300
hemiopt,10
v2dopt,0,,0,200
allsel,all
solve
FINISH
```

REFERENCES

[1] Cree Research Inc., Durham, NC 27713.

[2] Advanced Technology Materials, InC., 7 Commerce Drive, Danbury, CT 06810-4169, and Sterling Semiconductor.

[3] Shields V., Fekade K., and Spencer M. G., *Inst. Phys. Conf. Ser. NO.*, **137**, 21-24, IOP Publishing, Ltd. 1994.

[4] D. Jean, C. Duty, R. Johnson, S. Bondi, and W. J. Lackey, "Carbon Fiber Growth Kinetics and Thermodynamics Using Temperature Controlled LCVD," *Carbon*, **40** 9 1435-1445 2002.

[5] W.J. Lackey and Thomas L. Star, "Fabrication of Fiber -Reinforced Ceramic Composites by Chemical Vapor Infiltration: Processing, Structure and Properties," FIBER REINFORCED CERAMICS, Edited by K. S. Mazdiyasni, Noyes Publications, Park Ridge, New Jersey, p.397-450, 1990.

[6] Susan D. Allen, "Laser Chemical Vapor Deposition", Emergent Process Methods for High-Technology Ceramics, 8-10 Nov. Plenum Press, p. 397-413, 1984.

[7] S. D. Allen, R. Y. Jan, A. M. Mazuk, and S. D. Vernon, " Real Time Measurement of Deposition Initiation and Rate in Laser Chemical Vapor Deposition," *J. Appl. Phys.* **58** (1) p.327-331, July 1985.

[8] Jian Mi, Josh Gillespie, Ryan W. Johnson, Scott N. Bondi, and W. Jack Lackey, "Silicon Carbide Growth using Laser Chemical Vapor Deposition", *Solid Freeform Fabrication Symposium Proceedings*, Austin, TX, August, p. 510-523, 2003.

[9] J. Pegna, D. Messia, and W. H. Lee, "Trussed Structures: Freeform Fabrication Without the Layers," *Solid Freeform Fabrication Symposium Proceedings*,p.49-58, 1997.

[10] O. Lehmann and M. Stuke, "Generation of Three-Dimensional Free-Standing Metal Micro-Objects by Laser Chemical Processing," *Appl.Phys.A,*, **53**, p. 343-345, 1991.

[11] J. Maxwell, K. Larsson, M. Boman, P. Hooge, K. Willians, and P. Coane, "Rapid Prototyping of Functional Three-Dimensional Microsolenoids and electromagnets by High-Pressure Laser Chemical Vapor Deposition," *Solid Freeform Fabrication Symposium Proceedings*,p.529-536, 1998.

[12] M. Boman, H. Westberg, S. Johansson, and J. Schweitz, "Helica Microstructures Grown by Laser Assisted Chemical Vapour Deposition," *IEEE Micro-Electro mechanical Systems* p.162-167, 1992.

[13] R. Dean, P. Nordine, and C. Christodoulou, " A Novel Method for Fabricating 3D Helica THz Antennas Directly on Semiconductor Substrates," *SPIE Conf. on Terahertz Spectroscopy and Applications*, **3617**, p. 67-77, 1999.

[14] I. Zergioti, A. Hatziapostolou, E. Hontsopoulos, A. Zervaki, and G. Haidemnopoulos, "Pyrolytic Laser-Based Chemical Vapour Deposition of TiC Coatings," *Thin Solid Films*, **271**, p. 96-100, 1995.

[15] P. Chen and A. Visnapuu, "Atmospheric Laser Chemical Vapor Deposition of Iron-Carbon Composites," *J. Mater. Sci. Lett.*, **14**, p.1289-1291, 1995.

[16] Y. Hiura, Y. Morishige, and S. Kishida, "Laser chemical vapor deposition direct patterning of insulating film", *J. Appl. Phys.*, **69** (3) p.1744-1747,1991.

[17] L.Economikos, D. Kotecki, and R. Surprenant, "Controlling the Dimensions of Laser Chemical Vapor Deposited Metallurgy," *J. Electron. Packaging*, **118**, p. 7-10, 1996.

[18] J. Black, S. Doran, M. Rothschild, and D. Ehrlich, "Low-Temperature Laser Deposition of Tungsten by Silane- and Disilane-Assisted Reactions," *Appl. Phys. Lett.*, **56** (11), p. 1072-1074, 1990.

[19] G. Auvert, "Kinetics of mechanisms of CW Laser Induced Deposition of Metals for Microelectronics," *Appl. Surf. Sci.*, **43**, p. 47-53, 1989.

[20] B. Markwalder, M. Widmer, D. Braichotte, and H. Van Den Bergh, *J. Appl. Phys.*,**65** (6), p. 2470-2474, 1989.

[21] Modest M. Oprysko and Mark W. Beranek, " Nucleation effects in visible -laser chemical vapor deposition", *J. Vac. Sci. Technol. B*, **5**, (2), p. 496-503, Mar.-Apr. 1987.

[22] R. E. Terrill, K.H. Church, M. Moon, "Laser Chemical Vapor Deposition for Microelectronics Production", *IEEE Aerospace Conference*, Aspen, Co, Mar. 21-28, 1998, Proceedings. *Vol.1*, p.377-382, 1998.

[23] H. Moilanen, S. Leppavouri, and A. Uusimaki, "Laser-Induced Chemical Vapor Deposition in Piezoresistive Pressure Sensor Fabrication," *Sensor. Actuat. A-Phys.*, **41-42**, p. 150-155, 1994.

[24] H. Moilanen, L. Leppavouri, and A. Uusimaki, "Direct Writing of Piezoresistive Silicon Resistors Using Laser-Induced CVD," *J. Phys.*, **3**, (3), p. 457-464, 1993.

[25] M. Wanke, O. Lehmann, K. Muller, O. Wen, and M. Stuke, "Laser Rapid Prototyping of Photonic Band-Gap Micorstructrues," *Sciences*, **275**, p. 1284-1286, 1997.

[26] Pensl G., and Choyke W. J., *J., Physica B*, **185** 264-283 1993.

[27] Muller R. S., and Kamins T. I., *Device Electronics for Integrated Circuits*, Second Edition, Wiley, p. 54 1986.

[28] Humphreys R. G., Bimberg D., and Choyke W. J., *solid state comm.*, **39** 163-167 1981.

[29] Gaberstroh C., Helbig R., and Stein R. A., *J. of Appl. Phys.*, **76** 509-513 July 1994.

[30] Muench W. V., and Petterpaul E., *J. Appl.Phys.*, **48** 4831-4833 1977.

[31] Slack G. A., *J. Appl. Phys.*, **35** 3460-3466 1964.

[32] Son N. T., Chen W. M., Kordina O., Konstantinov A. O., Monemar B., Janzen E., Hofman D. M., Volm D., Drechsler M., and Meyer B. K., *Appl. Phys. Lett.*, **66** (9) 1074-1076 Feb. 1995.

[33] Muench W. V., and petterpaul E., *J. Appl. Phys.*, **48** (11) 4823-4825 Nov. 1977.

[34] Tachibana T., Kong H. S., Wang Y. C., and Davis R. F., *J. Appl. Phys.,***67** 6375-6381 1990.

[35] Schaffer W. J., Negley G. H., Irvin K. G., and palmour J. W., *MRS Symposium Proceedings*, **339** 595-600, MRS, Pittsburgh, PA 1994.

[36] Yamanaka M., Daiman H., Sakuma E., Misawa S., Yoshida S., *J. Appl. Phys.*, **61**, (2) 599-603 Jan. 1987.

[37] Larkin D. J., Neudeck P. G., Powell J. A., and Matus L. G., *Inst. Phys. Conf. Ser. No.* **137**, 51-54, IOP Publishing, Ltd. 1994.

[38] Agarwal A. K., Augustine G., Balakrishma V., Brandt C. D., Burke A. A., Chen L. S., Clarke R. C., Esker P. M., Hobgood H. M., Hopkins R. H., Morse A. W., Rowland L. B., Seshadri S., Siergiej R. R., Smith T. J. Jr., and Sriram S., *Tech. Dig. Int'l. Elect. Dev. Meeting*, p. 9.1.1-9.1.6 Dec. 1996.

[39] Patrick L., and Choyke W. J., *Physical Review B*, **2** (6) 2255-2256 Sep. 1970.

[40] Yoshida S., *Properties of Silicon Carbide*, (G. L. Harris, ed), p. 74, INSPEC, London, UK 1995.

[41] Lang-Luen Lee and Dah-Shyang Tsai, "Silicon Carbide Membranes Modified by Chemical Vapor Deposition using Species of Low Sticking Coefficients in a Silane/Acetylene Reaction System", *J. Am. Ceram. Soc*, **81** [1] 159-65 1998.

[42] W. Jack Lackey, Fohn A. Hanigofsky, Garth B. Freeman, Regina D. hardin and Ajit Prasad, "Continuous Fabrication of Silicon Carbide Fiber Tows by Chemical Vapor Deposition", *J. Am. Ceram. Soc.*, **78** [6] 1564-70 1995.

[43] 15. Ing-Chi Leu, Min-Hsiung Hon, and Yang-ming Lu, "Chemical Vapor Deposition of Silicon Carbide whiskers Activated by Elemental Nickel", *Journal of the Electrochemical Society*, **146** (1) 184-188 1999.

[44] 16. Z. R. Huang, B. Liang, D. L. Jiang, S. H. Tan, "Preparation of nanocrystal SiC powder by chemical vapour deposition", *Journal of materials Science*, **31** 4327-4332 1996.

[45] 17. Stefan Kavecky, Beata Janekova, Jana Madejova, Pavol Sajgalik, "Silicon carbide Powder Synthesis by Chemical Vapour Deposition form Silane/Acetylene Reaction system", *Journal of the European Ceramic Society*, **20** 1939-1946 2000.

[46] 18. Michael A. Pickering, Raymond L. Taylor and Foseph T. Keeley, "Chemically Vapor Deposited Silicon Carbide (SiC) for Optical Applications", *Nuclear Instruments and Methods in Physics Research A*, **291** 95-100 1990.

[47] T. Noda, H. Suzuki, H. Araki, F. Abe, M. Okada, "Formation of polycrystalline SiC film by excimer-laser chemical vapour deposition", *Journal of Materials Science Letters*, **11** 477-478, 1992.

[48] T. Noda, H. Suzuki, H. Araki, F. Abe, M. Okada, "Microstructure and growth of SiC film by excimer laser chemical vapour deposition at low temperatures", *Journal of Materials Science*, **28** [10] 2763-8, 1993.

[49] H. Suzuki, H. Araki, T. Noda, "Microstructure of SiC thin films produced on graphite by excimer-laser chemical vapour deposition", *Journal of Materials Science Letters*,**13**, 49-52, 1994.

[50] James E. Crocker, Haoyan Wei, Leon L. Shaw, and Harris L. Marcus, "SALDVI of SiC into Metal and Ceramic Powders", *Proceedings of the Solid Freeform Fabrication Symposium*, The University of Texas at Austin, p. 163-169, 2001.

[51] Ibrahim M. Ghayad, Erik Geiss, James E. Crocker, and Harrris L. Marcus, "Spot Joining of Si3N4 and SiC Ceramics Using Selective Area Laser Deposition (SALD) Technique", *Proceedings of the Solid Freeform Fabrication Symposium*, The University of Texas at Austin, p.170-174, 2001.

[52] Lianchao Sun, Kevin J. Jakubenas, James E. Crocker, Shay Harrison, Leon L. Shaw, and Harris L. Marcus, "In Situ Thermocouples in Macro-Components Fabricated Using SALD and SALDVI Techniques. I. Thermochemical Modeling", *Materials and Manufacturing Processes, Vol.***13**, No. 6, p. 859-882, 1998.

[53] Angus I. Kingon, Leonard J. Lutz, P. Liaw, and Robert F. Davis, "Thermodynamic Calculations for the Chemical Vapor Deposition of Silicon Carbide," *J. Am. Ceram. Soc.*, **66** [8] 558-566 1983.

[54] Chien C. Chiu, SeShu B. Desu, Zhi J. Chen, and Ching Yi Tsai, "Local Equlibrium Phase Diagrams: SiC Deposition in a Hot Wall LPCVD Reactor",*J. Mater. Res., Vol.* **9**, No.8, p. 2066-2071, 1994.

[55] George D. Papasouliotis, and Stratis V. Sotirchos, "On the Homogeneous Chemistry of the Thermal Decomposition of Methyltrichlorosilane", *J. Electrochem. Soc., Vol.* **141** No. 6 p. 1599-1611, 1994.

[56] Ching Yi Tsai, Seshu B. Desu, and Chien C. Chiu, "Kinetic Study of Silicon Carbide Deposited from Methylthrichlorosilane precursor", *J. Mater. Res., Vol.* **9**, No. 1, 1994.

[57] Theodore M. Besmann and Michael L. Johnson, "Kinetics of the Low-Pressure Chemical Vapor Deposition of Silicon Carbide", Proceedings of the International Symposium on Ceramic Materials and Components for Engineers (Las Vegas, NV, 1988) Edited by V. J. Tennery, *American Ceramic Society*, Westerville, OH, p. 443-456, 1989.

[58] Theodore M. Besmann, Brian W. Sheldon, Thomas S. Moss III, and Michael D. Kaster, "Depletion Effects of Silicon Carbide Deposition from Methylthrichlorosilane", *J. Am. Ceram. Soc.* **75** [10] p. 2899-2903, 1992.

[59] H. Sone, T. Kaneko, and N. Miyakawa, "In Situ Measurements and Growth Kinetics of Silicon Carbide Chemical Vapor Deposition form Methyltrichlorosilane", *J. Crys. Growth* **219** P. 245-252, 2000.

[60] F. Loumagne, F. Langlais, and R. Naslain, "Experimental kinetics study of the Chemical Vapor Deposition of SiC-Based Ceramics from CH_3SiCl_3/H_2 gas precursor", *J. Crys. Growth* **155** p. 198-204, 1995.

[61] D. Yu, A.B. Duncan, "Investigation of Induced Thermal and Fluid Transport Phenomena in Laser Assisted Chemical Vapor Deposition", ASME HEAT TRANSFER DIV PUBL HTD, ASME, FAIRFIELD, NJ, (USA), *vol.* **361** No. 4, p.183-191,1998.

[62] A. Kar and J. Mazumder, "Three-Dimensional Transient Thermal Analysis for Laser Chemical Vapor Deposition on Uniformly Moving Finite Slabs", *J. Appl. Phys.***65** (8), p. 923-2934, 1989.

[63] C. Garrido, B. Leon and M. Perez-Amor, " A Model to Calculate the Temperature Induced by a Laser", *J. Appl. Phys.* **69** (3), 1 February 1991.

[64] N. Arnold, P. B. Kargl, and D. Bauerle, "Modeling of Pyrolytic Laser Direct Writing: Noncoherent Structures and Instabilities", *J. Appl. Phys.* **82** (3), 1 August, 1997.

[65] Stephen M. Copley, "Mass Transport During Laser Chemical Vapor Deposition", *J.Appl. Phys.* **64** (4), 15 August, 1988.

[66] Chad Edward Duty, "Design, Operation and Heat and Mass Transfer Analysis of a Gas-Jet Laser Chemical Vapor Deposition". PhD dissertation, Gerorgia Institute of Technology, Mechanical Engineering, December 2001.

[67] Chad E. Duty, Ryan W. Johnson, Joshua Gillespie, Andrei Fedorov, and W. J. Lackey, "Heat and Mass Transfer Modeling of an Angled Gas-Jet LCVD System", *J. Appl. Phys. A* **77** (5) p. 697-705, 2003.

[68] D. L. Jean, "Design and Operation of an Advanced Laser Chemical Vapor Deposition System with On-line Control," Ph.D Dissertation, Georgia Institute of Technology 2001.

[69] Ryan William Johnson, "Process Development for the Manufacture of an Integrated Dispenser Cathode Assembly Using Laser Chemical Vapor Deposition". PhD dissertation, Gerorgia Institute of Technology, Mechanical Engineering, December 2005.

[70] Gary S. Fischman and William T. Petuskey, "Thermodynamic Analysis and Kinetic Implicatons of Chemical Vapor Deposition of SiC from Si-C-Cl-H Gas Systems," *J. Am. Ceram. Soc.*, **68** [4] 185-190 1985.

[71] G. Eriksson, "Thermodynamic Studies of High temperature Equilibria," *Acta Chem. Scand.*, **25** [7] 2651-58, 1971.

[72] T. M. Besmann, "SOLGASMIX-PV, A Computer Program to Calculate Equilibrium Relationships in Complex Chemical Systems," ORNL/TM-5575, Oak Ridge National Laboratory, Oak Ridge, TN, April 1997.

[73] JANAF Thermochemical Tables, 2^{nd} ed., Natl. Stand. Ref. Data. Ser. (U. S. Natil. Bur. Stand.), No. **37**, 1971.

[74] Chad. E. Duty, "Design, Operation, and Heat and Mass Transfer Analysis of a gas-jet Laser Chemical Vapor Deposition System," Ph.D. Dissertation, Georgia Institute of Technology, Nov 2001.

[75] David P. Stinton and W. J. Lackey, "Effect of Deposition Conditions on the Properties of Pyrolytic SiC Coatings for HTGR Fuel Particles," *Ceramic Bulletin*, **57** (6), 568, 1978.

[76] Thomas Strong Moss III: "The Chemical Vapor Deposition of Dispersed Phase Composites in the B-Si-C-H-Cl-Ar System," Ph.D. Dissertation, Georgia Institute of Technology, 1995.

[77] W. J. Lackey, S. Waidyaraman, B. N. Beckloff, T. S. Moss III, and J. S. Lewis, "Mass Transfer and Kinetics of the Chemical Vapor Deposition of SiC onto Fibers," *J. Mater. Res.*, Vol. **13**, No. 8, 2251-2261, August, 1998.

[78] Z. Kang, R. Johnson, J. Mi, S. Bondi, M. Jiang, J. Gillespie, W. J. Lackey, " Microstructure of Carbon fibers prepared by LCVD," *Carbon*, **42**, 2721-2727, 2004.

[79] W. J. Lackey, D. P. Stinton, G. A. Cerny, L. L. Fehrenbacher, and A. C. Schaffhauser, "Ceramic Coatings for Heat Engine Materials - Status and Future Needs," *Proceedings of International Symposium on Ceramic Components for Heat Engines*, October **17-31**, 1983, Hakone, Japan.

[80] Y. S. Touloukian, D. P. DeWitt, "Thermal Radiative Properties, Nonmetallic Solids," *Thermophysical Properties of Matter*, Volume **8**, 806-807, 1972.

[81] Y. S. Touloukian, R. W. Powell, C. Y. Ho, P. G. Klemens, "Thermal Conductivity, Nonmetallic Solids," *Thermophysical Properties of Matter*, Volume **2**, 22-23, 1970.

[82] Y. S. Touloukian, E. H. Buyco, "Specific heat, Nonmetallic Solids," *Thermophysical Properties of Matter*, Volume **5**, 10-14, 1970.

[83] Y. S. Touloukian, R. W. Powell, C. Y. Ho, P. G. Klemens, "Thermal Conductivity, Nonmetallic Solids," *Thermophysical Properties of Matter*, Volume **2**, 585-588-23, 1970.

[84] Y. S. Touloukian, E. H. Buyco, "Specific heat, Nonmetallic Solids," *Thermophysical Properties of Matter*, Volume **5**, 448-450, 1970.

[85] Michael Bauccio, "ASME Materials Reference Book," 2nd Edition, *The Mateirals Information Society*, ASM International, Materials Park, OH 44073-0002, 284-286,1994.

[86] Y. S. Touloukian, R. K. Kirby, R. E. Taylor, T. Y. R. Lee, "Thermal Expansion, Nonmetallic Solids," *Thermophysical Properties of Matter*, Volume **13**, 873.

[87] Waren M. Rohsenow, James P. Hartnett, Ejup N. Ganic, "Handbook of Heat Transfer Fundamentals," Second Edition, 6-24, 1985.

[88] Waren M. Rohsenow, James P. Hartnett, Ejup N. Ganic, "Handbook of Heat Transfer Fundamentals," Second Edition, 6-19, 1985.

VITA

Jian Mi , the daughter of Zhonghua Mi and Yanglin Li, was born in Beijing, China. She attended Tsinghua high school and graduated in 1994. Then she entered Tsinghua University in Beijing in the fall of 1994 and began to pursue her bachelor degree in Mechanical Engineering department. She got her Bachelor of Engineering degree in the fall of 1999. Then she worked for the charity organization of Hope Project of China for almost one year. In August of 2000, she was admitted as a Ph.D student by Mechanical Engineering Department of SUNY-Stony Brook. In January of 2001, she transferred from Stony Brook to Mechanical Engineering department of Georgia Institute of Technology to pursue her Ph.D degree. Her Ph.D advisor at Georgia Tech is Dr. Jack Lackey.